Time-resolved and equilibrium resonant X-ray studies of nematicity in cuprate superconductors

by

Naman Kumar Gupta

A thesis
presented to the University of Waterloo
in fulfillment of the
thesis requirement for the degree of
Doctor of Philosophy
in
Physics

Waterloo, Ontario, Canada, 2025

© Naman Kumar Gupta 2025

Examining Committee Membership

The following served on the Examining Committee for this thesis. The decision of the Examining Committee is by majority vote.

External Examiner:	Alex Frañó Associate Professor, Department of Physics, University of California, San Diego
Supervisor:	David Hawthorn Professor, Department of Physics and Astronomy, University of Waterloo
Internal Member:	Roger Melko Professor, Department of Physics and Astronomy, University of Waterloo
Internal-External Member:	Adam Wei Tsen Associate Professor, Department of Chemistry, University of Waterloo
Other Member(s):	Rob Hill Associate Professor, Department of Physics and Astronomy, University of Waterloo

Author's Declaration

This thesis consists of material all of which I authored or co-authored: see Statement of Contributions included in the thesis. This is a true copy of the thesis, including any required final revisions, as accepted by my examiners.

I understand that my thesis may be made electronically available to the public.

Statement of Contributions

This thesis primarily draws from three published papers (Refs. [1], [2], [3]), one currently under submission (Ref. [4]) and an advanced draft nearing submission. The material from these papers is integrated into Chapters 5, 6, 7, and 8 respectively. I am the sole first author on Ref. [2, 3] and shared first author on Ref. [1, 4].

In Chapter 5 adapted from Ref. [1], I worked with Martin Bluschke on data collection, data analysis, figure preparation and writing of the manuscript.

In Chapters 6 and 7 adapted from Ref [2] and [3], I designed the uniaxial strain device, performed data collection, data analysis, figure preparation and authored significant portions of the manuscripts, collaborating closely with my supervisor and incorporating feedback from co-authors and/or anonymous reviewers. Chapter 6 includes new datasets and additional analyses not found in Ref. [2] which is contained in an advanced draft of a manuscript nearing submission.

In Chapter 8, adapted from Ref. [4], is a collaboration between our group and Kyle Shen's group from Cornell University. I conceived of key experiments, identified the anisotropy in the peak shape, conducted majority of resonant scattering experiments, and contributed to data analysis. I contributed to the writing of the manuscript which was primarily drafted by Kyle Shen and David Hawthorn. A modified version of that manuscript highlighting my contributions is adapted as Chapter 8.

Minor modifications, such as adding section headings and repositioning supplementary sections for improved organization, have been made to enhance the overall structure of the thesis. All other chapters were authored by me for this thesis.

Abstract

Attracting four decades of experimental and theoretical investigations since the discovery of high-temperature superconductivity, cuprates have become an essential benchmark for the exploration of intertwined electronic symmetry-breaking phases such as superconductivity, magnetism, nematicity, charge or spin density wave order in a wider class of quantum materials. Understanding how these phases are intertwined is of general and fundamental interest to a wide range of quantum materials. This doctoral work attempts to disentangle and tune charge density wave (CDW) order and nematicity by studying their response under photo-induced excitation, variable hole-doping, compressive uniaxial stress, and in-plane magnetic fields.

Electronic nematicity refers to a breaking of rotational symmetry of the electronic structure from four-fold to two-fold in a manner that is not a straightforward result of crystalline symmetry. In the past, utilizing the element- and orbital-specific sensitivity of resonant X-ray scattering (RXS) our group has established electronic nematicity of Cu $3d$ orbitals in stripe-ordered cuprates, $(\mathrm{La}, M)_2\mathrm{CuO}_4$ where M = Nd, Sr, Eu and Ba. Extending equilibrium RXS work, here we use pump-probe time-resolved RXS to investigate non-equilibrium dynamics of $Q = 0$ nematic order and its association with both CDW order and lattice dynamics in $\mathrm{La}_{1.65}\mathrm{Eu}_{0.2}\mathrm{Sr}_{0.15}\mathrm{CuO}_4$. Harnessing the time-domain contrast between lattice and electronic degrees of freedom to disentangle signatures of lattice anisotropies and nematicity, we establish time-resolved RXS as an effective probe of nematicity dynamics. Comparing the pump-induced dynamics of nematic and CDW orders highlights their electronic origin and provides evidence that the CDW amplitude melts without the generation of significant topological defects, in contrast to other cuprates.

Navigating the cuprate phase diagram from heavily underdoped to overdoped regimes, we probe the relationship between electronic nematicity of the Cu $3d$ orbitals, charge order, superconductivity, and the pseudogap phase. In $(\mathrm{La}, \mathrm{Sr}, \mathrm{Nd}, \mathrm{Eu})_2\mathrm{CuO}_4$, we find evidence for vanishing electronic nematicity beyond the pseudogap phase, either by raising the temperature through the pseudogap onset temperature T^* or increasing doping through the pseudogap critical point, p^*. These results establish a clear link between electronic nematicity, the pseudogap, and its associated quantum criticality in overdoped cuprates. In heavily underdoped samples, however, we learn that nematic order is saturated, rendering it undetectable in equilibrium RXS. With the aid of non-equilibrium, time-resolved RXS, we find that nematic order remains present and detected in a sub-picosecond recovery. This underscores the complex nature of nematic phases, highlighting the importance of time-resolved experiments in disentangling electronic, lattice and spin degrees of freedom on ultrafast timescales.

Spin and charge density wave order in the cuprates are known to compete with superconductivity. We examine the interplay between structure and the formation of CDW order in the $La_{1.475}Nd_{0.4}Sr_{0.125}CuO_4$ by applying uniaxial stress to distort the structure and influence the formation of CDW order. We discover that the application of uniaxial stress along the Cu-O bond direction suppresses the CDW order, but does so only for CDW order propagating parallel to the applied stress. Providing insights into how CDW, superconductivity, nematicity, and structure are related and can be tuned relative to one another in cuprates.

Finally, we utilize RXS on thin films of bilayer superconductor $La_3Ni_2O_7$ to uncover the detailed magnetic structure of the antiferromagnetic parent state. We identify that the alternating magnetic moments exhibits a unidirectional character, being oriented parallel to the NiO_2 planes and perpendicular to the propagation direction of the spin-density-wave (SDW) order. The stripes form anisotropic domains with shorter correlation lengths perpendicular versus parallel to Q_{SDW}, revealing nanoscale rotational and translational symmetry breaking analogous to the cuprate superconductors.

Acknowledgements

Dave, words cannot express my gratitude for you. It is probably accidental good deeds from my past lives that we crossed paths. In all sincerity, thank you for your trust, patience, understanding, kindness, and guidance. Midst turbulence of all kinds in the last six years, including a world pandemic, you stood as a beacon of inspiration and gave a reason to keep marching on. I lucked out with you, thank you for everything!

I would like to thank my group members for always having my back during last minute sample preparations. Thank you Rantong and Mike for covering up potholes I leave during my haphazard workflow, you guys kept the show running. Thanks Chris, for initial days of graduate life, its all a blur now but I have a beard just like yours now, maybe it's soft X-ray radiation induced. When I started, I was adopted by theorists, my pseudo-group members. Thanks Kai for long walks into multi-dimensional, topological rabbit holes. Thanks Darren, Daniel and Alex, you guys were the spark in office, along with the explosive flames of Aritro. I will cherish that one and half year we had, when life was simple, and fun times were more frequent that we wanted. Shout out to Jen, Archana and Kai, for co-founding the Quantum Matter GradTalks – we had a good run, 21 sessions (insane!).

Thank you Ronny! Thank you Teak, Hoyoung, Enrico – you guys are the real rockstars! None of the synchrotron-based magic happens without you. Thank you Hiruy, I told you one day the strain would work. It took 5 years but it did, and maybe more to come, your insights and finesse brought the strain device to fruition. Thank you Stefan for trusting me with the keys to 335, I always see you as a cool uncle. Thanks to sample growth folks, and collaborators from all around, especially Martin, Chris, Mingu and Byjune Kim. I gravitate towards caffeine-maniac-lone-wolf behavior at synchrotrons, but working with you is made me rethink the value in team efforts.

Thank you to my advisory committee, Michel, Roger, and Rob. I have learned greatly about the scientific method through your feedback and comments in every meeting. Thank you Michel for not compromising on the standards even if it took me time. Thank you Rob for grounded experimental perspective throughout years. And yes, the cool dude from Perimeter, thank you Roger – for giving me a secret office (Does Dave know about it? Now he does heh). Thank you for introducing me to PIQuIL and welcoming me like one of yours. I appreciate it a lot. I cherish our categorical discussions about emergence and universality – something tells me we will collaborate in the future. You keep a sports-like fun alive in physics, kudos!

Lots of friends who kept sanity alive in zombie town, thank you Gyan and Aritro for keeping the rebel in me alive. The alter-ego still remains strong. Thank you 436 gang,

Pranav, Abhinav, Sunidhi, Yash for feeding me and making covid times livable. A sweet aggressive belly rub for Noah (wherever you are).

Big hearty thank you for friends and family back home. Jay, Tanmay, Vishal, Abhinandan, Mayank, Purvaj, Rohit and list goes on. Thank you Nana and Nani for so much love and blessings. And finally, Ma, Papa, and Nipun – this is all you, the origin story, you didn't give up on me. Thank you for always having my back! It looks like I might get this degree after all, we'll see.

Dedication

To my parents, who piggybacked me through the muddy part of the hike. I am enjoying this scenic viewpoint only because of you.

Table of Contents

Examining Committee ii

Author's Declaration iii

Statement of Contributions iv

Abstract v

Acknowledgements vii

Dedication ix

List of Figures xv

1 Introduction and Overview 1

2 Physics of cuprates and nematicity 5

2.1 Intertwined electronic phases in cuprates 7

2.1.1 Charge density wave (CDW) order 9

2.1.2 Low-temperature structual distortions 10

2.1.3 Pseudogap and Quantum Criticality 11

2.2 Nematic phases of matter 13

2.2.1 Motivation from liquid crystals 13

2.2.2 Electronic nematic order in cuprates superconductors 14
2.2.3 Electronic nematicity and possible mechanisms 14
2.3 Probing electronic nematicity using resonant soft X-ray scattering 15
2.3.1 On-resonance (001) Bragg peak 16
2.4 Motivation for our studies 19
2.4.1 Immediate future directions 22

3 Resonant soft X-ray Scattering **23**
3.1 Overview 23
3.2 X-rays and their interaction with matter 24
3.2.1 X-rays: Waves, photons, and synchrotron 24
3.2.2 Diffraction by an electronic distribution 25
3.2.3 Real and Reciprocal space 26
3.3 Theory of Resonant X-ray Scattering 28
3.3.1 A second order process 28
3.3.2 A quantum mechanical approach 28
3.3.3 Symmetry of scattering tensor and Orbital sensitivity 32
3.4 Time-Resolved Resonant X-ray Scattering 37
3.4.1 Motivation for a time-resolved probe 37
3.4.2 Introduction to tr-RXS 38
3.4.3 Mechanism of Laser Pump Excitation 39
3.4.4 Non-Equilibrium State and Relaxation Dynamics 39
3.5 Limitations of soft light and geometries 40

4 Synchrotron radiation and experimental setup **41**
4.0.1 Introduction 41
4.0.2 REIXS beamline at the Canadian Lightsource 43
4.0.3 Diffractometer geometry and motion stages at CLS 44

4.0.4 Detectors at CLS and scanning protocols . . . 46
4.0.5 High-field Diffractometer at BESSY . . . 46
4.1 X-ray Free Electron Lasers (XFELs) . . . 47
4.1.1 SSS beamline at the PAL XFEL . . . 48
4.1.2 Instrumental setup and configuration . . . 49
4.1.3 Spatial and Temporal Overlap . . . 49
4.1.4 Detector and Goniometer Geometry . . . 50
4.1.5 Experimental procedure for a pump-probe experiment . . . 50
4.2 Sample Preparation . . . 51
4.2.1 Determining crystallographic axes: Laue Diffraction . . . 52
4.2.2 Aligning real and reciprocal axes . . . 54
4.2.3 Mounting samples: Uniaxial stress device . . . 58

5 Time-resolved Nematicity Dynamics in Eu-LSCO 60
5.1 Overview . . . 60
5.2 Introduction . . . 61
5.2.1 Time-resolved resonant X-ray scattering (tr-RXS) . . . 64
5.3 Results . . . 65
5.4 Discussion . . . 69
5.4.1 Characterization of Q=(001) equilibrium temperature dependence. . 73
5.4.2 High-fluence pump-induced dynamics at Q=(001) . . . 74
5.4.3 Charge density wave detection at Q_{CDW} . . . 75
5.4.4 Time trace fitting schemes . . . 76
5.5 Experimental Procedure . . . 77

6 Evolution of nematic order with doping in stripe-ordered cuprates 82
6.1 Overview . . . 82
6.2 Introduction . . . 83

6.3 Methods . . . 86
6.4 Experimental procedure . . . 88
6.4.1 Experimental setup . . . 88
6.4.2 Data collection and analysis . . . 90
6.5 Results . . . 92
6.5.1 Low temperature structural distortions with doping . . . 92
6.5.2 Doping-Temperature evolution of electronic nematicity . . . 93
6.5.3 In Eu-LSCO and LBCO . . . 95
6.5.4 Nematicity dynamics via tr-RXS in Eu-LSCO . . . 97
6.5.5 Evolution of Charge Density Wave (CDW) order . . . 98
6.5.6 Nematicity and superconductivity . . . 100
6.6 Discussion . . . 102
6.7 Conclusions . . . 104

7 Tuning charge order and nematicity in cuprates via uniaxial strain 106
7.1 Overview . . . 106
7.2 Introduction . . . 107
7.3 Uniaxial Strain Device . . . 109
7.3.1 Experimental Procedure . . . 109
7.3.2 Measuring strain via structural Bragg peak displacements . . . 112
7.4 Results . . . 113
7.5 Uniaxial stress along [110] direction . . . 119
7.6 Conclusion . . . 120
7.7 X-ray absorption under uniaxial stress . . . 120

8 Anisotropic Spin Stripe Domains in Bilayer $La_3Ni_2O_7$ 121
8.1 Overview . . . 121
8.2 Introduction . . . 122

8.3 Measurement of Spin Configuration 125
8.4 Anisotropic, Unidirectional Magnetic Domains 126
8.5 Probing Magnetic Domain walls 127
8.6 Discussion 130
8.7 Materials and Methods 130

9 Conclusions **131**

References **133**

List of Figures

2.1 Crystal and electronic structure of cuprate superconductors 6
2.2 Cuprate Phase Diagram 8
2.3 Charge ordering in cuprates 9
2.4 Low-T structure of La-based cuprates 11
2.5 Evidence of quantum criticality 12
2.6 Nematic phase 13
2.7 Melting of a stripe phase and Pomeranchuk instability 16
2.8 Electronic nematicity as a measure of orbital asymmetry 17
2.9 Energy dependence of the (001) peak at the O K (a) and Cu L (b) edges . 18
2.10 Temperature dependence of the (001) Bragg peak intensity 19

3.1 The scattering geometry in the lab and crystal frame 27
3.2 Schematic representation of resonant and non-resonant scattering 29
3.3 Energy dependence of the atomic scattering form factors 32
3.4 On resonance orbital sensitivity in REXS 33
3.5 Azimuthal dependence of the (001) Bragg peak intensity 35
3.6 The SSS scattering chamber 38

4.1 Synchrotron radiation source 42
4.2 The RSXS scattering chamber 43
4.3 Motion stages and scattering geometry 45

4.4 The BESSY scattering chamber . . . 47
4.5 The SSS scattering chamber . . . 48
4.6 Setup for backscattering Laue diffraction geometry for single crystal orientation. . . . 52
4.7 Laue scattering images in back-scattering geometry . . . 53
4.8 Wire saw machine for cutting samples . . . 55
4.9 Top post cleaving . . . 56
4.10 Sample polishing . . . 57
4.11 Finished product, images under a microscope. . . . 59

5.1 $La_{1.65}Eu_{0.2}Sr_{0.15}CuO_4$ structure, equilibrium RXS results and tr-RXS experiment . . . 63
5.2 Ultrafast Nematicity in Eu-LSCO . . . 64
5.3 Temperature series at low fluence . . . 66
5.4 Comparison of CDW and nematicity dynamics . . . 68
5.5 Fluence dependence of $Q = (001)$ tr-RXS intensity . . . 70
5.6 Q=(001) equilibrium temperature dependence . . . 73
5.7 High fluence dynamics at O K resonances . . . 74
5.8 Charge scattering at Q_{CDW} . . . 75
5.9 Modelling of electronic and lattice dynamics . . . 76
5.10 Exponential model for electronic recovery dynamics . . . 80
5.11 Equilibrium XAS at O K . . . 81

6.1 Structural distortions and nematicity in Eu-LSCO . . . 85
6.2 Temperature dependence of (001) Bragg peaks in Nd-LSCO . . . 89
6.3 Evolution of electronic nematic order in Nd-LSCO . . . 94
6.4 Evolution of electronic nematic order in La-based cuprates . . . 96
6.5 Time-resolved signatures of nematicity in Eu-LSCO . . . 97
6.6 Tracking CDW order with doping in Nd-LSCO . . . 99

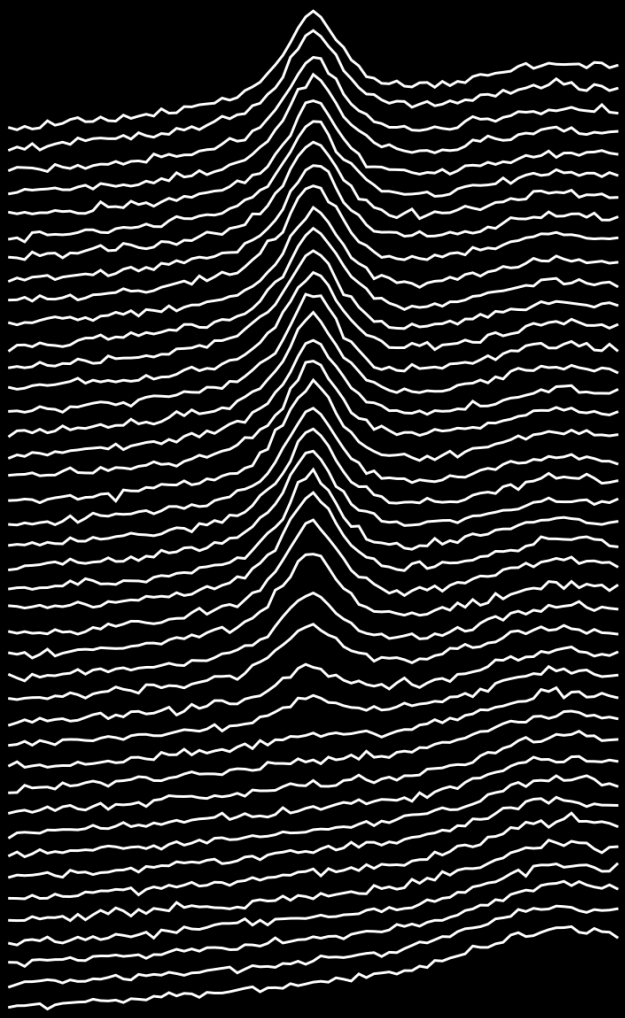
6.7 Tracking CDW order with doping in Eu-LSCO 101
6.8 Cuprate Phase Diagram 103

7.1 The crystal structure of $(La,M)_2CuO_4$ 108
7.2 Schematic of the uniaxial stress device 110
7.3 Schematic of uniaxial stress device in CLS scattering chamber 111
7.4 Characterizing strain percentage 112
7.5 Temperature dependence of the (0 0 1) Bragg peak at apical O-K edge under varying strain 114
7.6 Response of CDW Bragg peaks to applied uniaxial stress along bond direction 115
7.7 Temperature dependence of the structural-nematic (0 0 1) Bragg peaks for planar and apical atoms 116
7.8 Response of CDW Bragg peaks to applied uniaxial stress along non-bond direction 119
7.9 X-ray absorption under strain 120

8.1 Crystal structure and SDW order in $La_3Ni_2O_7$ 124
8.2 Azimuthal polarization dependence of SDW peak 125
8.3 Anisotropic Bragg peaks indicative of stripe-like SDW domains. 127
8.4 SDW order domain walls and polarization as a function of temperature . . 129

A painter should begin every canvas with a wash of black, because all things in nature are dark except where exposed by the light.

– Leonardo da Vinci



NEMATICITY

Chapter 1

Introduction and Overview

Strong correlations between valence electrons provide suitable conditions for spontaneous symmetry-breaking giving rise to intertwined electronic phases such as superconductivity, magnetism, nematicity, charge or spin density wave order. Transition metal oxides, such as cuprate superconductors, provide an excellent platform to (1) *host* such exotic quantum phases owing to wide choice between strongly correlated transition metal $3d$ state in isostructural compounds, (2) *study* intertwined phases in bulk single crystal robust to numerous experimental techniques ranging from transport to neutron scattering, and (3) *manipulate* them in a controlled fashion via chemical substitutions, epitaxial growths, uniaxial stress, photoexcitations, and magnetic fields as external perturbations.

Understanding the physics of cuprate superconductors has remained a central challenge in modern condensed matter physics. Unconventional superconductivity emerges in cuprates as holes are doped in the parent Mott insulating state. Since the discovery of high-temperature superconductivity in quasi-two-dimensional copper-oxide (cuprate) lattices, generations of theoretical and experimental groups have been captivated by the complex quantum phases of matter that emerge as functions of external perturbations. Our objective is to elucidate and disentangle the interconnected physics of charge, spin, and orbital textures, aiming to uncover potential links and universalities among these interactions. Thereby advancing and complementing existing studies through developing tuning mechanisms to control these quantum states of matter.

In Chapter 2, we discuss the physics of cuprate high-temperature superconductors as a quintessential example of the role of intertwined electronic orders in complex materials. Recent studies have shown that charge density wave (CDW) order, a spatial modulation of electronic charge, is a prevalent phase in cuprates, coexisting with and even competing

with superconductivity. This competition manifests as a suppression of the superconducting transition temperature where CDW order is strongest, while the onset of superconductivity likewise diminishes the CDW amplitude. In addition to CDW order, cuprates exhibit electronic nematicity which is characterized by the breaking of rotational symmetry in the electronic structure, from fourfold to twofold, often either spontaneously or through symmetry-breaking lattice distortions inherent to many cuprate materials. Nematic order is significant as it interacts with CDW order to favour unidirectional, stripe-like charge arrangements along specific crystalline axes, further influencing superconductivity. This interaction yields a complex system of coupled orders, where lattice distortions, electronic nematicity, CDW, superconductivity, and potentially other symmetry-breaking states such as inversion and time-reversal symmetry, collectively lead to nanoscale heterogeneity, novel excitations, dynamic responses, and intricate dependencies on material composition and disorder. These findings have recast the high-temperature superconductivity problem into a challenge of disentangling and understanding the relationships between these intertwined orders. Addressing this new problem provides a promising route to understanding the mechanism of superconductivity and to developing higher transition temperature superconductors.

In this thesis, we use resonant X-ray scattering to measure CDW order, structural order, and nematicity in the cuprates. Performing a X-ray diffraction experiment on resonance provides enhanced contrast in order to probe subtle ordering phenomena that is otherwise difficult to detect, but also to identify and differentiate different types of order (magnetic, lattice, charge, orbital), even when they overlap or occur simultaneously in time or temperature, by varying the X-ray energy and polarization. Utilizing the element- and orbital-specific sensitivity of resonant X-ray scattering in stripe-ordered cuprates, (La, M)$_2$CuO$_4$ with M = Nd, Sr, Eu and Ba, we study the low-temperature (0 0 1) Bragg peaks which on resonance gains sensitivity to electronic nematicity of Cu 3d orbitals. In Chapter 3, we delve in the details of equilibrium Resonant X-ray Scattering (RXS) and time-resolved Resonant X-ray Scattering (tr-RXS). We employ RXS-based experiments to investigate the electronic structure of local and global symmetries, aiming to differentiate intertwined symmetry-breaking phases. By applying controlled perturbations to the system, RXS enables us to examine the response of charge order, nematicity, and structural distortions, providing a mechanism to tune and disentangle their roles. Ultimately, this approach offers a pathway to understanding and potentially controlling the superconducting state. In Chapter 4, we discuss X-ray radiation sources, details of beamline layout, experimental protocols at synchrotron facilities and sample preparation carried out at Hawthorn Lab, University of Waterloo.

In Chapter 5, building on our discovery of $Q = 0$ nematic order in canonical La-based

stripe-ordered cuprates, we utilize a 50 μJ/cm^2 laser pump to photo-excite the system, driving electronic nematicity into a non-equilibrium state which exhibits ultrafast recovery on sub-picosecond timescales. We probe and record the recovery of $Q = 0$ nematic order as it stabilizes, aiming to isolate the intrinsic nematic component from co-existing symmetry breaking phases such as CDW order and structural distortions in the system. Observations reveal ultrafast recovery timescales along planar atomic layers, while spacer-layer atoms remain unaffected by the pump, marking successful isolation of $Q = 0$ electronic nematicity at optimal dopings.

Upon establishing the time-evolution dichotomy as an independent probe of nematic character, in Chapter 6, we present a systematic study of three stripe-ordered cuprates across a wide doping range, encompassing most of the generic cuprate phases, to position nematic order within the existing cuprate phase diagram. We find that in overdoped cuprates, nematicity appears to vanish as we exit the pseudogap phase boundary, which is established through transport and angle-resolved photoemission spectroscopy (ARPES) measurements. In two different stripe-ordered cuprates, nematicity vanishes at the same critical point associated with the putative quantum criticality, suggesting a deep link between nematicity and the pseudogap, as well as the possible nematic nature of the quantum critical point with characteristics resembling those of Fe-based superconductors. Furthermore, we analyze the cooperation between CDW order and nematicity by examining an increase in nematicity as an uptick in the (001) Bragg peak signal associated with planar atoms at CDW onset temperatures. Due to challenges associated with low-temperature measurements at synchrotrons, we concisely investigate nematicity within the superconducting dome in two stripe-ordered samples, observing signs of saturation, or possibly even competition, between nematicity and superconductivity. In heavily underdoped samples, where equilibrium RXS measurements do not show any nematicity signatures, time-resolved RXS (tr-RXS) reveals a saturated nematic order. This finding indicates a possible coexistence of electronic uniaxial and structural anisotropies, which can be disentangled by the application of uniaxial stress amongst other external perturbations.

Chapter 7 discusses application of in-plane compressive uniaxial stress along the Cu–Cu and Cu–O–Cu bond directions, observing an anisotropic suppression of CDW order by a factor of two along the strained direction. This induces a softening in the sharp structural transition, preceding conditions that lead to the suppression of charge order. However, the response of nematicity under these modified conditions remains challenging to characterize due to changed group symmetries under strain. We detect minimal or no changes in response to strain along the Cu–O–Cu bond direction, suggesting a potential role of stripe orientation in the manifestation of charge and orbital textures in La-based cuprates.

Placing the significance of RXS and cuprates in a broader context in Chapter 8, we

also study a recently discovered bi-layer novel superconductor, $La_3Ni_2O_7$, to characterize its detailed magnetic structure. We unveil alternating magnetic moments that exhibit a distinctly unidirectional character, being oriented parallel to the NiO_2 planes and perpendicular to the propagation direction of the spin-density wave (SDW) ordering. Through analysis of the azimuthal dependence of the polarization response of SDW peak, we clarify the presence of an antiferromagnetic, incommensurate spin order that possesses a nematic character with orthogonal domains in the plane. Our findings highlight the novel physics of $La_3Ni_2O_7$ and underscore the importance of RXS in elucidating low-energy spin, charge, and orbital order. The insights gained reveal the profound link between these orders and the underlying electronic structure of strongly correlated quantum materials.

Chapter 2

Physics of cuprates and nematicity

High-temperature superconductors (HTS), particularly cuprates superconductors, have been a major focus of condensed matter physics since their discovery in 1986 by Bednorz and Müller [5]. These materials, characterized by layers of copper-oxide (CuO_2) planes, exhibit superconducting transition temperatures (T_c) far above the theoretical limit predicted by the Bardeen-Cooper-Schrieffer (BCS) theory of conventional superconductivity [6]. The discovery of superconductivity in $La_{2-x}Ba_xCuO_4$ at 35 K set a new paradigm, rapidly followed by the discovery of Yttrium Barium Copper Oxide ($YBa_2Cu_3O_7$) with a T_c of 93 K, enabling superconductivity above the boiling point of liquid nitrogen [7] opening avenues for the next generation of technological advances.

The discovery of unconventional superconductivity in cuprates sparked extensive theoretical and experimental efforts to understand their higher than expected superconducting transition temperature, T_c. Early models of cuprate superconductivity, such as the resonating valence bond (RVB) theory proposed by Anderson [8], suggested that superconductivity in these systems arises from strong correlations and a novel pairing mechanism involving spin singlets rather than conventional electron-phonon interactions. This was soon followed by proposals that spin fluctuations, rather than lattice vibrations, mediate the pairing in cuprates [9]. Despite the early enthusiasm, no single theory has been universally accepted to explain the mechanism of high-T_c superconductivity in cuprates [10]. The phase diagram is further complicated by the emergence of the enigmatic pseudogap phase with partially gapped Fermi surface, and strange metal phases with linear-in-temperature resistivity – along with various charge and spin ordered states, suggesting a deeper connection between different ground states [11, 12, 13]. These co-existing orders, combined with the strong electronic correlations inherent to these materials, have posed a significant challenge to theoretical understanding.

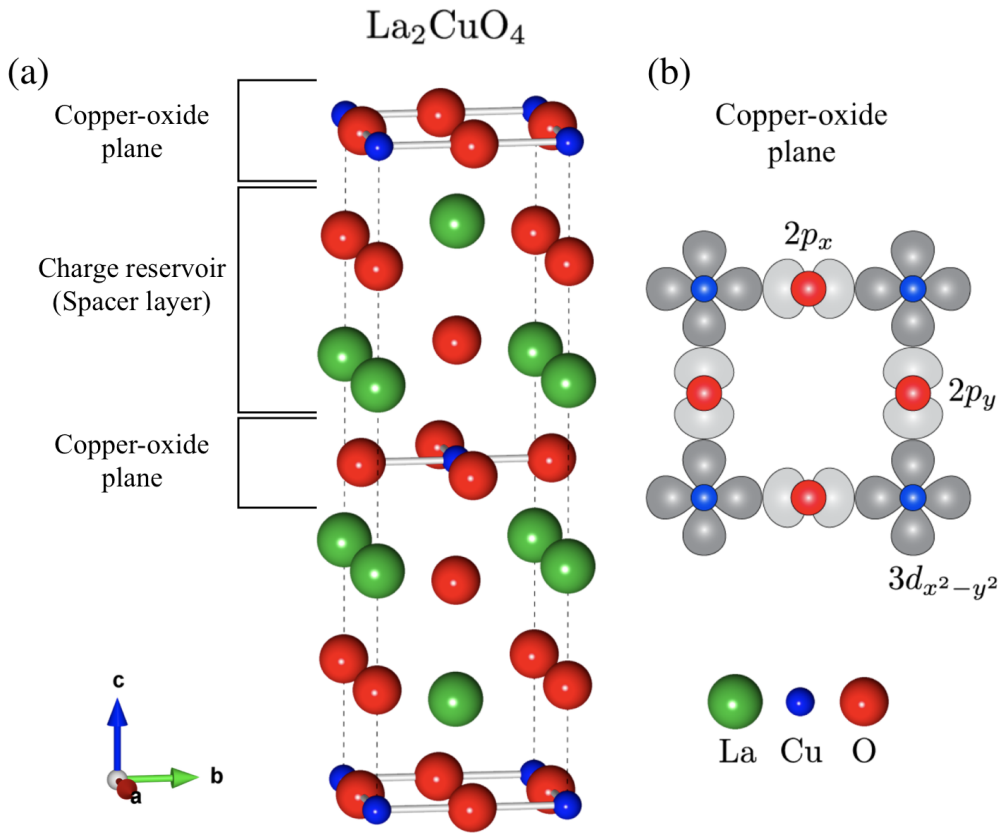


Figure 2.1: (a) Crystal structure of the cuprate superconductor La_2CuO_4. Arrow labeled a, b, c are crystallographic axes. In La_2CuO_4, La atoms are substituted with Sr or Ba to give $La_{2-x}Ba_xCuO_4$ (LBCO) and optionally co-doped with Nd or Eu atoms to give $La_{1.6-x}Nd_{0.4}Sr_xCuO_4$ (Nd-LSCO) and $La_{1.8-x}Eu_{0.2}Sr_xCuO_4$ (Eu-LSCO) cuprates which are the primary focus of the thesis. (b) A schematic of the electronic structure of the CuO_2 planes. In cuprates, the generic structural unit is the (quasi) two-dimensional CuO_2 plane whose electronic structure, close to the Fermi level, involves hybridization of a $3d_{x^2-y^2}$ hole on the copper sites with an in-plane $2p_x$ and $2p_y$ oxygen orbitals.

Experimentally, considerable progress has been made through the use of powerful techniques such as angle-resolved photoemission spectroscopy (ARPES), scanning tunneling microscopy (STM), and resonant X-ray scattering (RXS) amongst others [11, 12, 13, 14]. These methods have revealed key features of the electronic structure, such as the Fermi surface evolution with doping, the existence of nodal and antinodal gaps, and the dynamics of charge and spin correlations [15]. However, the precise nature of the pseudogap and its relation to superconductivity remains one of the outstanding questions in the field. Recently, time-resolved resonant X-ray scattering (tr-RXS) and resonant X-ray scattering (RXS) have emerged as powerful tools for probing the dynamic behaviour and electronic structure of these materials providing sensitivity to both electronic and structural order with high temporal and spatial resolution. This chapter highlights the key ingredients in the physics of cuprates, focusing on experimental motivation for using tr-RXS and RXS.

2.1 Intertwined electronic phases in cuprates

The structure of cuprates plays a critical role in the emergence of their novel physical properties (see Fig. 2.1). The undoped parent compound consists of copper-oxide (CuO_2) layers interleaved with insulating spacer layers. Doping of the CuO_2 planes is achieved by altering the chemical composition of the spacer or charge reservoir layers, which either removes electrons (hole doping) or introduces electrons (electron doping) into the (quasi-) two-dimensional CuO_2 planes. For example, the lanthanum-based cuprate superconductors are hole-doped derivatives of the Mott-insulating parent compound La_2CuO_4.

The hole doping phase diagram of cuprates is a hallmark of their complex, low-energy physics phenomena. In the undoped state, the compound behaves as a Mott insulator, where electrons are localized at their lattice sites due to strong Coulomb repulsion. By varying the carrier concentration within the CuO_2 planes, the strong Coulomb repulsions are partially mitigated, enabling electrons to delocalize and hop across the quasi-2D lattice structure. As charge carriers are introduced via hole (or electron) doping, long-range magnetic order is suppressed, and superconductivity emerges in a dome-like region of the phase diagram. One of the long-standing challenges in understanding the key physics of cuprates is the interplay of different phases that emerge upon hole doping: superconductivity, antiferromagnetism, charge-density waves (CDWs), and the pseudogap phase [13, 12, 16]. The pseudogap, which opens as a partial gap in the Fermi surface at temperatures above T_c and up to a pseudogap transition temperature, T^* [17, 18, 19, 20, 21] remains a central mystery.

The pseudogap phase appears at temperatures above the superconducting critical tem-

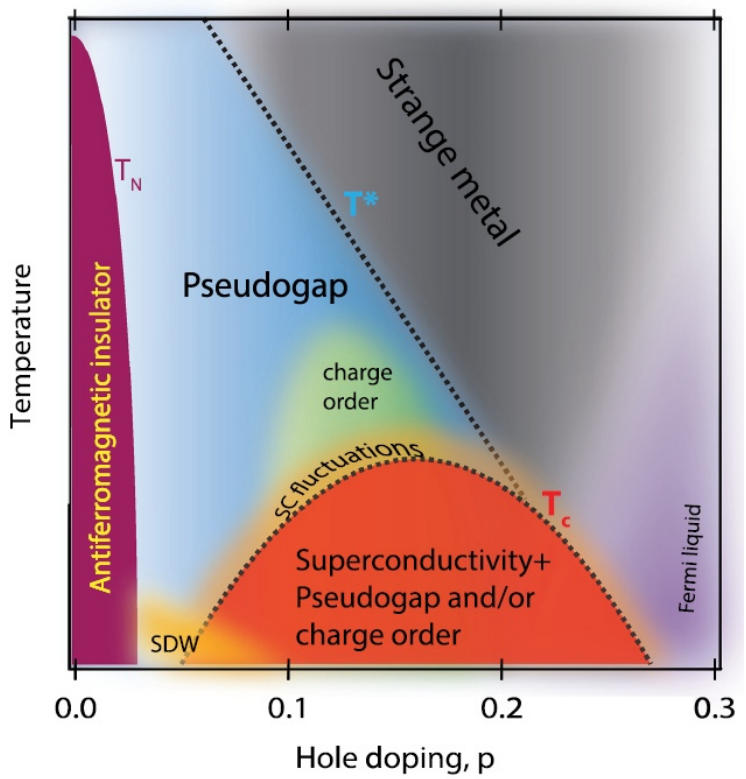


Figure 2.2: **Cuprate Phase Diagram** Schematic phase diagram of cuprates superconductors as a function of hole-doping. When the parent antiferromagnetic Mott insulators is doped by substituting an electropositive atom in the spacer layer, it exhibits various electronic symmetry-breaking phases as shown. As holes are introduced into the system, the insulating phase is suppressed, giving rise to a dome-shaped superconducting region that persists up to higher doping levels, where it competes with the charge density wave (CDW) order. In addition to superconductivity, other notable phases such as the pseudogap, strange metal, and spin-density wave (SDW) orders have been identified as generic features of the cuprate phase diagram. Figure adapted from [22] with permission.

perature T_c but below a characteristic temperature T^*, where an energy gap opens in the electronic excitation spectrum [18, 21, 23]. However, unlike in the superconducting state, this gap does not imply the formation of Cooper pairs. The pseudogap phase exhibits partial suppression of the electronic density of states near the Fermi level, leading to unusual transport and thermodynamic properties [24, 19]. The nature of this phase, whether it is

a precursor to superconductivity or a competing phase, remains an open question.

The complex interplay of charge, spin, and lattice degrees of freedom in cuprates leads to a rich phase diagram, featuring exotic phases that challenge our fundamental understanding of electron correlations and superconductivity. Unveiling the nature of these phases and their relationship to superconductivity is crucial for both advancing condensed matter theory and for potential technological breakthroughs. Cuprates, as part of the broader family of quantum materials, share many of their key features with other unconventional superconductors, such as iron- and nickel-based superconductors, and even structurally different systems such as twisted bilayer graphene (TBLGs) [25]. A unifying theme in these materials is the role of electronic correlations, which give rise to a variety of competing ground states. In these families, the superconducting state emerges from a parent antiferromagnetic phase, and unconventional superconductivity is believed to be mediated by spin fluctuations rather than phonons [9, 26].

2.1.1 Charge density wave (CDW) order

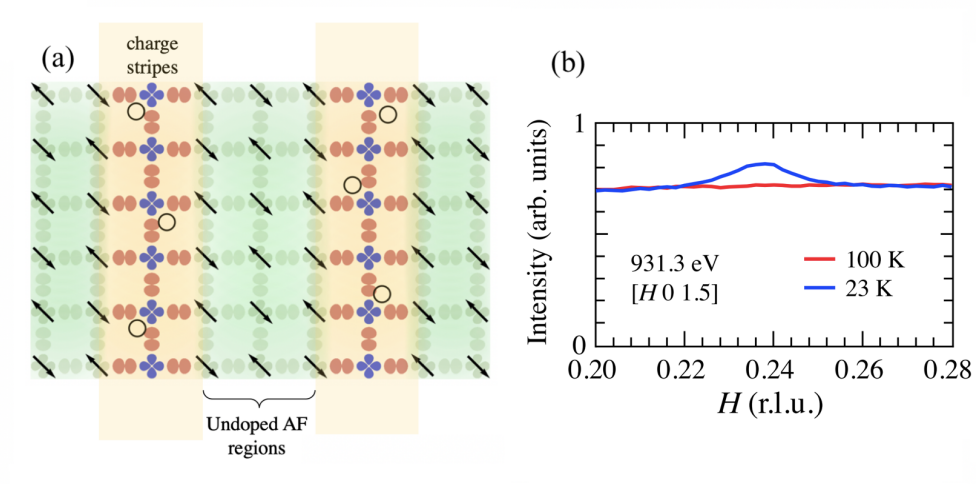


Figure 2.3: Unidirectional charge ordering in Lanthanum based cuprates: (a) Schematic of charge stripe order in Nd-LSCO at $p = 1/8$ hole doping. Spontaneous segregation of holes into unidirectional charge stripes occur, shown by orange shade. These stripes follow a (lattice) period-4 stripe-like charge correlations in the Lanthanum-based cupratess, (b) Detection of a CDW signal in a La-based cuprate, Nd-LSCO at $p = 1/8$ hole doping, using RSXS performed at Cu L edge. Adapted from Ref. [27] and Ref. [28] with permission.

Unidirectional spin and charge order ('stripes') were first observed in the cuprates by neutron scattering measurements by Tranquada *et al.* in 1995 [29]. Charge density wave (CDW) order is now recognized as a generic phase in cuprate superconductors [13, 14, 30]. Resonant X-ray scattering studies have provided direct evidence of static CDW order in materials such as $YBa_2Cu_3O_{6+x}$ [31, 32, 33], $Bi_2Sr_2CaCu_2O_{8+x}$ [34, 35], and (La, M)$_2CuO_4$ substituted with M = Nd, Sr, Eu and Ba [36, 37, 38, 39].

Furthermore, CDW order is known to compete with superconductivity across a wide range of hole doping [13, 40, 41]. CDW order is evidenced by a broad and weak peak above the fluorescent background signal in resonant scattering at a particular $\boldsymbol{Q}$ value[1]. As shown in Fig. 2.3(b), the $\boldsymbol{Q}_{\text{peak}}$ value for $p = 1/8$ Nd-LSCO is (0.236, 0, 1,5), the broad character of the peak indicates the short range order with a correlation length of around 70 Å [28].

2.1.2 Low-temperature structual distortions

An important aspect of Lanthanum-based cuprates, (La, M)$_2CuO_4$ substituted with M = Nd, Sr, Eu and Ba is a low-temperature orthorhombic (LTO) phase to low-temperature tetragonal (LTT) structural phase transition [42, 43, 44]. As shown in Fig. 2.4, the average structures of these phases can be described by the in-plane Cu atom coordinated by six oxygen atoms, such that it forms a grid of tilted, almost rigid, corner sharing CuO_6 octahedra. Based on the hole doping levels and temperature, four structural phases are observed in Nd-LSCO: the high-temperature tetragonal (HTT) phase with space group $I4/mmm$, the low-temperature orthorhombic (LTO1) phase ($Bmab$), the low-temperature tetragonal (LTT) phase ($P4_2/ncm$) phase, as well as the LTO2 phase ($Pccn$) which is an intermediate phase between LTO and LTT with reduced orthorhombicity.

At high temperatures, the CuO bonds in the CuO_2 layers are parallel to the ab-plane of the unit cell being in HTT structure. However, as one lowers the temperature, mismatch between the Cu-O and La-O bond lengths causes strain which is alleviated by structural distortions achieved by tilting of these octahedra. As a consequence, on cooling the space group changes, and the unit cell of the LTO phase is rotated by 45 degrees. As shown in Fig. 2.4, in the LTO phase the octahedra tilt along $[1\ 1\ 0]_{\text{HTT}}$ direction, whereas in the LTT phase the tilt axis alternates between $[0\ 1\ 0]_{\text{HTT}}$ and $[1\ 0\ 0]_{\text{HTT}}$ from plane to plane [44] as shown in Fig. 2.8a.

In the LTT phase, the orientation of these distortions — which change direction by 90 degrees between adjacent layers — help stabilize charge and spin order in the copper oxide

[1] Around (±0.236 0 1.5) in La-based cuprates.

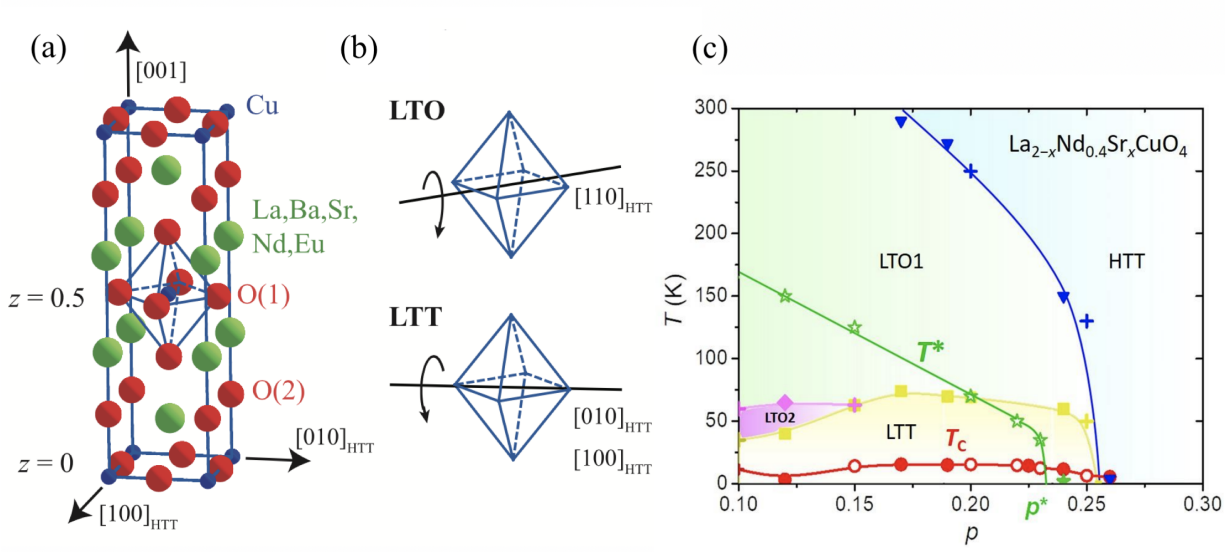


Figure 2.4: (a) Unit cell of Nd-LSCO in the high-temperature tetragonal phase (HTT). O(1) and O(2) are in-plane and apical oxygen sites, respectively. (b) is described in the text. (c) Structural phase diagram of Nd-LSCO with different structural phases as described in the text. (a) and (b) reused from Ref. [39]. Phase diagram adapted from [45] with permission.

plane [29, 46]. This structural transition is known to induce the C_4 symmetry breaking of the average electronic structure within an individual CuO_2 plane [39].

2.1.3 Pseudogap and Quantum Criticality

Rotational and translational symmetry-breaking phases in the pseudogap region have been confirmed as consistent and distinct features in the cuprate phase diagram through various methods. Appearing in the non-superconducting state, the simultaneous occurrence of these phases in energy and temperature makes it hard to determine if the pseudogap is a distinct phase or a result of overlapping instabilities [13, 16, 11], as one moves across the phase diagram with changes in temperature and hole doping.

Recent work has shown that charge density waves (CDWs) fluctuate and might co-exist with superconductivity, possibly driving the pseudogap behavior [31]. Studies with scanning tunneling microscopy (STM) have also shown that the PDW state has local patterns tied to charge order [48]. Additionally, time-resolved experiments hint at fluctuating

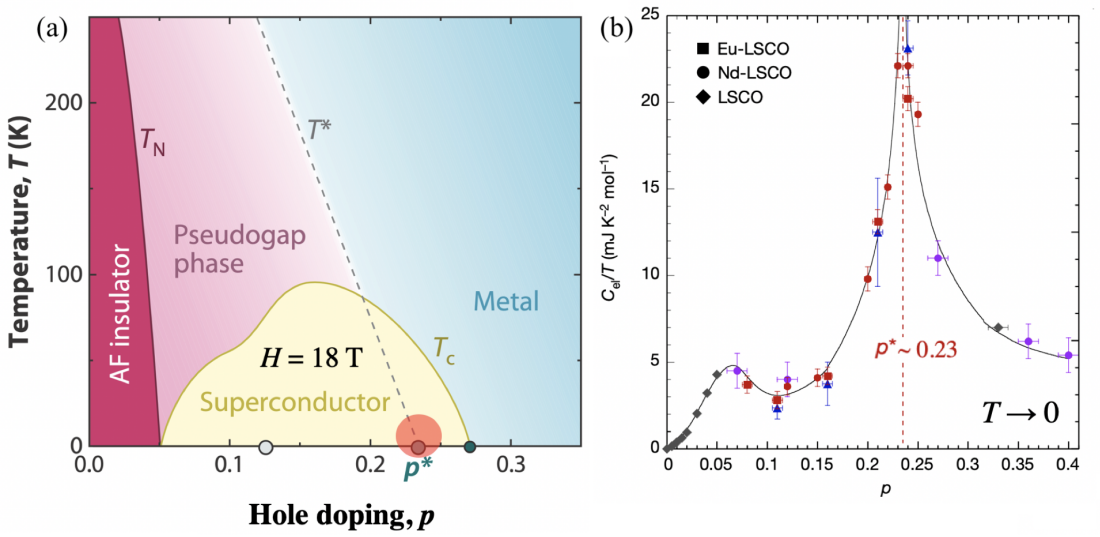


Figure 2.5: Evidence of quantum criticality in Nd-LSCO: A quantum critical point (QCP) occurs when the phase transition temperature of a material is suppressed to absolute zero. (a) shows the schematic phase diagram with the putative QCP at the point where the pseudogap phase ends. (b) Specific heat measurements on La-based cuprates: Superconductivity is suppressed to sub-Kelvin temperatures by applying a magnetic fields in the samples to investigate the behavior of electronic specific heat with doping. The authors argue that the strongly peaked electronic specific heat at p^* which exhibits a $\log(1/T)$ dependence is a signature of a QCP in these materials. Image (a) adapted from [12] and image (b) reused from [47] with permission.

orders that stabilize at lower temperatures [49]. The link between these electronic instabilities, superconductivity, and the pseudogap has sparked discussions about a potential quantum critical point (QCP) at zero temperature, similar to those found in heavy-fermion systems, organics, and pnictides [12, 50]. New measurements suggest the pseudogap may be connected to a QCP, drawing further comparisons between cuprates and iron-based superconductors, which are their closest relatives [51].

Existing proposals and recent reports of this putative pseudogap QCP in different cuprate families — based on the change in carrier density [52], Fermi surface transformation [53, 54], torque-magnetometry measurements [55], strong mass enhancement via quantum oscillation studies [56], and specific heat measurements (see Fig 2.5) at low temperatures in large magnetic fields [47]. These findings suggest that, as hole doping increases, the electronically ordered phases end and the system transitions to Fermi liquid behavior.

As shown in Fig. 2.5, for Nd-LSCO, the possible pseudogap QCP is located within the superconducting dome at a hole doping of about 0.23 [53]. It has been suggested that quantum fluctuations near this QCP enhance superconducting pairing [12, 56, 57]. There have been several experimental and theoretical efforts to understand the nature and effects of these quantum fluctuations at the pseudogap QCP [12, 56, 57, 58]. Recent advances include reports of divergent nematic fluctuations detected through elastoresistance measurements [59], as well as stronger electronic nematic fluctuations observed using Raman scattering [60] near the endpoint of the pseudogap phase. Both of these findings suggest the existence of a nematic quantum critical point.

2.2 Nematic phases of matter

2.2.1 Motivation from liquid crystals

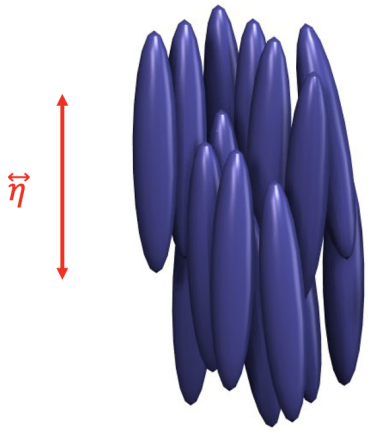


Figure 2.6: Schematic of a nematic phase from classical liquid crystal. The nematic direction η is a headless unit vector derived from the spatial and temporal average of orientation of long axis of the molecules.

Classically, a liquid-crystalline phase can be categorized as an intermediate phase between liquid and solid states of matter. Nematic[2] liquid crystals resemble elongated rod-like molecules which — on cooling or increasing the concentration — undergo a transition from a disordered isotropic state to a state having orientational order but positional disorder. As

[2]genitive of $\nu\eta\mu\alpha$ (nêma, "thread")

the system is cooled or the anisotropic interactions are reduced, free energy is minimized through the loss of rotational freedom [61] causing the rod-like molecules to align parallel to each other along a statistically preferred orientation specified by a headless unit vector, referred to as the director, shown as a red arrow in Fig 2.6.

Furthermore, liquid crystalline phases can also choose between other ordered states based on similar free energy arguments, for instance a smectic phase is realized when the rod-like molecules lose spatial freedom organizing themselves into layers perpendicular to the alignment axis. Such a configuration would break both translational and rotational symmetries in a single direction with possibly different magnitudes for both, however, the molecules are still free to move and rotate in the perpendicular plane in which they remain disordered [61].

2.2.2 Electronic nematic order in cuprates superconductors

Examples for nematic phases include high-T_c superconductors. An electronic nematic phase occurs when the electronic structure breaks the rotational (point group) symmetry but leaves the translational (lattice group) symmetry intact. For cuprates superconductors, first reports of an electronic nematic phase include measurements of anomalous anisotropy in the in-plane resistivity in $YBa_2Cu_3O_{6+x}$ (YBCO) and $La_{2-x}Sr_xCuO_4$ (LSCO) by Ando *et al.* [62] in 2002. Despite the already known orthorhombic nature of the unit cells in YBCO the temperature dependence of the in-plane anisotropy of resistivity could not be entirely described by the structural transitions, leading to the proposition of an electronic nematic phase in YBCO.

Electronic nematicity has emerged as a key feature of cuprate superconductors [11, 16]. Experimental evidences of electronic nematicity distinct from structural anisotropy now include reports from bulk transport in YBCO [62, 63, 64], scanning tunneling microscopy (STM) measurements in $Bi_2Sr_2CaCu_2O_{8+x}$ [65, 66], and inelastic neutron experiments in YBCO [67]. Recently, Achkar *et al.* demonstrated that the resonant X-ray scattering measurements of the (001) Bragg peak provide sensitivity to electronic nematicity in stripe-ordered cuprates, $(La, M)_2CuO_4$ substituted with M = Nd, Sr, Eu and Ba [39].

2.2.3 Electronic nematicity and possible mechanisms

As described in section 2.2, electronic nematicity refers to a breaking of rotational symmetry of the electronic structure in a manner that is not a straightforward result of crystalline symmetry, such that an additional electronic nematic order parameter, distinct from the

structure would be required to describe the resulting phase. Such a state can be difficult to identify in materials that have orthorhombic structures, which would naturally couple to any electronic nematic order and vice versa. Moreover, the manifestation of nematic order may depend on the details of the crystal structures of the materials, such as whether the structure is tetragonal or orthorhombic.

There have been a few suggestions to realize the mechanism for the formation of a nematic phase [16, 68]. One way would be through thermal or doping-induced (partial) melting of a stripe (smectic) phase such that it regains translation symmetry but retains orientational ordering — a proposed vestigial nematic state [68, 69, 70]. For instance, in cuprate superconductors existence of CDW order is well-established at 1/8th doping where periodic superstructure of charge modulation break both translation and rotational symmetry. Increasing temperature or hole-doping in such a system might allow breaking long-range order and fashion itself into local stripe order that gathers a statistically preferred direction — an average rotational symmtery breaking of sorts — while keeping the translational invariance intact.

Alternatively, the second approach starts from the momentum space structure of a metallic system, a Fermi liquid type approach. This phenomenological approach proceeds by considering fermions having a well-defined Fermi surface and quasiparticles. The idea comes from Pomeranchuck [71] who showed that the if some of the Landau parameters for a Fermi liquid are negative and large enough to overcome the stabilizing effects of Fermi pressure, then a thermodynamic (Pomeranchuk) instability occurs, causing the system to spontaneously lower their symmetry [72, 73, 74]. For instance, as shown in Fig 2.7 for a simple 2D circular Fermi surface, a Pomeranchuk instability will cause an elliptical distortion causing the momentum structure to transition down into a residual C_2 rotational symmetry and show anisotropic electronic/orbital signatures with a concomitant local average orientation.

2.3 Probing electronic nematicity using resonant soft X-ray scattering

Our study uses resonant soft X-ray scattering (RSXS) measurements of the (001) Bragg peak to probe electronic nematicity in the in Nd-LSCO. Previous work by Achkar *et al.* [39] showed that the resonant X-ray scattering measurements of the (001) Bragg peak provide sensitivity to electronic nematicity. Understanding how this measurement reveals electronic nematicity requires examination of the crystal structure of $(La, M)_2CuO_4$ substituted with

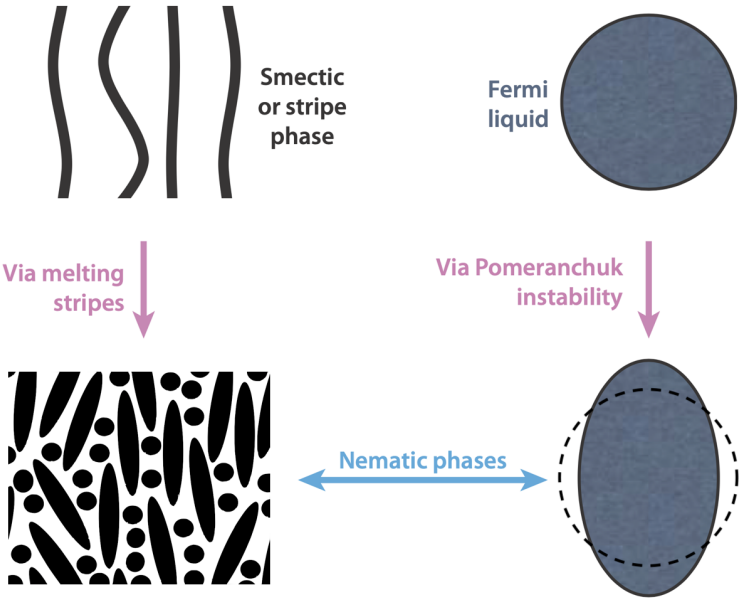


Figure 2.7: Two possible mechanisms for the existence of a nematic phase: via thermal (or quantum) melting of a stripe phase such that it regains translational invariance with an average rotational symmetry breaking; and through the elliptical distortion of the Fermi surface — caused by hole doping or temperature or possibly quantum effects — of a metallic circular Fermi surface via a Pomeranchuk instability. Figure from [16] with permission.

M = Nd, Sr, Eu and Ba. As discussed in 2.1.2, upon cation doping (x), they exhibits a structural phase transition from the LTO to LTT phase at temperatures between 30 – 150 K depending on the material and doping levels. The LTT phase is characterized by tilting of the CuO_6 octahedra along the a or b axes such that each individual CuO_2 layer structurally breaks C_4 rotational symmetry as shown in Fig. 2.4.

2.3.1 On-resonance (001) Bragg peak

Resonant X-ray scattering of the (001) Bragg peak provides a direct measure of the difference in the symmetry of the electronic structure between neighbouring layers [39]. Off resonance or with conventional X-ray diffraction, the (001) Bragg peak is forbidden, based

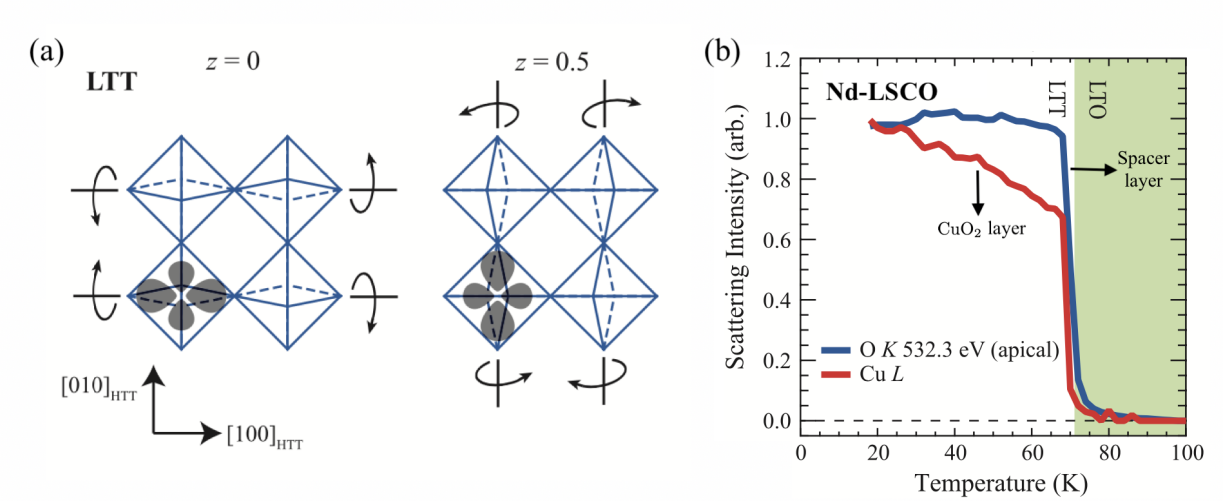


Figure 2.8: Electronic nematicity as a measure of orbital asymmetry: (a) CuO_2 planes showing the octahedral tilt pattern in neighboring layers ($z = 0$ and 0.5) in the LTT phase. The structural C_4 symmetry-breaking and electronic nematicity alternates between neighboring planes, $z = 0$ and $z = 0.5$. (b) Temperature dependency of the (001) Bragg peak at photon energy tuned to atoms in the CuO_2 layer and the spacer layer. The different temperature dependences can be understood in terms of an electronic nematic order in the CuO_2 planes that has a temperature dependent susceptibility and provides a contribution to the (001) peak intensity in addition to any contribution to that is induced by the lattice potential via structural distortions. (a) and (b) taken from Ref. [39] with permission.

on the ionic positions of atoms in the LTT or LTO phases. However, resonant X-ray scattering is sensitive to orbital symmetry as established in section 3.3.3, which differs for atoms in neighbouring layers in the LTT phase. Moreover, by tuning the photon energy to correspond to different atoms within the unit cell, the electronic symmetry breaking of the CuO_2 planes – which contain the Cu d and O p states that cross Fermi energy E_F and are most relevant to the low energy physics of the cuprates – can be differentiated from the La_2O_2 spacer layer, which do not have states that cross E_F but would be sensitive to changes to their orbital symmetry induced purely by structural distortions. In Fig. 2.9 we show how the (001) peak responds to change in temperature and resonance energy for LBCO.

Achkar *et al.* showed that the temperature dependence of the (001) peak intensity exhibited a dichotomy when the photon energy is tuned to different atoms in the neighboring layers of the Nd-LSCO unit cell [39]. As we see in Fig. 2.10, an abrupt 1st order increase at

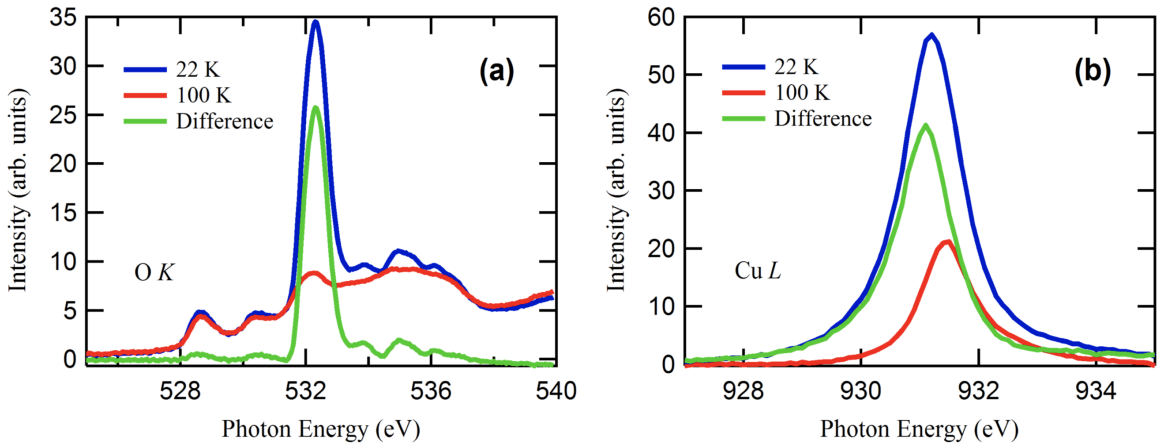


Figure 2.9: Energy dependence of the (001) peak at the O K (a) and Cu L (b) edges in x = 0.125 LBCO. Background intensity has been removed from all spectra with a constant offset for clarity. Figure adapted from [75] with permission.

the LTO $\rightarrow$ LTT transition consistent with previous measurements of the structural transition was observed when the photon energy is at the La M edge ($\sim$826 eV) or an energy associated with apical oxygen ($\sim$533.5 eV) – atoms in the La_2O_2 spacer layer. However, a more gradual temperature dependence is observed when the photon energy is tuned to the Cu L edge ($\sim$931.5 eV) or an energy associated with in-plane O ($\sim$528.5 eV) – atoms in the CuO_2 planes. The difference in temperature-dependence can be understood in terms of an electronic nematic order in the CuO_2 planes that has a temperature dependent susceptibility and provides a contribution to the (001) peak intensity in addition to any contributions induced by the lattice potential. Effectively this is akin to an internal strain applied to individual spacer layer by the lattice distortion, with the electronic structure of the CuO_2 planes (probed by the (001) peak intensity at the Cu L edge exhibiting a response that depends on the electronic nematic susceptibility.

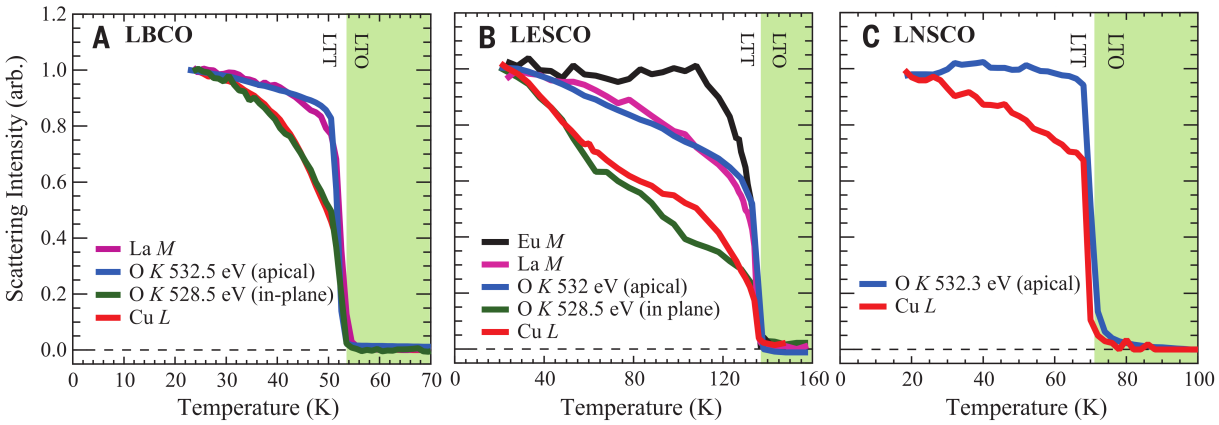


Figure 2.10: Temperature dependence of the (001) Bragg peak intensity: The intensities are normalized by the corresponding low-temperature values, $I_{(001)}(T)/I_{(001)}(20\text{ K})$ with photon energy tuned to the spacer layer atoms, or La M, apical O K, and copper-oxide layer atoms in-plane O K, Cu L edges for LBCO, Eu-LSCO, and Nd-LSCO. Figure reproduced from [39] with permission.

2.4 Motivation for our studies

Understanding Nematic phases under external perturbations

With the freedom RXS provides in choosing a transition edge, we can explore the impact of uniaxial strain and magnetic fields on materials with different crystallographic structures, including materials that are 4-fold symmetric and do not intrinsically favour unidirectional charge ordering. In these systems, the application of directional strain may have a dramatic effect, potentially stabilizing long-range unidirectional charge. Uniaxial strain proves to be a useful way in understanding the role of directional crystal deformations — which influences the way how orbitals overlap in the neighbouring sites and layers — in the correlated electronic states of matter. This selection allows us to decouple co-existing symmetry breaking phases providing a way to understand the behaviour of the electronic structure under changing point group symmetries.

The study of electronic symmetry-broken phases in cuprates requires experimental techniques sensitive to electronic order and its dynamics – along with sensitivity to ionic position to disentangle the role of structural dynamics. A combination of Resonant X-ray scattering (RXS) and Time-resolved resonant X-ray scattering (tr-RXS) has emerged a powerful team for probing these phases, as it allows for element-specific measurements

with high sensitivity to electronic and magnetic ordering.

Understanding Fluctuations and Non-equilibrium Phenomena

The study of non-equilibrium phenomena in cuprates—where the system is driven out of its ground state by external perturbations such as laser pulses—has gained significant interest in recent years. These studies have revealed the existence of transient states that are not accessible in thermal equilibrium. For instance, light-induced superconductivity, where a femtosecond laser pulse can transiently enhance superconducting-like coherence in a non-superconducting material, has been demonstrated in cuprates [76, 77]. Time-resolved X-ray scattering provides the ideal tool to investigate such non-equilibrium states, as it can resolve both the electronic and lattice dynamics with high temporal precision, helping researchers uncover new quantum phases and interactions that emerge far from equilibrium.

In equilibrium studies, RXS has been used to map out the static properties of CDW and nematic orders in quantum materials. Time-resolved techniques, particularly in the context of cuprates, open up a new dimension of study by providing insight into how various electronic and structural phases evolve and fluctuate in real-time. The temporal dynamics of charge and spin ordering, as well as the coupling between electronic, lattice, and spin degrees of freedom, can now be tracked with unprecedented precision. tr-RXS and resonant X-ray scattering (RXS) are ideal for such studies, as they are element-specific, sensitive to both electronic and magnetic orders. Unleashing a tool capable of not just probing but also distentangling electronic and structural changes fron ultrafast timescales (from femtoseconds to picoseconds).

Time-resolved resonant X-ray scattering experiments allow discerning electronic and structural degrees of freedom on a sub-picosecond recovery scale. In Chapter 5, we isolate the electronic recovery in the first few ps, while the structural distortions recover on larger time scales — thus, disentangling structural and electronic components of the rotational symmetry breaking. Tr-RXS adds a novel tool to selectively detect nematicity via non-equilibrium recovery of the electronic ground state. Providing key insights into how charge and spin orders evolve in response to photoexcitation, revealing how competing orders collapse or persist in the nonequilibrium state [49]. For example, tr-RXS studies of $La_{2-x}Ba_xCuO_4$ have demonstrated the suppression of CDW order following ultrafast photoexcitation, suggesting that symmetry-breaking phases can be controlled on ultrafast timescales [49].

Role of Quantum Fluctuations and Quantum Critical Points

In Eu-LSCO and Nd-LSCO, the putative pseudogap QCP lies, inside the superconducting dome, around the hole doping of 0.23 [53]. It has been proposed that quantum fluctuations enhance superconducting pairing interactions in the vicinity of this putative QCP [12]. Making them suitable candidate for studying the relation between the three symmetry-breaking phase, that is CDW order, electronic nematic order and structural phase transitions. Nematic order is often linked to quantum critical points, where continuous phase transitions occur at zero temperature. Quantum criticality in cuprates is thought to govern much of the strange metallic behavior and may play a central role in the pseudogap regime. Understanding nematic quantum critical points could provide deep insights into the broader field of quantum materials and strongly correlated electron systems.

One of the central open questions in the field of high-temperature superconductivity is the role of fluctuations—particularly fluctuations of symmetry-breaking phases—in the mechanism of superconducting pairing. In cuprates, charge density wave (CDW) and spin density wave (SDW) fluctuations have been observed in close proximity to the superconducting phase. Time-resolved studies allow us to track the evolution of these fluctuations and their interaction with the superconducting state. Capturing the rapid dynamics of phase transitions and fluctuations in cuprates. This becomes particularly important for observing transient states, such as light-induced superconducting phases or short-lived symmetry-breaking orders, which cannot be accessed with static measurements. By synchronizing X-ray pulses with laser-induced perturbations, tr-RXS can reveal how electronic and structural orders evolve in real-time, offering a unique window into the fast dynamics of cuprate materials.

Exploring Hidden Ordering and Non-equilibrium Phenomena

One of the most exciting developments in the use of time-resolved techniques is their ability to probe *hidden* or fluctuating orders that are not detectable in equilibrium. For example, tr-RXS has been used to reveal fluctuating CDW order that exists only on ultrafast timescales and vanishes in equilibrium measurements. This ability to detect short-lived or hidden phases is a powerful tool for uncovering the full complexity of the cuprate phase diagram and understanding the dynamics that govern high-temperature superconductivity [78].

In our work in heavily underdoped samples of Eu-LSCO we discover that nematic order is saturated, rendering it undetectable as dichotomy in T-dependence of the (001) peak in RXS. Surprisingly, we discover that nematic order is still present in Eu-LSCO x =

0.08, for instance, via non-equilibrium, ultrafast pump-probe measurements. At the base temperature, T = 20 K, we laser pump the system, and detect a clear sub-ps suppression of electronic nature from the planar layer atoms whereas the spacer layer atoms do not show any suppression. This underscores the complex nature of nematic order, and how it can elude detection even in systems where they are well-established.

2.4.1 Immediate future directions

Nematicity has gained attention due to its potential role in enhancing or competing with superconductivity. In iron-based superconductors, nematic order often appears in close proximity to the superconducting phase, suggesting a possible connection between the two phenomena [79]. In cuprates, the relationship between nematicity and superconductivity remains less clear, but the observation of nematic fluctuations in the pseudogap phase points to the possibility that nematicity could play a role in the pairing mechanism itself [60]. Understanding the interplay between nematic phases, charge order, and superconductivity is crucial for developing a comprehensive theory of high-T_c superconductivity.

Fluctuations, particularly spin and charge fluctuations, play a central role in the physics of cuprates and other correlated electron systems. In the cuprates, spin fluctuations have long been considered a potential pairing glue in place of the electron-phonon interactions central to conventional superconductors [9]. These fluctuations are strongest near antiferromagnetic ordering, which is suppressed as doping increases. The region of the phase diagram where superconductivity is maximized appears to coincide with the emergence of strong quantum fluctuations, suggesting that they play a key role in the formation of Cooper pairs [13]. Recent experimental efforts using quantum oscillations, inelastic neutron scattering, and time-resolved spectroscopy have provided indirect evidence for quantum criticality in cuprates. These experiments suggest that a QCP, tied to the suppression of competing orders like antiferromagnetism or charge order, may play a role in optimizing the superconducting properties of these materials [56]. Understanding the precise role of quantum fluctuations and critical points in cuprates is crucial for elucidating the pairing mechanism and could guide the search for new materials with even higher T_c.

Chapter 3

Resonant soft X-ray Scattering

3.1 Overview

In this thesis, we utilize resonant X-ray scattering to investigate hole-doped transition metal oxide heterostructures, specifically cuprate and nickelate superconductors, which exhibit complex electronic ordering phenomena. The physics of collective ordering of charge, spin and orbital degrees occurs at low energies, generally, affecting a small portion of the valence electrons close to the Fermi level of the transition metal ions involved. Systemic investigation of these ordering tendencies requires experimental techniques capable of probing both static and dynamic properties at energies associated with exact elemental (resonant) edges. Two such techniques are **equilibrium resonant X-ray scattering** (RXS) and **time-resolved resonant X-ray scattering** (tr-RXS). While equilibrium RXS elucidates the static properties and symmetries of these materials, tr-RXS provides insights into their ultrafast dynamics and possible transient stabilization, allowing a way to gather dynamical insights by probing the evolution of orders under external perturbations.

Conventional X-ray diffraction (XRD) remains a century-old, standardized tool to probe the spatial, microscopic description of the underlying ionic-atomic structure as well as the degree of crystalline order, via measurement of the position and width of relevant Bragg peaks. The atomic scattering cross-section for X-rays is proportional to Z^2, where Z is the atomic number, XRD signal is greatly influenced by heavier dopant atoms in the TMO heterostructures [80] such as cuprates and nickelates. This forbids resolving the physics of the charge, spin and orbital degrees of freedom close to the Fermi level for lighter elements like oxygen and copper. Resonant X-ray scattering (RXS) combines aspects of X-ray diffraction with X-ray absorption spectroscopy.

RXS probes weak ordering phenomena that is otherwise difficult to detect, and furthermore identify and disentangle different orders (magnetic, lattice, charge, orbital), even when they overlap or occur simultaneously in time or temperature, by varying the X-ray energy and polarization. It works by tuning the incident photon energy to an X-ray absorption edge, i.e. an energy sufficient to excite a core electron of a particular element into an unoccupied state. Near an X-ray absorption edge, the resonant effect enhances the scattering cross-section which now varies the scattering amplitude of the Bragg peaks strongly with photon energy. Unlike off resonance, the amplitude now depends on details of the electronic structure, such as the valence, spin state or orbital symmetry of the unoccupied electronic states. It is important to choose the transition edge such that it not only enhances the cross section but also keeps it in the low-energy range near the Fermi energy of the transition metal ion. In our case of the $3d$ TMOs, the most relevant dipole-allowed transition is from $2p$ to $3d$, called the $L_{2,3}$ or L_3 edge, which lies in the soft X-ray regime between $100 - 2000$ eV. The copper L_3 edge is at $E \sim 930$ eV and oxygen K edges at $E \sim 530$ eV is the primary focus for our studies. Worthwhile to note is a compromise involved: the range of wavelength for soft X-rays drastically limits the q-space access for the experimental geometries, restricting us to only a handful of allowed Bragg peaks and ordering events.

3.2 X-rays and their interaction with matter

Parts of theoretical treatment of resonant X-ray scattering presented in this chapter has been adapted and modified from my Master's thesis [81].

For the scope of this thesis, we will consider monochromatic beams travelling perpendicular to the direction of the electric and magnetic field. For a simplistic theoretical treatment, we consider electric fields only, characterizing X-rays by a wavelength λ, or wavenumber $k = 2\pi/\lambda$.

3.2.1 X-rays: Waves, photons, and synchrotron

Assuming the X-ray beam is monochromatic and perfectly collimated, we apply the approximation of a plane wave. The classical description of the spatial and temporal variation of a linearly polarized, electromagnetic plane wave propagating along the z-axis can be expressed as

$$\boldsymbol{E}(\boldsymbol{r}, t) = \hat{\boldsymbol{\epsilon}}\, E_0 e^{i(\boldsymbol{k}.\boldsymbol{r} - \omega t)}, \tag{3.1}$$

where the $\hat{\boldsymbol{\epsilon}}$ and $\boldsymbol{k}$ contains information about the direction of polarization and wavevector, respectively.

3.2.2 Diffraction by an electronic distribution

We begin by considering non-resonant, elastic scattering of incident X-rays by a charge distribution. In general, an atom can be modelled as a spatial charge distribution with some radial dependence for electron density, as $\rho(\boldsymbol{r})$. With our approximation of incident X-rays as a plane wave front as described in Eqn. (3.1) — we can rewrite diffraction as the phase difference, $|(\boldsymbol{k}_{\text{out}} - \boldsymbol{k}_{\text{in}}) \cdot \boldsymbol{r}|$, caused by an unequal traversal of optical path length of two (or more) scattered wavefronts. The scattered wavefronts interfere constructively (and destructively) giving a diffraction pattern. Often we formalize it with the momentum transferred, $\boldsymbol{q} = \boldsymbol{k}_{\text{out}} - \boldsymbol{k}_{\text{in}}$, to the scattered wavefront, and then integrating it over entire charge distribution as,

$$f(\boldsymbol{q}) = \int \rho(\boldsymbol{r}) e^{i\boldsymbol{q}\cdot\boldsymbol{r}} d\boldsymbol{r}, \tag{3.2}$$

where $f(\boldsymbol{q})$ is the atomic form factor. The full atomic form factor, in the quantum mechanical treatment depends on the energy of the incident photons.

Building up from our simplistic treatment of atoms as scattering entities [82], we now consider crystals that can be classified as structures composed of periodic arrangements of atoms that form a Bravais lattice. We modify Eqn. (3.2) to include the structural information by discretely summing over the lattice sites as

$$S(\boldsymbol{q}) = \sum_{\boldsymbol{R}} f(\boldsymbol{q}) e^{i\boldsymbol{q}\cdot\boldsymbol{R}}, \tag{3.3}$$

where $\boldsymbol{R} = n_1\boldsymbol{a}_1 + n_2\boldsymbol{a}_2 + n_3\boldsymbol{a}_3$ points to the location of the atom, and $\{\boldsymbol{a}_1, \boldsymbol{a}_2, \boldsymbol{a}_3\}$ are the primitive lattice vectors. The discrete Fourier transform $S(\boldsymbol{q})$ can be thought of as a crystal structure factor for a simple periodic arrangement. The scattering intensity $|S(\boldsymbol{q})|^2$ attains a maxima when the momentum transfer for the scatterers satisfy the Laue condition, $\boldsymbol{q} \cdot \boldsymbol{R} = 2\pi m$, where m is an integer.[1]

For a more realistic treatment of (complex) periodic arrangements with multiple atoms in each unit cell, we consider $\boldsymbol{R} = \boldsymbol{R}_n + \boldsymbol{r}_j$ where $\boldsymbol{R}_n$ points to the center of unit cell n and

[1] This allows us to define a complete set of the reciprocal lattice vectors which according to crystal and geometry of the experiment — gives us accessible Miller indices, referred to as Bragg peak positions.

$\boldsymbol{r}_j$ locates the different atoms within the unit cell relative to $\boldsymbol{R}_n$. The updated structure factor can be written as:

$$S(\boldsymbol{q}) = \overbrace{\sum_{\boldsymbol{r}_j}^{A,B,C...} f_j(\boldsymbol{q}) e^{i\boldsymbol{q}\cdot\boldsymbol{r}_j}}^{\text{unit cell structure factor}} \underbrace{\sum_{\boldsymbol{R}_n}^{N} e^{i\boldsymbol{q}\cdot\boldsymbol{R}_n}}_{\text{lattice part}}, \tag{3.4}$$

where $A, B, C...$ are distinct atoms in the unit cell, and N is the total unit cells in the crystal. The scattering intensity $|S(\boldsymbol{q})|^2$ in Eqn. (3.4) can be considered as having lattice contribution from different unit cells, and contribution from different atoms within the unit cell. For our interest, in a real (single) crystal we can assume $N \to \infty$ thus making the lattice contribution proportional to a Dirac delta function, $\sum_{\boldsymbol{G}} \delta(\boldsymbol{q} - \boldsymbol{G})$. This brings us to the Laue condition for scattering, $\boldsymbol{q} = \boldsymbol{G}$. An important observation to note is the scattering intensity being dictated only by the unit cell structure factor in this assumption.

3.2.3 Real and Reciprocal space

A perfect crystalline form is a periodic repetition of a unit cell structure which in real space is defined by primitive lattice vectors in real space, or also called unit vectors of direct lattice as $\{\boldsymbol{a}_1, \boldsymbol{a}_2, \boldsymbol{a}_3\}$. For such a crystal, the condition for maxima of scattering intensity is repeated for Eqn. (3.3) when $\boldsymbol{q} \cdot \boldsymbol{R} = 2\pi m$, where m is an integer, and for Eqn. (3.4) when $\boldsymbol{q} = \boldsymbol{G}$. This Laue formulation allows us to define reciprocal space using real space primitive lattice vectors as

$$\boldsymbol{b}_i = 2\pi \frac{\boldsymbol{a}_j \times \boldsymbol{a}_k}{v_0}, \tag{3.5}$$

where v_o is the volume of the unit cell, and $\{i, j, k\}$ are indices of direct lattice unit vectors, and they follow right-handed cyclic notation.

More generally from $\boldsymbol{q} = \boldsymbol{G}$, the set of reciprocal space vectors can be represented in these three equations:

$$\boldsymbol{a}_1.(\boldsymbol{k}_{\text{out}} - \boldsymbol{k}_{\text{in}}) = 2\pi h, \tag{3.6}$$
$$\boldsymbol{a}_2.(\boldsymbol{k}_{\text{out}} - \boldsymbol{k}_{\text{in}}) = 2\pi k, \tag{3.7}$$
$$\boldsymbol{a}_3.(\boldsymbol{k}_{\text{out}} - \boldsymbol{k}_{\text{in}}) = 2\pi \ell, \tag{3.8}$$

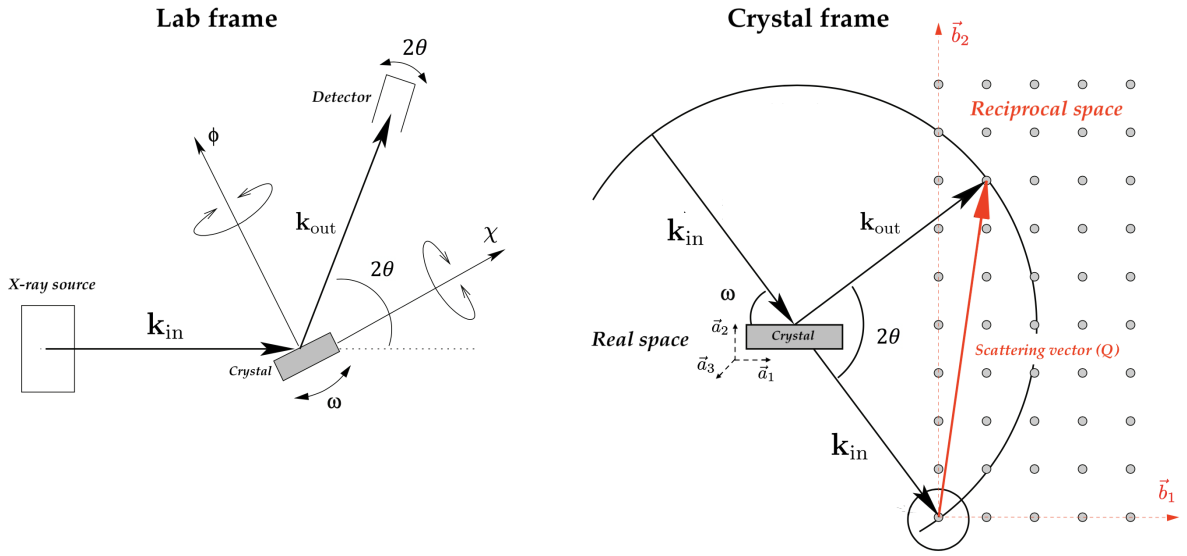


Figure 3.1: The scattering geometry in the lab and crystal frame, where $\{\boldsymbol{a}_1, \boldsymbol{a}_2, \boldsymbol{a}_3\}$ denote the direct lattice unit vectors, and $\{\mathbf{b}_1, \boldsymbol{b}_2\}$ stand for the reciprocal space unit vectors. The red solid line denotes the scattering vector, $\boldsymbol{q} = \boldsymbol{k}_{\text{out}} - \boldsymbol{k}_{\text{in}}$.

where h, k, ℓ are Miller indices and $G = h\boldsymbol{b}_1 + k\boldsymbol{b}_2 + \ell\boldsymbol{b}_3$, here $\{\boldsymbol{b}_1, \boldsymbol{b}_2, \boldsymbol{b}_3\}$ form the basis vectors of the reciprocal space.

Notably, Fig. 3.1 shows the scattering geometry and different possible degrees of angular freedom. Most RSXS diffractometers operate in 2-circle mode with fixed χ and ϕ while keeping the detector in the scattering plane. Navigation in reciprocal space is achieved by the rotation of sample ω or θ_s and detector arm 2θ once the sample is correctly oriented. During the process of alignment and orientation, we use the χ and ϕ motors to make sure the Bragg peak under investigation is correctly centered on the detector. At the experimental facilities, REIXS beamline in Canadian Light Source (CLS) for instance, a user interface called **fourc** (comes under a widely used software **spec**) allows navigating these scans and data acquisition easier using principles of diffraction. It can operate under the scattering geometries, reciprocal lattice vectors, and other constraints mentioned by the user. It uses the general form of Laue equations, and has pre-written macros that take the crystal parameters and orientation into account to achieve desired scattering geometries.

3.3 Theory of Resonant X-ray Scattering

3.3.1 A second order process

Resonant X-ray scattering is a "photon in-photon out" technique, where light (photon) gets scattered by matter (electron cloud) — the photon energy is tuned exactly to match the energy difference between the occupied (electronic) state and the unoccupied valence state. In this two step process, a 'hole' is left behind which interacts with other (un)occupied states to gain stability. As depicted in the cartoon Fig. 3.2 when the photon energy is off-resonance the excitation process does not involve an intermediate state Ψ_m where the absorption and the scattering cross section is dramatically low, however, as we tune to the resonant energy there is a strong enhancement of the scattering cross section, which now picks up information about the correlated ordering and symmetry-breaking phenomenon (involving the d orbital states of the transition metal ion of the TMOs). We mostly consider resonances dealing with $2p \rightarrow 3d$ transitions, which involve $L_{3,2}$ edges of $3d$ orbital of cuprate superconductors.

3.3.2 A quantum mechanical approach

As discussed in Ref. [83, 84, 85], for our description of resonant scattering, we can obtain a time-dependent, matter-radiation interaction Hamiltonian as

$$H_{\text{int}} = \sum_{\text{electrons}} \overbrace{\frac{e^2}{2mc^2}\boldsymbol{A}^2}^{\substack{\text{Thompson}\\ \text{scattering}}} - \overbrace{\frac{e}{mc}\boldsymbol{p}\cdot\boldsymbol{A}}^{\substack{\text{Resonant}\\ \text{scattering}}}, \tag{3.9}$$

the vector potential $\boldsymbol{A}(\boldsymbol{r}, t)$ of the incident photon interacts with the electrons in the material, $\boldsymbol{p}$ is the momentum operator, and m is the mass of the electron.

We begin by considering the interaction of an incoming photon with an electronic configuration (ground) state $|\Psi_{\text{GS}}\rangle$, or simply $|G\rangle$ (see Fig. 3.2 as well). In resonant elastic X-ray scattering, the incoming photon absorption with wavevector, $\boldsymbol{k}$) and polarization, $\boldsymbol{\epsilon}$ causes the electrons to transition out of state $|G\rangle$ into an intermediate state $|\Psi_m\rangle$, or $|I\rangle$ which then decays back to the initial state $|G\rangle$ by emitting a photon $(\boldsymbol{k'}, \boldsymbol{\epsilon'})$. The introduction of the intermediate state $|I\rangle$ is crucial as it makes the probe sensitive to the electronic transition and consequently the electronic structure or charge textures in the

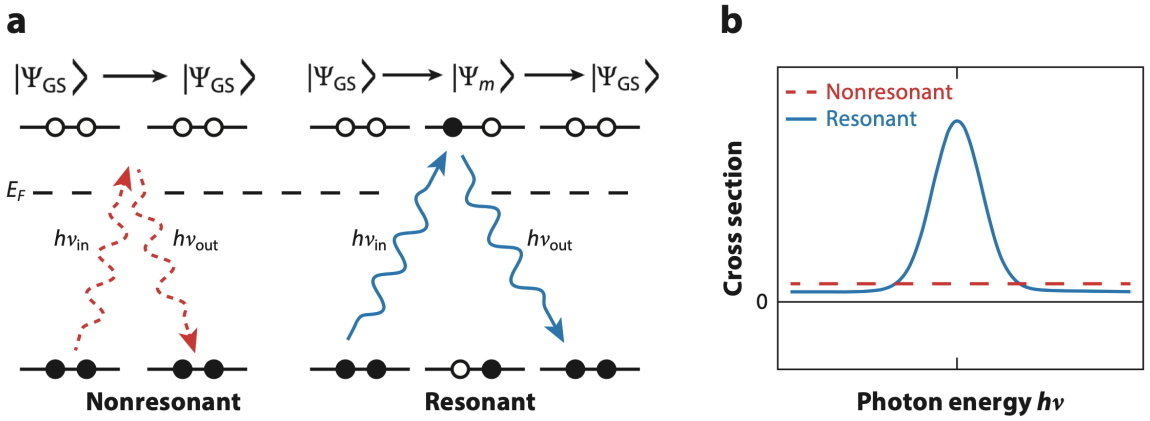


Figure 3.2: Schematic representation of resonant and non-resonant scattering: (a) In non-resonant scattering the excitation process does not involve intermediate states, whereas resonant scattering occurs when the incident photon energy ($h\nu_{\text{in}}$) is tuned to promote an electronic transition from the ground state $|\Psi_{\text{GS}}\rangle$ to an intermediate state $|\Psi_m\rangle$. The subsequent, or the second order process of recombining of the excited electron with the core hole results in the creation of an outgoing (scattered) photon with energy $h\nu_{\text{out}}$. (b) The different photon energy dependence of resonant and non-resonant processes, showing enhancement in the cross-section occurring at the selected resonant edge. Figure taken from [14] with permission.

ground state. Note, this cannot be achieved with Thompson (elastic) scattering where no electronic transition are involved. The two cases can be depicted as cartoon schematics in Fig. 3.2.

To investigate the process in terms of transition matrix and scattering cross-section, we apply the Hamiltonian in Eqn. (3.9) on $|G\rangle$. In order to do so, we first choose a Coulomb gauge, $\boldsymbol{\nabla} \cdot \boldsymbol{A} = \boldsymbol{0}$ to introduce a quantized photon vector field potential $\boldsymbol{A}(\boldsymbol{r}, t)$ that has the form of a traveling wave as

$$\boldsymbol{A}(\boldsymbol{r}, t) = \sqrt{\frac{2\pi\hbar c}{V|\boldsymbol{k}|}} \sum_{\boldsymbol{k}} \boldsymbol{\epsilon} \left(a_k(t) e^{i\boldsymbol{k}\cdot\boldsymbol{r}} + a_k^\dagger(t) e^{-i\boldsymbol{k}\cdot\boldsymbol{r}} \right), \tag{3.10}$$

where $a_{\boldsymbol{k}}^\dagger$ and $a_{\boldsymbol{k}}$ are photon creation and annihilation operators respectively. The vector potential introduced above is linear in annihilation and creation operators which means to obtain a second order elastic process, it would have to act twice on $|G\rangle$. This implies that

allowed terms quadratic in $\boldsymbol{A}$ would contribute to first order and the contribution of allowed linear order terms in $\boldsymbol{A}$ would need second order perturbation theory treatment to capture the two-step resonant elastic scattering process. We rewrite Eqn. (3.9) by separating the Hamiltonian into a non-resonant (H_1) and a resonant (H_2) scattering contribution, summed over all electrons labeled via i:

$$H_{\text{int}} = H_1 + H_2 = \overbrace{\sum_i \frac{e^2}{2mc^2}\,[\boldsymbol{A}(\boldsymbol{r}_i,t)]^2}^{H_1:\ |G\rangle\to|G\rangle} - \overbrace{\sum_i \frac{e}{mc}\,\boldsymbol{p}_i\cdot[\boldsymbol{A}(\boldsymbol{r}_i,t)]}^{H_2:\ |G\rangle\to|I\rangle\to|G\rangle}. \tag{3.11}$$

We calculate the transition rate matrix [80, 83, 86] for H_1 and H_2, as:

$$T_1 = \langle G|H_1|G\rangle \quad \text{and} \quad T_2 = \sum_m \frac{\langle G|H_2^*|I_m\rangle\,\langle I_m|H_2|G\rangle}{\hbar\omega_{\boldsymbol{k}} - (E_m - E_g) + i\Gamma/2}. \tag{3.12}$$

plugging in H_1 and H_2 we get:

$$T_1 = \frac{hc}{V|\boldsymbol{k}|}\frac{e^2}{mc^2}\,(\boldsymbol{\epsilon}^*\cdot\boldsymbol{\epsilon})\sum_i \langle G|e^{i(\boldsymbol{k}-\boldsymbol{k}')\cdot\boldsymbol{r}_i}|G\rangle\,, \text{and} \tag{3.13}$$

$$T_2 = \frac{hc}{V|\boldsymbol{k}|}\frac{e^2}{mc^2}\sum_{m\ \text{states}} \frac{\langle G|\sum_{j=1}^N \boldsymbol{\epsilon}'^*\cdot\boldsymbol{p}_j e^{-i\boldsymbol{k}'\cdot\boldsymbol{r}_j}|I_m\rangle\,\langle I_m|\sum_{j'=1}^N \boldsymbol{\epsilon}\cdot\boldsymbol{p}_{j'} e^{i\boldsymbol{k}\cdot\boldsymbol{r}_{j'}}|G\rangle}{\hbar\omega_{\boldsymbol{k}} - (E_n - E_g) + i\Gamma/2}. \tag{3.14}$$

Note that the system transitions from the ground state $|G\rangle$ with energy E_g to an intermediate state $|I_m\rangle$ with energy E_m, and Γ represents the full-width at half-maximum of the distribution of all possible intermediate states I_m with respective energies — more commonly known as the lifetime of the intermediate states. The transition rate[2] in this quantum mechanical treatment can be described using perturbation theory by Fermi's Golden Rule, as:

$$w = \frac{2\pi}{\hbar}\,|T_1 + T_2|^2\,\delta\left(\hbar\omega_{\boldsymbol{k}} - \hbar\omega_{\boldsymbol{k}'}\right). \tag{3.15}$$

We sew up these arguments together by considering a scattering photon flux $\Phi = cn_k/V$ where n_k is the number of photons with wavevector $\boldsymbol{k}$ in a solid angle $\mathrm{d}\Omega$ which then gives us the differential scattering cross section as $d\sigma/d\Omega = w/\Phi$. Last point to note is the

[2]The probability that an electron will undergo a transition per unit time from one state to another.

conversion of delta function to a differential element dE to sum over photons with all k. Finally, we obtain:

$$\frac{\mathrm{d}\sigma}{\mathrm{d}\Omega} = \frac{e^4}{m^2c^4}\Bigg|(\boldsymbol{\epsilon}^* \cdot \boldsymbol{\epsilon})\overbrace{\sum_i \langle G|\, e^{i(\boldsymbol{k}-\boldsymbol{k}')\cdot\boldsymbol{r}_i}\,|G\rangle}^{\mathcal{F}(\boldsymbol{Q})} + \sum_{m\ \text{states}} \frac{\langle G|\sum_{j=1}^{N} \boldsymbol{\epsilon}'^{*}\cdot\boldsymbol{p}_j e^{-i\boldsymbol{k}'\cdot\boldsymbol{r}_j}\,|I_m\rangle\langle I_m|\sum_{j'=1}^{N}\boldsymbol{\epsilon}\cdot\boldsymbol{p}_{j'}e^{i\boldsymbol{k}\cdot\boldsymbol{r}_{j'}}\,|G\rangle}{\hbar\omega_{\boldsymbol{k}} - (E_m - E_g) + i\Gamma/2}\Bigg|^2 . \tag{3.16}$$

where $\mathcal{F}(\boldsymbol{Q})$ is the Fourier transform of the charge density, $\rho(\boldsymbol{r})$. In the above equation, the first term is the differential scattering cross section contribution from non-resonant Thompson scattering — which also follows the general relation between the scattering length and differential cross-section for non-resonant scattering processes. The second term in Eqn. (3.16) is the resonant (charge) scattering differential cross-section. At resonance the magnitude of the scattering intensity dramatically increases (see Fig. 3.2(b)), thus the measured intensity of a diffraction peak at resonance is dominated by the resonant contribution from the scattering cross-section. Naturally, there is an added background intensity that comes from the non-resonant processes. We can further simplify the second term by using the dipole approximation by Taylor expanding the exponential terms, as

$$e^{i\boldsymbol{k}\cdot\boldsymbol{r}} \simeq (1 + \boldsymbol{k}\cdot\boldsymbol{r} + (\boldsymbol{k}\cdot\boldsymbol{r})^2/2 + ...). \tag{3.17}$$

In our investigations for orbitals and charge textures, only the first-order terms contribute significantly[3]. Furthermore, we can re-write the momentum operator using the commutator identity $\boldsymbol{p} = \frac{m}{i\hbar}\boldsymbol{r}(E_m - E_g)$ and after dropping higher order terms, the final expression for the differential cross-section of resonant scattering can be simplified as:

$$\left(\frac{\mathrm{d}\sigma}{\mathrm{d}\Omega}\right) \propto \left|(\boldsymbol{\epsilon}'\cdot\boldsymbol{\epsilon})\ \mathcal{F}(\boldsymbol{Q}) + \sum_{m\ \text{states}} \frac{\langle G|\,(\boldsymbol{\epsilon}'\cdot\boldsymbol{D})^{\dagger}\,|I_m\rangle\langle I_m|\,(\boldsymbol{\epsilon}\cdot\boldsymbol{D})\,|G\rangle}{\hbar\omega_{\boldsymbol{k}} - (E_m - E_g) + i\Gamma/2}\right|^2 , \tag{3.18}$$

where $\boldsymbol{D} = \sum_j \boldsymbol{r}_j$ is the dipole operator. Note from the denominator in Eqn. (3.18) that resonant scattering will be amplified at energies where one can virtually excite an electron into some intermediate state, i.e. at an absorption edge. The differential cross section represented by Eqn. (3.18) relates to the atomic scattering form factor, $f(\omega)$, as

$$\left(\frac{\mathrm{d}\sigma}{\mathrm{d}\Omega}\right) \propto |f(\omega)|^2 \tag{3.19}$$

[3]Interested reader might find multipole expansion in Ref. [83, 87].

Thus $f(\omega)$, which is a complex quantity should vary and be enhanced in proximity to the absorption edge. This is, indeed, observed in the experiments as shown in Fig. 3.3. Re-examining the quantum mechanical treatment[4] in terms of atomic scattering form factors proves to be useful as the X-ray absorption spectroscopy (XAS) measurements not only exhibit enhancement but also become sensitive to the orbital, charge and spin degrees of freedom at the absorption edges. Furthermore, the polarization dependence of Eqn. (3.18) can be taken into account by using a tensor formulation of $f(\omega)$, as discussed in the next section.

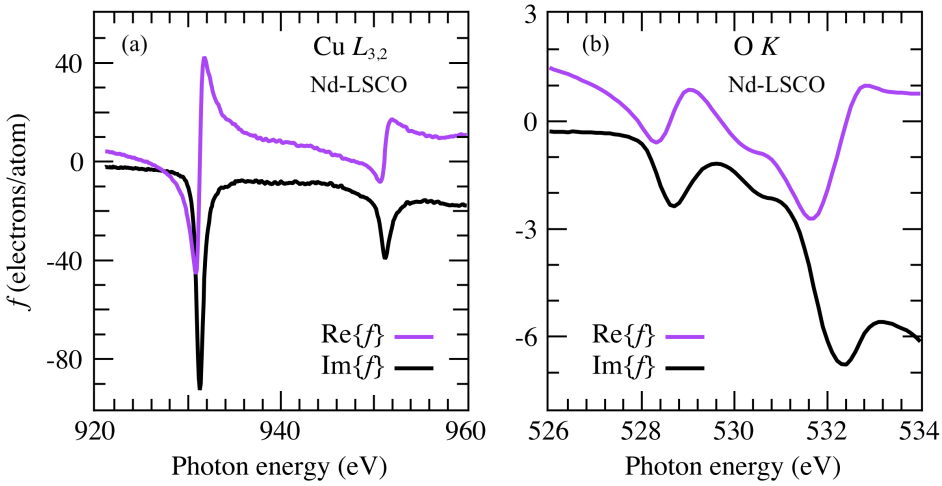


Figure 3.3: The atomic scattering form factors, $f(\omega)$, as a function of photon energy through the (a) Cu L and (b) O K absorption edges for Nd-LSCO determined from the XAS measurements. Figure reprinted from Ref. [28] with permission.

3.3.3 Symmetry of scattering tensor and Orbital sensitivity

As described in the previous section, near an X-ray absorption edge, the resonant effect enhances the scattering amplitude which now varies strongly with photon energy and, unlike off resonance, depends on details of the electronic structure, such as the valence, spin state or orbital symmetry of the unoccupied electronic states. The absorption coefficient is peaked at this (resonance) energy because a transition is now allowed from an occupied core state to an unoccupied state. The peaks in the absorption spectra exhibit sensitivity

[4] A more rigorous connection is explored in Ref. [88].

to the unoccupied holes. For instance, the Cu L edge ($2p \rightarrow 3d$) probes unoccupied $3d$ states, the O K edge ($1s \rightarrow 2p$) probes unoccupied $2p$ states and the La, Ba, Eu or Nd M edges ($3d \rightarrow 4f$) probe unoccupied $4f$ states.

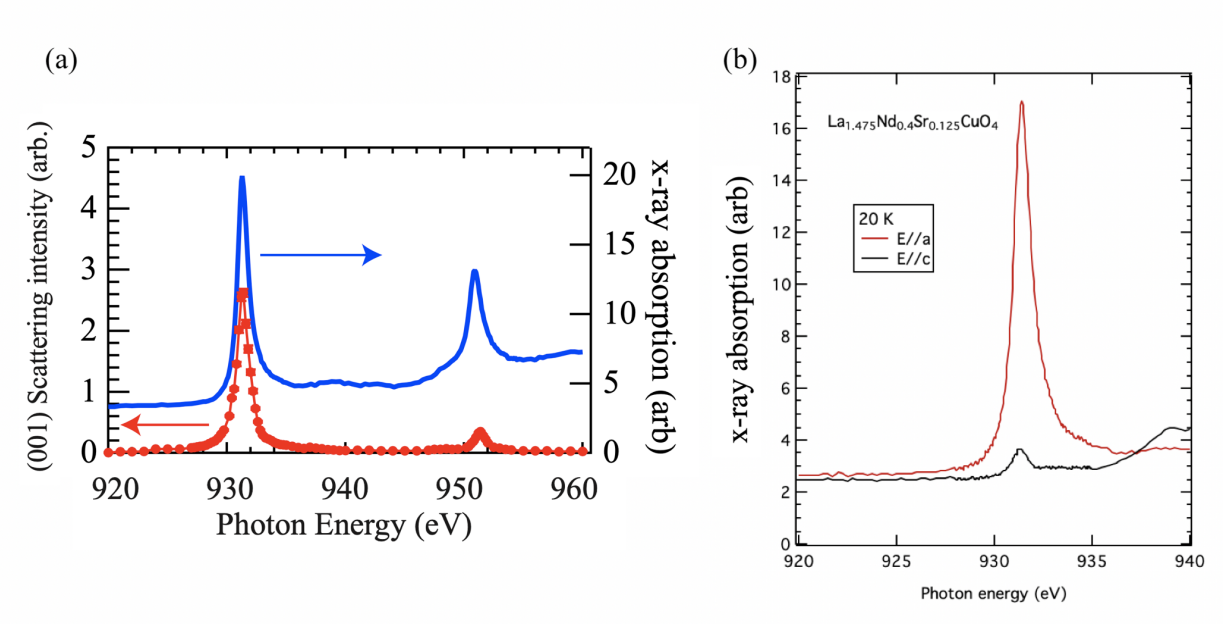


Figure 3.4: On resonance orbital sensitivity in RXS. (a) Enhancement of X-ray scattering on resonance: The resonant X-ray scattering intensity (red) and X-ray absorption (blue) as a function of incident photon energy through the Cu L absorption edge (2p to 3d transition) for the (001) Bragg peak of LBCO. (b) Polarization dependence of the X-ray absorption signal along different crystallographic directions (a and c), showing a large enhancement with polarization direction — indicating that it develops sensitivity to not only the hole occupation but also the symmetry of the holes associated with Cu $3d_{x^2-y^2}$ orbitals here. Figure (a) taken from the supplementary material of Ref. [39] and figure (b) is from the data collected by previous members of our group.

In multi-ion electronic environment configurations, like tetragonal, octahedral, or orthorhombic coordinations, not only does the system break atomic/ionic spherical symmetry but also influences the way it scatters light. This anisotropy depends on the incident photon energy and polarization of the light, which can be encapsulated by a tensor representation.

The atomic scattering form factor can be treated as a tensor quantity [88] like

$$I \propto \left(\frac{\mathrm{d}\sigma}{\mathrm{d}\Omega}\right) \propto \left|\sum_j (\boldsymbol{\epsilon}_{\mathrm{in}}^{\dagger} \cdot \hat{f}_j(\omega) e^{i\boldsymbol{q}\cdot\boldsymbol{r}_j} \cdot \boldsymbol{\epsilon}_{\mathrm{out}})\right|^2, \tag{3.20}$$

where $\boldsymbol{\epsilon}_{\mathrm{in}}$ and $\boldsymbol{\epsilon}_{\mathrm{out}}$ are incident and scattered photon polarization.

For a Cu $3d_{x^2-y^2}$ orbitals, neglecting spins, involved at energies for Cu L edge, the scattering tensor would obey certain symmetries. The off diagonal elements would be zero, while the x and y components would be identical. Similarly, for a p_x (or p_y) orbital, the x component would be finite and the y component would be zero. The polarization dependence of the X-ray absorption signal, in Fig. 3.4, depicts that as we move the polarization of incident light along different crystallographic axes — we become sensitive to the symmetry of these holes. Thus, on resonance, resonant X-ray scattering develops sensitivity to hole occupation as well as the symmetry of the holes, to further access orbital symmetry.

For a general triclinic system we can write the scattering tensor (at atomic sites j) as:

$$\hat{S}(\boldsymbol{q},\omega) = \sum_{j \text{ sites}} \hat{f}_j(\omega) e^{i\boldsymbol{q}\cdot\boldsymbol{r}_j} \sim \begin{pmatrix} f_{xx}(\omega) & f_{yx}(\omega) & f_{zx}(\omega) \\ f_{xy}(\omega) & f_{yy}(\omega) & f_{zy}(\omega) \\ f_{xz}(\omega) & f_{yz}(\omega) & f_{zz}(\omega) \end{pmatrix},$$

where the components of $\hat{f}$ are complex. For system of our interest, like tetragonal and orthorhombic symmetries: resonant charge scattering contributions would contribute to the diagonal elements whereas magnetic scattering contributions can be present at both diagonal and off-diagonal terms of the scattering tensor. Furthermore, the polarization and the diagonal elements of the scattering tensor can give us information about the orbital asymmetry, by investigating the azimuthal dependence of the ratio of two incident photon polarization. That is to say, different types of order would have different azimuthal dependence. We briefly discuss distinguishing between different ordering phenomena in Chapter 2 and Chapter 8 with Bragg peaks corresponding to specific symmetry breakings. Thus, RXS is a combination of structural and electronic probes giving us a novel way to investigate complex strongly correlated systems with co-existing phases by tuning the photon energy and incident photon polarization.

Case study: Azimuthal dependence relative to the incident polarization

To characterize the measure of in-plane orbital anisotropy probed via the (001) Bragg peak, we begin by writing out the structure factor for the Bragg peak at Cu atoms. It

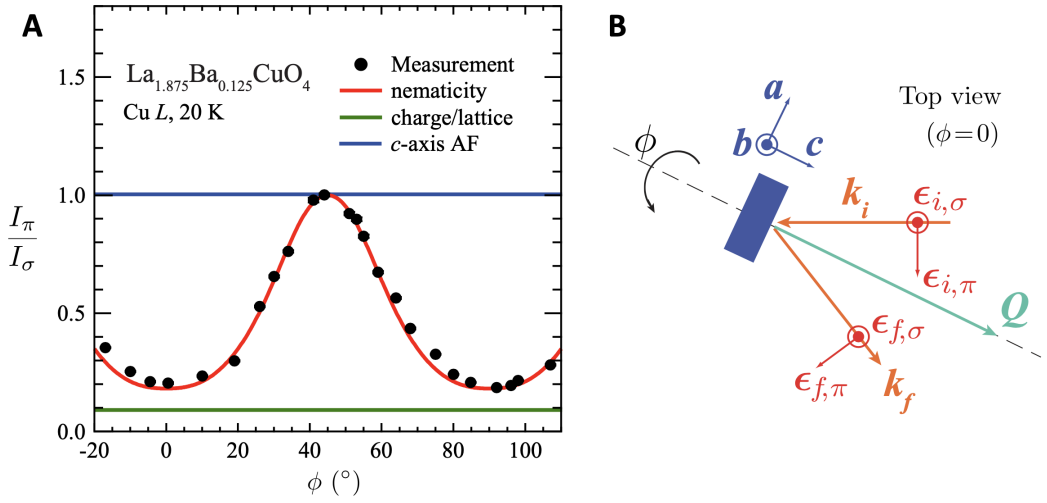


Figure 3.5: (a) Azimuthal dependence of the (001) Bragg peak intensity: The azimuthal dependence of I_π/I_σ provides strong confirmation that the (001) peak at Cu L edge is measuring electronic nematicity and not charge ordering or antiferromagnetic order, which would behave differently following from the symmetry of the scattering tensor. (b) Scattering geometry for the azimuthal dependent measurement described in the text. Figure taken from the Supplementary material of [39].

is convenient as their ionic position remains unchanged, with octahdral tilts in the LTT phase, as the tiliting axes passes through the Cu atoms in the unit cell.

$$S(001)_{\mathrm{Cu}} = \boldsymbol{\varepsilon}_{\boldsymbol{f}}^{*} \left(F_{\mathrm{av}}(z=0) + e^{i\pi} F_{\mathrm{av}}(z=0.5) \right) \boldsymbol{\varepsilon}_{\boldsymbol{i}}, \tag{3.21}$$

where $\boldsymbol{\varepsilon_i}$ (and $\boldsymbol{\varepsilon_f}$) denote incident (and scattered) photon polarization, and F_{av} is a tensor representation of the average atomic scattering form factor for Cu in neighbouring planes $z = 0$ and $z = 0.5$, as

$$F_{\mathrm{av}}(z) = \begin{bmatrix} f_{aa,\mathrm{av}}(z) & 0 & 0 \\ 0 & f_{bb,\mathrm{av}}(z) & 0 \\ 0 & 0 & f_{cc,\mathrm{av}} \end{bmatrix}. \tag{3.22}$$

It is worthwhile to note that for conventional (non-resonant) scattering, both $F_{\mathrm{av}}(z = 0)$ and $F_{\mathrm{av}}(z = 0.5)$ have identical terms, which makes the (001) intensity go to zero. Furthermore, on-resonance the diagonal components of the average atomic scattering form

factor — determined by local intra-unit cell anisotropic interaction — follow symmetry of the rotation between layers as

$$f_{cc,\mathrm{av}}(z=0) = f_{cc,\mathrm{av}}(z=0.5), \tag{3.23}$$
$$f_{bb,\mathrm{av}}(z=0) = f_{aa,\mathrm{av}}(z=0.5), \text{and} \tag{3.24}$$
$$f_{aa,\mathrm{av}}(z=0) = f_{bb,\mathrm{av}}(z=0.5). \tag{3.25}$$

We define the measure of in-plane anisotropy for the Cu $3d$ orbital in $z = 0$ and $z = 0.5$ layers as

$$\eta = f_{aa,\mathrm{av}}(z) - f_{bb,\mathrm{av}}(z), \tag{3.26}$$

which from symmetry conditions is identical to

$$\eta = f_{aa,\mathrm{av}}(z=0) - f_{aa,\mathrm{av}}(z=0.5). \tag{3.27}$$

The scattering intensity for the (001) at Cu L edge from Eqn. (3.21) can be written as:

$$I(001) \propto |S(001)|^2 = \left| \boldsymbol{\varepsilon_f^*} \begin{bmatrix} \eta & 0 & 0 \\ 0 & -\eta & 0 \\ 0 & 0 & 0 \end{bmatrix} \boldsymbol{\varepsilon_i} \right|^2 . \tag{3.28}$$

The expression for (001) peak scattering intensity in Eqn. (3.28) can be experimentally validated to hold for an electronic rotational symmetry breaking signature by measuring its azimuthal dependence relative to the incident polarization — scattering geometry shown in Fig. 3.5 (b). The azimuthal dependence of I_π/I_σ providing strong confirmation that the (001) peak at Cu L edge is measuring electronic nematicity of the Cu $3d$ states and has a form given by Eqn. (3.28).

Other ordering fashions and charge modulations signatures would lead to a different azimuthal dependency. Fig. 3.5 shows how modulations between planes of the average charge or lattice position or antiferromagnetic ordering of the average c-axis component of the Cu magnetic moment would behave differently from electronic nematicity. We utilize this capability of RXS later in Chapter 6 to distill the magentic ordering of the antiferromagentic spin structure Bragg peak in LNO327. An azimuthal scan at photon polarizations parallel and perpendicular to the scattering plane can differentiate between modulations of charge/lattice, AFM ordering, and electronic nematicity.

3.4 Time-Resolved Resonant X-ray Scattering

3.4.1 Motivation for a time-resolved probe

Equilibrium resonant X-ray scattering (RXS) is invaluable for characterizing static symmetry-breaking phases; however, it offers limited insight into the dynamic behavior of these phases, particularly under non-equilibrium conditions. In contrast, time-resolved resonant X-ray scattering (tr-RXS) enables the study of ultrafast processes on femtosecond (10^{-15} s) to picosecond (10^{-12} s) timescales, thus offering a dynamic perspective on phase evolution following laser-induced excitation. tr-RXS is especially effective for investigating transient states arising post-photoexcitation, in which symmetry can be broken or restored on ultrafast timescales.

The utility of tr-RXS in cuprates and other strongly correlated materials in understanding the physics of electronic symmtery-breaking phases is vast. Previous investigations into the non-equilibrium lattice and charge-order dynamics in $La_{2-x}Ba_xCuO_4$ at $x \approx 1/8$ [49, 89] have demonstrated that optical excitations via mid- and near-infrared laser pump pulses (85 meV and 1.55 eV) induce a transient state in which stripe-like charge density wave (CDW) order is suppressed on a sub-picosecond timescale. This suppression has been associated with the emergence of transient, light-induced superconductivity, observed in $La_{2-x}Eu_xSr_yCuO_4$ (LESCO) within a similar timeframe [89]. More recently, charge order in $La_{2-x}Ba_xCuO_4$ has been found to exhibit transverse fluctuations that can be stimulated by optical pumping, potentially enhancing in-plane superconducting tunneling between charge stripes. Whether light-induced superconductivity arises through competition with static charge order or via interaction with fluctuating charge order, it is evident that these phases are dynamically coupled. Despite extensive research on the dynamic interplay between CDW order and superconductivity, there remains a gap in understanding the role of nematic order within these processes [90, 91, 92]. Therefore, a systematic study of non-equilibrium nematicity in cuprates is highly warranted. Furthermore, in strongly correlated systems, quantum criticality often plays an underlying role between different electronic ordering tendencies. In cuprates, the proximity to a quantum critical point enhances fluctuations among charge, spin, and nematic orders. tr-RXS is optimally suited to capture these fluctuations in real time, providing crucial insights into how quantum criticality influences the interplay among superconductivity, CDW, and nematic order.

3.4.2 Introduction to tr-RXS

Time-resolved pump-probe spectroscopy has become an essential tool for investigating non-equilibrium dynamics in condensed matter physics, especially in systems with strongly correlated electrons, such as cuprates [93, 94]. A powerful extension of traditional RXS that enables the study of ultrafast dynamics in quantum materials. By using an ultrafast laser pulse to excite the system, followed by a delayed X-ray probe pulse, tr-RXS can capture and disentangle the electronic and structural order parameters by recording the recovery from femtosecond-picosecond to microsecond timescales. The techniques is highly effective in studying emergent phenomena in cuprates, including charge density wave (CDW) order, nematicity, and transient superconducting states, which often arise near the Fermi energy (E_F) [89].

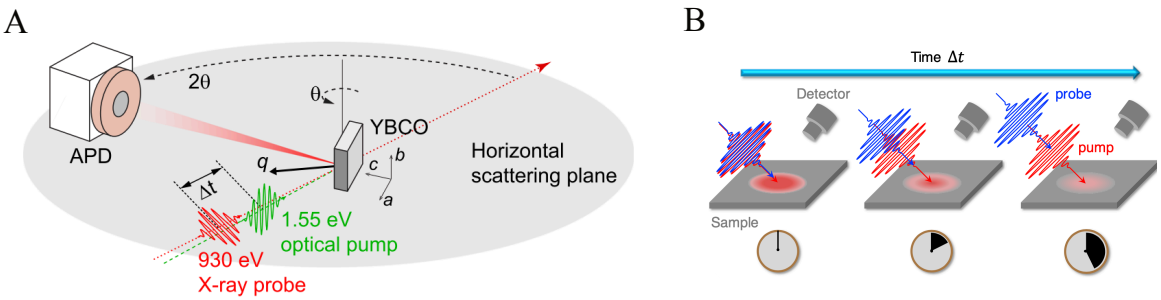


Figure 3.6: Experimental geometry of the tr-RXS experiment at SSS beamline at PAL-XFEL. Principle of the pump-probe method for ultrafast spectroscopies: The pump and probe pulses are incident on the sample at $\Delta t = 0$ and the response of the system after photoexcitation ($\Delta t > 0$) is studied. Δt is the time delay between the pump and probe pulses. Figure adapted from Ref. [91] with permission.

The core principle involves exciting the system with an intense ultrafast laser pulse (the pump), which drives the system into a non-equilibrium state by generating a population of high-energy "hot" electrons. A second, time-delayed X-ray pulse (the probe) tuned to elemental resonance then measures the transient response of the electron system (as described in the equilibrium RXS section), providing insight into the relaxation processes that follow the excitation. By using ultrafast pump pulses with controlled fluences[5] to derive the system out of equilibrium, tr-RXS experiments reveal the temporal hierarchy

[5]the fluence is defined as the energy per unit area delivered by the pump pulse

of relaxation dynamics that govern the interplay between superconductivity, charge order, and other low-energy states near E_F.

3.4.3 Mechanism of Laser Pump Excitation

The pump pulse in time-resolved experiments is typically in the optical or infrared range, with photon energies tuned to excite electrons near the Fermi level [95]. In cuprates, where low-energy physics is dominated by strong electron correlations, the interaction of the pump pulse with electronic states near E_F initiates a complex cascade of processes. The absorption of photons creates non-thermal electron populations by promoting electrons to higher energy states, resulting in a distribution that deviates significantly from equilibrium [96].

These hot electrons transfer energy to the lattice and other collective excitations, such as phonons, spin waves, or even charge order, depending on the material and excitation conditions. In cuprates, this interaction with collective modes is crucial, as it underpins the coupling between electronic and structural degrees of freedom that gives rise to competing orders [97]. Such coupling can drive transient states where superconductivity is enhanced or suppressed, providing a controlled method for studying the interplay between superconducting and charge-ordered phases [98].

3.4.4 Non-Equilibrium State and Relaxation Dynamics

The non-equilibrium state generated by the pump pulse evolves on ultrafast timescales as electrons begin to relax through electron-electron and electron-phonon interactions. The subsequent dynamics depend on the complex interplay between relaxation and scattering processes. In cuprates, relaxation often involves reorganization of both the charge and spin distributions, leading to the formation of transient electronic phases that can differ significantly from equilibrium behaviour [99].

Probing the system during this relaxation period provides valuable insight into the hierarchy of interactions in cuprates. For instance, time-resolved studies have shown that CDW order can be suppressed or modified in response to photoexcitation, allowing researchers to probe the delicate balance between competing orders [90, 92]. Furthermore, some studies have observed light-induced superconductivity in non-equilibrium states well above the equilibrium critical temperature T_c, which suggests that the interactions stabilizing superconductivity can be dynamically enhanced under certain conditions [89].

Near E_F, the low-energy electronic states in cuprates are strongly affected by the presence of a Mott insulating gap and doping-induced states. These features contribute to the complex electronic landscape, where superconductivity, charge order, and nematicity coexist in close competition [94]. Time-resolved pump-probe experiments can probe these states as they allow for direct observation of transient effects that provide insights into the underlying interactions governing these orders. The ability to selectively excite and probe electronic states near E_F is especially valuable in cuprates, where the physics of pseudogap and superconducting phases is sensitive to small energy shifts and subtle variations in electronic order [95]. The key advantage of tr-RXS is its ability to probe nonequilibrium dynamics, such as the melting and recovery of CDW order in YBCO, or the transient formation of superconducting states. For example, in stripe-ordered cuprates like Nd-LSCO and LBCO, tr-RXS has revealed how charge and spin orders respond to ultrafast perturbations, providing insights into the competition between these orders and superconductivity.

3.5 Limitations of soft light and geometries

Although RXS has established itself as a novel probe for disentangling strongly correlated phases of matter in TMOs, there are challenges and limitations. Using soft X-rays dramatically limits the momentum transfer to a very limited region of the reciprocal space unlike the freedom with hard X-rays. Along with limited reciprocal space access to ordering phenomenon, this makes the application of magnetic field and uniaxial stress a challenging task due to cutting of incoming beam with equipment. Sample environments at experimental facilities are maintained under ultra-high vacuum conditions because of the large absorption coefficient of air (or low photon path lengths) at soft X-ray energies. The absorption coefficient is greatly influenced by the transition edge (photon energy), geometry (incident and scattering angles), and polarization causing saturation effects in the observed peak spectrum. The penetration depth of soft X-rays is limited — 100 atomic layers or less depending on the transition edge — which in our study of layered TMO heterostructures prevents us from measuring the c-axis correlation length via a (001) peak that would help us understand inter-layer coupling better.

Chapter 4

Synchrotron radiation and experimental setup

4.0.1 Introduction

The progress of resonant X-ray scattering as a technique has been greatly influenced by the development of brilliant X-ray radiation light sources such as synchrotrons and free electron lasers. Synchrotron light sources are experimental megastructures that accelerate electrons at relativistic speeds in a circular orbits. In this thesis, we focus on the experiments performed on 3^{rd} generation sources including Canadian Light Source (CLS), Saskatoon, Canada and BESSY II Ring, Berlin, Germany, and free electron laser (FEL) at Pohang Accelerator Laboratory (PAL-XFEL), Pohang, South Korea.

Resonant scattering experiments are performed at a synchrotrons owing to their capability in generating highly resolved spatial and spectral distribution of the photon flux (x-rays beam) with tunable energy and polarization. Making it an ideal source to detect signal intensities off and on-resonance for both soft and hard x-rays. A schematic diagram of a synchrotron and free electron laser is shown in Fig. 4.1. Through the use of insertion devices which are arrangement of magnets producing magnetic fields in alternating directions, electrons are restricted to a path tracing oscillatory motion to generate photon radiation. After a series of insertion devices and bending magnets, the synchrotron radiation is transmitted to the beamlines, or the respective endstations.

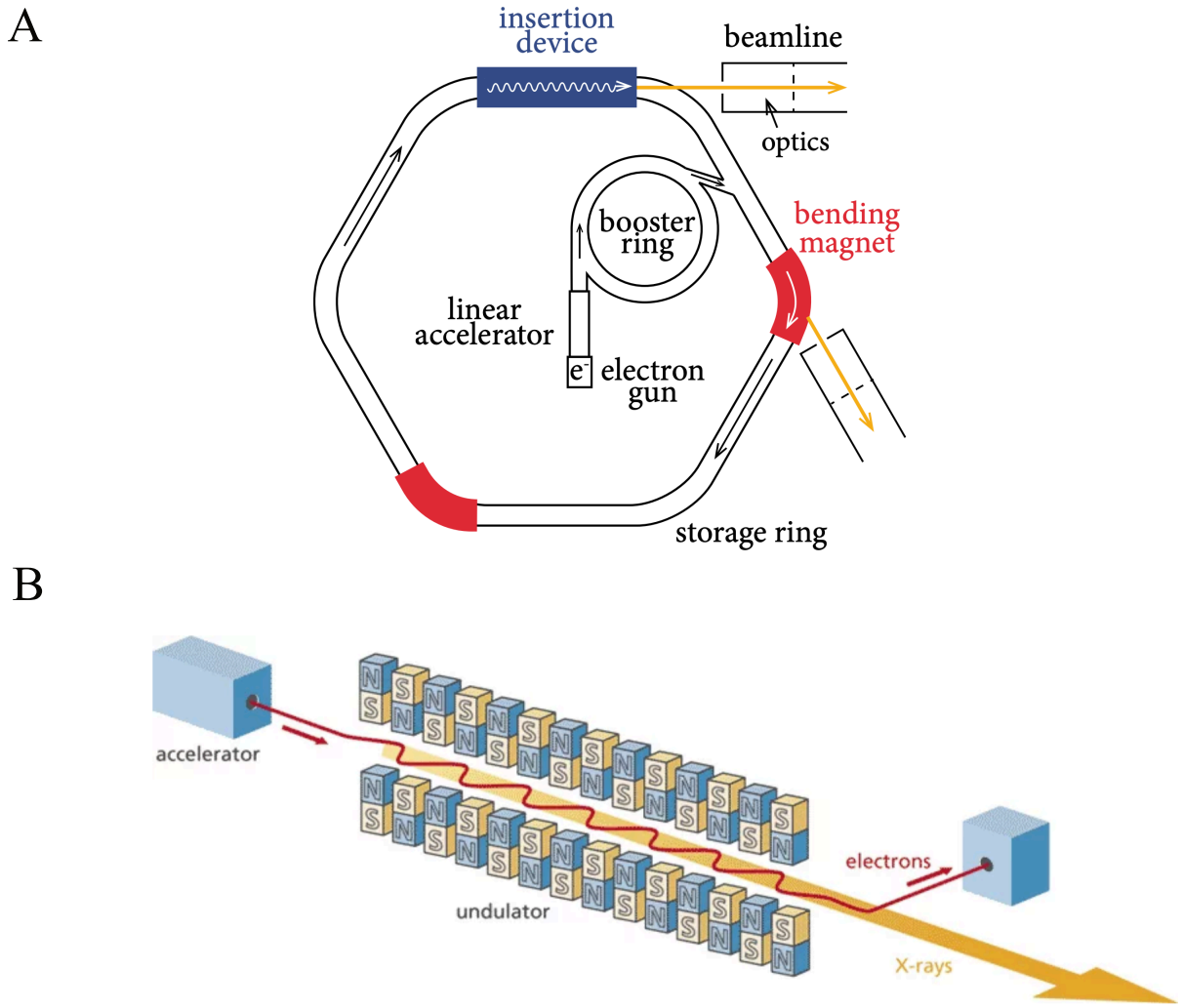


Figure 4.1: A schematic diagram of a, A: synchrotron radiation source, and B: X-ray free electron laser source. Figure reused from Ref. [100].

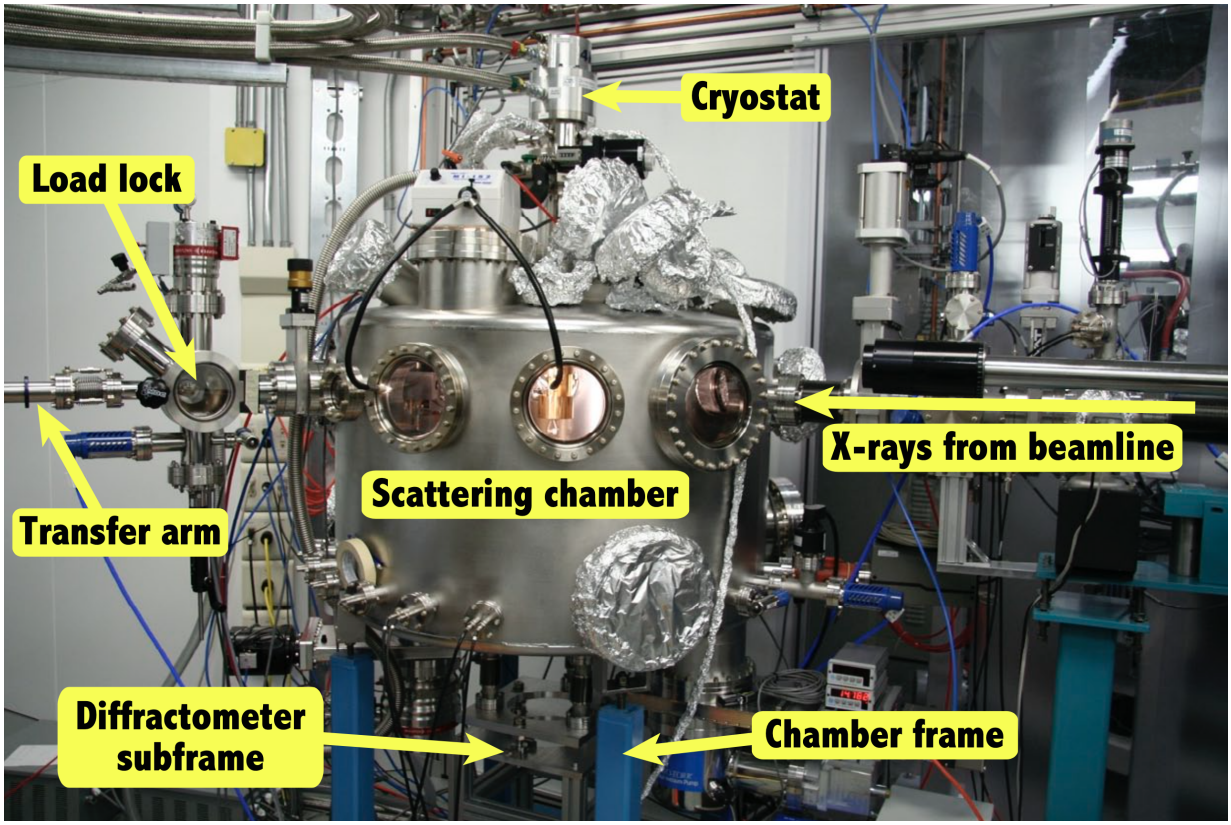


Figure 4.2: The RSXS scattering chamber at the CLS's REIXS beamline. Image reproduced from Ref. [27] with permission.

4.0.2 REIXS beamline at the Canadian Lightsource

Majority of the equilibrium resonant scattering experiments presented in this thesis were carried out at the REIXS (Resonant Elastic and Inelastic X-ray Scattering) beamline at the Canadian Light Source (CLS) in Saskatoon, Canada. Before reaching the ultra-high-vacuum (UHV) chamber — where the scattering experiment is performed[1] — the synchrotron radiation passes through a optical arrangement containing a monochromator and exit slits. This optical configuration at the REIXS beamline houses a variable line spacing plane grating monochromator, with different gratings and coatings on a plane mirror to

[1]The main chamber at REIXS beamline as well as the storage ring is maintained under UHV with pressures less than 10^{-9} Torr. This is done not only to prevent the deposition of contaminants of sensitive optical instruments but also to maintain mean photon path of soft x-rays which is suscpetible to even low pressures.

optimize flux at photon energies spanning the full energy range of the beamline.

In Fig. 4.2, the main scattering chamber for resonant elastic scattering is presented. After passing through the monochromator and exit slits, the (soft) x-rays from the REIXS beamline enter this chamber. The sampleholder is mounted on an in-vacuum four-circle diffractometer [101] that allows alignment of the incident X-ray beam on the sample under investigation to access the desired Bragg peaks. To the left is the load lock and the transfer arm which is used to store and transfer samples into the scattering chamber. Top of the assembly houses a closed cycle cryostat which is connected to the sampleholder with copper braids too achieve cooling down to low temperatures. The base temperature for measurements is around 20 Kelvin.

4.0.3 Diffractometer geometry and motion stages at CLS

The sample to be studied is mounted on the sampleholder as shown in Fig. 4.3. There are six motors (or degrees of freedom) available within limits. The purpose of the layered, calibrated motor assembly is to allow flexibility of operations for the user during the sample alignment process, for example to center in-plane Bragg peaks at the desired detector height. Apart from alignment, it also gives accessibility to more $\boldsymbol{q}$ addresses in the reciprocal space. The x, y, and z stages/motors can achieve translations of ± 7.5 mm, χ and ϕ motors can access motions of $\pm 7^{\circ}$. The main action happens through $\theta - 2\theta$ scans — which are essentially synchronous and restricted motion of the θ[2] and 2θ motors in such a way that it corresponds to the desired reciprocal space scans. Figure 4.3 shows how a different combinations of real space motor movement help us navigate different directions in the reciprocal space depending on the incident photon energy, distance to the detector other than the θ and 2θ motor positions.

Resonant X-ray scattering measurements involve scanning q-values in reciprocal space to gather information about the width, amplitude and position of the Bragg peak.

Another important technical aspect of this sample receptacle-holder assembly is the change in sample position, or equivalently the location of the beam on the sample surface with change in temperature. At CLS, the thermal expansion (contraction) effect is minimized and channeled along the θ and z motion stages with the help of the support structure consisting of oblique thin-walled stainless steel tubing. Making it easier to systematically re-center the corresponding Bragg peak upon changing temperatures in a set of measurements.

[2]sometimes called the ω motor. This is done to avoid the confusion that 2θ is twice the θ — which only holds for the (00ℓ) scans.

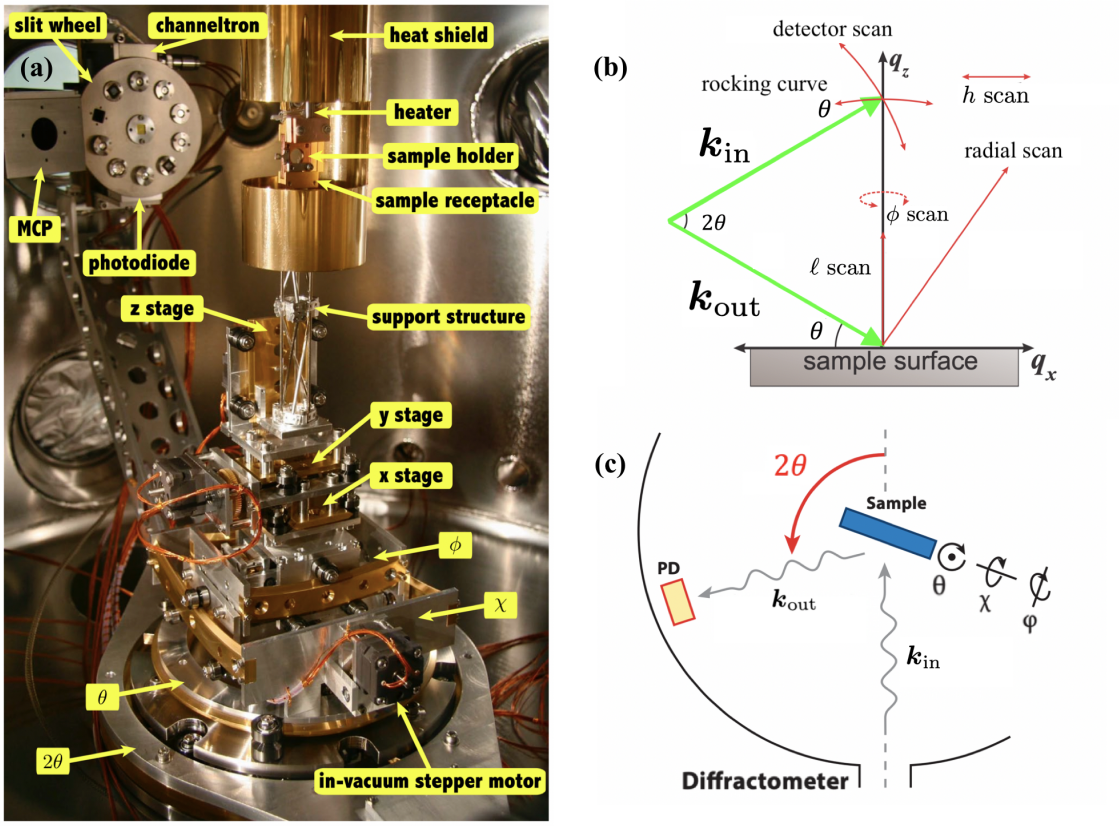


Figure 4.3: Motion stages and scattering geometry: (a) The four-circle diffractometer assembly in the RSXS scattering chamber, (b) Schematic diagram of the translations of real space motions to their corresponding reciprocal space scans, (c) Schematic diagram of the top view of the four-circle diffractometer assembly. Figure (a) reused from Ref. [27] with permission. Figure (c) adapted from Ref. [14].

4.0.4 Detectors at CLS and scanning protocols

In the scattering chamber at CLS, there are detectors attached to the 2θ arm. The data collection in the upcoming chapters include the usage of a micro-channel plate (MCP), a silicon drift detector (SDD), a photodiode (PD), and a channeltron (ChT). The approximate distance of these detectors is 30 cm from the sample position. The MCP detector provides single-event counting, 2D position sensitive detection of soft x-ray photons, it has a diameter of about 25 mm. This becomes very useful in aligning the Bragg peak, and detecting weaker signals over the entire active area, for instance, a charge ordering signal (as described in section 2.1.1) has a wider and weaker spread in q-space, and is still easily recorded via a h-scan. The PD is sensitive to a large range of photon energies with a linear response for higher photon energies, this makes it suitable for the high flux of the direct beam or an x-ray fluorescence measurement. A slit wheel containing different filters and slits gives the control over the energy resolution and intensity saturation of the signal based on the incoming flux. The SDD measures the energy range of an incoming photons, and is suitable for low-energy x-rays providing a decent energy resolution for high count rates, the peaking time can be changed to avoid saturation of the signal.

4.0.5 High-field Diffractometer at BESSY

The High-Field Diffractometer is an endstation suited for XAS and equilibrium RXS in magnetic fields up to 7 Tesla, and temperatures down to 4 K. Providing an excellent combination for studying electronic symmetry-breaking phases in quantum materials in high magnetic fields and low temperatures, especially relevant to stripe-ordered cuprates where superconductivity onsets below 20 K which is the base temperature constraint with closed cycle cryostat beamlines such as CLS and PAL.

Low temperature measurements in Chapter 6 were conducted at UE46-PGM1 beamline in BESSY II, Berlin, Germany. The endstation is equipped with a high-magnetic field chamber, featuring a rotatable superconducting magnetic coil capable of generating magnetic fields up to 7 T in any orientation relative to the sample surface. Both the sample and detector are mounted on rotatable motors (ω and 2θ), allowing for scattering experiments in high magnetic fields with in-plane fields for certain geometries. However, the rotatable magnet imposes certain constraints on the achievable scattering geometries. Fixed slits provide accessible angular windows for 2θ in the ranges $0° < 2\theta < 66°$ and $84° < 2\theta < 96°$. Figure 2.18 presents a schematic of the available scattering geometries under an applied field with the magnet oriented at 0°. This allows us to investigate the (001) Bragg peaks

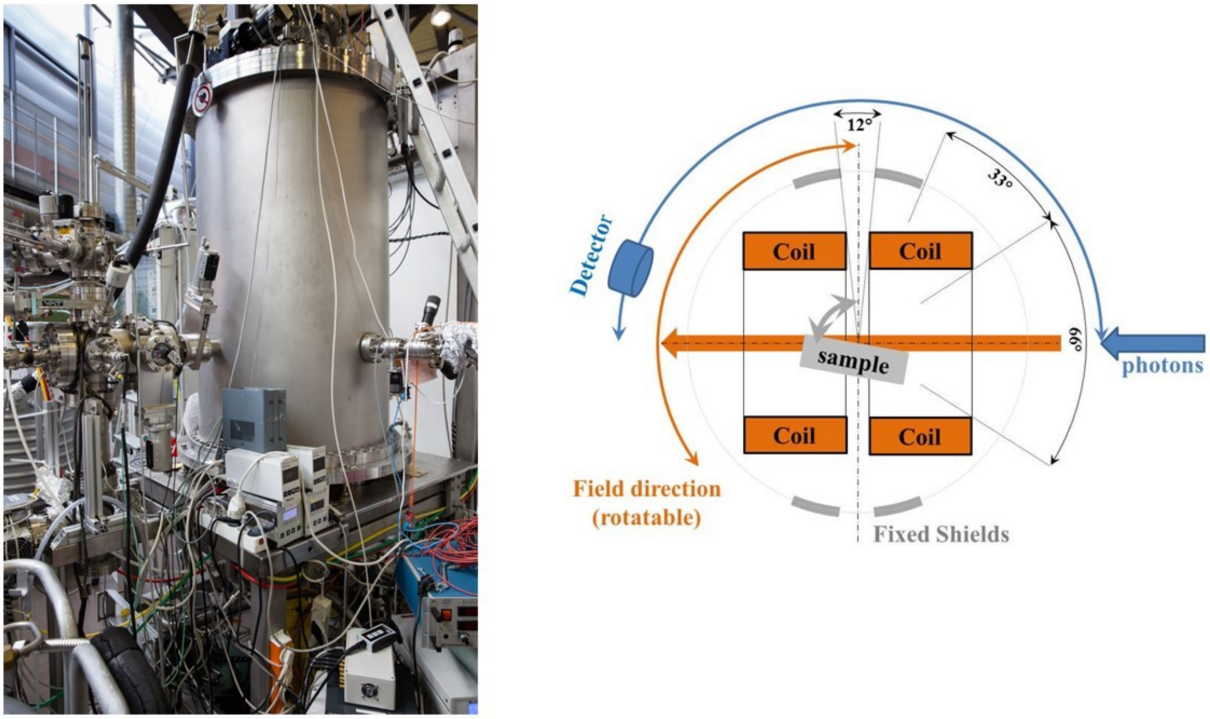


Figure 4.4: View of the High-Field Diffractometer (left) and schematic representation of the scattering plane (right). Image reused from Ref. [102].

under in-plane magnetic fields at Cu L and Nd M resonances, but restricts the beam at the O K resonance.

4.1 X-ray Free Electron Lasers (XFELs)

X-ray Free Electron Lasers (XFELs) are state-of-the-art facilities that generate high-intensity, ultra-short x-ray pulses using self-amplified spontaneous emission (SASE) from relativistic electron beams traversing undulators. XFELs provide unprecedented brightness in the x-ray regime, achieving photon energies from hundreds of eV to several keV, with temporal resolutions down to femtoseconds. This allows XFELs to probe atomic-scale dynamics in real-time, making them invaluable for studying ultrafast phenomena in fields such as condensed matter physics, chemistry, and biology.

4.1.1 SSS beamline at the PAL XFEL

The time-resolved Resonant Soft X-ray Scattering (tr-RSXS) facility[3] at the Pohang Accelerator Laboratory X-ray Free Electron Laser (PAL-XFEL) has been established to probe dynamic electronic ordering phenomena in strongly correlated materials with high temporal resolution. The endstation at PAL-XFEL facilitates ultrafast x-ray scattering, enabling the study of temporal dynamics in materials exhibiting charge, spin, and orbital orders. The tr-RSXS utilizes femtosecond pulses to capture transient states and dynamic processes in materials, specifically catering to an energy range of 400 eV to 1300 eV with a time resolution of approximately 100 fs, achievable without jitter correction [91].

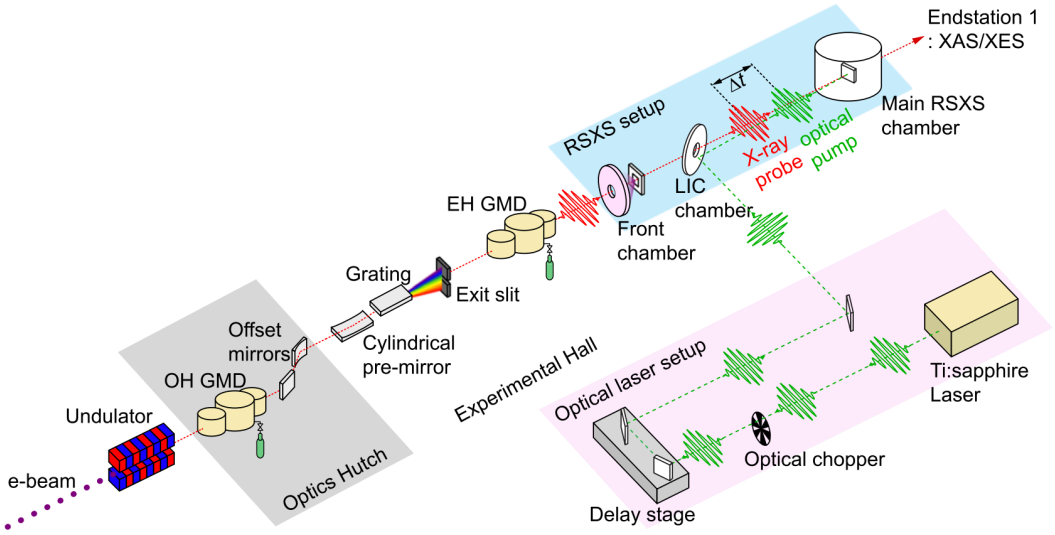


Figure 4.5: Schematic of the SSS beamline. From upstream (lower left), (1) the accelerated electron beam and the planar undulator, (2) the OH-GMD and horizontal offset mirrors in the OH (gray), (3) the pre-mirror and grating set, (4) the EH-GMD, and (5) the RSXS system (light blue). The optical laser system is shown in pink at the lower right. Image reused from Ref. [27] with permission.

[3] An incomplete survey of the time-resolved instrumentation is provided. I would like to acknowledge the immense help and support of the beamline scientists who are experts in the optical nuances of the experiment, in-depth discussion of which is beyond the scope of this thesis.

4.1.2 Instrumental setup and configuration

The Soft X-ray Scattering and Spectroscopy (SSS) beamline provides the x-ray source. Electron beams accelerated and passed through a series of planar undulators with a 35 mm period to generate free-electron laser radiation via self-amplified spontaneous emission (SASE). The primary "pink beam" generated has a pulse energy of around 200 μJ at 850 eV, producing approximately 2×10^{12} photons per pulse [91].

The pump-probe system at PAL-XFEL uses an optical laser synchronized with the x-ray beam. The Ti:sapphire laser delivers pulses with a wavelength of 800 nm and a duration of 40 fs, and its repetition rate reaches up to 1080 Hz, typically operating at 60 Hz in experimental conditions. The laser energy is adjusted using motorized attenuators, and delay stages provide temporal control up to 2.6 ns, with spatial overlap maintained by beam stabilization systems. The facility achieves a cross-correlation time resolution of approximately 110 fs, determined through optical transmission measurements on a YAG crystal, with an estimated jitter-free time-zero (t_0) [91].

4.1.3 Spatial and Temporal Overlap

Achieving spatial and temporal overlap between the optical laser and x-ray pulses is critical for the success of pump-probe experiments. The optical laser is introduced into the main chamber at an angle nearly parallel to the x-ray path, achieved through a centrally holed mirror system. This allows the x-ray beam to pass through the mirror while the optical pulse reflects onto the sample. The spatial alignment is finely tuned by adjusting the laser reflection angle to ensure the pulses overlap precisely on the sample. The spatial alignment is monitored using a YAG crystal; when both pulses meet at the same spatial point, their interaction can be detected by observing changes in the YAG crystal's fluorescence or the scattered intensity.

Temporal overlap, the synchronization of the x-ray and laser pulses to femtosecond accuracy, is achieved by varying the delay between the two pulses using a mechanical delay stage. This stage adjusts the optical path length of the laser, effectively shifting the arrival time of the optical pulse relative to the x-ray pulse. Temporal zero (denoted as t_0) is found by monitoring the cross-correlation signal, typically using changes in optical transmission through a YAG crystal as a function of delay. This method provides a time resolution of approximately 100 fs.

4.1.4 Detector and Goniometer Geometry

The detection system at PAL-XFEL consists of an avalanche photodiode (APD) and a multi-axis goniometer for precise angular control. The APD is configured as a point detector with an active area of 3 mm, positioned at variable distances from the sample (ranging from 80 mm to 160 mm) to adjust the detected solid angle. A primary feature of this setup is the goniometer, which provides six-axis control (translation and rotation) for the sample. The goniometer enables sample rotation in both the azimuthal and polar directions, permitting comprehensive coverage of reciprocal space during data collection.

The APD is mounted on a differentially pumped rotating flange, allowing for 2θ rotation, critical for angle-resolved measurements. Two additional photodiodes are used: a Si PIN diode for intensity calibration and a fast GaAs photodiode for time-resolved measurements, with the latter offering a temporal resolution of 30 ps. Together, these systems allow for a high degree of flexibility in capturing the desired scattering signals, critical for complex tr-RSXS experiments.

4.1.5 Experimental procedure for a pump-probe experiment

A standard tr-RXS experiment in characterizing a Bragg peak assosiated with a symmtery breaking phase proceeds as follows:

The sample, often a single crystal or thin film, is affixed to a flag-style sample holder. This holder is then mounted on the goniometer in the main RSXS chamber. Precise alignment of the sample relative to the x-ray beam path is achieved by translating and rotating the goniometer. Then, spatial and temporal overlaps are established between the x-ray and optical laser pulses, as described earlier. Initial alignment is conducted at room temperature, and any fine adjustments are made based on fluorescence and transmission measurements from the YAG crystal.

With the optical laser off, a baseline RSXS measurement is taken at specific x-ray energies resonant with atomic edges of interest. These baselines capture the static properties of the sample. The optical laser is then turned on to initiate the desired electronic or structural dynamics within the sample. The delay time (Δt) between the x-ray pulse and the laser pulse is varied using the mechanical delay stage, allowing for a time-resolved study of the dynamics as they evolve post-excitation.

Scattered x-ray intensity is measured by the APD as a function of Δt, capturing the temporal evolution of resonant scattering intensities. Shot-to-shot data is recorded to minimize noise, with each time step averaged over several pulses. A high-speed digitizer is

used to collect signals from both APD and photodiodes, synchronized with the PAL-XFEL pulse to allow for precise, time-stamped data collection.

4.2 Sample Preparation

This section has been adapted from my Masters thesis [81].

Before performing the experiment at the synchrotron, there are certain things to be taken care of, like: a clean surface, properly mounted samples on a sampleholder (that will eventually fit the sample receptacle at the CLS), and most importantly well-aligned reciprocal axes for the Bragg peak to be studied. The last part is crucial because as we mentioned in section 3.1, RSXS has limited access to the q-space unlike the hard x-rays. Other factors that needs proper characterization include, possible twinning or mosaic spread, polishing defects, χ and ϕ offset angles — not only does it constitute good practice but also saves valuable time during the limited shifts available at the CLS.

4.2.1 Determining crystallographic axes: Laue Diffraction

Before performing any mechanical operations like cutting, cleaving, or polishing on the single crystal sample to suit the purpose of the experiment, it is important to record the orientation of the sample (which is grown as a boule). Laue diffraction is an useful technique to determine the orientation of the crystal using hard x-rays by having a large number of diffraction peaks impinged on a photographic film in order to gain information about the crystal symmetry and orientation. For a simple crystal, and a monochromatic x-ray source, only a few diffraction peaks are visible, since a single scattering angle will satisfy Bragg's law for each crystal plane. The Laue method uses a Tungsten x-ray source with a wide spread in energy, so as to get more diffraction peaks, that can be analyzed to determine crystal symmetry and orientation. These diffraction Bragg peak positions are recorded using Fujifilm imaging plates, which uses a high-emission, photo-stimulated phosphor, which accurately detects and stores x-ray energy illumination spots in its phosphor particles. These plates are then scanned without exposing to light and the resulting pattern is analyzed, as shown in Fig. 4.7.

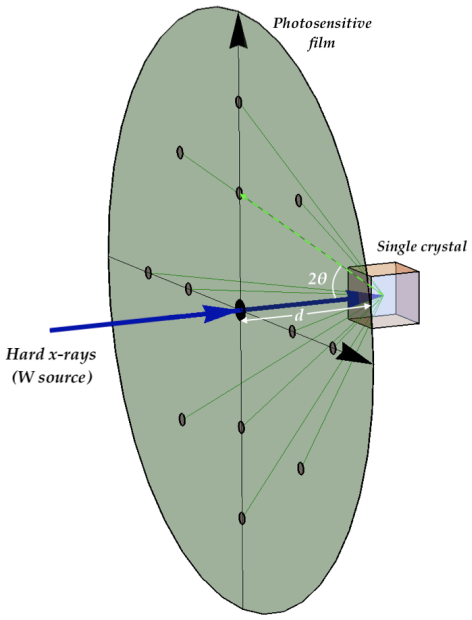


Figure 4.6: Setup for backscattering Laue diffraction geometry for single crystal orientation.

Laue scattering can be operated in transmission or back-scattering geometry. For thick single crystals, Laue back scattering geometry is more suitable as shown in Fig. 4.6, the x-rays produced by the Tungsten target are incident (shown in blue) on a stationary crystal behind the photosensitive plate which then scatters them (shown in green) back towards the x-ray tube. For each crystal plane, in a particular sample orientation, d and θ are fixed, so x-rays with wavelength $n\lambda$ will satisfy Bragg's law and diffract in the direction making an angle 2θ with the incident x-ray beam. The diffracted beams will cross through the plane perpendicular to the x-ray beam creating a series of Laue spots corresponding to different crystal planes ($d_{hk\ell}$) and the Bragg peaks ($hk\ell$).

Our main subject of investigation in this thesis are La-based cuprates, in Fig. 4.7(a) we

see the Laue diffraction pattern by the crystal boule of Nd-LSCO with unknown orientation. We know the space group for our single crystal is $I4/mmm$ and lattice constants are, $a = b = 3.787$ Å, $c = 13.24$ Å. Our aim is to align the single crystal along the [001] crystallographic direction: we begin by a random crystal orientation Fig. 4.7(a), which resembles being close to [100] direction[4] Performing the Laue diffraction again, this time

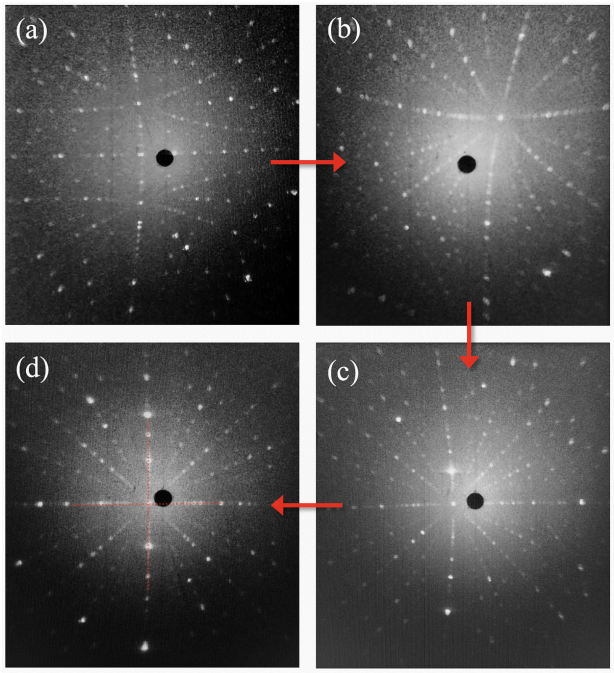


Figure 4.7: Laue scattering images in back-scattering geometry: Aligning a single crystal in a desired crystallographic direction. Images (a) to (d) are Laue scattering photographs from a single crystal alignment procedure. Starting from a random crystal orientation in (a), to polishing and cutting to achieve the crystal oriented along the desired [001]. Details are described in the text.

with one of the adjacent faces of the sample facing the beam (first red arrow operation), and we get (b) which looks close to being oriented [001]. Fig. 4.7(b), however, has offset in χ, ϕ and θ which can be calculated and corrected to achieve our desired orientation of c perpendicular to the sample surface. We account for these angular (χ, ϕ and θ) corrections (second red arrow) on the goniometer to get to Fig. 4.7(c), then we cut our samples. When the angular offset is less than 5°, I have found it useful to polish on an incline rather

[4]We know this by running a Laue simulation of the crystal parameters on OrientExpress software. Since we are not interested in the individual Bragg peaks, I have skipped superimposing the simulated pattern.

than cutting the samples (third red arrow) – after polishing and correcting for a small χ offset we get almost perfect [001] alignment in Fig. 4.7(d). The more accurately this alignment is done, the lesser time we have to invest at the synchrotron[5]. Once we have the correct angles, the next step involves cutting, cleaving, and polishing depending on the nature of the measurement. One thing which is worth mentioning is, even after getting the exact angles it requires extreme caution to precisely cut and polish the crystals along those directions — often in the process of aligning one angle, the other develops an offset. The order in which these corrections are approached make the job slightly easier.

4.2.2 Aligning real and reciprocal axes

Cutting: Wire Saw

After performing the Laue diffraction, the crystal boule on the goniometer is transferred to a wire saw to perform cuts along the desired crystallographic axes. A wire saw is essentially a tungsten[6] (or steel) wire which spools on two discs, running from one to another in such a way that the wire achieves a cutting action by going back and forth over the sample — by dragging a grit of boron carbide across the sample surface — it begins by a shallow scratch but because of the weight on the wire it seeps in until the entire thickness of the samples is cut. Fig. 4.8 shows the wire saw's cutting action, and how the weight can be modulated to achieve accuracy while making the first scratch. The general approach is to achieve one good flat surface and then re-check it with Laue diffraction again until the desired orientation is decent enough, this step can require several iterations. After a flat, well-oriented surface is achieved, we proceed to the next step of cleaving (or polishing-etching) the sample to expose a clean surface which would receive the synchrotron radiation in the scattering chamber at the CLS.

Polishing: to orient and achieve a flat surface

Polishing has to done in multiple stages, with careful transition from a coarser microgrit polishing paper to a fine one. If the aim of polishing is just to correct a small χ offset, or get a flat surface to provide a base of cleaving — one can be slightly careless about it and just use a single 20 micrometer grit paper, since the polished surface would be stuck

[5]These operation can take days sometimes to get perfect alignment, but often justified in worth by the ease of aligning the desired peaks at the CLS.

[6]Preferred because of its stiffness but difficult to re-spool.

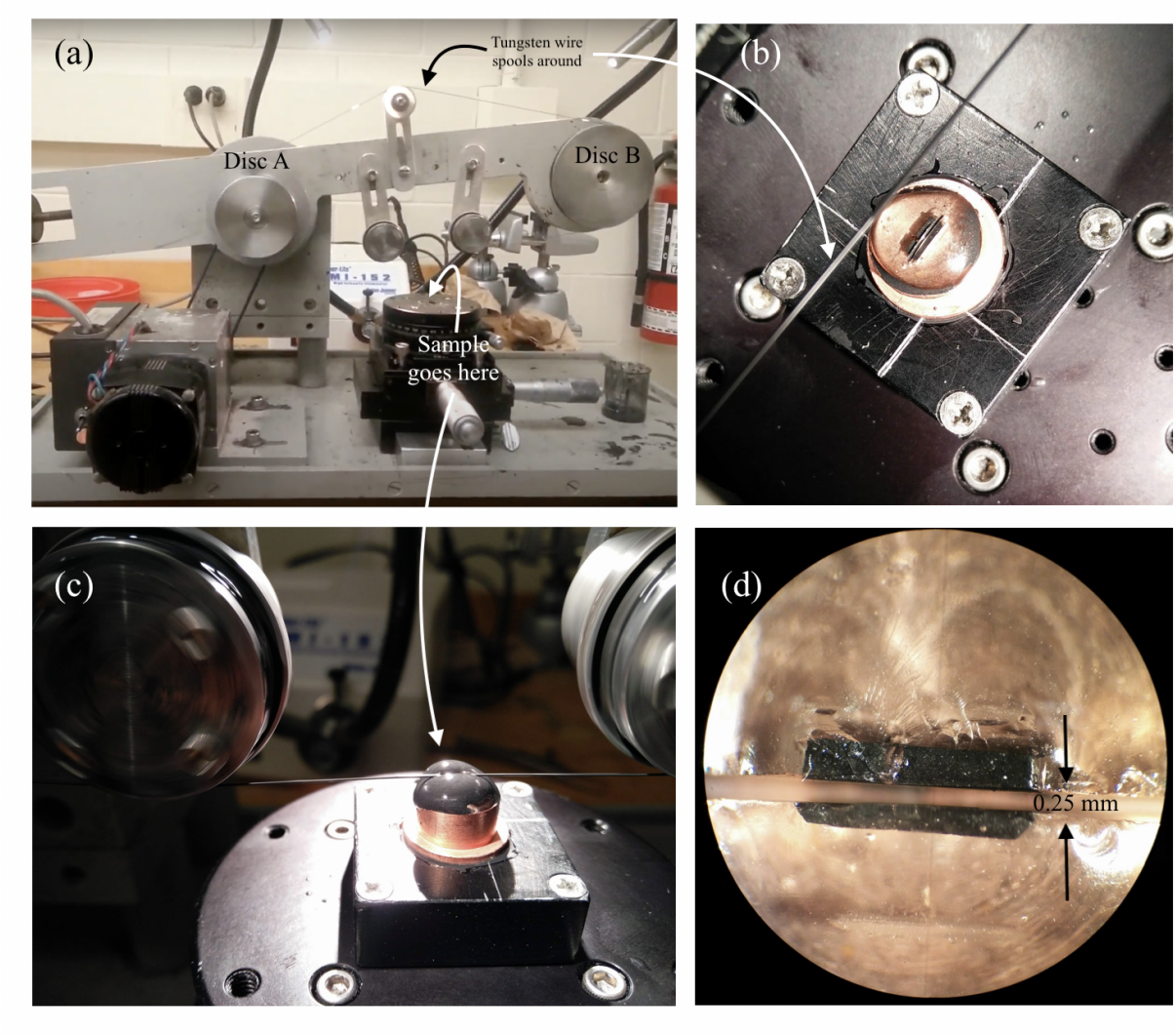


Figure 4.8: Wire saw machine for cutting samples: (a) shows the wire saw assembly, (b) and (c) show the cutting motion by the Tungsten wire in action, and (d) shows the completed task of cutting a single crystal sample along a particular direction. Working and details discussed in the text.

to the base and not exposed to the synchroton beam. More details discussed in the next polishing section.

Cleaving: Top post and anvil-blade

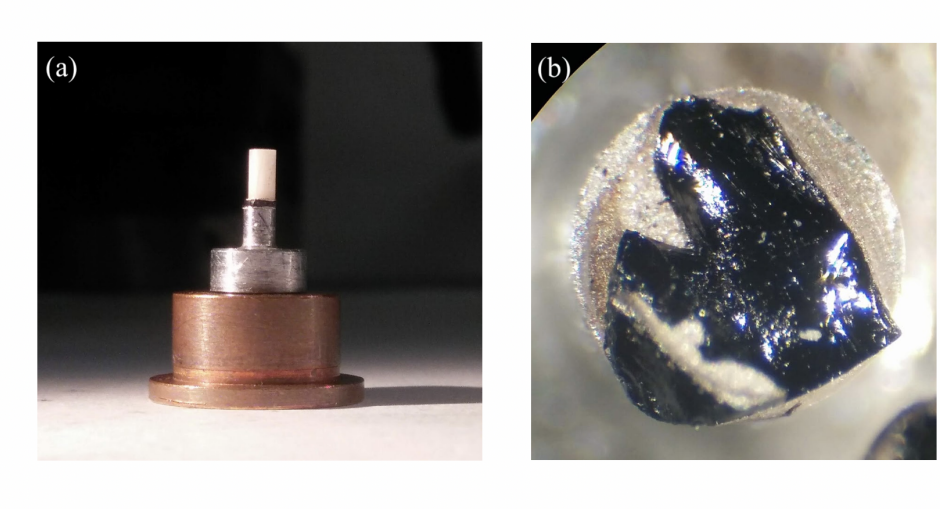


Figure 4.9: Top post cleaving: (a) shows the sample sandwiched between the copper plug and the cleaving post with silver epoxy bonding the sample surfaces, (b) Thee sample is cleaved after a quick, horizontal impulse is imparted on the top post.

A clean surface is crucial for a good (or any[7]) signal intensity. After getting a flat surface, we use a copper plug and a top post attached to the top and bottom ends of the sample as shown in Fig. 4.9(a) — it is generally easier to get a good cleave along the weaker crytallographic axes, in Nd-LSCO it is the *c*-axis. We use silver epoxy (EPO-TEK H20E) as it has a stronger bond than the interlayer bonding in Nd-LSCO (if applied and cured correctly); thus on giving the top-post a strong flick — the sample is fractured/cleaved exposing a clean surface. Speculatively, I have found cleaving to become more difficult with increasing hole-doping[8]. There is an additional capability at the load lock at the CLS and the UHV chamber in our lab of using blade and anvil sample cleaver, which applies pressure to the side of the sample causing it to fracture in vacuum, exposing a fresh surface.

[7]If the surface is not properly cleaved, it is common to not find any peak, or a very feeble peak intensity: both cases are undesirable.

[8]The Nd-LSCO, x=0.24 sample took about 10 cleaving attempts to get a good surface, and still the signal intensity was almost non-existent at the CLS.



Figure 4.10: Surfaces after sample polishing techniques with a micro grit paper and a granite slab assembly in our lab. Details discussed in the text.

Polishing: to prepare a clean surface to be beam-exposed

If the polished surface is to be exposed to the synchroton beam in the RSXS chamber, one needs to exercise caution as the penetration depth of soft x-rays is small (around 100 nm) which means a first few rough layers and contaminants can be a problem. Polishing to prepare a surface is useful in cases when the physical dimension of the crystal has to follow certain restrictions, like before mounting on a uniaxial stress device, the sample has to be of $2 \times 1 \times 0.5$ mm to make sure the applied mechanical stress is not asymmetric. Due to the delicate nature of the sample, all polishing action is done by hand on a custom built assembly which includes a 4 cm diameter Aluminum rod, a granite slab, and a slot to keep the rod's face perpendicular to the slab where we lay the polishing micro-grit paper. The process needs a special water-based solution, which acts as a lubricant as well as a coolant to avoid unnecessary chipping off and fracturing of the sample-face. We begin by positioning the sample with the copper plug at the flat face of an aluminum rod 4.10(a) with the sample surrounded by a Stycast (a glassy substance that ensures the sample does not cracks or chips off once polishing begins). We start off with a coarse 20 μm Aluminum carbide micro-grit paper, the surface of the sample looks like 4.10(b) once polished with it. We then follow up with finer micro grit papers from 0.3 to 0.05 μm to obtain a surface that looks like 4.10(c). The order in which the grit size is varied is important for imperfections to be minimal, although, the surface looks very smooth and featureless after completing the process and washing with acetone — we still do not get a (001) peak on this surface[9].

[9]This was especially non-trivial, because the Laue diffraction would use hard x-rays and would show a perfect pattern, ignoring surface sensitive details.

There is a very thin layer of contaminants, imperfections and mechanical stresses that dramatically affects the absorption of soft x-rays. The last step is chemical etching to get rid of surface contamination and defects.

Chemical etching

The idea of chemical etching is often used[10] for surface sensitive probes which are highly dependent on penetration depth and first few clean layers. We use Br-etching, where the sample surface is exposed to an alcoholic solution of concentrated Bromine. The rate of etching is important to be controlled, this can be calculated based on the crystal composition, and a solution with a suitable concentration or Br ions and exposure time is obtained — this solution will eat away the first few layers giving us a clean surface, almost comparable[11] to its cleaved counterpart. The eating away is more or less uniform, although, one important factor is the quality of polishing, sharp edges etch faster and might end up producing an overall rough surface. Liquid Bromine is notorious for being corrosive and requires a fuming hood to operate, some friends from the Chemistry Department have been kind enough to help me out with this step.

If we do not need the samples to be mounted on a uniaxial stress device, we generally cleave and perform the measurement instead of going through the pain of cutting in special dimensions, polishing upto a certain surface perfection, and using Br-etching to eat away a few bad atomic layers.

4.2.3 Mounting samples: Uniaxial stress device

In general, when mounting samples that would go in the UHV chamber, silver epoxy serves as an excellent candidate as the contact between the sample and the sampleholder. The silver epoxy not only retains good thermal and electrical conductivity at such low temperatures and pressures, but also retains the strength with almost no diffusion of lighter gases (or contaminants) which can be bad for the measurement. For non-strain experiments, the application and removal of silver epoxy is generally straightforward, the removal can be tricky sometimes either via scraping gently with a scalpel or ultrasonic vibrations in an acetone solution. However, the design of the uniaxial stress device sampleholder plate

[10] Attempts of Br-etching on cuprates go back to late 1980s [103].

[11] We were lucky in many ways than I care to admit: as mentioned earlier there is no proper soft x-ray experiment test possible before the main CLS shift. The concentration of Bromine turned out to be perfect for our case and we ended by getting a decent (001) and CDW signal in the polished sample.

requires the samples to be 2 mm long, 1 mm wide and 0.2 mm thick (see Fig. 4.11) (with c-axis facing out of the plane in our study) — there is a shallow (0.15 mm) valley where the bottom of the sample fits to ensure uniform strain. This makes things slightly tricky as we need to set a very thin flat layer of epoxy, then the sample rests on top of that, and finally the two ends of the sample are covered in epoxy, this makes the stress align along one direction, and cancel stray off-uniaxial stresses. I have found it almost impossible to reuse a sample after the experiment is performed, either the sample is cracked or the epoxy removal leads to breaking of the sample. Mounting samples and the role of epoxy will be discussed in detail in Chapter 7.

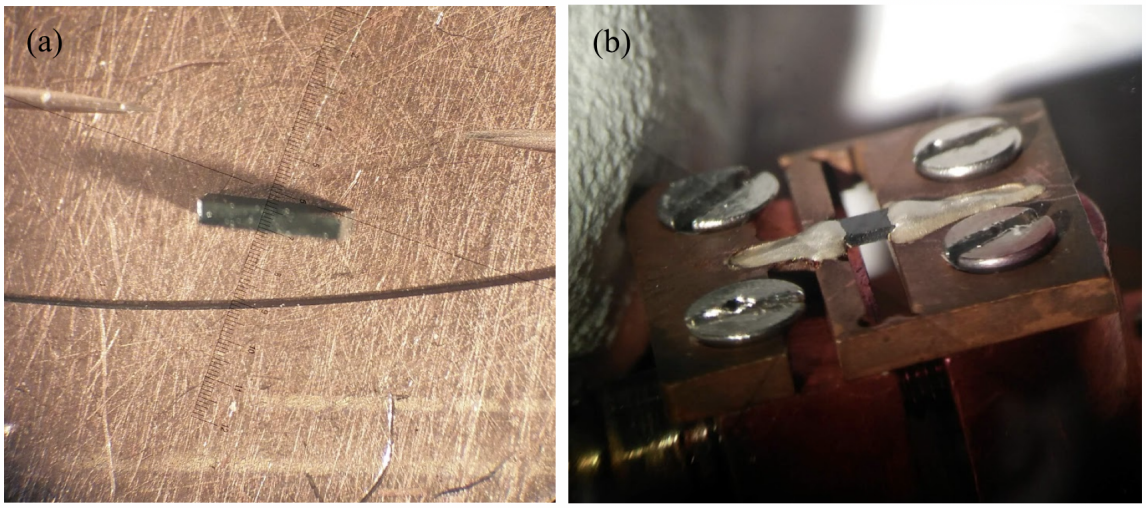


Figure 4.11: Finished product: Nd-LSCO samples 2 mm long, 1 mm wide and 0.2 mm thick. (a) Polished and etched, (b) mounted on the uniaxial stress device sampleholder plate. (a) shows a strand of author's hair to give a sense of scale.

Chapter 5

Time-resolved Nematicity Dynamics in Eu-LSCO

This chapter has been adapted from Ref. [1], titled: Orbital-selective time-domain signature of nematicity dynamics in the charge-density-wave phase of $La_{1.65}Eu_{0.2}Sr_{0.15}CuO_4$.

5.1 Overview

Understanding the interplay between charge, nematic, and structural ordering tendencies in cuprate superconductors is critical to unraveling their complex phase diagram. Using pump-probe time-resolved resonant x-ray scattering on the (0 0 1) Bragg peak at the Cu L_3 and O K resonances, we investigate non-equilibrium dynamics of $Q_a = Q_b = 0$ nematic order and its association with both charge density wave (CDW) order and lattice dynamics in $La_{1.65}Eu_{0.2}Sr_{0.15}CuO_4$. The orbital selectivity of the resonant x-ray scattering cross-section allows nematicity dynamics associated with the planar O $2p$ and Cu $3d$ states to be distinguished from the response of anisotropic lattice distortions. A direct time-domain comparison of CDW translational-symmetry breaking and nematic rotational-symmetry breaking reveals that these broken symmetries remain closely linked in the photoexcited state, consistent with the stability of CDW topological defects in the investigated pump fluence regime.

5.2 Introduction

Quantum materials with strong electronic correlations typically exhibit a variety of intertwined electronic ordering tendencies that have very similar, or even identical, energy and temperature scales [104]. These include, for example, antiferromagnetism, charge- and spin-density waves, orbital order, superconductivity and nematicity. A famous case highlighting the importance of intertwined order is the cuprate high-temperature superconductors [11, 13]. Quite recently, charge density wave (CDW) order, a translational-symmetry-breaking modulation of low-energy charge degrees of freedom, was identified as a generic phase of the cuprates that co-exists and competes with superconductivity [105]. This competition has been observed as a function of temperature, hole-doping, applied magnetic fields, uniaxial strain and optical pumping [31, 40, 106, 90, 107, 108, 109, 92, 110]. In addition to CDW order, cuprates also exhibit nematic order [111, 112, 113, 62, 114, 115, 67, 64, 116, 117, 60, 118], a breaking of the rotational symmetry of the electronic structure within the CuO_2 planes from four-fold to two-fold symmetric (C_4 rotational symmetry breaking).

Electronic liquid crystal phases with varying combinations of broken rotational and translational symmetries have been theorized [119, 16], thus making it desirable to probe each broken symmetry independently. When present, electronic nematic order is able to couple to CDW order favoring a unidirectional character of the CDW. While spontaneous rotational symmetry breaking has been predicted in many early theoretical studies of doped antiferromagnets [120, 121, 122, 123, 124, 125, 126], the effect of quenched disorder in real materials can be significant resulting in locally preferred stripe orientations and pinning of stripe fluctuations, which can obscure both macroscopic anisotropies as well as intrinsic energy and temperature scales [127]. Alternately, when the crystal structure explicitly breaks the C_4 rotational symmetry of the CuO_2 planes, the lattice itself provides an orienting potential for intrinsic nematic correlations. For example, this is the case in the 3-dimensional CDW state of orthorhombic $YBa_2Cu_3O_{6+\delta}$ (YBCO) [128, 106, 90, 107] as well as in the low-temperature tetragonal (LTT) phase of '214' cuprates such as $La_{2-x}Ba_xCuO_4$, $La_{1.6-x}Nd_{0.4}Sr_xCuO_4$ and $La_{1.8-x}Eu_{0.2}Sr_xCuO_4$. Although these orthorhombic crystal structures naturally induce rotational asymmetry in their electronic structure, nematicity is identified with an additional temperature dependent enhancement of this rotational asymmetry, driven by undirectional CDW formation or strong electronic correlations, such as nearest neighbour Coulomb repulsion of planar O states or exchange interactions [129, 130, 118, 131].

A recent breakthrough involved the identification of an equilibrium resonant x-ray scattering (RXS) signature of nematic order in various 214 cuprate superconductors and its relationship to both the crystal structure and CDW order [39, 2]. In these measurements,

nematicity was probed by measuring the (001) Bragg peak using photons tuned to the Cu L_3, the O K and the La M_5 resonances. The (001) reflection is forbidden in the high temperature structural phases of these materials but is detectable on resonance in the LTT phase ($T < T_{\mathrm{LTT}} \approx 135$ K). Fig. 5.1(A) schematically depicts the layered 214 cuprate structure. The intensity of the (001) reflection is a measure of the contrast between the resonant scattering form factors of corresponding ions in neighbouring layers along the c direction. From symmetry arguments, this contrast results from a local ab-plane anisotropy which rotates by $\pi/2$ around the c-axis with each consecutive layer [39]. By choosing incident photon energies associated with the various accessible core-valence resonances it is possible to probe the local ab-plane anisotropy associated with the valence electronic states of each ion independently. When the incident photon energy matches the La M_5 (835 eV) or the apical O K (532.4 eV) resonances the $Q = (001)$ RXS intensity is a measure of the anisotropic structural distortion associated with the LTT phase and a single order parameter-like onset of intensity is observed at T_{LTT}. In contrast, the (001) reflection measured at the Cu L_3 resonance (931.7 eV) or the planar O K resonance (528.7 eV) is additionally sensitive to nematicity in the CuO_2 planes. Fig. 5.1(C) shows the equilibrium temperature-dependence of the $Q = (001)$ RXS intensity at the apical O K and Cu L_3 resonances in $La_{1.65}Eu_{0.2}Sr_{0.15}CuO_4$ (LESCO). At the Cu L_3 resonance, the initial onset of intensity near 135 K corresponds to T_{LTT}, whereas the additional upturn near 75 K indicates the enhancement of nematic order, whose temperature dependence is correlated with the breaking of translational symmetry measured at $Q_{\mathrm{CDW}} = (0.264\ 0\ 1.5)$ [39].

Equilibrium studies of the (001) Bragg peak require detailed temperature dependent measurements in order to isolate the electronic nematic component. Here we present a non-equilibrium measurement approach based on time-resolved resonant x-ray scattering (tr-RXS), in which we are able to disentangle electronic and lattice contributions to the (001) Bragg peak by virtue of their distinct responses to optical pumping combined with the orbital selectivity of the RXS cross section. Pump-probe experiments on cuprates make use of optical laser pulses to excite non-equilibrium populations of hot electrons or drive vibrational modes of the lattice. At low pump fluences these experiments have been successful at revealing important information about the low-energy excitations of equilibrium ordered states [132, 97, 133, 134, 135, 136, 110, 92], whereas with higher pump fluences states of matter far from equilibrium can be accessed, such as photoinduced superconductivity [89, 137, 138, 139, 140, 141] or states with renormalized onsite Coulomb interactions [142]. Here we report the first pump-probe time- and orbital-resolved investigation of nematicity in a cuprate superconductor. We carefully study the response of both the lattice anisotropy and electronic nematicity as a function of fluence in order to establish a perturbative regime, in which nematicity dynamics can be studied without strongly

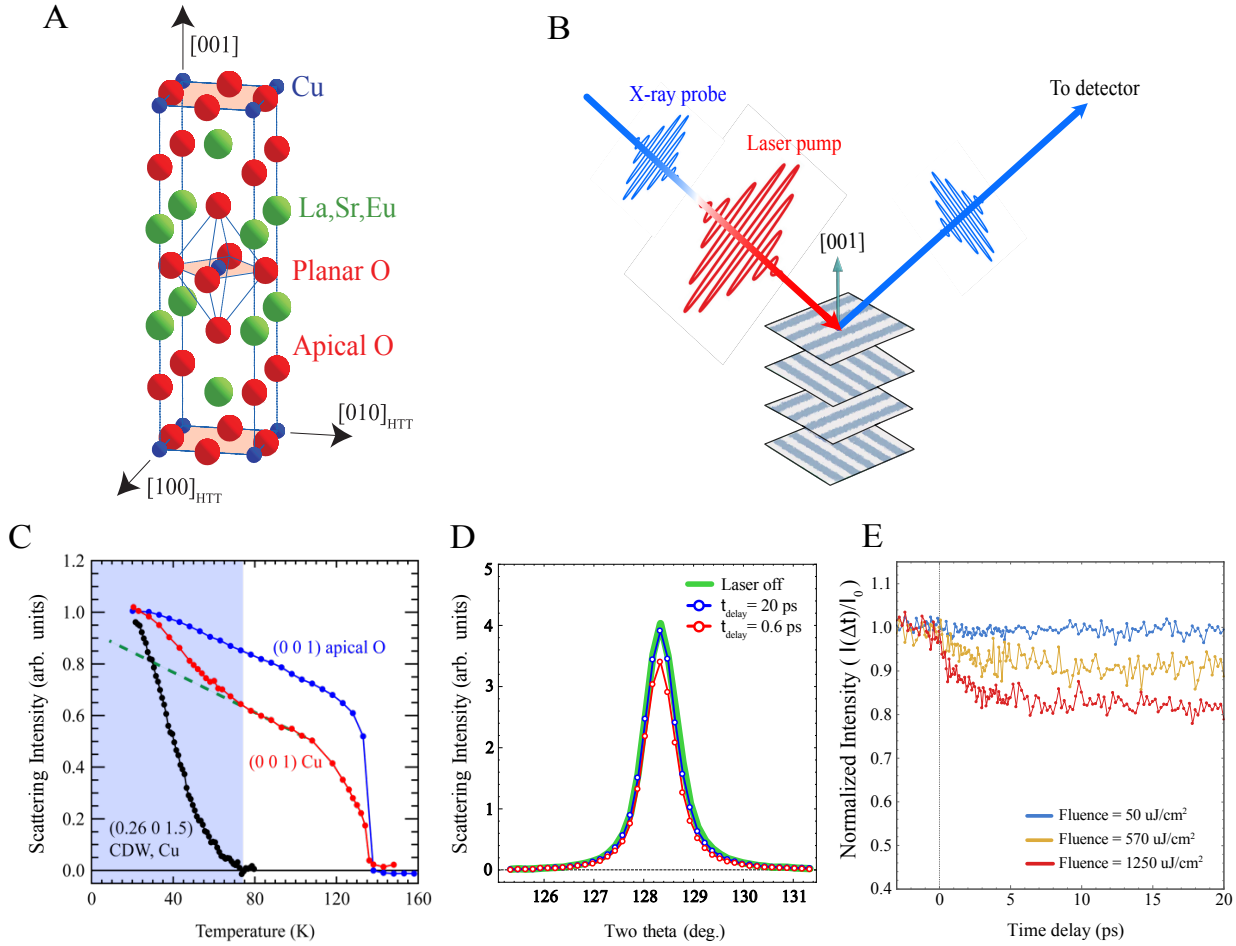


Figure 5.1: $La_{1.65}Eu_{0.2}Sr_{0.15}CuO_4$ structure, equilibrium RXS results and tr-RXS experiment. (A) Crystal structure of LESCO. The crystal axes are labelled according to the high-temperature tetragonal (HTT) setting, and the CuO_2 planes are highlighted in pale red. (B) Schematic depiction of the pump-probe geometry used to access the $Q = (001)$ peak originating from the layer alternating *ab*-plane anisotropy. (C) Equilibrium temperature dependence of the apical O K RXS intensity at $Q = (001)$ compared with the Cu L_3 RXS intensity at $Q = (001)$ and $Q_{\mathrm{CDW}} = (0.26\ 0\ 1.5)$. (D) Planar O K tr-RXS intensity at $Q = (001)$ probed along the $(00L)$ direction in a $\theta - 2\theta$ scan. The equilibrium peak profile is compared with scans taken 0.6 ps and 20 ps after excitation with 1.55 eV pump photons at a fluence of 50 μJ/cm^2. (E) tr-RXS intensity at the apical O K resonance for $Q = (001)$ at 20 K as a function of pump-probe delay. The pump-probe response is sensitive only to the anisotropy induced by the LTT structural distortion and becomes unobservable for low fluences.

disturbing related lattice degrees of freedom.

5.2.1 Time-resolved resonant X-ray scattering (tr-RXS)

Equilibrium RXS by Achkar et al. and Gupta et al. made use of differences in the temperature dependence to measure nematic order, however, in Bluschke, Gupta et al. [1] we investigate the dynamics of nematic order on ultra-fast timescales using optical pump-X-ray probe resonant X-ray scattering at the Pohang FEL [90]. Our experiments involved exciting the sample with a femtosecond, 800 nm pump laser with 50 μJ/cm^2 disrupting the CDW order and nematic order. The orbital selectivity of the resonant X-ray scattering cross-section allows nematicity dynamics associated with the planar O $2p$ and Cu $3d$ states to be distinguished from the response of anisotropic lattice distortions.

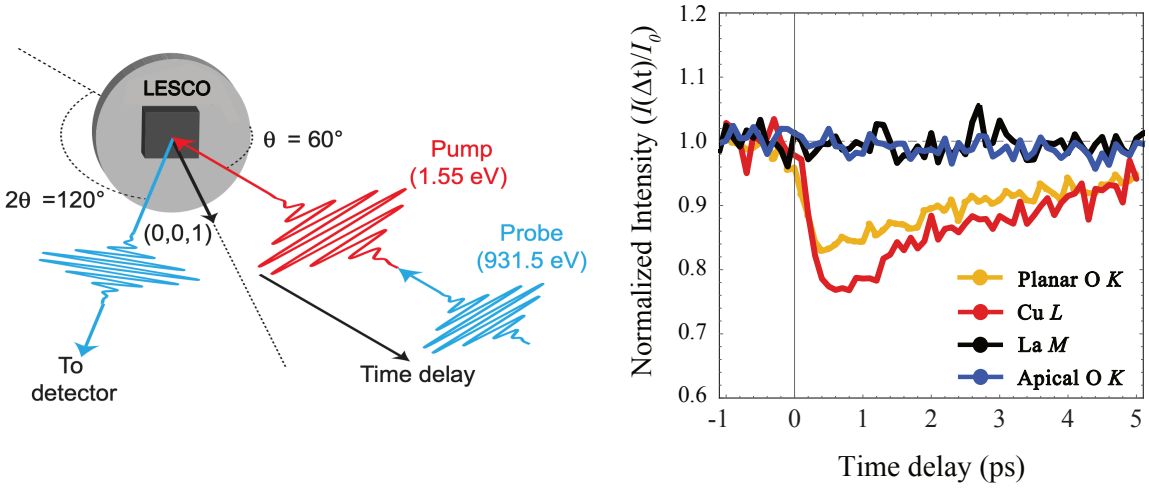


Figure 5.2: **Ultrafast Nematicity in $La_{1.65}Eu_{0.2}Sr_{0.15}CuO_4$** (A) Schematic depiction of the pump (laser) - probe (X-ray) geometry accessing the $Q = (001)$ Bragg peak at Cu L edge. (B) tr-RXS Bragg peak intensity at the planar and spacer layer atomic resonances for $Q = (001)$ at 20 K as a function of pump-probe delay.

We find that the recovery associated with the dynamics of the (001) Bragg peak at the planar layer atoms display a fast and large recovery on ultrafast timescales of 5-10 picosecond. However, the spacer layer atoms La M or apical oxygen K edge seem to have negligible response at low-fluences. These dynamics confirm an electronic origin to the nematic order.

5.3 Results

In this section we describe the results of pump-probe tr-RXS measurements of LESCO, probing at momentum transfer $Q = (001)$. Single crystal of $La_{1.65}Eu_{0.2}Sr_{0.15}CuO_4$ was grown using the travelling solvent floating zone technique at the Université Paris-Saclay. The data presented was collected on a sample which was cleaved in air to expose a clean surface with an approximate [001] orientation. The sample dimensions were approximately 2.5 mm $\times$ 1 mm $\times$ 1 mm. The system is excited using 50 fs pulses of a 1.55 eV (800 nm) Ti:sapphire laser, and then probed at varying time delays with respect to the excitation using 80 fs soft x-ray pulses. The experiment was performed using the Resonant Soft X-ray Scattering (RSXS) instrument [91] at the Pohang Accelerator Laboratory X-ray Free Electron Laser (PAL-XFEL), operating at a 60 Hz repetition rate. In Fig. 5.1(D) we plot a representative scan of the $Q = (001)$ peak taken along the $(00L)$ direction at 20 K and with probe photons tuned to the planar O K resonance. In order to visualize the pump-induced peak intensity changes which we discuss throughout this report, we have plotted the corresponding scans taken immediately after ($\sim$ 0.5 ps) and at a longer time delay (20 ps) with respect to the excitation for a pump fluence of 50 μJ/cm^2. Figure 5.1(B) schematically depicts the pump-probe geometry with respect to the layer-alternating anisotropy in the low-temperature CDW state.

In order to first identify and isolate the pump-induced response of the lattice, we show in Fig. 5.1(E) the $Q = (001)$ tr-RXS intensity measured at the apical O K resonance as a function of pump-probe delay. The choice of the apical O resonance guarantees sensitivity to rotational symmetry breaking driven by the LTT structural distortion, without electronic contributions associated with the CuO_2 planes. The LTT structure demonstrates a slow response to optical pumping, characteristic of lattice dynamics, which become vanishingly small for low pump fluences.

When measured at the planar O K or Cu L_3 resonances the $Q = (001)$ RXS intensity is sensitive to rotational symmetry breaking associated with both the LTT lattice distortion as well as with electronic nematicity of the CuO_2 planes. Based on the fluence-dependent tr-RXS measurements presented in Fig. 5.1(E), we identify a low-fluence regime (approx. $F < 100$ μJ/cm^2) in which the optical pump does not induce a significant response in the lattice. Fig. 5.3 shows the low fluence (50 μJ/cm^2) dynamics observed for incident photons tuned to the apical O K, the planar O K and the Cu L_3 resonances, and for a series of temperatures below and above T_{CDW}. Whereas the $Q = (001)$ RXS intensity at the apical O K resonance is unperturbed with this low pump fluence, measurements at the planar O K and the Cu L_3 resonances detect a large and fast response to pumping, clearly distinct from the LTT structural dynamics. Importantly, the temperature dependence of the fast

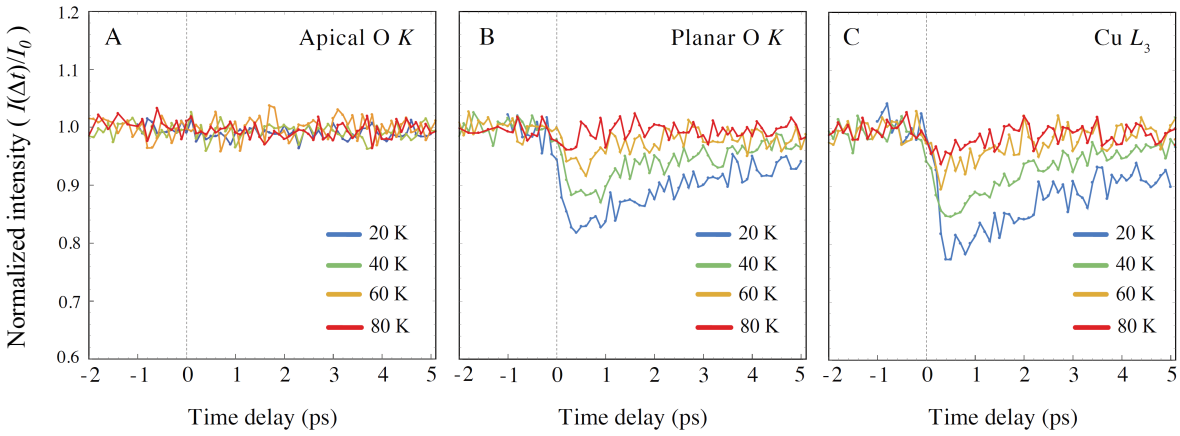


Figure 5.3: **Temperature series at low fluence.** Normalized tr-RXS intensity $(I(\Delta t)/I_0)$ at $Q = (001)$ as a function of pump-probe delay in LESCO ($x = 0.15$) with $T_{\mathrm{CDW}} \approx 75$ K [143, 39]. Pump photon energy 1.55 eV and fluence 50 μJ/cm^2. (A) The tr-RXS intensity at the apical O K resonance, sensitive only to structural distortions, is unperturbed by the optical pump at this low fluence. The planar O K resonance (B) and the Cu L_3 resonance (C) are sensitive to pump-induced nematicity dynamics in the CDW phase.

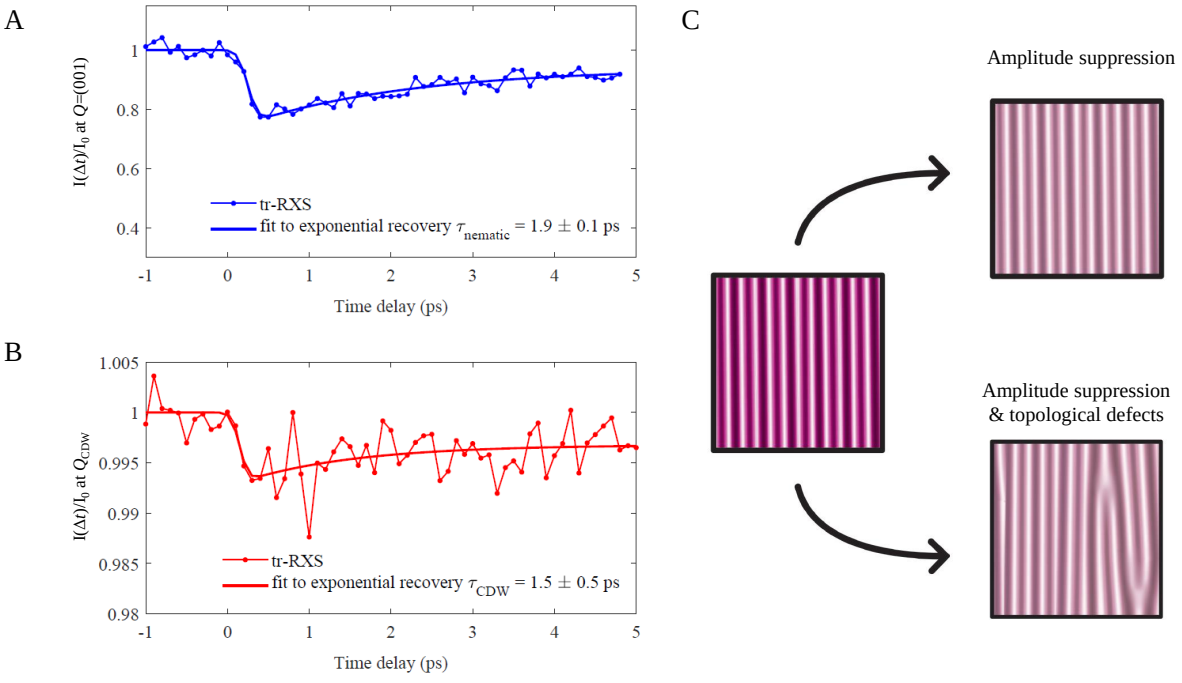
(001) peak dynamics at the planar O K and the Cu L_3 resonances is correlated with the onset of CDW order, indicating that the fast dynamics are associated with electronically driven rotational symmetry breaking.

Having established the coincident onset of broken rotational and translational symmetry as a function of temperature, it is of interest to ask if and how these broken symmetries remain linked in the photoexcited state. We address this question by probing the photoexcited dynamics of the CDW translational symmetry breaking at $Q_{\mathrm{CDW}} = (0.26\ 0\ 1.74)$. Fig. 5.4(A-B) compares the time-domain response of the Cu L_3 $Q = 001$ and Q_{CDW} RXS intensities at 20 K and with a pump fluence of 50 μJ/cm^2. Despite the lower signal-to-noise ratio of the Q_{CDW} measurement, the two orders appear to be suppressed and recover together. Each data set is plotted together with a single-exponential fit to the recovery dynamics. When interpreting the normalized intensities in Fig. 5.4(A-B) it is important to consider that $I(\Delta t)$ and I_0 refer to total scattering intensities at $Q = (001)$ and Q_{CDW}, including all background signals at those Q vectors. At the Cu L_3 resonance and $Q = (001)$ the background scattering is dominated by orbital anisotropy of the Cu d states resulting

from the LTT structural distortion which alters the crystal field environment around each Cu atom. This LTT contribution is only weakly effected by the pump (see Fig. 5.1(E)), but accounts for $\approx 80\%$ of the total intensity. At Q_{CDW} the background scattering is dominated by fluorescence and diffuse scattering, and constitutes slightly more than 99% of the total signal at this Q. Accordingly, the dynamics observed in Fig. 5.4(A-B) correspond to almost complete supressions of the nematic and CDW orders respectively. The dynamics are also similar to the pump-induced CDW dynamics reported under similar conditions for $La_{2-x}Ba_xCuO_4$. [135, 136]

At higher fluences, where both the lattice and electronic subsystems are significantly excited, it is more challenging to differentiate contributions to the $Q = (001)$ RXS intensity. In order to do so, we study the fluence dependence of the tr-RXS signal for various temperatures and at each resonance. Fig. 5.5(A) shows the fluence dependence of the planar O K resonance $Q = (001)$ suppression at 20 K ($T < T_{\mathrm{CDW}}$) and at 100 K ($T > T_{\mathrm{CDW}}$), immediately following the pump excitation (pump-probe delay +0.5 ps). On the same plot we show the corresponding fluence dependence of the apical O K resonance $Q = (001)$ suppression at 20 K (pump-probe delay +0.7 ps). The apical O measurement captures the fluence-dependent response of the lattice at short time delays. Similarly, the dynamics observed at the planar resonance trend towards a lattice-like response as the temperature is increased beyond T_{CDW}. As the pump fluence is increased, a discrepancy develops between the 20 K data at the apical resonance and the 100 K data at the planar resonance. This discrepancy may result from the temperature-dependent susceptibility of the LTT distortion to optical pumping, whose time-domain response is expected to be a complicated function of both temperature and pump fluence. Alternately, the stronger response seen in the 100 K planar resonance data may correspond to the suppression of high-temperature residual nematicity, associated with either a purely nematic state or with weak short-range CDW correlations.

The apical O K fluence scan in Fig. 5.5(A) has been fit with a line (shaded red) to determine the slope of the fluence-dependent suppression of the LTT distortion. This slope is then subtracted from fluence-dependent measurements taken at the planar O K resonance for a series of temperatures. The resulting curves are normalized to the maximum pump-probe effect observed at high fluence and plotted together in Fig. 5.5(B). The response of nematicity to optical pumping saturates at a pump fluence which is either constant or increasing slightly with temperature. In contrast, if the pump-induced effect were driven purely by the post-pump evolution of the transient electronic temperature, one may have expected a decreasing saturation fluence at higher temperatures. Accordingly, this indicates that the suppression of nematic order at short time delays is associated with the establishment of a non-thermal electronic state [144].



S

Figure 5.4: **Comparison of CDW and nematicity dynamics.** (A) CDW translational-symmetry breaking dynamics and (B) nematic rotational-symmetry breaking dynamics measured at $Q_{\mathrm{CDW}} = (0.26\ 0\ 1.74)$ and $Q = (001)$ respectively. Both data sets were taken at 20 K using probe photons resonant to the Cu L_3 resonance. (C) Schematic depiction of CDW degradation via amplitude suppression or the combination of amplitude suppression and topological defect formation.

5.4 Discussion

Differentiating translational and rotational-symmetry breaking in CDW-ordered cuprates is difficult but of fundamental interest [145, 66, 116, 33, 146, 147, 148, 149, 107]. Of the known stripe-ordered cuprates, $La_{2-x}Ba_xCuO_4$ with $x \sim 1/8$ demonstrates the most pronounced CDW and has therefore remained a prototype for CDW diffraction studies. Previous tr-RXS studies of $La_{2-x}Ba_xCuO_4$ have focused on the pump-induced response of the Q_{CDW} reflection, associated with translation symmetry breaking in the CDW phase, and have treated the $Q = (001)$ reflection purely as a reference probe of the LTT lattice distortion [139, 141, 135, 136]. Here we show that the tr-RXS intensity at $Q = (001)$ in the related material LESCO can be an extremely sensitive probe of both LTT lattice dynamics, as well as nematicity dynamics, depending on the choice of probe photon energy.

Selective measurements of CuO_2 plane nematicity dynamics demonstrate that rotational symmetry breaking in the photoexcited state remains coupled to the translational symmetry breaking observed at Q_{CDW}. In contrast, the dynamics observed at the apical O resonance and shown in Fig. 5.1(E) are typical of the lattice response to photo-excitation in cuprates [150, 93], and have no apparent sensitivity to CDW order. Hot electrons excited by the optical pump decay via electron-phonon coupling mediated channels, eventually exciting the entire phonon bath and weakening the LTT distortion over several picoseconds. In contrast, the nematic signal observed below T_{CDW} and plotted in Fig. 5.3(B-C) is suppressed within hundreds of femtoseconds, consistent with the direct electronic coupling of nematicity to the photoexcited electronic population. Alternately, the fast suppression may involve the participation of phonon modes which are strongly coupled to the CuO_2 plane electronic degrees of freedom, such as the transverse acoustic and optical phonon modes, which are known to experience a softening at the CDW wave vector in the CDW phase. [151] The subsequent recovery of the nematic signal unfolds over several picoseconds, comparable to the timescale of the LTT suppression, suggesting a scenario in which the recovery of the electronic nematic ground state occurs via an electron-phonon coupling mediated transfer of energy to the lattice. The recovery of the LTT distortion proceeds over a significantly longer time scale associated with the time it takes for acoustic phonons generated in the pump process to leave the probed region.

Similar to liquid crystals, which can be characterized by both a nematic and a smectic order parameter [152], the low temperature states of the cuprates appear to be characterized by rotational (Ising nematic) and translational (CDW) symmetry breaking order parameters. These orders are distinct, opening up the possibility that nematic order may survive the melting of CDW order in at least some range of parameter space. A close inspection of Fig. 5.3(B) and Fig. 5.3(C) reveals that although the low fluence suppression

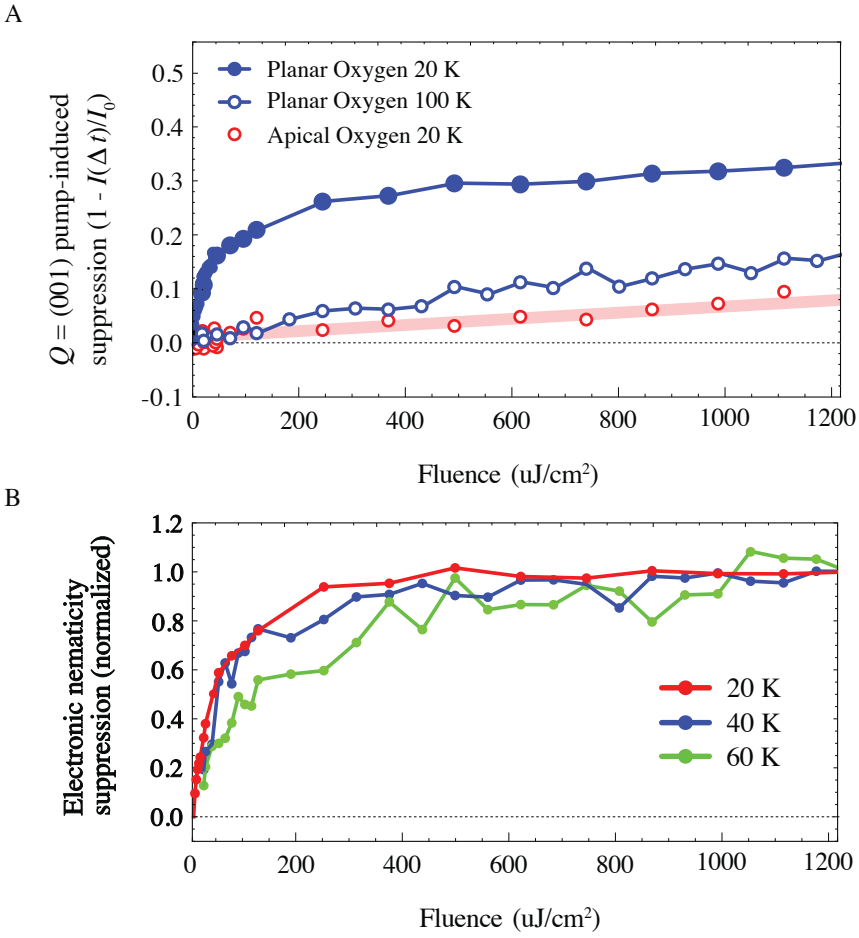


Figure 5.5: **Fluence dependence.** (A) Pump-induced suppression $(1 - I(\Delta t)/I_0)$ of the O K resonance $Q = (001)$ tr-RXS intensity at short time delay as a function of fluence. The 20 K signal at the planar O K resonance comprises both lattice and electronic contributions, while the apical resonance is sensitive only to structural anisotropy. The signal at the planar O K resonance is also shown at $T = 100$ K $> T_{\mathrm{CDW}}$ where its fluence dependence is qualitatively similar to that observed at the apical O K resonance. The shaded red line is a linear fit to the apical O K resonance data. (B) Fluence-dependent suppression of the electronic nematic signal at +0.5 ps (near maximum suppression). The fluence dependent response of the lattice is captured by a linear fit to the 20 K apical O data plotted in red in (A) and then subtracted from fluence-scans collected at the planar O K resonance inside the CDW phase.

of nematic order remains largely locked to the onset of CDW order, residual dynamics are observed at 80 K, above the nominal T_{CDW} determined from equilibrium energy-integrated RXS. This observation may be understood as evidence of nematic order existing in the absence of CDW translational symmetry breaking, similar to observations of nematic order outside the CDW dome in overdoped $La_{1.6-x}Nd_{0.4}Sr_xCuO_4$ [2]. Alternately, these residual nematicity dynamics may track weak amplitude, short range CDW correlations similar to those observed at high temperatures by resonant inelastic x-ray scattering measurements [153, 154]. Whatever the precise origin, residual nematicity at high-temperatures may also be responsible for the slight discrepancy between the 100 K planar O and the 20 K apical O fluence dependences shown in Fig. 5.5(A).

Comparing the non-equilibrium dynamics of the CDW and nematic orders provides insight into the role of photoexcited topological defects in suppressing CDW order. While the CDW order parameter is described by a wavevector, an amplitude and a phase, the nematic order parameter is simply described by an Ising-like director and an amplitude. Translational symmetry breaking in the CDW phase may be degraded either by amplitude suppression or by the introduction of topological defects such as discommensuration lines and dislocations, which suppress long-range phase coherence. Previous investigations have observed both the presence [155, 135, 92] and absence [153] of topological defects in photo-induced phase transitions of CDW systems. When present, photo-excited topological defects have been shown to decay over a longer time scale than the recovery of the amplitude mode, thus leading to two time scales in the CDW recovery dynamics [155]. In contrast, nematic order is expected to recover with the amplitude. In Fig. 5.4(C) two scenarios are depicted schematically, one in which a defect-free uniaxial CDW is suppressed via pure amplitude suppression, and one in which CDW topological defects are additionally generated by the pump excitation. The observation that CDW and nematic order recover together following photoexcitation (Fig. 5.4(A-B)) is consistent with a scenario in which the pump does not excite a significant number of CDW topological defects. Alternate fits to these recovery dynamics using two exponential recovery terms are presented in the Supplementary Information. These do not improve the quality of the fits. In the bilayer cuprate $Bi_2Sr_2CaCu_2O_{8+\delta}$ (Bi2212), equilibrium scanning tunneling microscopy studies have demonstrated that CDW topological defects are observed at locations where the nematic order parameter is spatially fluctuating [116]. In the case of LESCO, the strong potential defined by the LTT distortion – to which the CDW is nearly commensurate – suppresses pump-induced fluctuations of the nematic director that would otherwise result in the formation of CDW dislocations. We emphasize that such a pinning scenario does not preclude the existence of static CDW defects which are simply not perturbed at low pump fluences.

Understanding the role of CDW topological defects in the photoinduced dynamics of the cuprates is relevant to understanding the relationship between CDW order and superconductivity. In the cuprate superconductor YBCO, where the uniaxial LTT distortion is absent, the locations of CDW discommensuration lines have been associated with the presence of superconductivity, whose optical melting leads to a strengthening of the CDW phase coherence [92]. In contrast, CDW order in $La_{1.875}Ba_{0.125}CuO_4$ is insensitive to T_c [156], and the phase-resolved topology of the CDW domain network remains stable against temperature above both the CDW and LTT transitions, melting only for $T > T_{LTO}$ where four-fold symmetry is restored in the CuO_2 plane [157]. It is therefore not surprising that, in the related material LESCO, the 50 $\mu J/cm^2$ optical pump used in our experiment does not generate significant changes in the CDW topology. Our result is also reminiscent of the photoinduced CDW dynamics observed in the 214 stripe-ordered nickelate $La_{1.75}Sr_{0.25}NiO_4$, where it was argued that the photoexcited state involves both amplitude and phase fluctuations of the CDW, but that topological defects are not created due to the large energy cost associated with reconfiguring a large number of spins and charges in the coupled charge- and spin-stripe phase [158].

Identifying the local physics associated with rotational symmetry breaking observed via macroscopic probes [111, 112, 64, 159, 117] often proves to be a challenge. Here we have demonstrated an orbital-selective time-resolved probe of electronic nematic order which accompanies the CDW phase in LESCO. The $Q = (001)$ RXS signal averages over the entire ab-plane ($Q_a = Q_b = 0$) while simultaneously being sensitive to intra-unit-cell asymmetries of the Cu $3d$ and O $2p$ states. The evolution of nematicity dynamics as they are gradually unlocked from the translational symmetry breaking CDW order with additional hole-doping is not fully understood. Future studies may investigate pump-induced nematicity dynamics across the cuprate phase diagram, with a particular focus on the phase region just below the pseudogap critical point, where electronic nematic order was recently reported to persist in the absence of a translational-symmetry breaking CDW [2]. More generally, our results demonstrate the ability to capture the ultrafast behavior of non-equilibrium nematicity dynamics using tr-RXS, thereby paving the way for future tr-RXS studies of $Q = 0$ nematic correlations in other systems such as $1T-TiSe_2$, which exhibits an ordered stacking of 3 uniaxial CDW's with distinct wavevector orientations [160].

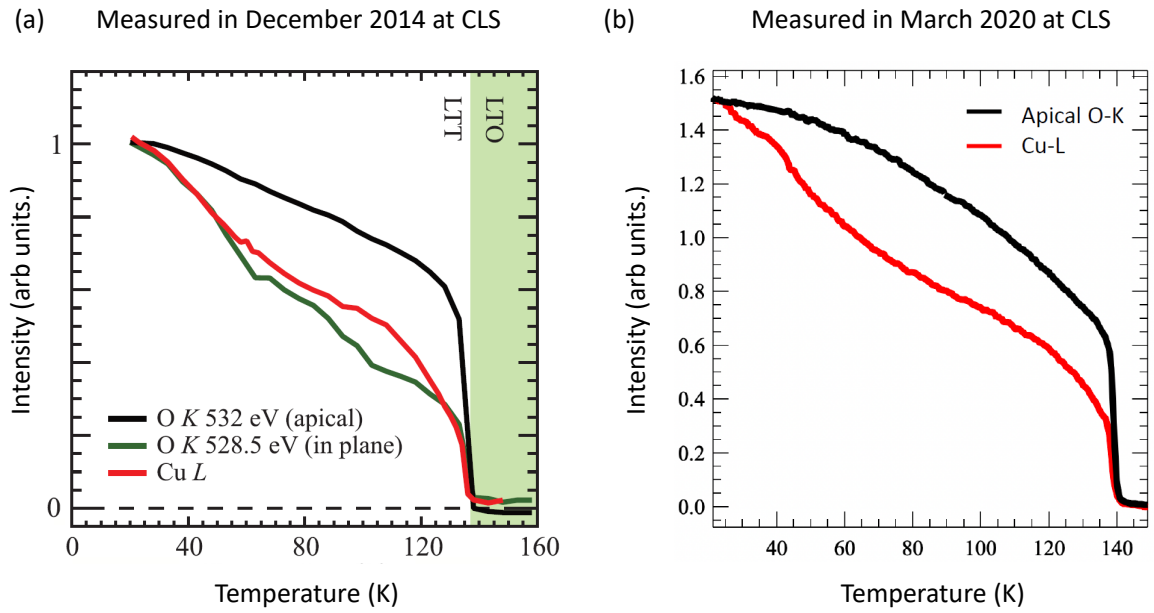


Figure 5.6: Q=**(001) equilibrium temperature dependence.** (a) Comparison of the temperature dependent Q=(001) intensity measured at the apical O K, the planar O K, and the Cu L_3 resonances. These data were collected in December 2014 in the context of Ref. [39]. (b) Comparison of the temperature dependent Q=(001) intensity measured at the apical O K and the Cu L_3 resonances. These data were collected in March 2020 in preparation for the non-equilibrium measurements presented in the main manuscript.

5.4.1 Characterization of Q=(001) equilibrium temperature dependence.

The $La_{1.8-x}Eu_{0.2}Sr_xCuO_4$ single crystal investigated in this study is the same sample investigated in the context of Ref. [39], where the equilibrium temperature dependence of the Q =(001) reflection at the Cu L_3, the planar O K and the apical O K resonances was measured. These data are reproduced in Fig. S5.6(a), as well as in Fig. 1(b) of the main manuscript. In order to exclude sample aging effects and to verify the stability of the doping level, we measured the equilibrium temperature dependence of the (001) reflection at both the planar and apical O K resonances at the REIXS beamline of the Canadian Light Source (CLS), before performing the pump-probe measurements at the Pohang Accelerator Laboratory x-ray free electron laser (PAL-XFEL). These data are presented in Fig. S5.6(b). The temperature dependent (001) intensity at the apical O K resonance

verifies the integrity of the crystal structure and the expected low-temperature tetragonal (LTT) phase. The temperature dependence at the planar O K resonance can be used to infer T_{CDW} and is thus an approximate measure of the doping level, which appears to have remained stable at $x = 0.15$ since the measurements presented in Ref. [39].

5.4.2 High-fluence pump-induced dynamics at Q=(001)

In Fig. S5.7(a) we plot the low temperature (20 K) pump-induced dynamics at the apical and planar O K resonances for a series of pump fluences. The apical O data demonstrates the time-resolved suppression of the LTT distortion and is identical to the data plotted in Fig. 5.7 of the main manucript, but shown for a shorter range of time delays. At the planar O K resonance the low-fluence signal is dominated by nematicity dyanamics, which is the focus regime of the main manuscript, whereas at higher fluences nematicity dynamics are observed together with the suppression of the LTT distortion. These data are presented in Fig. S5.7(b). In Fig. S5.11, x-ray absorption spectroscopy (XAS) at the O K edge is shown for reference, indicating the features corresponding to the planar and apical O resonances.

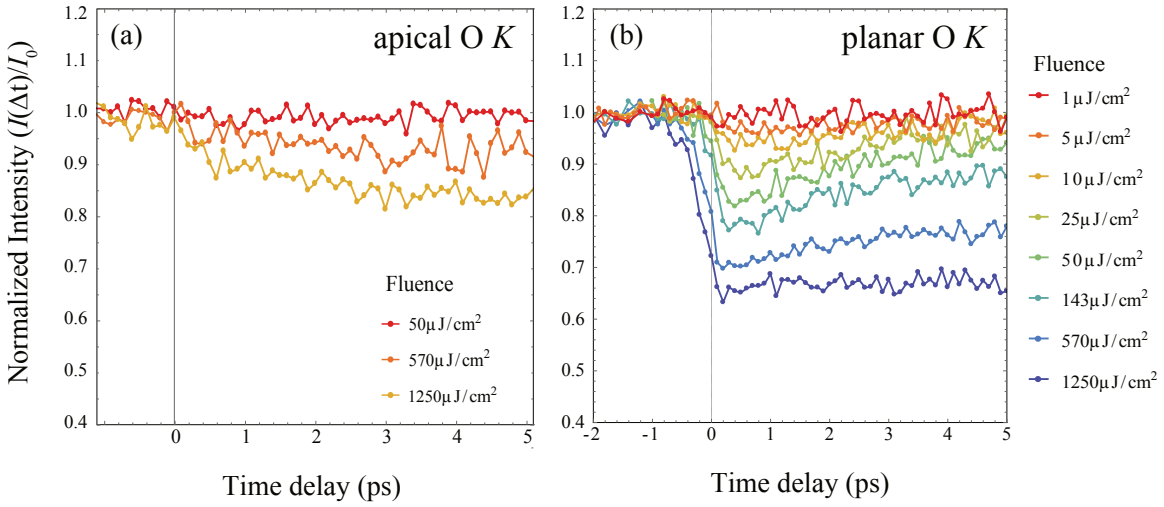


Figure 5.7: **High fluence dynamics at O K resonances.** (a) Q=(001) pump-induced dynamics measured at the apical oxygen K resonance at 20 K. (b) Q=(001) pump-induced dynamics measured at the planar oxygen K resonance at 20 K.

5.4.3 Charge density wave detection at Q_{CDW}

In Fig. S5.8 an angular (theta) scan through Q_{CDW} at 20 K is plotted both in equilibrium, as well as out-of-equilibrium at 0.5 ps following excitation with a 1350 μJ/cm^2 pump pulse. These scans were collected using an avalanche photodiode with a 2 mm aperature, at a distance of 90 mm from the sample. The Q_{CDW} reflection was observed at the Cu L_3 resonance (931.7 eV) using a detector angle (Two theta) of 164° corresponding to an out-of-plane momentum transfer of $L = 1.74$. This geometry was chosen based on previous experience to minimize the variation of the background intensity as a function of the incidence angle theta. The component of the momentum transfer parallel to the CuO_2 planes was aligned with the Cu-O-Cu bond direction by locating the equilibrium (103) Bragg peak at the REIXS enstation of the CLS and then transfering the sample in this orientation to the RSXS endstation at the PAL-XFEL.

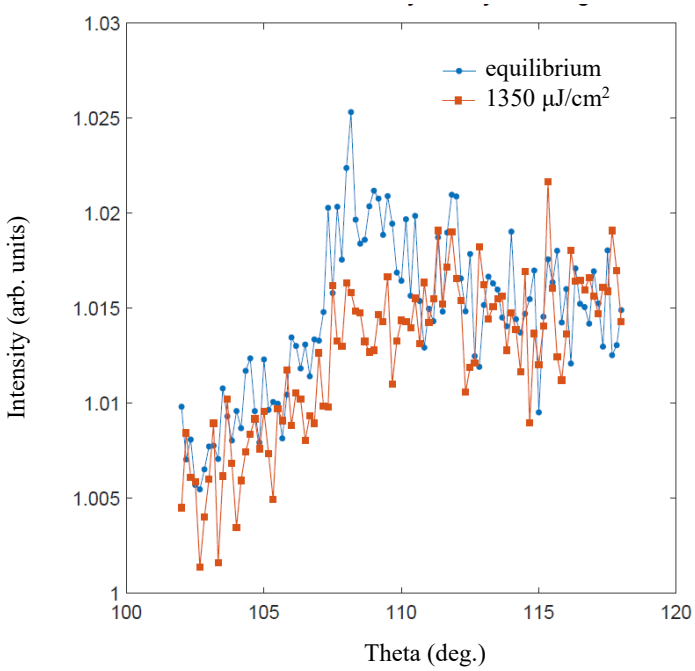


Figure 5.8: **Charge scattering at Q_{CDW}** The CDW scattering intensity is measured in and out of equilibrium as a function of incidence angle (theta) in a laser on/off scan. The laser on data was collected at a time delay of +0.5 ps following the pump excitation.

5.4.4 Time trace fitting schemes

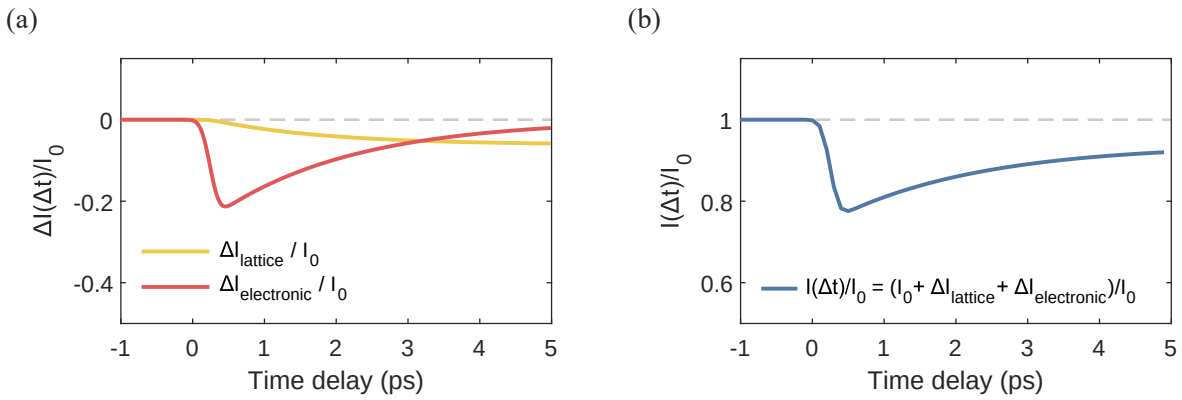


Figure 5.9: **Modelling of electronic and lattice dynamics.** (a) The model for time-dependent suppression of scattering intensity associated with electronic order, i.e. CDW or nematic, is compared with the model for lattice-like dynamics. (b) The full model for time dependent scattering observed at the Cu L_3 resonance comprises both electronic and a lattice like dynamics.

The time-resolved resonant x-ray scattering (tr-RXS) intensities presented in Fig. 3 of the main manuscript are modelled using an approach in which the dynamics are divided into an electronic (nematic or CDW) and a lattice contribution. The electronic contribution experiences a time-resolution limited suppression (step function at $\Delta t = 0$), and an exponential recovery with time constant τ_1.

$$\Delta I_{electronic}(\Delta t) = \begin{cases} 0 & \Delta t < 0 \\ -a_1 \exp^{-\Delta t/\tau_1} & \Delta t \geq 0 \end{cases}$$

In contrast, the dynamic response of the lattice, e.g. the LTT distortion, is not immediately activated by the incident pump photons but onsets exponentially with time constant τ_2 as energy is transferred from the hot electronic system to the lattice.

$$\Delta I_{lattice}(\Delta t) = \begin{cases} 0 & \Delta t < 0 \\ a_2(\exp^{-\Delta t/\tau_2} - 1) & \Delta t \geq 0 \end{cases}$$

In order to reduce the number of fitting parameters, $\tau_2 = 1.6$ ps is determined from fitting to the $\Delta I_{lattice}$ model to the dynamics measured at the Apical O K resonance (Fig. 1(E) of main manuscript). τ_2 is then held constant when fitting the electronic dynamics measured at Cu L_3 resonance. Examples of the time-dependent dynamics of the electronic and lattice models are shown in Fig. S5.9(a). The quantity being modelled is the time-dependent scattering intensity normalized to the equilibrium scattering intensity ($I(\Delta t)/I_0$). The full model, shown in Fig. S5.9(b) is achieved by summing the equilibrium scattering I_0 with the functions representing the time dependent suppression of scattering intensity with electronic and lattice like dynamics. The entire sum is normalized to I_0 and then convolved with a gaussian of width 110 fs to account for the finite temporal resolution of the experiment.

$$I(\Delta t)/I_0 \;=\; (\; I_0 \;+\; \Delta I_{electronic} \;+\; \Delta I_{lattice}\;)/I_0 \;\;.$$

When fitting the data presented in Fig. 3 of the main manuscript, an alternate model for the electronic dynamics was considered, comprising two exponential recovery terms.

$$\Delta I_{electronic}(\Delta t) = \begin{cases} 0 & \Delta t < 0 \\ -a_0 \exp^{-\Delta t/\tau_0} - a_1 \exp^{-\Delta t/\tau_1} & \Delta t \geq 0 \end{cases}$$

Fits using 1 versus 2 exponentials for the electronic recovery dynamics are compared in Fig. S 5.10, along with their residuals. In the case of the $Q = (0\ 0\ 1)$ scattering, the fit with 2 exponential recovery terms returns twice the same time constant, confirming that the recovery is well described by a single exponential. For the Q_{CDW} scattering, the fit with 2 exponential recovery terms returns time constants $\tau_0 = 0.7$ ps and $\tau_1 = 4.2$ ps. For Q_{CDW}, the fits using one and two exponentials to model the recovery are essentially indistinguishable from one another.

5.5 Experimental Procedure

The optical pump pulses were produced using a 1.55 eV Ti:Sapphire laser and delivered to the sample approximately collinear to the trajectory of the probing XFEL pulse. The pump repetition rate was set to 30 Hz such that every second XFEL pulse probes the optically excited system (for positive time delays), while the others probe the equilibrium state. The optical pump spot size (∼650 μm × 550 μm) was significantly larger than the XFEL probe spot size, so as to minimize the spatial inhomogeneity of the pumping

observed by the probe. The optical pump was σ-polarized (parallel to the CuO_2 planes and the θ rotation axis) so as to ensure a constant orientation of the polarization with respect to the crystal axes for all incidence angles θ. A test of the $Q = (001)$ tr-RXS intensity at the Cu L_3 resonance indicated that the pump-induced $Q = (001)$ dynamics are independent of the choice of pump polarization (parallel or perpendicular to the CuO_2 planes). The pump laser fluence was controlled using a motorized attenuator consisting of a half-wave plate and two broadband thin film polarizers. The reported fluences correspond to the incident fluence after correcting for the different pump (and probe) incidence angles used when probing the (001) Bragg Peak at different resonant photon energies. The duration of the pump pulse was $\sim$ 50 fs and the delay time between the arrival of the pump and probe pulses was controlled by a mechanical delay stage. Spatial and temporal overlap of the pump and probe spots was achieved using a Ce:YAG crystal (YAG). Absorption of the soft x-ray pulse in the YAG generates free carriers giving rise to a measurable change in its optical properties. After positioning both spots at the same location on the YAG, temporal overlap was achieved by scanning the pump delay stage and monitoring the optical transmission. The overall time resolution achieved at the RSXS endstation is approximately 110 fs.

Equilibrium resonant X-ray scattering: Equilibrium resonant X-ray scattering measurements of both the $Q = (001)$ Bragg peak and the Q_{CDW} peak were performed at the REIXS beamline [101] of the Canadian Light Source on the same sample studied which was subsequently studied by tr-RXS. A subset of these data are presented in Fig. 5.1(C) of the main manuscript. These temperature dependent peak intensities were collected with σ-polarized photons (polarized parallel to the planar CuO_2 bonds). The indicated reciprocal lattice units (r.l.u.) are defined using real-space lattice constants $a = b = 3.79$ Å and $c = 13.14$ Å, where the a and b lattice constants are oriented along the planar CuO_2 bonds reflecting the high-temperature tetragonal crystal symmetry.

Time-resolved resonant x-ray scattering: The tr-RXS measurements presented here were performed at the RSXS endstation of the PAL-XFEL in a vacuum of 2×10^{-8} mbar. A base temperature of $\sim$ 20 K was achieved in our experiment using a liquid Helium flow cryostat. Probe XFEL pulses with π-polarization were produced at a repetition rate of 60 Hz through self-amplified spontaneous emission by passing a 3.15 GeV electron beam through the undulators of the Soft X-ray Scattering and Spectroscopy beamline. A plane grating monochromator was used to achieve monochromatic pulses with a bandwidth of $\sim$ 0.5 eV, tuned to the relevant soft x-ray resonances: Cu L_3 (931.7 eV), La M_5 pre-edge (832 eV), apical O K (532.4 eV) and planar O K (528.7 eV). The XFEL pulse duration and spot size were approximately 80 fs and 130 μm $\times$ 250 μm respectively. Scattered x-rays were detected using an avalanche photodiode with a 1 mm aperture positioned at

150 mm from the sample.

Data Analysis: The normalized tr-RXS intensities plotted in Fig. 5.1(E), Fig. 5.3, and Fig. 5.4 of the main manuscript correspond to the ratio of the tr-RXS intensity $I(\Delta t)$ measured at time delay Δt after the pump arrival, and the equilibrium RXS intensity I_0 measured before the pump arrival. In turn, $I(\Delta t)$ and I_0 are both obtained by normalizing the scattering intensity recorded on the avalanche photodiode by the incident XFEL pulse intensity obtained from a Krypton gas monitor detector located downstream from the grating monochromator. The data in these time-delay scans were binned to the nominal step size of the mechanical delay stage (100 fs for the first 5 ps after excitation). A description of the models used to fit the tr-RXS time traces is provided in the Supplementary Information. In order to capture the saturating effect of the pump, in the main manuscript Fig. 5.5(A) we plot $(1 - I(\Delta t)/I_0)$, and in Fig. 5.5(B) we plot the same quantity after subtraction of the structural background as described in the text.

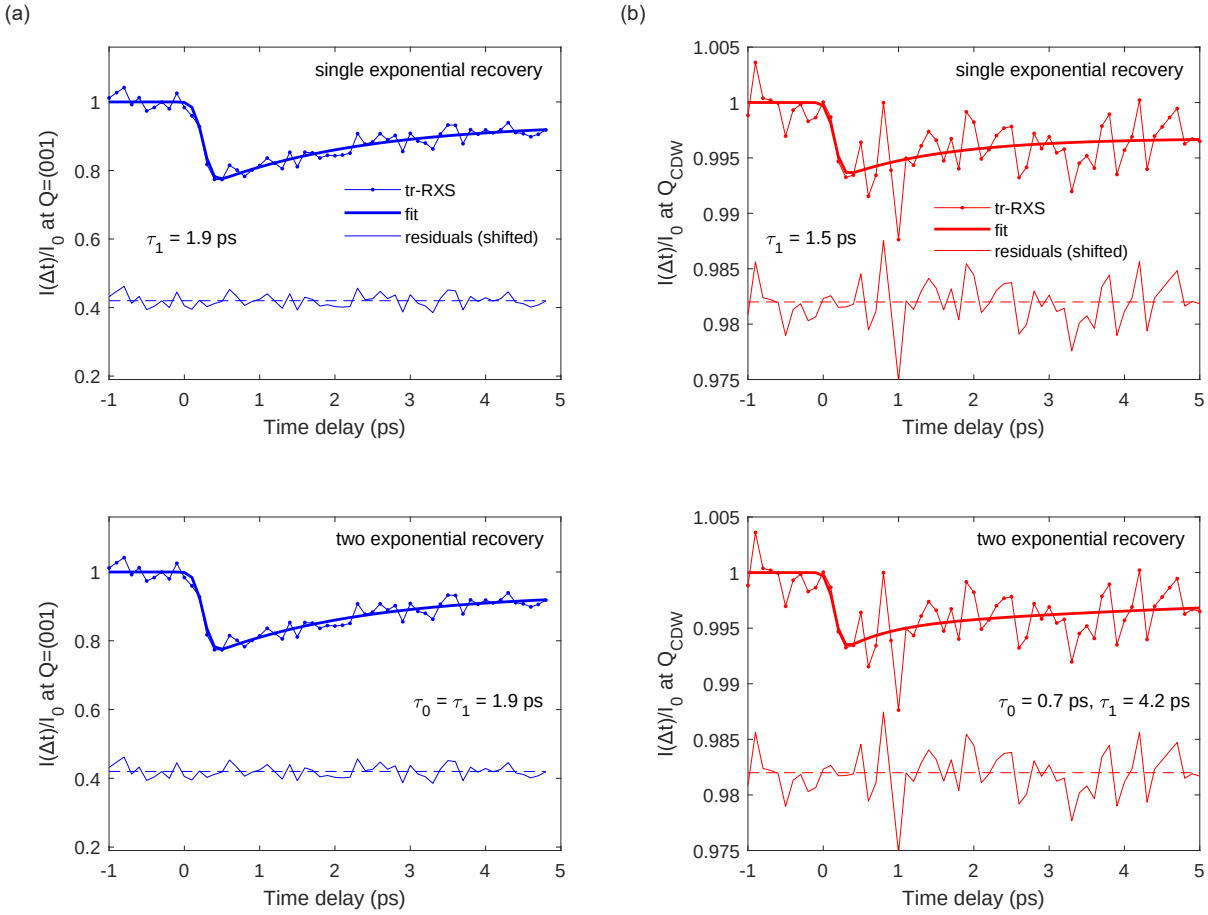


Figure 5.10: **One and two exponential model for electronic recovery dynamics.** Comparison of fits to the tr-RXS data presented in Fig. 3 of the main manuscript at (a) $Q = (0\ 0\ 1)$ and (b) Q_{CDW}, using models with one and two exponential recovery terms to capture the electronic dynamics. In each case the residuals are shown, shifted to within the field of view. The two fits to $Q = (001)$ data shown in (a) are identicle to one another, whereas the fits to Q_{CDW}in (b) are distinct but almost indistinguishable.

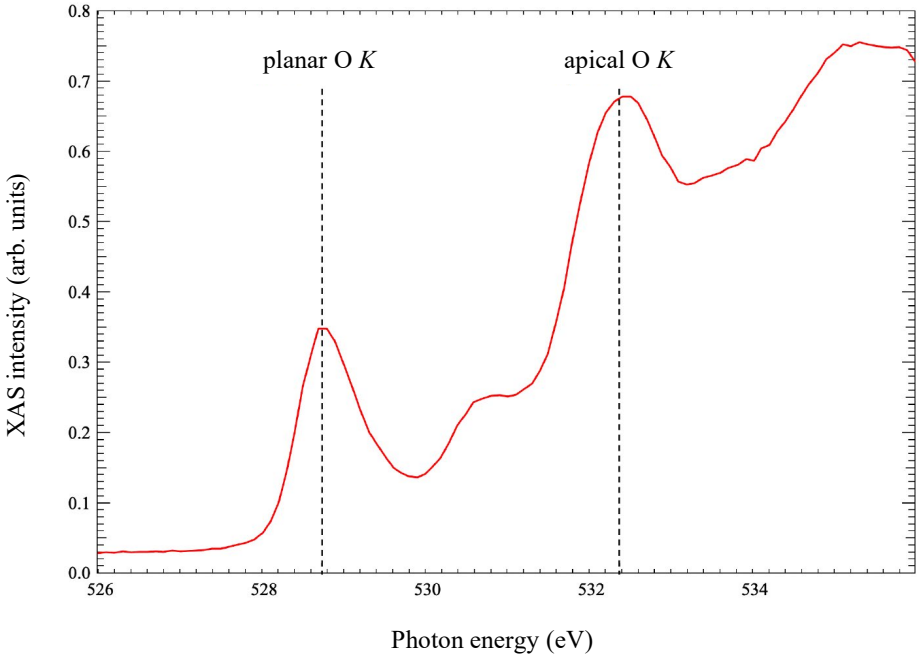


Figure 5.11: **O K XAS.** Equilibrium XAS measured across the O K edge at 20 K in the total electron yield mode.

Chapter 6

Evolution of nematic order with doping in stripe-ordered cuprates

Parts of this chapter has been adapted from Ref. [2], titled: Vanishing nematic order beyond the pseudogap phase in overdoped cuprate superconductors. The new results on Eu-LSCO presented in this chapter is an advanced manuscript nearing submission.

6.1 Overview

During the last decade, translational and rotational symmetry-breaking phases — density wave order and electronic nematicity — have been established as generic and distinct features of many correlated electron systems, including pnictide and cuprate superconductors. However, in cuprates, the relationship between these electronic symmetry-breaking phases and the enigmatic pseudogap phase remains unclear. We utilize equilibrium and time-resolved resonant X-ray scattering in stripe-ordered cuprates, $(\mathrm{La}, M)_2\mathrm{CuO}_4$ substituted with M = Nd, Sr, Eu and Ba to navigate the cuprate phase diagram, probing the relationship between electronic nematicity of the Cu $3d$ orbitals, charge order, and the pseudogap phase as a function of doping. We find evidence for a considerable decrease in electronic nematicity beyond the pseudogap phase, either by raising the temperature through the pseudogap onset temperature T^* or increasing doping through the pseudogap critical point, p^*. These results establish a clear link between electronic nematicity, the pseudogap, and its associated quantum criticality in overdoped cuprates. Our findings anticipate that electronic nematicity may play a larger role in understanding the

cuprate phase diagram than previously recognized, possibly having a crucial role in the phenomenology of the pseudogap phase.

We confirm a cooperative coupling between the $Q_x = Q_y = 0$ electronic nematic order and $Q_x \sim 1/4$ wavevector CDW order, which breaks both rotational and translational symmetry. Surprisingly, however, in heavily underdoped samples, we discover that nematic order is saturated, rendering it undetectable in equillibrium RXS. With the aid of non-equilibrium, ultrafast pump-probe measurements, we discover that nematic order is still present and detected in a clear sub-picosecond suppression.

6.2 Introduction

Strongly correlated electron systems, such as cuprate and iron-based superconductors, display a rich interplay between various electronic symmetry breaking orders. In cuprates superconductors, the co-existence of electronic ordering tendencies with superconductivity holds paramount importance. In this chapter, we interrogate the possibility that the cuprates exhibit a connection between electronic nematic order, the pseudogap, and its associated QCP. In the pnictide superconductors, which are similar in many respects to the cuprates, electronic nematic order is more clearly established experimentally, and there have been reports of nematic fluctuations [161], non-Fermi liquid transport [162], and a change in the topology of the Fermi surface associated with a nematic QCP [163].

Electronic nematicity refers to a breaking of rotational symmetry of the electronic structure in a manner that is not a straightforward result of crystalline symmetry, such that an additional electronic nematic order parameter, beyond the structure, would be required to describe the resulting phase. The manifestation of nematic order may therefore depend on the details of the crystal structure of the materials, such as whether the structure is tetragonal or orthorhombic. However, such a state can be difficult to identify in materials that have orthorhombic structures, which would naturally couple to any electronic nematic order and vice versa. Despite these challenges, experimental evidence for electronic nematic order that is distinct from the crystal structure includes reports of electronic nematicity from bulk transport [62, 64, 63] and magnetometry measurements [55] in YBCO, scanning tunneling microscopy (STM) [66, 65, 164] in $Bi_2Sr_2CaCu_2O_{8+\delta}$ (Bi2212), inelastic neutron scattering [67] in $YBa_2Cu_3O_y$ (YBCO), and resonant X-ray scattering [39] in $(La,Nd,Ba,Sr,Eu)_2CuO_4$. Moreover, STM studies in Bi2212 have reported intra unit cell nematicity disappearing around the pseudogap endpoint [165], which also seems to be a region of enhanced electronic nematic fluctuations [59, 60]. In YBCO, there have also been reports of an association between nematicity and the pseudogap onset temperature [64, 55].

Nematic ordering can result from strong correlations, such as a Pomeranchuk instability of the $t-J$ model, or from the Coulomb repulsion between holes on nearest-neighbour O [72, 73]. A recent advance in this regard was the identification of electronic nematic order in the (La, M)$_2$CuO$_4$ with M = Nd, Sr, Eu and Ba family of cuprates using resonant soft X-ray scattering [39, 2]. These studies showed a $Q_x = Q_y = 0$ electronic nematic order that is enhanced by the formation of translational-symmetry-breaking CDW order. Notably the nematic order is distinct from the CDW order: with clear signatures of nematic order present at temperatures and dopings where no evidence of CDW order is found [2].

We employ resonant X-ray scattering to measure electronic nematic order in the cuprates $La_{1.6-x}Nd_{0.4}Sr_xCuO_4$ (Nd-LSCO), $La_{1.8-x}Eu_{0.2}Sr_xCuO_4$ (Eu-LSCO) , and $La_{2-x}Ba_{0.4}xCuO_4$ (LBCO) as a function of doping and temperature, to explore the relationship of electronic nematicity with the pseudogap phase. The onset temperatures of structural phases, superconductivity, and CDW order vary in LBCO, Nd-LSCO, and Eu-LSCO, investigating them together provides an opportunity to explore the role of electronic nematicity with generic phases in the cuprate phase diagram. For instance, Eu-LSCO and Nd-LSCO have different CDW order onset temperatures but they both show uptick in the nematic signal at the T_{CDW}. Furthermore, the role of a putative quantum critical point [47] in Nd-LSCO and Eu-LSCO in hole-doped cuprates remains unclear, measurements of Eu- and Nd- substituted samples can provide useful insights in the relationship between co-existing phenomenon at low temperatures. Recent signatures of quantum criticality and electronic structure change include a divergence in the heat capacity [47], a change in the electronic structure from angle-dependent magnetoresistance (ADMR) measurements [54] in the vicinity of the QCP at $x = 0.23$, and the onset of the pseudogap [53]. Our main result is that we observe a vanishing of the electronic nematic order in Nd-LSCO as hole doping is either increased above $x = 0.23$, which has been identified as the QCP doping for this system [47], or when temperature is increased above the pseudogap onset temperature T^* [53]. These observations indicate that electronic nematicity in Nd-LSCO is intimately linked to the pseudogap phase.

The crystal structure of (La, M)$_2$CuO$_4$ in the LTT phase is depicted in Fig. 6.1A. Importantly, this structure exhibits tilts of the CuO_6 octahedra about the CuO bond directions (the a or b axes of the high temperature tetragonal, HTT, unit cell). The axes of these octahedral rotations alternate between neighbouring layers, such that the overall space group of the crystal structure is tetragonal, but the point group of atoms in individual layer breaks C_4 rotational symmetry. The schematic in Fig. 6.1(a) show octahedron cages in the LTO (Low Temperature Orthorhomic) and LTT (Low Temperature Tetragonal) phases. Upon cooling they exhibit a structural phase transition via change in the tilting axes and angles of the octahedrons – from LTO phase with octahedral tilts along [110]

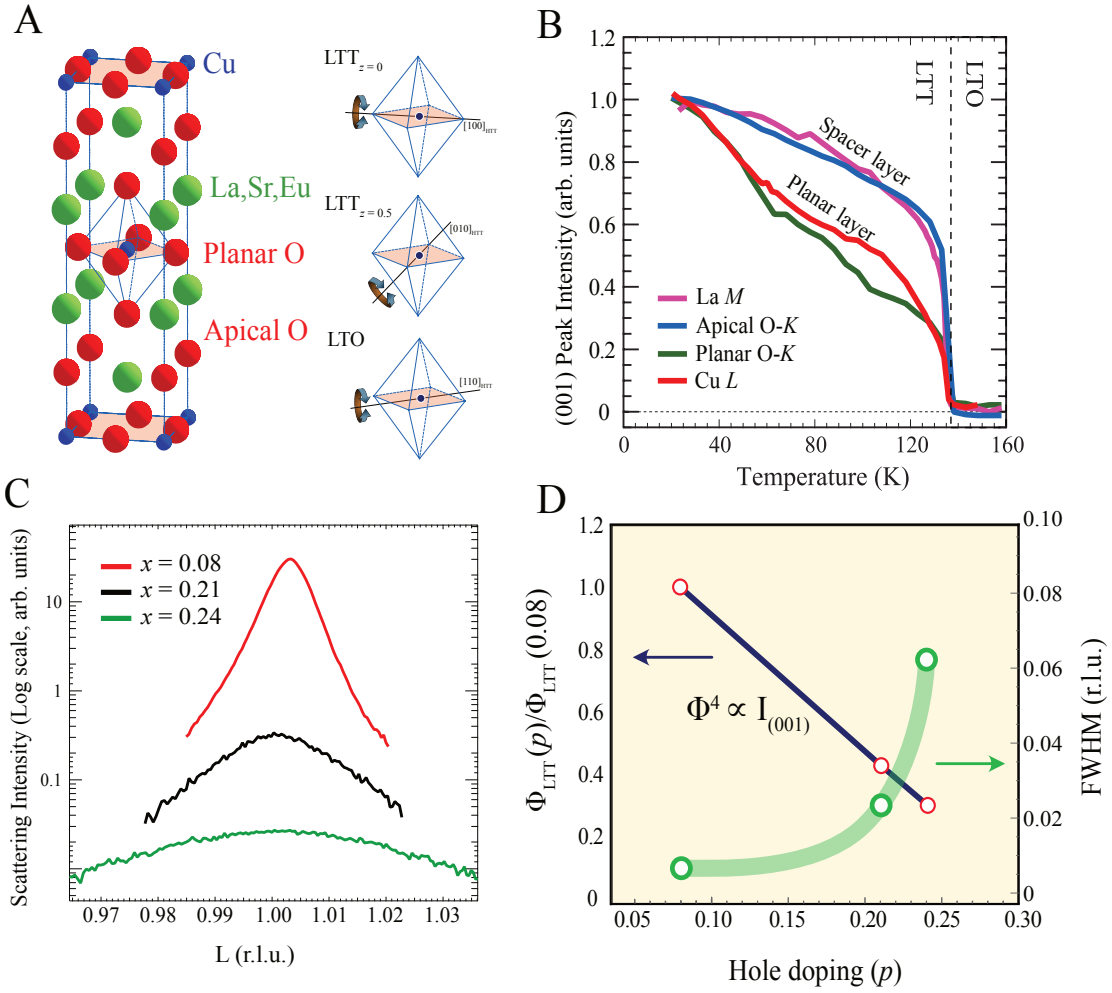


Figure 6.1: **Structural distortions and nematicity in Eu-LSCO**: (a) Crystal structure and structural distortions in stripe-ordered cuprates $(La, M)_2CuO_4$ where M = Eu, Nd, Sr, (b) Temperature dependence of the (001) Bragg peak intensity in Eu-LSCO. The intensities are normalized by base temperature value at T = 20 K, the La M-, Eu M-, O K-, and Cu L-edges. The dichotomy in the temerature evolution between spacer and planar layer atoms stems from electronic nematicity. (c) The scattering intensity vs. L through the (001) peak at the apical O resonance (533 eV) for Eu-LSCO dopings $x = 0.08$, 0.021 and 0.24. (d) The peak width along L increases with increases doping, indicating a decrease in the size of LTT structural domains at high doping

axis to LTT phase where the tilt axis alternates between neighbouring layers as [100] and [010]. The LTT structure is crucial for the detection of the forbidden (001) Bragg peaks on atomic resonances where it enhances sensitivity to orbital asymmetry.

6.3 Methods

The identification of electronic nematicity by resonant soft X-ray scattering (RXS) in the (La, M)$_2$CuO$_4$ cuprates exploits the coupling of nematic order to symmetry breaking structural distortions – specifically phases resulting from the tilting of CuO$_6$ octahedra occur at low temperatures. Our study uses RXS measurements of the (001) Bragg peak to probe electronic nematicity in (La, M)$_2$CuO$_4$. Previous work by Achkar et al. [39] showed that the resonant X-ray scattering measurements of the (001) Bragg peak provide sensitivity to electronic nematicity. Understanding how this measurement reveals electronic nematicity requires examination of Nd-LSCO's crystal structure. Nd-LSCO exhibits a structural phase transition from the low-temperature orthorhombic (LTO) to the low-temperature tetragonal (LTT) phase at temperatures between 60 and 90 K, depending on doping [43, 45]. The LTO phase is characterized by tilting of the CuO$_6$ octahedra along an axis in the CuO$_2$ plane, but diagonal to the Cu-O bond. In the LTT phase, the axis by which the CuO$_6$ octahedra are tilted rotates 45 degrees to be along either the a or b axes, such that each individual CuO$_2$ layer structurally breaks C_4 rotational symmetry, as shown in Fig. 6.1A. The axis of rotation of the octahedra, however, rotates by 90 degrees between neighboring layers, producing a crystal structure that is tetragonal, despite having orthorhombic layers. Consequently, probes that average over the (neighboring) layers would yield the same result along the a and b axes and may not reveal nematic order.

Resonant X-ray scattering of the (001) Bragg peak, however, provides a direct measure of the difference in the symmetry of the electronic structure between neighboring layers [39, 36]. Off resonance or with conventional X-ray diffraction, the (001) Bragg peak is forbidden, based on the ionic positions of atoms in the LTT or LTO phases. However, resonant X-ray scattering is sensitive to orbital symmetry, which differs for atoms in neighboring layers in the LTT phase. Moreover, by tuning the photon energy to correspond to different atoms within the unit cell, the electronic symmetry-breaking of the CuO$_2$ planes — which contain the Cu d and O p states that cross the Fermi level and are most relevant to the low-energy physics of the cuprates — can be differentiated from the La$_2$O$_2$ spacer layer, which does not have states that cross but would be sensitive to changes to their orbital symmetry induced purely by structural distortions.

Achkar et al. [39] showed that the temperature dependence of the (001) peak intensity

exhibited a dichotomy when the photon energy was tuned to different atoms in the unit cell. An abrupt first-order-like increase at the LTO $\rightarrow$ LTT transition (consistent with previous measurements of the structural transition) was observed when the photon energy is at the La-M edge ($\sim 826\,\mathrm{eV}$) or an energy associated with apical oxygen ($\sim 532.3\,\mathrm{eV}$) — atoms in the La_2O_2 spacer layer [39]. However, a more gradual temperature dependence was observed when the photon energy is tuned to the Cu-L edge ($\sim 931.5\,\mathrm{eV}$) or an energy associated with in-plane O ($\sim 528.5\,\mathrm{eV}$) — atoms in the CuO_2 planes. The different temperature dependencies can be understood in terms of a metanematic order, in analogy to a metamagnetic order in magnetism.

Electronic nematic order in the CuO_2 planes has a temperature-dependent susceptibility and couples to the lattice order. This provides an additional nematic contribution to the (001) structural Bragg peak. Effectively, this is akin to an internal strain applied to individual CuO_2 planes by the lattice distortion, with the electronic structure of the CuO_2 planes (probed by the (001) peak intensity at the Cu-L edge) exhibiting a response that depends on the electronic nematic susceptibility. Nematic order couples naturally to both unidirectional CDW order and to symmetry breaking structural distortions, making its observation and role relative to other orders difficult to isolate from a trivial byproduct of the lattice symmetry or from the presence of unidirectional CDW, which can break both translational symmetry and rotational symmetry. Importantly, Achkar et al. also showed that this electronic nematic order is coupled to, but distinct from, CDW order. Recently, in Bluschke, Gupta et al, [1] the observation of distinct nematic order via the temperature dependence of the (001) peak at different absorption edges was validated by ultra-fast optical pump, X-ray probe measurements of the (001) peak in $La_{1.65}Eu_{0.2}Sr_{0.15}CuO_4$. As described in Chapter 5, showing a significant, sub-ps suppression of the (001) peak at photon energies associated with the Cu L and in-plane O, but a weak and significantly slower suppression of the (001) peak at energies associated with La or apical oxygen, consistent with distinct structural and Ising-nematic order parameters.

In this chapter, we investigate electronic nematicity as a function of doping (through the pseudogap QCP, p^*) and temperature (through the pseudogap onset, T^*). Since our measure of electronic nematicity requires the LTT phase, the measurement to record its response crossing the pseudogap phase onset temperature requires a sample with $T_{\mathrm{LTT}} > T^*$, which is achieved here at a doping level of $x = 0.225$ in Nd-LSCO and $x = 0.21$ in Eu-LSCO [1].

[1] the pseudogap critical doping, $p^* = 0.23$ is established in Ref. [47] for Eu-LSCO and Nd-LSCO

6.4 Experimental procedure

6.4.1 Experimental setup

The measurements are conducted at the in-vacuum four-circle diffractometer at CLS's REIXS endstation. These samples were provided by collaborators and grown using travelling solvent floating zone (TSFZ) method. We measured the (001) peak and charge density wave (CDW) order at different temperatures — varying in the steps of 2 to 3 K — for these doping levels. The measurements for a resonance-edge at a series of temperatures in the LTT phase takes around 8-10 hours to accomplish. Investigating a sample at a fixed hole doping, at three atomic resonances for instance, with test alignment and data reproduction tests take up to 50 hours of experimental beamtime.

For this scheme of doping series measurement, we need a cleaved surface to get a decent surface and good signal intensity, this is achieved by preparing the sample before the beamtime at the synchrotron. The samples are characterized via Laue diffraction which helps in marking a/b axes for easier alignment as well as looking for twinning and other imperfections. In order to expose a fresh surface, samples are cleaved beforehand in our lab and then kept in an clean and dry environment until the experiment. The cleaved samples are mounted on a copper plug with silver epoxy — which is a good conductor and retains strength at low temperatures and ultrahigh vacuums — such that the cleaved ab-face is parallel to the sampleholder surface and at $\theta = 0$ geometry c-axis and the incident photon beam are collinear. Once mounted on the sampleholder, the assembly goes in the load lock chamber until it is brought down to near-UHV pressures, only them the valve to the main scattering chamber is opened and the sample is inserted in the sample receptacle slot into the four-circle diffractometer-gonimoter's center of rotation. The position is screwed in place using an externally controlled in-situ screwdriver arm to avoid any undesired displacements.

The first step is the coarse alignment by eye using the cross hairs on the telescope which are very carefully aligned to the beamspot line-of-sight. Once we locate the a good spot on the sample under investigation, we start with fine tuned calibration using X-ray absorption spectroscopy (XAS) measurements at Cu L edge for instance. After locating a decent spot of the sample, we proceed to align the crystallographic axes using the structural Bragg peaks — at low temperatures, which is a tetragonal structure, we can access (004), (103), and (-103) Bragg peaks — at an incident photon energy of 2200 eV. We use the MCP detector to visually center the Bragg peaks and record the respective motor values which are then used to set the orientation matrices in the SPEC macros, allowing up to access the reciprocal space by desired Miller indices.The lattice parameters for Nd-LSCO samples

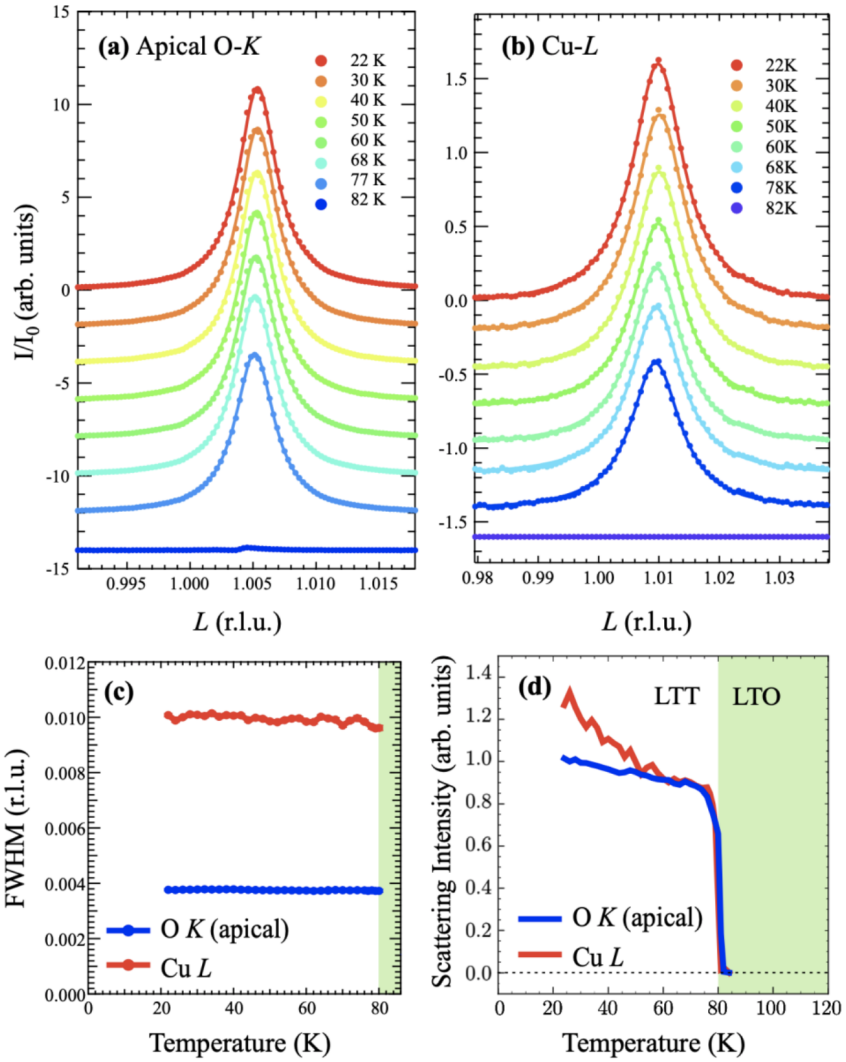


Figure 6.2: **Temperature dependence of (001) Bragg peaks in Nd-LSCO at** $x = 0.17$: Temperature dependence of the (001) Bragg peaks at (a) apical O-K edge ($\sim 532\,\text{eV}$) and (b) in-plane Cu-L edge ($\sim 931.5\,\text{eV}$). Solid lines are Lorentzian fits to the data (filled circles) at different temperatures. The peak intensity decreases with increasing temperature, but the width remains constant. (c) The T dependence of the FWHM of the Lorentzian fits for the (001) peak at the apical O-K and Cu-L edges. (d) The scattering intensity (peak amplitude of the Lorentzian fits) for both edges. The intensities for the apical O-K signal are normalized by the corresponding low-temperature values, $I_O(001) \approx 24\,\text{K}$, with the intensity for the Cu-L edge scaled to match the O-K intensity at a temperature below the LTO $\rightarrow$ LTT transition.

were taken to be $a = b = 3.787$ Å and $c = 13.24$ Å for finding and recording Bragg peak positions.

Once the sample is aligned, we move to the Cu L and apical O K edge to locate and confirm the (001) Bragg peak. Validation generally includes measuring the peak at low temperature and then warming up the sample and comparing the (001) peak intensity which should dramatically drop down after LTT:LTO transition as it is only permitted in the LTT phase. We, then, perform a series of ℓ-scan[2] measurements around (001) peak at different temperature values. The measured peaks shapes are then fitted to a Lorentzian function to get information about peak intensity, peak area, full-width half-maxima (FWHM), and the peak position in ℓ.

6.4.2 Data collection and analysis

The data collection process involves calibration of the motor positions, incident photon energy, and count time alongside validating any drifts caused by beamline's operation parameters. There are changes which can be mitigated like described in Section 4.0.3, the assembly is designed in a way to reduce the change with temperature mostly to z and θ degree of freedom, which makes it slightly easier for us to confirm if the incident beam is hitting the same 'good' spot on the sample.

Although, it depends on the detector how the exact steps for data analysis are proceeded, however, a general scheme is as follows:

- **Pre-fitting procedures:** Normalizing the scattered signal with the intensity of the incident beam — to make sure fluctuations in any physical parameters at the beamline or the storage ring is accounted for — thus providing a common ground to compare signal intensity with changes in temperature, reciprocal axes, and other degrees of freedom.

- **Higher harmonic correction:** Before moving to background subtraction, it is important to check any potential signal contribution from second-order light, unfortunately, the latter often causes a difficulty in recording the (001) peak intensity at the apical O K edge. Higher harmonics are produced in the undulator and is difficult to be contained or filtered by the monochromator which only allow light of only certain wavelength to pass through. Thus, an on-resonance geometry that

[2] achieved by performing a $\theta - 2\theta$ scan in which both the sample and detector rotate at the same rate

allows the forbidden (001) peak also permits the structural (002) Bragg peak at *almost* the same (2θ) detector position. Ways to correct this include, switching to an energy resolved detector, or moving slightly towards the shoulder of the (001) peak — which is broader in reciprocal space than the (002) peak — thus away from the (002) Bragg peak geometry, the intensity at the shoulder/falling edge responds approximately proportional to the actual peak intensity and can be carefully validated by fitting Lorentizans and comparing full-width half-maxima (FWHM). Other ways can include subtracting the signal at higher temperature devoid of (001) peak.

- **Background subtraction:** We generally fit a third order polynomial (or fifth in some cases) with the signal intensity/detector count at detector positions sufficiently away from the peak shape under investigation. Ideally the background polynomial fit should not change by varying the degree of polynomial[3] or a few points up and down. Especially for the (001) peak, sometimes it is also good to validate the background subtracted signal with the high temperature signal subtraction — as (002) peak exists but no (001) signal is prsent in the LTO phase — to make sure any saturation effects in the detector used. Irregularities can also be detected once we start fitting a Lorentzian line shape — by looking at residual (= fitted data - actual data) shapes — in terms of large error in FWHM or offsets at few temperatures.

- **Lineshape fitting:** Post-background subtraction, the Bragg peaks we measure are Lorentzian line shapes [4]; after subtracting the polynomial background, we fit to:

$$L(x) = c_0 + \frac{A}{1 + 4\left(\frac{x - x_0}{w}\right)^2} \tag{6.1}$$

  where, A is the amplitude, w is the FWHM, c_0 is a constant offset

  Once the fitting schedule is satisfactorily completed, we can extract the fitting parameters — and after checking different fitting schemes and plotting error bars with the best fit parameters – we proceed to plot them trying to understand the underlying physics.

[3] We generally use cubic fits, I have tried changing the degree of polynomial between 3 to 6 for the (001) peak and a good background fit does not respond much to it.

[4] Past investigations by our group [39] as a function of energy and detector positions and temperature.

6.5 Results

We employ resonant X-ray scattering to investigate electronic nematicity and CDW order in Eu-LSCO, Nd-LSCO, and LBCO over a wide range of Sr hole doping. Measurements are performed at the REIXS beamline at the Canadian Light source in Saskatoon on single crystal samples of $La_{1.6-x}Nd_{0.4}Sr_xCuO_4$ with $x = 0.125$, 0.17, 0.18, 0.19, 0.225 and 0.24 as well as $La_{1.8-x}Eu_{0.2}Sr_xCuO_4$ with $x = 0.08$, 0.11, 0.125, 0.15, 0.21 and 0.24, along with $La_{1.905}Ba_{0.095}CuO_4$. In addition, we measured $La_{1.44}Nd_{0.4}Sr_{0.17}CuO_4$ at BESSY UE46-PGM1 high-field beamline in Berlin, enabling us to reach a lower base temperature up to 4 K in one of the samples to understand the connection of nematicity with the onset of the superconductivity. Ultra-fast optical pump, X-ray probe measurements were conducted at the Pohang XFEL SSS beamline in Pohang on Eu-LSCO at $x = 0.08$, 0.15, and 0.24 to differentiate between saturation and absence of nematic order.

Nd-LSCO	$x = 0.125$	$x = 0.17$	$x = 0.18$	$x = 0.19$	$x = 0.225$	$x = 0.24$
Eu-LSCO	$x = 0.08$	$x = 0.11$	$x = 0.125$	$x = 0.15$	$x = 0.21$	$x = 0.24$

Table 6.1: Sr hole-doping x values in single crystal samples of $La_{1.6-x}Nd_{0.4}Sr_xCuO_4$ (Nd-LSCO) and $La_{1.8-x}Eu_{0.2}Sr_xCuO_4$ (Eu-LSCO) measured by resonant X-ray scattering in this chapter

In this paper, using equilibrium and time-resolved resonant X-ray scattering (RXS), we explore the relationship between nematic, CDW, superconducting orders in $(La, M)_2CuO_4$ substituted with Nd, Sr, Eu and Ba as a function of hole doping. Covering a large swath of the phase diagram, we identify that nematic order in overdoped $(La, Eu, Nd, Sr)_2CuO_4$ is suppressed outside the pseudogap phase (above T^* and p^*) and is present in the absence of identifiable CDW order [2]. Surprisingly, using time-resolved RXS, we find that in heavily underdoped samples, where structural distortions are strongest, nematic order is evident in time-resolved RXS but is saturated by the strong lattice distortion in equilibrium RXS measurements. Furthermore, we record a saturation of nematic order below the superconducting transition temperature in optimally doped $x = 0.17$ Nd-LSCO. These results indicate that elucidating the complex physics of nematicity in cuprates may entail disentangling its coupling from structure, superconductivity, and CDW order.

6.5.1 Low temperature structural distortions with doping

The structural distortions have been connected with stabilizing unidirectional CDW order in the LTT and (Low temperature Less Orthorhomic) LTLO phases, and naturally couple

to and enhance electronic nematic order in La-based cuprates. Importantly, how these structural phases manifest; (1) the degree of octahedral tilts, (2) the onset temperature of the LTT or LTLO phases depends on both the concentration, and ionic radius of the cations (Nd, Ba, Sr, Eu) that are substituted into the La_2O_2 layers. The substitution of Sr^{2+} or Ba^{2+} for La^{3+} has two roles, varying the hole doping in the CuO_2 planes and impacting the structural distortions (Fig. 6.1c). The magnitude of the octahedral tilts in the LTT phase is known to decrease with increasing Sr^{2+} or Ba^{2+} doping [45, 166]. Thus, the extent to which structural distortions impact nematic and CDW orders may vary with doping.

To characterize the magnitude of the structural distortions across the phase diagram, we measured the (001) peak intensity and width (FWHM) as a function of Sr doping. We find that the intensity of the (001) peaks decreases with increasing doping, as shown in Fig. 6.1c. A conversion of our integrated intensity to a change in Φ shown below shows a roughly linear dependence of the tilt angle with increasing doping, this is consistent with the doping dependence of the octahedral tilt angle, Φ, which previous studies in LBCO and Nd-LSCO have shown to decrease upon hole doping, eventually vanishing at high dopings and temperatures into the HTT structural phase [167, 166]. Notably, in contrast, the LTT phase transition temperature, T_{LTT} is weakly doping dependent and is not set by the tilt angle [42, 168, 2].

We also measure the width in L of the (001) Bragg peak as a function of hole doping. We record an increase in the peak width with increasing doping – at low doping, the width of the peak in L has been identified to be associated with the absorption length into the sample [39] and is not a measure of the c-axis correlation length of the structural or nematic order. This is evidenced by a peak width that varies with photon energy, tracking the variation in absorption length with energy [39]. Consequently, the size of LTT structural domains along the c-axis at low doping is larger than the measured absorption length. However, as doping increases to $x = 0.21$ and $x = 0.24$, the peak width exceeds the limit given by the absorption length. This indicates that shorter range LTT structural domains are found in $x = 0.21$ and 24 samples, with the domain size decreasing with increasing doping.

6.5.2 Doping-Temperature evolution of electronic nematicity

In Nd-LSCO

In Fig. 6.3, we show the intensity of the (001) peak as a function of temperature (T) at the Cu-L edge (probing the CuO_2 planes) and the O-K edge at an energy sensitive to apical O

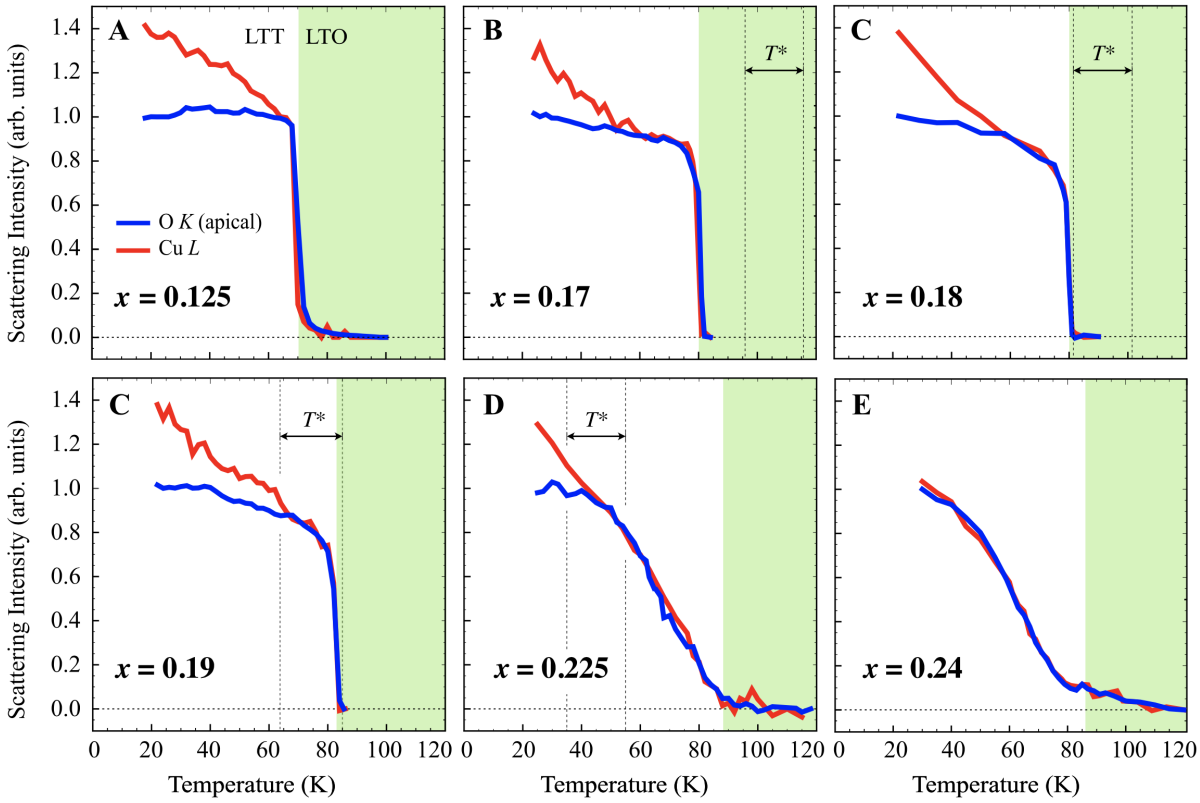


Figure 6.3: **Evolution of electronic nematic order in Nd-LSCO**: Figure 2. Doping and temperature dependence of the (001) Bragg peak intensity in Nd-LSCO. The intensities of the (001) Bragg peak as a function of temperature with photon energy tuned to the apical O-K (blue) and Cu-L (red) edges for $La_{1.6-x}Nd_{0.4}Sr_xCuO_4$ with Sr doping levels: $x = 0.125, 0.17, 0.18, 0.19, 0.225$ and 0.24. The white and green regions indicate the LTT phase and the LTO phase, respectively. The O-K and Cu-L data are arbitrarily scaled to match in intensity below the LTT phase transition in order to highlight differences in temperature dependence. The dotted lines mark the pseudogap onset temperature, T^*, in Nd-LSCO based on the high field electrical resistivity measurements from Ref. [53]. Data on the $x = 0.125$ sample is reproduced from Ref. [39].

(probing the La_2O_2 layer). Note, here the data at the different edges is arbitrarily scaled to match in intensity below the LTO $\rightarrow$ LTT phase transition to highlight the difference in temperature dependence for different doping levels. The onset temperature of electronic nematicity, T_{EN}, is identified as the temperature where the (001) peak first exhibits a

notable deviation between Cu-L and apical O-K edges. In Fig. 2A, data at $x = 0.125$ from Ref. [39] is reproduced, which showed a distinct difference in the T dependence of the (001) peak for measurements at the Cu-L and O-K edges. As the doping is increased in Nd-LSCO, a similar difference in the peak intensity between Cu-L and O-K edges is observed for $x = 0.17, 0.18, 0.19$ and 0.225 (see Fig. 6.3 A to E). However, for $x = 0.24$, as the hole doping is increased across the pseudogap QCP (at $x \approx 0.23$), within the measurement accuracy we detect no difference in the T dependence of the (001) peak when measured at the apical O-K and Cu-L edges (see Fig. 6.3E).

Notably, we also observe that for $x = 0.225$, within the measurement accuracy, we detect no difference in the T dependence of the (001) peak at the apical O-K and Cu-L edges above the pseudogap onset temperature T^*, but a distinct difference in temperature dependence below T^* (T^* is identified in Ref. [53] by the resistivity upturn at 50 K in $x = 0.22$ and 40 K in $x = 0.23$). Our **principal conclusion** from this result is that static, long-range ordered electronic nematicity in Nd-LSCO is a characteristic of the pseudogap phase, vanishing either upon traversing the QCP with increasing doping or by increasing the temperature above T^*.

6.5.3 In Eu-LSCO and LBCO

In Fig. 6.4, we present the T dependence of the (001) Bragg peaks at 931.3 eV (red), Cu L_3 edge, and at 533 eV (blue), the O K edge at a photon energy that is sensitive to apical-O atoms in Eu-LSCO and LBCO.

Similar to Nd-LSCO, a clear difference in the temperature dependence for the apical O and Cu L resonances for samples with doping between $x = 0.11$ and 0.21. However, for Eu-LSCO at $x = 0.21$ (Fig. 6.4G) the difference in the T dependence only onsets below the pseudogap onset temperature, T^*, above which both the Cu and apical O energies show similar evolution up to the T_{LTT}. Moreover, in Fig. 6.4G as the doping is increased to $x = 0.24$, above the pseudogap p^* (see Fig. 6.4), the difference in temperature dependence between the Cu L and apical O resonances vanishes.

This difference in the temperature evolution, with an additional T dependence observed at the Cu L edge, indicates that electronic nematic order are present in the psuedopap phase, but not in the neighbouring strange metal phase. This correspondence between the observation of nematic order and the psuedogap phase first found in Nd-LSCO [2] is now reproduced in Eu-LSCO. Previous studies have established in La-based cuprates that by replacing the rare-earth substitution from Nd(-LSCO) to Eu(-LSCO) the onset temperature of the structural LTT phase is doubled while the onset of the pseudogap phase dictated by

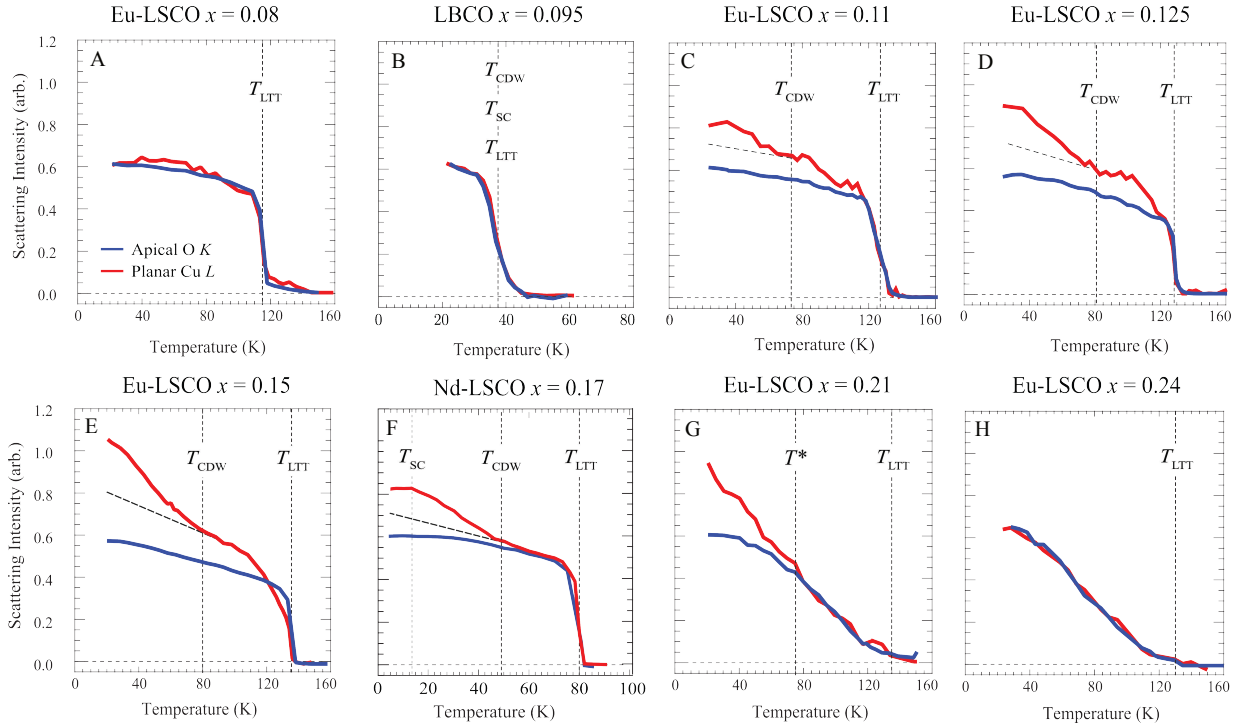


Figure 6.4: **Evolution of electronic nematic order in La-based cuprates**: (A-F) The intensities of the (001) Bragg peak as a function of temperature with photon energy tuned to the apical O K (blue) and Cu L (red) edges. The dichotomy in the T-dependency of the planar Cu atoms (red) and spacer apical O atoms (blue) is interpreted as rotational symmetry-breaking of the electronic structure. Data for samples of three familes with Eu-LSCO, Nd-LSCO and LBCO is presented over a wide doping range. The white and green regions indicate the LTT phase and the LTO phase, respectively. The dotted vertical lines mark the pseudogap onset temperature, T^*, in Eu-LSCO $x = 0.21$ based on measurements from Ref. [53]. The slanted dashed line are presented as a guide to eye to highlight deviation of the (001) peak at Cu L edge when CDW phase onsets. T_{SC} represents superconducting transition temperature in two samples.

the electronic physics remains at the same temperature [169, 19]. Despite this difference between Eu- and Nd-LSCO, we find a vanishing signature of electronic nematicity beyond the pseudogap phase in the Eu-substituted LSCO tracking similarly as Nd-substituted. This key result provides a validation and generalization for our earlier findings the Nd-LSCO system. Reinforcing conclusions from Gupta et al. [2] that electronic nematicity is associated with the pseudogap phase, either as an order that is stabilized by the pseudo-

gap phase or as a symmetry breaking order that is more intrinsically tied to origins of the pseudogap. Obtaining vanishing signatures in both rare-earth doping series – with differences in superconducting transition, structural distortions, space group symmetry, charge order – hints at a deeper link between electronic nematicity and pseudogap in overdoped cuprates.

6.5.4 Nematicity dynamics via tr-RXS in Eu-LSCO

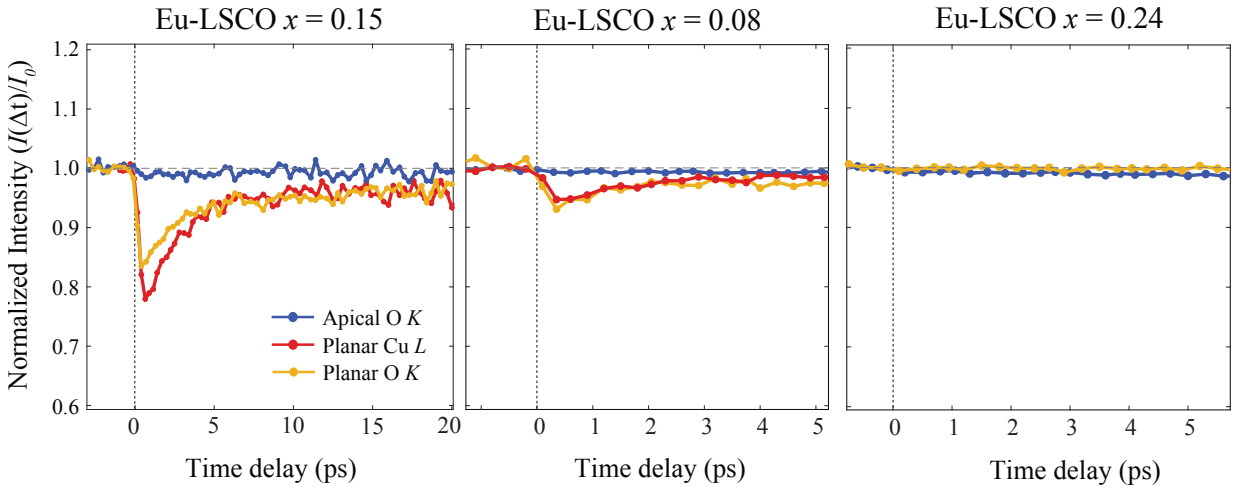


Figure 6.5: **Time-resolved signatures of nematicity in Eu-LSCO**: Normalized tr-RXS intensity (I(Δt)/I0) at $Q = (001)$ as a function of pump-probe delay in Eu-LSCO at $x = 0.15$, 0.08 and 0.25 at 20 K. Pump photon energy 1.55 eV and fluence ~ 150 μJ/cm^2. The tr-RXS intensity at the apical O-K resonance, sensitive only to structural distortions, is unperturbed by the optical pump at this low fluence. The planar O K resonance and the Cu L resonance are sensitive to ultrafast nematicity dynamics. We identify presence of nematic ordering in Eu-LSCO $x = 0.08$ which is not evident in equilibrium RXS. However, in $x = 0.24$, nematicity remains undetected above the base temperature of 20 K.

Extending measurements from Bluschke, Gupta et al. [1] in Chapter 5 to isolate nematicty in time-domain recovery via photoexcitation at fixed temperature, we investigate a series of samples. For $x = 0.15$ sample, we record a rapid decrease followed by slow relaxation in the intensity of the (001) peak intensity at the Cu-L edge upon photoexcitation by laser (pump). In contrast, for the apical O-K edge, no significant change is detected under the same conditions. A similar behavior is observed in the $x = 0.08$ but not in the $x = 0.24$ sample. This behavior suggests the presence of electronic nematic order in the

$x = 0.15$ and $x = 0.08$ samples, which is suppressed by the 800 nm laser pump. This pump-induced suppression of the (001) peak intensity in the $x = 0.08$ sample provides evidence for nematic order, despite the absence of a discernible T-dependence difference between the apical O K-edge and Cu L-edge measurements for this sample (see Fig. 6.4A). The apparent discrepancy between the T-dependence and pump-probe measurements can be reconciled by having an electronic nematic order that is present but exhibits weak temperature dependence. This may result from coupling to octahedral distortions, which are most pronounced at low doping levels and may therefore have a greater tendency to control the T-dependence of the nematic order.

Furthermore, the (001) peak in the overdoped Eu-LSCO x=0.24 sample does not show photo-induced suppression at either the Cu L or the apical O K edge. This aligns with the observation of vanishing nematicity established by our T-dependence measurements shown in Fig. 6.4H. These findings highlight the intricate nature of nematic order and its potential to evade detection, even in systems where its presence has been well-established. The combination of RXS and tr-RXS provides robust tools for detecting Q=0 nematic order in cuprates and other quantum materials.

6.5.5 Evolution of Charge Density Wave (CDW) order

Trying to understand the relation between the three symmetry-breaking phases, we recorded the CDW signal at different doping levels in LBCO, Eu-LSCO, and Nd-LSCO.

In Nd-LSCO

In Nd-LSCO, we observe CDW order in $x = 0.125$ and $x = 0.17$ samples but not for $x = 0.18, 0.19$, or 0.24 above the base temperature (22 K) of the measurements as shown in Fig. 6.6. The onset temperature of CDW order is consistent with the recent Seebeck coefficient measurement in Nd-LSCO [170]. In contrast, SDW order has been observed at low temperature up to a doping as high as $x = 0.26$ by elastic neutron scattering. However, the onset of SDW order ($T_{\mathrm{SDW}} = 35\,\mathrm{K}$ in $x = 0.19$) occurs at lower temperatures than our observations of electronic nematicity [171]. This shows that the existence of stripe-like CDW or SDW order, that breaks both translational and rotational symmetry, does not appear to be solely responsible for the electronic nematicity. Rather, electronic nematicity is either a distinct order or a melted stripe phase that retains rotational symmetry-breaking but not the translational symmetry-breaking of the CDW or SDW order [68]. A schematic phase diagram for Nd-LSCO that summarizes the doping evolution of the LTO $\rightarrow$ LTT phase

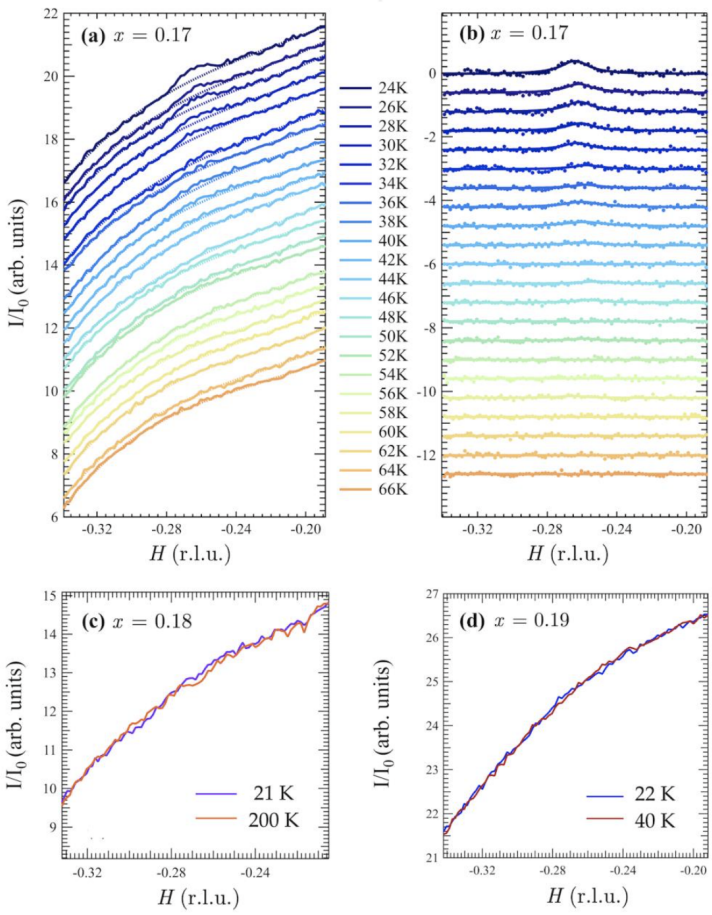


Figure 6.6: **Tracking CDW order with doping in Nd-LSCO**: (a) Measured intensity for scans as a function of H at various temperatures through the $\mathbf{Q} = (-0.26, 0, 1.5)$ CDW peak at $x = 0.17$ at various temperatures at Cu L edge. A cubic polynomial (dashed curve) is fit to the fluorescent background and subsequently subtracted from the data. (b) The polynomial background-subtracted data for $x = 0.17$. Solid lines are Lorentzian fits to the background-subtracted data (filled circles). In both (a) and (b), the data at different temperatures are offset for clarity. (c) and (d) Measured intensity through $\mathbf{Q} = (-0.26, 0, 1.5)$ for (c) $x = 0.18$ and (d) $x = 0.19$ at high temperature and at our base temperature ($\sim$22K), showing the absence of measurable CDW order in these samples.

transition, the onset of CDW order, and our evidence for long-range ordered electronic nematicity, with onset temperature $T_{\rm EN}$, is depicted in Fig. 6.8.

Notably, there has been a recent report in the related material LSCO [172], which remains in the LTO phase, that CDW order persists to higher doping levels than in Nd-LSCO; with CDW observed up to at least $p = 0.21$ – which is past the point where the Fermi surface transitions from hole-like to electron-like.

In Eu-LSCO

We search for CDW order $Q_{\mathrm{CDW}} \sim (-0.25\ 0\ 1.5)$ using resonant X-ray scattering at the Cu L edge in Eu-LSCO samples of doping $x = 0.08$, 0.15, 0.21, and 0.24; as well as $x = 0.095$ LBCO and $x = 0.17$ Nd-LSCO. Previous studies of Eu-LSCO at dopings of x=0.11, 0.125, 0.15, have detected CDW order onset [143, 36, 39] between 50K and 80K. Our measurements in x= 0.15 reproduced these previous findings (Fig. 6.7). Extending our measurements to more overdoped ($x = 0.21$ and $x = 0.24$), or underdoped ($x = 0.08$) reveleaved no evidence for CDW order above our base temperature of 20 K at these dopings (see Fig. 6.4). Notably, in Eu-LSCO, with its high LTT transition temperature, the CDW onset temperature falls below the LTT transition, enabling us to track the coupling between the electronic nematic order parameter and CDW order. Achkar et al. [39] showed in Eu-LSCO at $x = 0.15$ that the (001) peak at the Cu L edge is enhanced when CDW order onsets, but no anomaly in temperature dependence of the apical O. Non-equilibrium, ultrafast pump-probe measurements by Bluschke, Gupta et al [1] confirm a connection between CDW order and concomitant nematic order in Eu-LSCO at $x = 0.15$. Here we observe (Fig. 6.4) in Eu-LSCO with $x = 0.11$ and 0.125 that similar enhancements of the (001) peaks at the Cu L edge, without corresponding enhancements at apical O, are seen in other dopings below the onset of CDW order. As the $x = 0.21$ sample shows evidence of nematic order below T^*, this sample exhibits a region of the phase diagram below T^* and p^* where evidence nematic order is found in the absence of observable CDW order, consistent with previous measurements in Nd-LSCO [2].

6.5.6 Nematicity and superconductivity

When the superconducting transition lies in our detection range set by the existence of the LTT phase, we can measure the response of the (001) Bragg peak at T_c, probing the connection of electronic nematicity and superconductivity. We achieve such a scenario in two samples, (1) underdoped LBCO with $T_c = 33$ K (at CLS base temp of 20 K) and optimally doped $x = 0.17$ LNSCO with $T_c = 17$ K (at BESSY with base temp of 4 K).

In the Nd-LSCO sample, the (001) Bragg peak intensity measured at the Cu L edge flattens below T_C, potentially indicating a competition between static nematic order and

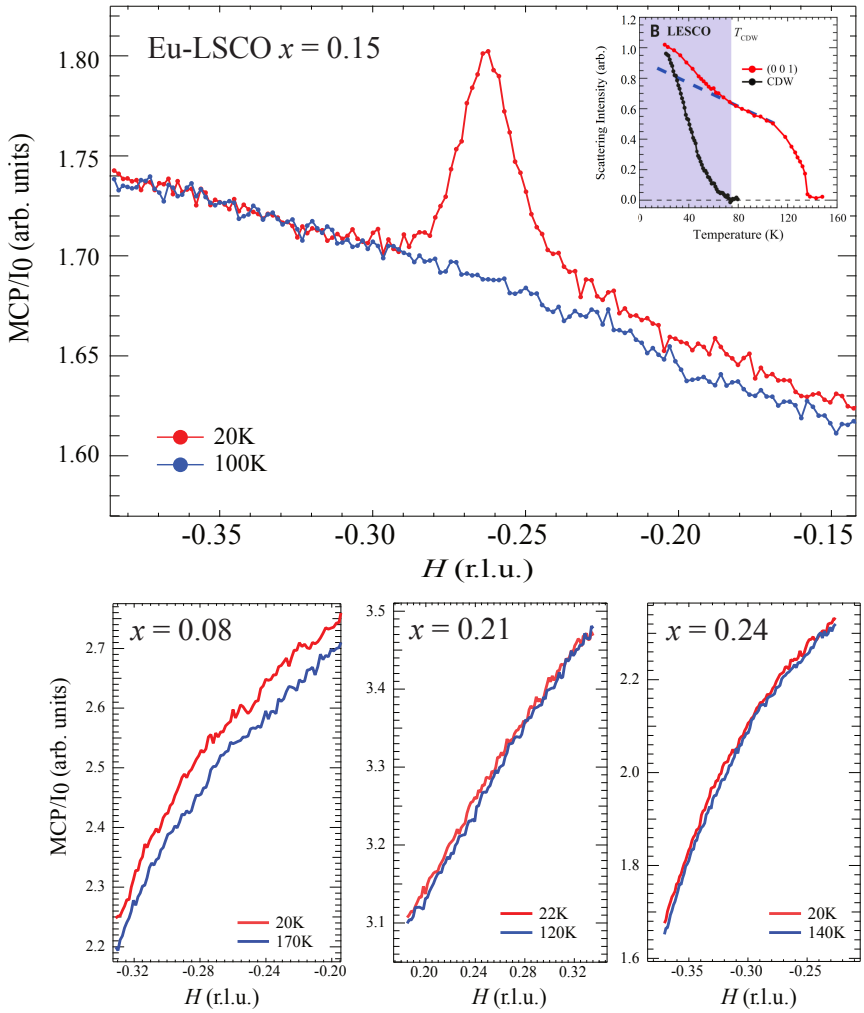


Figure 6.7: **Tracking CDW order with doping in Eu-LSCO**: We present H-scans through the CDW wavevector in Eu-LSCO at $x = 0.08$, 0.15, 0.21, and 0.24. Using RXS, we find a CDW order peak at $x = 0.15$. However, we do not detect a CDW order at $x = 0.08$, 0.21, and 0.24 up to our base temperature of 20 K.

superconductivity. The plateau in Fig. 6.4 F below 17 K can be interpreted as a potential suppression of nematic response. Our observation can either hint at a direct competition between nematic order and superconductivity or one mediated through charge density wave order. Superconductivity suppresses CDW order, which in turn is coupled to nematic order, hinting at possible extension. Suppression of nematic order with the onset of super-

conductivity may also contribute the lack of a clear nematic signature in LBCO $x = 0.095$, where T_C, T_{CDW} and T_{LTT} coincide, see Fig. 6.4B.

6.6 Discussion

In the cuprates, CDW and superconducting orders are present in a wide family of materials. However, the CDW and superconducting transition temperatures, as well as key properties of these orders (correlation length, CDW period, ...) can depend not only on hole doping but on unresolved details of the materials. A possible explanation for some of this variation may be a result of the complexity that results from coupling of superconducting, charge density wave and nematic and structural orders and how those orders are influenced disorder. For instance, these coupled orders present the possibility of various intriguing regimes. For instance, orders may fluctuate relative to each other, as has been suggested to explain the unusual T dependence of CDW order in YBCO in terms of phase fluctuations between CDW and superconducting orders [41], particularly if the coupled orders have similar energy and temperature scales. Alternately, when the temperature or energy scale of one of the coupled orders is much larger than the others, it may dominate the behavour of the other orders. This selection across Nd- and Eu-LSCO doping series establish a clear co-operation between the rotational and translation symmetry breaking order parameters. The co-operation between intra-unit cell and inter-unit cell symmetry breaking suggests that the onset of static CDW order can provide favoring orienting potential for the electronic nematic phase. A possible situation can involve melting of the CDW stripes to create a more amalgamated vestigial nematic state [70, 68, 173] that extends beyond the CDW dome in these alternating uniaxial stripe charge modulations. In $x = 0.095$ LBCO, CDW order is found with $T_{\rm CDW} \simeq 40$K. Notably, $T_{\rm CDW}$ at in this sample is coincident with both $T_{\rm LTT}$ and T_C, consistent with previous hard X-ray scattering studies [44].

Such a situation may occur with the coupling of nematic and structural orders in Eu-LSCO. At low doping, where the octahedral tilts are largest, the coupling of these tilts with electronic nematic order may be such that the nematic order is quickly saturated by the structural distortions or too small to be distinguished from trivial structural contributions. Conversely, it is possible that the relationship is inverted at higher doping, where the physics of electronic nematic order plays a significant role in driving structural distortions – ie a making the structural transition driven by electronic nematic tendencies.

Our observation that electronic nematic order in Nd-LSCO and Eu-LSCO is associated with the pseudogap phase is reinforced by recent measurements in other cuprate families that do not exhibit the LTT structural phase, indicating that an electronic nematic phase

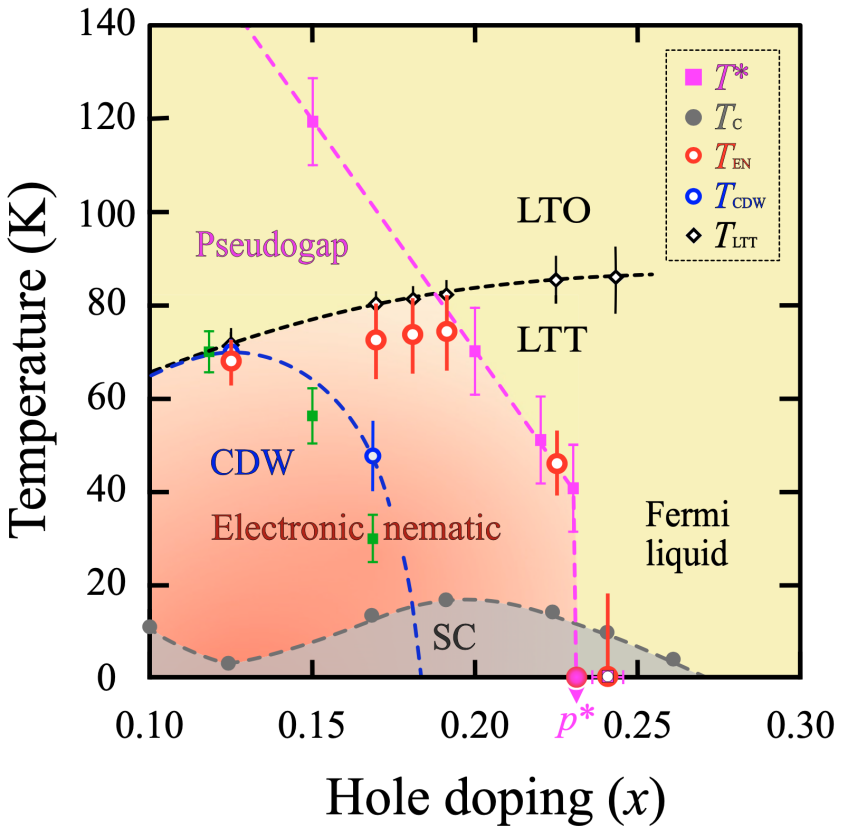


Figure 6.8: **Cuprate Phase Diagram for Nd-LSCO**: The doping-temperature phase diagram of Nd-LSCO. The structural phase transition from the LTO to LTT phase, T_{LTT} (black diamonds). The onset temperature of the charge density wave (CDW) order, T_{CDW}, using our resonant X-ray scattering measurement (blue circles) and recent Seebeck coefficient [170] measurement (green squares). The red circles mark the onset of the electronic nematic order in the LTT phase, T_{EN}. The superconducting (SC) transition temperature, T_c (grey circles), has been reported in Ref. [45] on the same series of samples as used for our RSXS measurements. The existence of a quantum critical point at $p^* \approx 0.23$ has been identified in Ref. [47]. The pseudogap onset temperature, T^* (purple squares), as a function of hole doping is measured via the onset of the upturn in electrical resistivity $\rho(T)$ in Ref. [53]. The black, purple, blue, and grey dotted lines are a guide to the eye.

terminating at the QCP in overdoped cuprates may be a generic property of the cuprate phase diagram. Specifically in Bi2212, low-temperature STM measurements indicate a

disappearance of nematicity at the pseudogap QCP [165], and recent elasto-resistance [59] and Raman scattering [60] measurements have shown dynamical electronic nematic fluctuations that are enhanced — in the overdoped region between $p = 0.20$ and 0.23 — and nematic quantum criticality which is consistent with the putative quantum critical point for Bi2212 at $p^* \approx 0.22$.

The questions remain whether electronic nematicity is fundamentally linked to the origins of the pseudogap or is simply stabilized when the pseudogap onsets, and what role, if any, quantum nematic fluctuations play in the physics of the cuprates. In the proximity of p^*, it has also been established that the electronic structure of the cuprates undergoes a Lifshitz transition from a small Fermi surface or Fermi arcs in the pseudogap phase to a large hole-like Fermi surface at higher doping in Nd-LSCO [53, 54, 20] and other cuprate families [30, 174, 165]. Perhaps most notably, in Bi2212 [165] the Lifshitz transition was shown to occur simultaneously with the disappearance of nematicity, similar to what we observe in Nd-LSCO. This change in the nature of the Fermi surface may provide the conditions for the presence or absence of electronic nematicity. Or, as suggested by recent theoretical proposals [175], the doping dependence of the electronic nematicity observed here may account for the change in the Hall number around the Lifshitz transition.

It is also possible that the nematicity observed here represents a "vestigial nematicity" that is connected to the pseudogap phase. It has been recently highlighted that in contrast to a CDW order, which can open a gap in the Fermi surface, electronic nematic order is a $Q_{x,y} = 0$ order and is not expected to open a gap in the Fermi surface [70, 173]. As such, one would not anticipate a natural connection between the pseudogap, which is evidenced by the opening of an antinodal gap, and electronic nematicity. However, a "vestigial nematic" state—derived from disordering a unidirectional CDW, but lacking long-range order—may open up a gap and is plausibly connected to the pseudogap phase [173]. Such a vestigial nematic state is consistent with our measurements, where nematicity is present in the pseudogap phase, but also at dopings and temperatures where CDW order is not observed.

6.7 Conclusions

We report the evidence for vanishing electronic nematic order in the vicinity of the QCP at $x = 0.23$ that has been identified in Nd-LSCO and Eu-LSCO and other cuprates. This suggests that nematicity may be the fluctuating order responsible for the quantum critical phenomena at this point. Consequently, nematicity may play a larger role in understanding the cuprate phase diagram that has been previously recognized, possibly

having a key role in the nature of the pseudogap phase or impacting the superconducting transition temperature. In this chapter, we investigated six Nd-LSCO samples and six Eu-LSCO samples at different Sr hole doping levels. Along with investigating the electronic nematic order via equilibrium RXS near the end of the pseudogap phase in Nd-LSCO and Eu-LSCO, we employ the tr-RXS to validate the vanishing signature of nematicity in overdoped $x = 0.24$ Eu-LSCO system slightly outside the pseudogap phase. Investigations of $x = 0.08$ Eu-LSCO via tr-RXS unveiled a saturated nematic phase that equilibrium RXS cannot detect. We also documented the CDW signal, and report that it vanishes beyond $x = 0.18$ which is in agreement with previous similar studies using other experimental probes. Possible scenarios for these observations include the existence of a zero-temperature nematic QCP and/or a nematic character to the pseudogap regime in this family (as suggested in Ref. [55]). This suggests that nematicity is associated with the pseudogap and may possibly be the fluctuating order responsible for the quantum critical phenomena near the pseudogap QCP. Consequently, nematicity may play a larger role in understanding the cuprate phase diagram that has been previously recognized, possibly having a key role in the nature of the pseudogap phase.

Chapter 7

Tuning charge order and nematicity in cuprates via uniaxial strain

This chapter has been adapted from Ref. [3], titled: Tuning charge density wave order and structure via uniaxial stress in a stripe-ordered cuprate superconductor.

7.1 Overview

Spin and charge density wave order in the cuprates are known to compete with superconductivity. In the stripe order $(La,M)_2CuO_4$ family of cuprates, spin and charge order occur as unidirectional order that can be stabilized by symmetry breaking structural distortions, such as the low temperature tetragonal (LTT) phase. Here we examine the interplay between structure and the formation of charge density wave (CDW) order in the LTT phase of $La_{1.475}Nd_{0.4}Sr_{0.125}CuO_4$ by applying uniaxial stress to distort the structure and influence the formation of CDW order. Using resonant soft x-ray scattering to measure both the CDW order and (0 0 1) structural-nematic Bragg peaks, we find that the application of uniaxial stress along the Cu-O bond direction suppresses the (0 0 1) peak and has the net effect of reducing CDW order, but does so only for CDW order propagating parallel to the applied stress. We connect these observations to previous work showing an enhanced superconducting transition temperature under uniaxial stress; providing insight into how CDW, superconductivity, nematicity, and structure are related and can be tuned relative to one another in cuprates.

7.2 Introduction

In the cuprate superconductors, spin and charge density wave orders [29, 31, 40], superconductivity and electronic nematic order [62, 64, 39, 66, 65] are intertwined, often co-existing and competing [11, 13, 69]. How these orders manifest and relate to each other depends on a number of factors including the doping, the level of disorder and the crystalline structure (tetragonal or orthorhombic, single layer or bilayer, lattice constants, etc). An approach to vary the crystalline structure, while keeping doping and disorder constant, is the application of uniaxial stress. Examination of the subsequent response of charge density wave (CDW), nematic, and superconductivity orders to uniaxial stress provides a powerful pathway to understand the relationship of these intertwined orders.

Application of uniaxial stress in the cuprates has been shown to result in significant changes in the superconducting transition temperature and spin or charge density wave orders [176, 177, 178, 179, 180, 107, 181, 182, 183, 184]. In the stripe-ordered cuprates $La_{1.74}Eu_{0.2}Sr_{0.16}CuO_4$ and $La_{1.48}Nd_{0.4}Sr_{0.12}CuO_4$, uniaxial stress applied in the *ab* plane enhances the superconducting transition temperature, T_C [177, 176]. More recent work in $La_{1.885}Ba_{0.115}CuO_4$ (LBCO), showed a similar enhancement of T_C, along with an accompanying suppression of magnetic order, as measured from muon spin rotation (μSR) spectroscopy [184, 179]. This result is indicative of a competition between magnetic order and superconductivity that can be tuned by uniaxial stress.

Other studies have examined the impact of uniaxial stress on charge density wave order. In $YBa_2Cu_3O_{6+x}$ (YBCO), $\sim$1% compressive uniaxial strain enhances (2D) CDW order and results in a unidirectional (3D) CDW order [180, 107]. An alternate approach in $YBa_2Cu_3O_{6+x}$ showed that tensile strain induced in thin films grown on an orthorhombic substrate results in a suppression of CDW order perpendicular to the strain [183]. However, in $La_{1.875}Sr_{0.125}CuO_4$ (LSCO), uniaxial stress was found to enhance CDW order propagating perpendicular to the applied stress and suppress CDW order propagating parallel to the applied stress [181, 185].

How uniaxial stress impacts CDW order depends on details of a materials crystals structure. For instance, in LSCO, the structure is in the low-temperature orthorhombic (LTO) phase, characterized by tilts of CuO_6 octahedra about an axis diagonal to the Cu-O bond. For unidirectional CDW order propagating approximately along [100] and [010] (parallel to the Cu-O bond), the structure does not establish a preferred direction, providing an opportunity for the formation of domains of both [100]- and [010]-oriented CDW order [186, 187]. Consequently, the application strain along [100] was interpreted to detwin the CDW order to favor only domains of unidirectional CDW order propagating along [100] for stress applied along [010] [181].

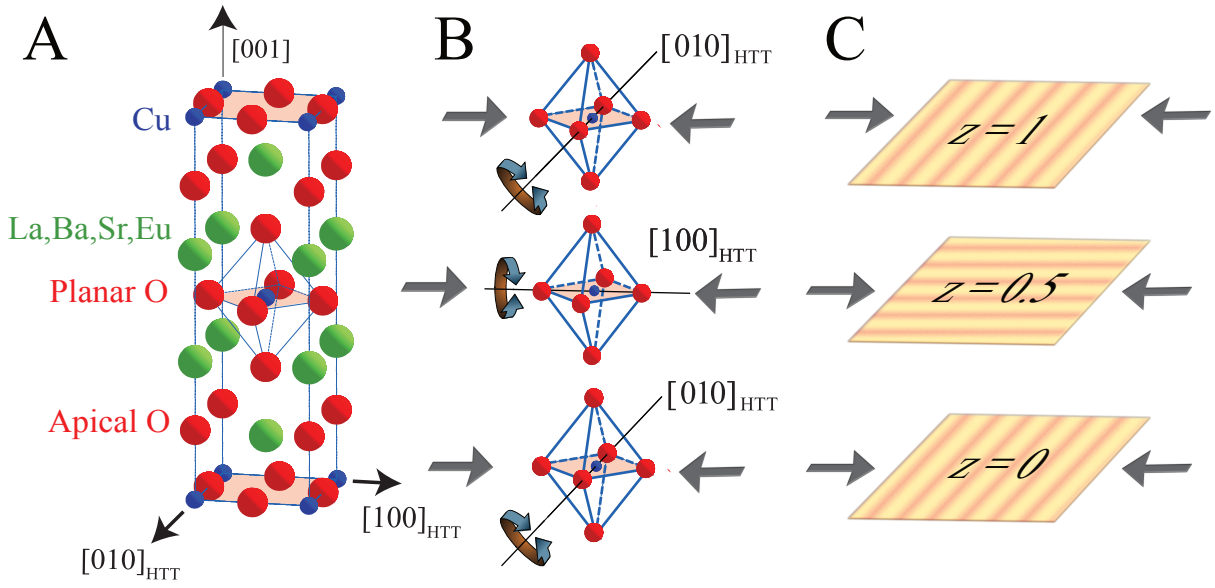


Figure 7.1: **A** The crystal structure of $(La,M)_2CuO_4$ in the high temperature tetragonal (HTT) phase. Two CuO_2 planes at $z = 0$ and $z = 0.5$ are present within a single unit cell. **B** In the low temperature tetragonal (LTT) phase CuO_6 octahedra tilt along the Cu-O bond direction, with the tilt axis alternating between a and b for neighbouring layers. Uniaxial stress along a will be parallel to the tilt axis for half the layers and perpendicular to the tilt axis for the other half of the layers. **C** The orientation of unidirectional stripe order alternates between neighbouring layers. Uniaxial stress along a will be parallel or perpendicular to the CDW propagation wavevector, depending on the layer.

However, in many stripe-ordered cuprates, the application of strain may play a different role than in LSCO. In $(La,M)_2CuO_4$ substituted with larger rare earth ions Nd, Eu or Ba, a low temperature tetragonal (LTT) phase can be induced that is characterized by octahedral tilt axes parallel to the Cu-O bonds [188, 189]. Numerous studies have recognized that the LTT structure stabilizes stripe order, with several compounds exhibiting stripe order to onset at the LTO to LTT phase transition [29, 156, 44]. The reason for this association is that the LTT structure, shown in Figure 1, induces anisotropy in the electronic structure, such as the hopping between Cu and O (t_{pd}), the nearest neighbour exchange interaction, J, or the charge transfer energy Δ_{pd} [72, 190]. This anisotropy is thought to stabilize unidirectional stripe order that, within an individual layer, is oriented parallel or perpendicular to the octahedral tilt axis. Importantly, although each individ-

ual layer breaks C_4 rotational symmetry due to the octahedral tilts, the axis by which the octahedra tilt rotates by 90° between neighbouring CuO_2 planes such that the crystal structure remains tetragonal, as depicted in Figure 1B. Consequently, unidirectional spin and charge order in neighbouring layers alternates between propagating along [100] and [010] [29, 191], as depicted in Figure 1C.

Unlike in LSCO without Nd, Eu or Ba substitution, the structural distortion of the LTT phase serves to detwin the CDW order within an individual layer. As such, the application of uniaxial stress may be used to explore the role of anisotropy of the electronic structure on CDW order, rather than the balance of population of [100] and [010] domains within a layer. As shown in Figure 7.1, the application of a uniaxial stress along the [100] direction will act along the tilt axis for half of the layers and perpendicular to the tilt axis for the other half of the layers, affecting the anisotropy of the electronic structure differently for the two orientations of layers.

7.3 Uniaxial Strain Device

Using a custom uniaxial stress device as described in Figure 7.3, uniaxial stress was applied parallel to [100] axis of the high-temperature tetragonal (HTT) unit cell. The sample was measured both unstrained and with applied uniaxial stress. The magnitude of the applied stress imparted to the sample is not characterized in the device. However, the maximum strain is estimated to be of less than 0.2% and the stress less than < 0.5 GPa. With applied stress, the CDW Bragg peaks were measured for CDW order propagating both parallel and perpendicular to the applied stress.

7.3.1 Experimental Procedure

Resonant x-ray scattering measurements were performed at the REIXS beamline at the Canadian Light Source [192], on a sample of $La_{1.475}Nd_{0.4}Sr_{0.125}CuO_4$, fragments of which have been studied in past reports of x-ray absorption spectroscopy [193] and resonant x-ray scattering [28, 39]. The CDW (-0.24 0 1.5) and (0 -0.24 1.5) Bragg peaks were investigated at a photon energy corresponding to the peak of the Cu-L_3 absorption edge (931.3 eV). Note, measurements of the CDW peaks are shown as raw data, normalized only to the incident beam intensity, but otherwise free of any background subtraction. In addition, to examine the LTO to LTT structural phase transition, we measured the (0 0 1) Bragg peak beak at the Cu-L edge (931.3 eV) and at an energy associated with the apical oxygen

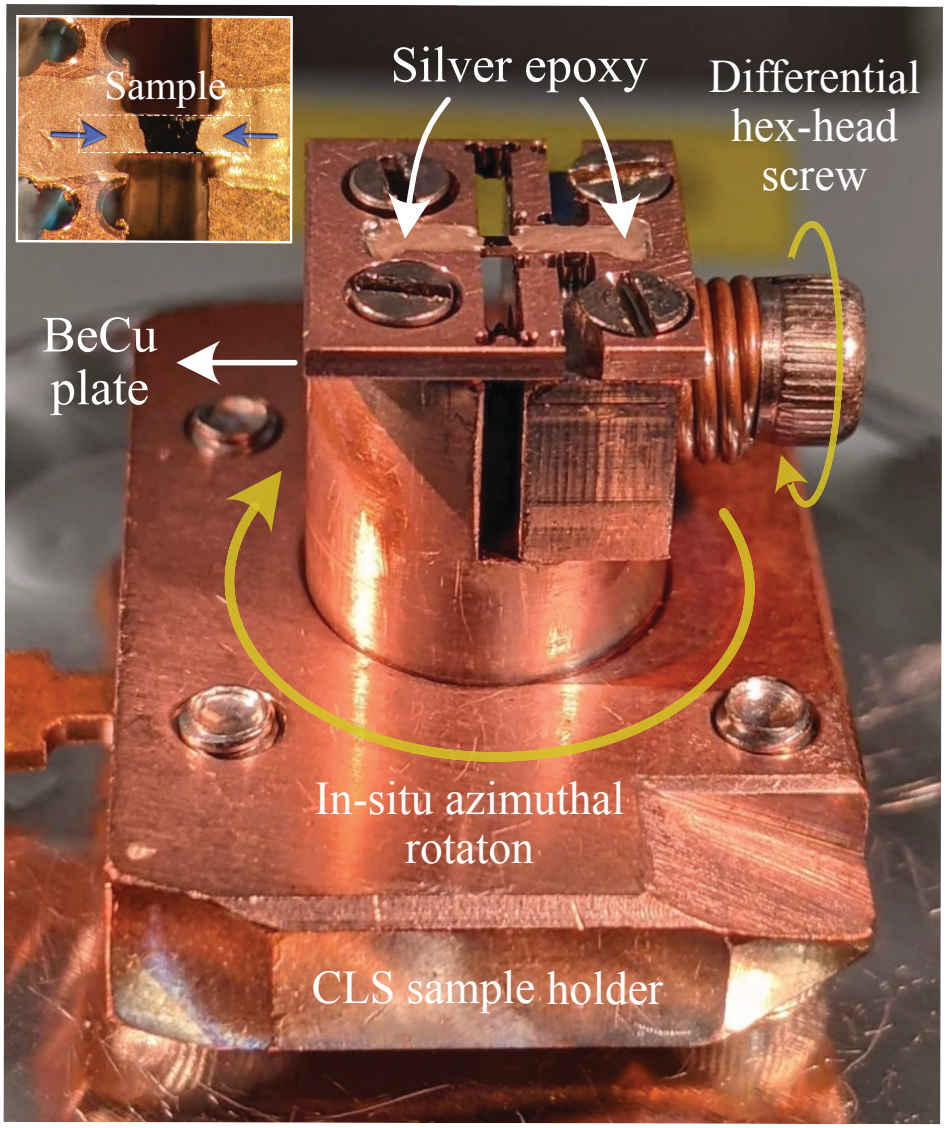


Figure 7.2: Schematic of the uniaxial stress device. Rotation of a differential screw is used to apply uniaxial stress to a sample that is mounted to a BeCu plate. The device can be actuated in vacuum and at low temperatures in order to change the applied stress or to rotate the device azimuthally to orient the strain parallel or perpendicular to the horizontal scattering plane of the diffractometer. The sample shown in the inset is set in position using silver epoxy.

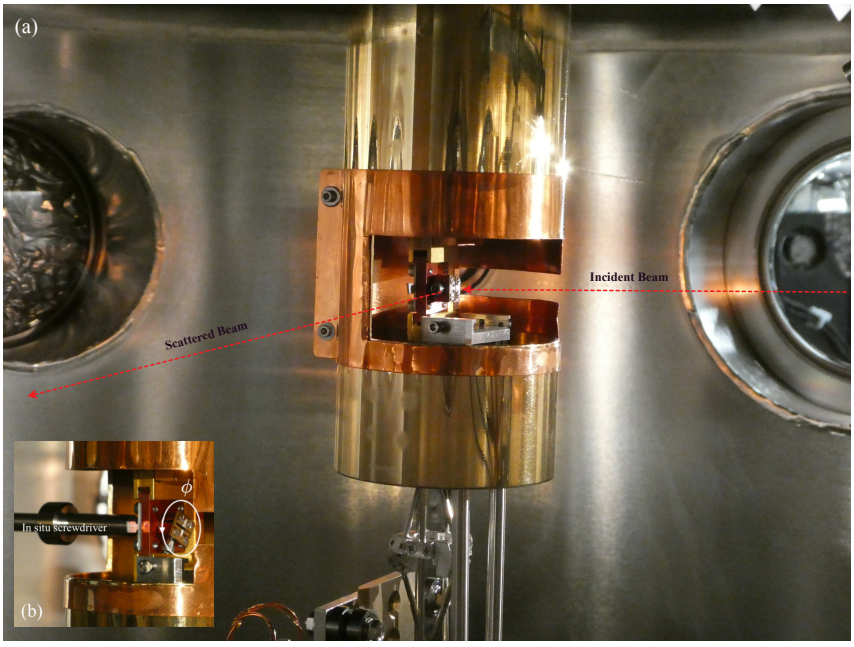


Figure 7.3: Uniaxial stress device in CLS scattering chamber: View from the RSXS chamber's window showing the uniaxial stress device with the sample mounted. (b) The screw at the base of the device — can be rotated with an in situ screwdrives — provides the azimuthal degree of freedom, allowing under strain switching between (h 0 ℓ) and (0 k ℓ) Bragg peaks.

(533.3 eV). The sample was orientated by measuring the (0 0 4), (-1 0 3) and (0 -1 3) structural Bragg peaks at 2200 eV, with all Bragg peaks indexed to the high temperature tetragonal phase.

The sample was cut and polished to form a rectangular *ab* face sample of dimensions 2 x 0.5 x 0.2 mm. Unixial stress was applied parallel to the longest axis of the sample, which is oriented parallel to [100]. Subsequent to polishing, the sample's surface was etched with bromine. The application of uniaxial stress was applied by mounting the sample on a custom mechanically-actuated stage, depicted in Figure S1. The sample is mounted on a BeCu plate that has been machined with notch flexures to enable motion along a single axis, but provide a degree of stiffness to bending or tilting. The sample is positioned in a groove in the BeCu plate, with the edges encapsulated above and below with EPO-TEK H2OE silver epoxy in an effort to apply uniform stress. The BeCu plate is affixed to two Cu blocks that can be translated relative to one another by actuating a differential screw that

enables small controlled displacements between the plates, resulting in uniaxial compressive or tensile stress on the sample. A novel feature of the strain device is the capability to rotate the device azimuthally under stress, in-vacuum and at low temperature in order to orient the direction of the applied stress either parallel or perpendicular to the scattering plane of the diffractometer. As such, stress can be applied to the sample along the a-axis and CDW peaks can be investigated along both (-0.24 0 1.5) and (0 -0.24 1.5) without needing to thermally cycle or remount the sample.

7.3.2 Measuring strain via structural Bragg peak displacements

Unfortunately, our device does not apriori measure the magnitude of the applied stress. However, by measuring the structural Bragg peaks before and after the application of uniaxial stress, we can identify that the peak positions do not shift by amounts larger than the accuracy of our measurements. This limits the in-plane (or c-axis) compressive strain to be less than 0.2%. Given the $C_{11} = 267$ GPa in related materials [194], this strain limit corresponds to an uniaxial stress along [100] of < 0.5 GPa.

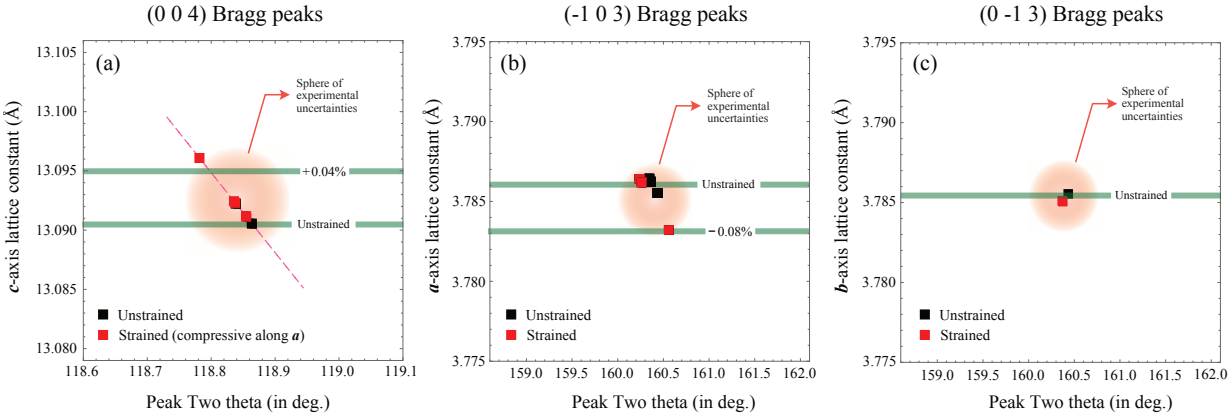


Figure 7.4: Characterizing strain percentage with [100] uniaxial strain: From the shifting of (0 0 4), (-1 0 3) and (0 -1 3) structural Bragg peaks at 2200 eV. Our determination of the upper limit of compressive uniaxial strain comes out to be 0.2%, based on our observation that Bragg peaks do not shift by amounts larger than the accuracy of our measurements. Panel (c) corroborates the uniaxial character of the applied strain.

7.4 Results

In this study we utilize resonant soft x-ray scattering to study the impact of uniaxial strain on both the structural phase transition and the CDW order in $La_{1.475}Nd_{0.4}Sr_{0.125}CuO_4$ (LNSCO). We find that the application of stress along [100] reduces the intensity of the CDW peak at $Q_{CDW} = (-0.24\ 0\ 1.5)$ by a factor of ~ 2, while having little impact on its correlation length or temperature dependence. In contrast, the applied [100] stress has only modest impact on the intensity of the CDW peak at $(0\ -0.24\ 1.5)$. The overall suppression of CDW order due to uniaxial stress is consistent with competition between CDW order and superconductivity. More specifically, uniaxial stress along [100] modifies the anisotropy of the electronic structure in a manner that suppresses CDW order, and thus in turn enables the enhancement of the superconducting transition temperature [177, 179, 184].

Resonant x-ray scattering measurements presented in this study were performed on a cut, polished cuboidal sample of $La_{1.475}Nd_{0.4}Sr_{0.125}CuO_4$. The CDW $(-0.24\ 0\ 1.5)$ and $(0\ -0.24\ 1.5)$ Bragg peaks were investigated at a photon energy corresponding to the peak of the Cu-L_3 absorption edge (931.3 eV). Note, measurements of the CDW peaks are shown as raw data, normalized only to the incident beam intensity, but otherwise free of any background subtraction. Measurements were found to be reproducible to an accuracy of $\sim 2\%$ of the total signal. In addition, to examine the LTO to LTT structural phase transition, we measured the (0 0 1) Bragg peak beak at the Cu-L edge (931.3 eV) and at an energy associated with the apical oxygen (533.3 eV).

First we examine the impact of uniaxial stress on the structure. As shown in Figure 2, the temperature dependence of the (0 0 1) peak measured at the apical O-K edge in an unstrained configuration, exhibits a sharp transition to the LTT phase at 70 K, consistent with previous unstrained measurements on this sample [39, 2]. The application of stress along [100] results in a decrease in the (0 0 1) peak intensity at low temperatures, as well as, a more gradual temperature dependence, indicating a change in the structure under uniaxial stress. Details of the structural changes induced by uniaxial stress cannot be fully resolved by measuring a single Bragg peak. However, since the (0 0 1) peak results from a difference in the orbital symmetry of apical O atoms between neighbouring $(La,M)_2O_2$ layers [36, 38, 39], the more gradual temperature dependence of the (0 0 1) peak under applied stress is understood to be associated with a reduction in the difference in orbital symmetry between neighbouring layers. This reduction may result from changes in the angles by which CuO_6 octahedra tilt out of the ab plane and/or changes in the octahedral tilt axis away from the Cu-O bond direction.

Notably, the strain dependence of the (0 0 1) Bragg peak in Figure 2 is in qualitative agreement with recent reports hard x-ray scattering study of the LTO-LTT transition

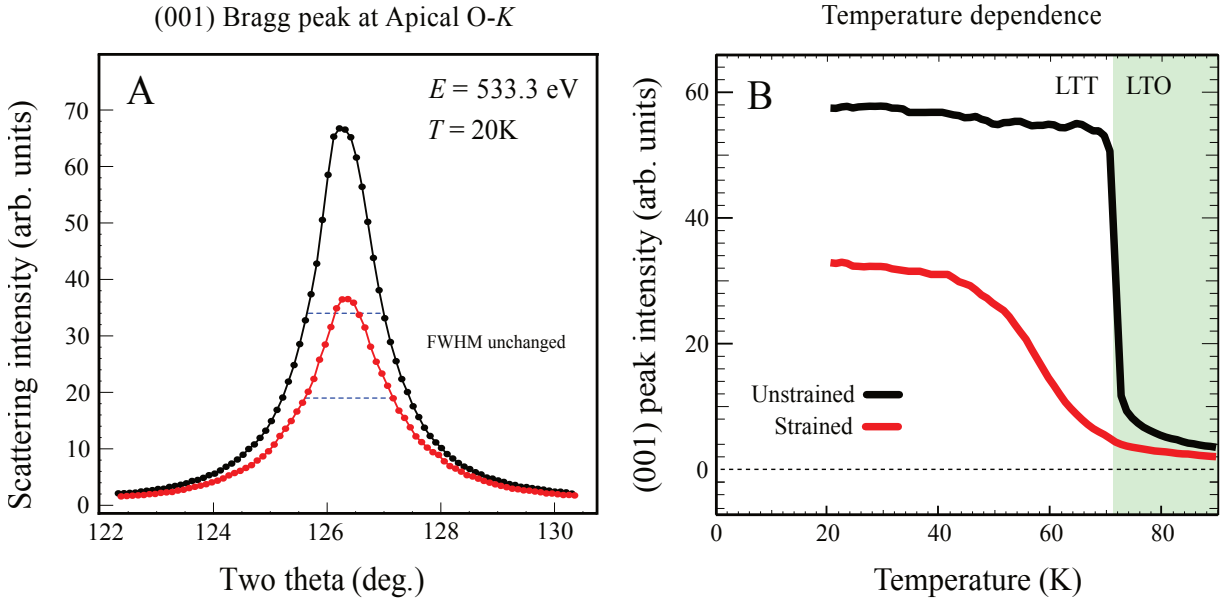


Figure 7.5: Temperature dependence of the (0 0 1) Bragg peak at apical O-K edge under varying strain (increasing as shown by an arrow). Scattering intensity is normalized at 20 K. The inset shows a theta-2theta scan of the (0 0 1) Bragg peak on-resonance at the apical O-K edge, comparing the strained (red) and the unstrained (black) case. Notably, the peak intensity drops upon applying uniaxial stress. The green-shaded region (above 70 K) depicts the LTO phase in the unstrained case.

under unaxial stress in another stripe-ordered cuprate $La_{1.885}Ba_{0.115}CuO_4$ [184], albeit with stress applied along [110] instead of along [100]. In that study, Guguchia *et al.* [184] show the LTT transition to be completely suppressed for compressive uniaxial stress above $\sigma_{[110]}$ ∼0.06 GPa. However, for lower stress values ($\sigma_{[110]}$ ∼0.017 GPa), the LTT phase remains, but with the LTT Bragg peak intensity suppressed, the onset temperature only weakly dependent on stress, and the LTO-LTT transition broadened [184], qualitatively similar to the dependence on uniaxial stress dependence of the (0 0 1) we observe in LNSCO for stress applied along [100] in the range of pressure applied.

In figure 3, we show the impact of uniaxial stress on CDW order. When the sample is unstrained, we observe comparable peak intensities for the (−0.24 0 1.5) and (0 −0.24 1.5) peaks. The response of CDW order to uniaxial stress, however, is asymmetric. Whereas uniaxial stress along [100] reduces the intensity of the (−0.24 0 1.5) Bragg peak by a factor of ∼ 2 at 20 K, this same stress has minimal impact on the intensity of the (0 −0.24 1.5)

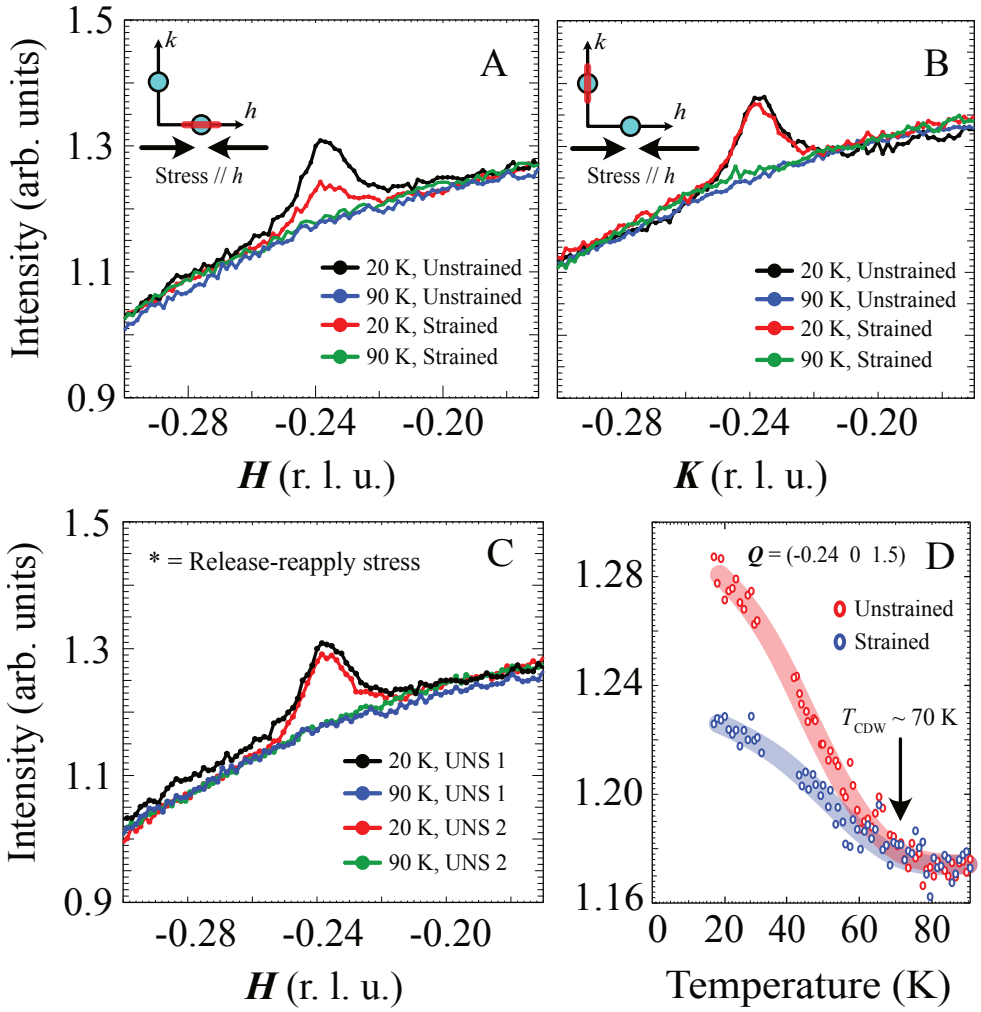


Figure 7.6: Response of CDW Bragg peaks to applied uniaxial stress along [100]. **A**) and **B**) Intensity at 20 K and at 90 K, above the CDW ordering temperature, for the unstrained and strained case. In **A**) measurements are shown through the Bragg peak (−0.24 0 1.5) peak position, corresponding to CDW order propagating parallel to the applied stress. In **B** measurements are shown through the Bragg peak (0 −0.24 1.5) peak position, corresponding to CDW order propagating perpendicular to the applied stress. **C**) Measurements through (−0.24 0 1.5) in the unstrained configuration, before (UNS 1) and after releasing (UNS 2) applied stress to the sample. **D**) The temperature dependence at (−0.24 0 1.5) with and before strain (UNS1). The onset temperature of the CDW order is similar in the strained and unstrained configurations. All panels show raw data.

Bragg peak. Moreover, although the intensity of the $(-0.24\ 0\ 1.5)$ peak decreases with the application of stress, the width of the Bragg peak, associated with the CDW correlation length along the a-axis, is unaffected.

In both cases, the application of uniaxial stress does not change the background measured at 90 K, which is dominated by x-ray fluorescence from the sample. Charge density fluctuations at high temperatures, as have been reported in other studies [195, 182], may also occur but cannot be resolved unambiguously in this set of measurements.

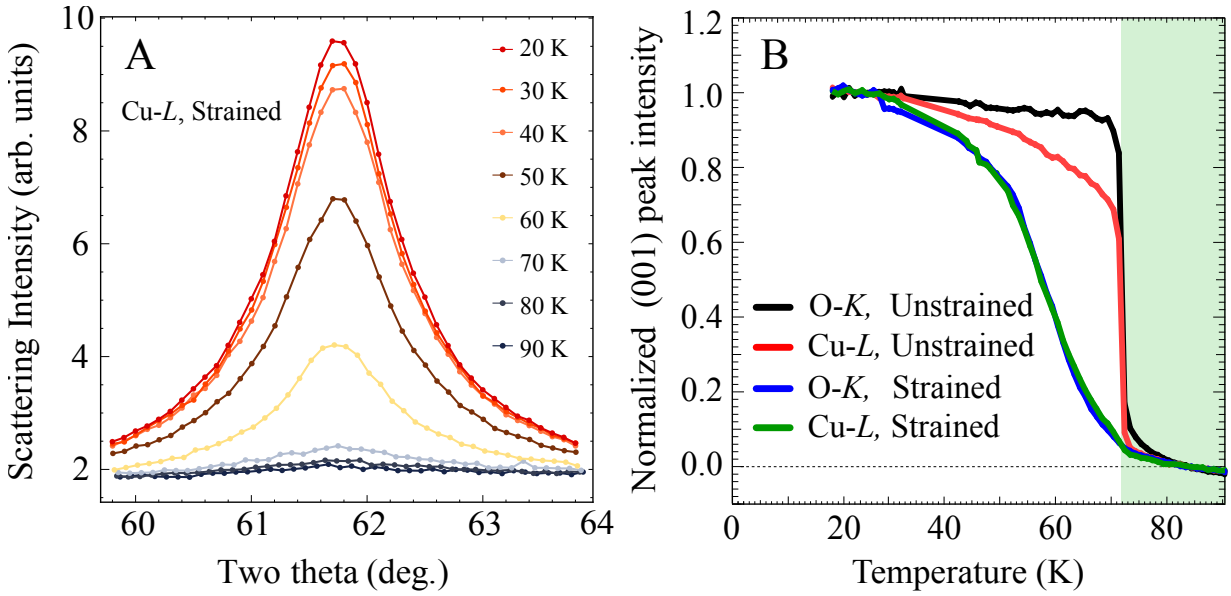


Figure 7.7: Temperature dependence of the structural-nematic (0 0 1) Bragg peaks for planar and apical atoms. **A** Temperature evolution of the theta-2theta scans of the (0 0 1) Bragg peak at the Cu-L edge under in-plane, compressive uniaxial stress. **B** Comparison of temperature dependence of the (0 0 1) peak measured at the Cu-L (931.3 eV) and apical O-K edge (533.3 eV) energies for unstrained and strained case. Scattering intensity is normalized at 20 K. The temperature evolution of the (0 0 1) peak at the two energies differs in the unstrained case [39], but evolves similarly under uniaxial stress.

The temperature dependence of the intensity at $(-0.24\ 0\ 1.5)$ in strained and unstrained configurations is shown in Figure 3D. This shows that the onset temperature is not strongly impacted by strain (we are unable to clearly resolve a change in T_{CDW}), with the main impact of strain being the reduction in peak intensity in the region where CDW order exists.

To verify that the strain-induced suppression in the (−0.24 0 1.5) peak intensity is not associated with an irreversible degradation of the sample (cracking, buckling, etc.) upon straining, we released the stress and remeasured the sample in an unstrained configuration (UNS 2). These measurements show a recovery of the original CDW peak intensity (see UNS 1 in Figure 3C), as well as a recovery of the (0 0 1) peak temperature dependence.

Notably, our results with uniaxial compressive stress differ from reported measurements in LNSCO with uniaxial tensile stress by Boyle *et al.* [182]. They also observe a reduction in the CDW peak intensity at low T under stress. However, where we find T_{LTT} and T_{CDW} are unchanged by the compressive stress we applied, they report that a tensile strain of $\varepsilon_a = +0.046 \pm 0.026\%$ reduced both T_{CDW} and T_{LTT} by 29 K. Moreover, they do not observe an appreciable broadening of the LTT transition or reduction in the (0 0 1) peak intensity at low temperatures, as we observed in our study. This may indicate a marked difference in the impact of tensile versus compressive stress or in the magnitudes of stress applied in the two studies, warranting further investigation.

The compressive stress dependence observed in our study is also in contrast to that of reports in LSCO, where CDW order occurs within the LTO structural phase. In LSCO, CDW propagating along the a and b axes would be degenerate in an unstrained crystal, giving rise to domains of unidirectional CDW order that run along both a and b within an individual layer [181]. As such, even a small uniaxial strain along a or b can break the degeneracy, detwinning the CDW such that only a or b oriented CDW order occur, consistent with the measurements of Choi *et al.* [181]. Notably, in LSCO application of strain beyond that required to detwin the CDW order did not further enhance the CDW order [181]. Connecting the observations to our results in LNSCO, the application of uniaxial strain here does not have a similar effect of detwinning CDW order – enhancing CDW order along b and suppressing CDW order along a. This is likely due to octahedral tilts along a and b in the LTT structure already being effective at detwinning the CDW order within individual layers.

In our study, uniaxial stress modifies the octahedral distortions characteristic of the LTT phase, which subsequently impacts the in-plane anisotropy of the electronic structure within an individual layer, such as the nearest-neighbour hopping and exchange interactions. This change in the electronic anisotropy, in turn, can affect the amplitude of CDW order. Structural refinements of CDW order in the LTT phase of LBCO have identified that CDW order within an individual layer propagates along a direction parallel to the bent O-Cu-O bonds as depicted in Figure 1 [191]. While it is not clear how the electronic anisotropy of the individual layers changes in response to anisotropic strain, one might expect that the electronic anisotropy increases for the layers with the applied stress parallel to the straight O-Cu-O bonds and decreases for layers with the applied stress perpendicular

to the straight O-Cu-O bonds. If this is indeed the case, our findings of a suppression of CDW order along H (parallel to the applied stress) indicate that a reduction in electronic anisotropy of a layer results in a reduction of CDW order, but the converse need not be the case.

Ultimately, the net effect of applying uniaxial stress along the Cu-O bond direction is to suppress CDW order. This is in accordance with observed increases in the superconducting transition temperature by applying stress in the [100] direction in LNSCO [177] and related systems $La_{1.65}Eu_{0.2}Sr_{0.15}CuO_4$ [177] and $La_{1.885}Ba_{0.115}CuO_4$ [179] that share the LTT structure with LNSCO. As such, at least part of the increase in T_c may be attributed to the competition of CDW order with superconductivity. Namely, uniaxial stress affects the anisotropy of the electronic structure in a manner that suppresses CDW order, resulting in an enhancement of superconductivity.

In addition to investigating CDW order, we also probe the $Q_x = Q_y = 0$ electronic anisotropy by measuring the temperature dependence of the (0 0 1) Bragg peak under uniaxial strain at the Cu-L edge, in addition to O-K edge (at an energy corresponding to apical oxygen).[39, 2, 1] As shown in Figure 4, the temperature dependence of the (0 0 1) peak intensity is different and more gradual when measured at the Cu-L relative to the O-K edge, consistent with previous studies without strain [39, 2]. However, uniaxial stress appears to eliminate this difference in the T dependence.

Achkar *et al.* [39] argued that this difference in temperature dependence is due to electronic nematic order that is coupled to CDW order and is in addition electronic asymmetry that directly results from the structure distortions. Moreover, although the (0 0 1) peak measures the difference in orbital symmetry between neighbouring layers, in the unstrained case the symmetry of the crystal structure is such that this difference in the interlayer orbital asymmetry maps to a measure of nematicity within a single layer. However, because of the inequivalence of neighbouring layers under anisotropic strain, this mapping is not valid, complicating the interpretation of the (0 0 1) peak T-dependence under uniaxial stress.

The lack of a difference in the T-dependence between Cu-L and apical O-K measurements may indicate that uniaxial stress suppresses electronic nematic order within individual layers. However, it may also indicate that nematic order remains strong and is perhaps saturated. In this scenario, uniaxial stress may align electronic nematic order between neighbouring layers, such that signatures of it cancel in measurements of the (0 0 1) Bragg peak. Future work will be required to differentiate the origin of this anomalous result.

7.5 Uniaxial stress along [110] direction

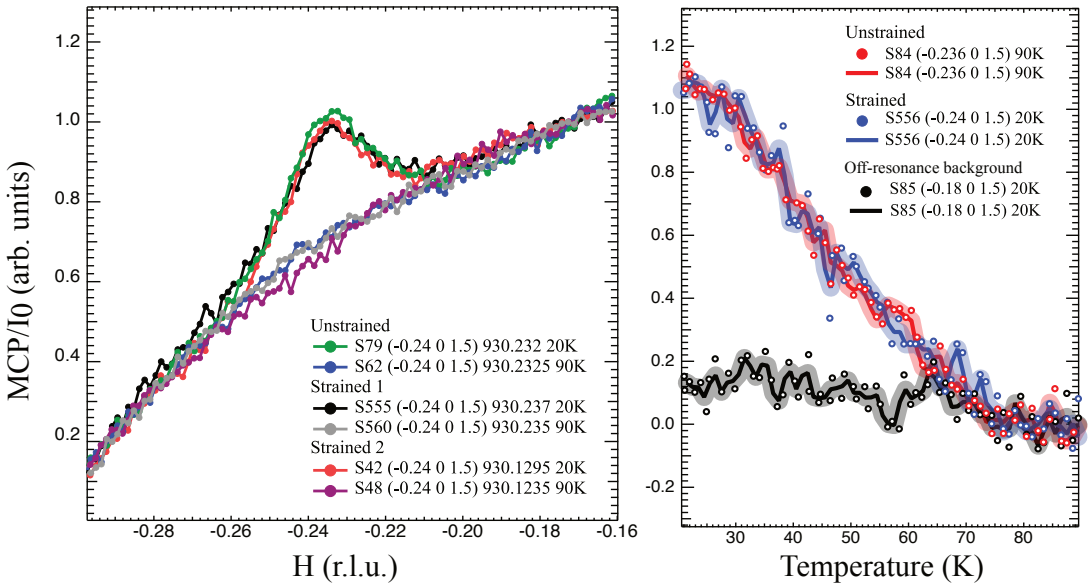


Figure 7.8: Response of CDW Bragg peaks to applied uniaxial stress along [110]. On left, we measure intensity at 20 K and at 90 K, above the CDW ordering temperature, for the unstrained and strained case. On right, the temperature dependence at $(-0.24\ 0\ 1.5)$ with and without strain. The onset temperature of the CDW order is similar in the strained and unstrained configurations.

Application of uniaxial strain applied along different crystallographic directions ([110] vs. [100] vs. [001]) can provide insights into the formation of CDW order and how its properties (correlation length, strength, periodicity, ...) may differ in the different cuprate material systems [177, 182, 184]. Strain along [110] vs. [100] may have the opposite effect – suppressing CDW order and enhancing CDW order respectively. For instance, previous work by Takeshita et al. [177] on the impact of uniaxial strain on superconductivity in $La_{1.64}Eu_{0.2}Sr_{0.16}CuO_4$ (Eu-LSCO) exhibited a pronounced anisotropy in the uniaxial strain effect – not only between in-plane and out-of-plane pressures but also within the tetragonal CuO_2 plane. They find that pressure applied along the [110] direction yielded a significant response, whereas pressure along the [100] direction produced negligible changes in T_c [177]. This in-plane anisotropy was attributed to a strong correlation between the symmetry of one-dimensional stripes and the strain symmetry induced within the CuO_2 plane.

Along with the [100]-strain direction results presented in this chapter, we also performed compressive uniaxial strain experiments along the [110] crystallographic direction in $La_{1.475}Nd_{0.4}Sr_{0.125}CuO_4$ (Nd-LSCO). We detect minimal or no changes in CDW order with response to strain along the Cu–Cu bond direction, suggesting a potential role of stripe orientation in the stabilizing of charge and orbital textures in La-based cuprates.

7.6 Conclusion

In conclusion, we find that in $La_{1.475}Nd_{0.4}Sr_{0.125}CuO_4$, uniaxial stress along [100] suppresses the magnitude of CDW order parallel to the applied stress, but has little impact on CDW order propagating perpendicular to the applied stress. We attribute this suppression to modification of the electronic asymmetry within the CuO_2 planes rather than a detwinning of CDW order, seen in LSCO. Signatures of nematic order, as observed via the relative temperature dependence of the (0 0 1) peak at the Cu-L edge and O-K edge, are also observed to be suppressed by uniaxial strain. This suppression of CDW order is likely linked to the enhancement of superconductivity under uniaxial stress along [100] direction.

7.7 X-ray absorption under uniaxial stress

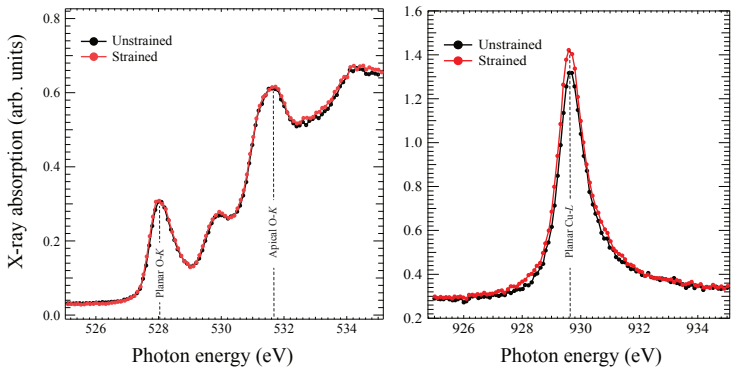


Figure 7.9: The X-ray absorption spectra remains robust under compressive uniaxial stress. This plot serves as benchmark for no odd features or shifts in resonance energies that are introduced upon applying strain.

Chapter 8

Anisotropic Spin Stripe Domains in Bilayer $La_3Ni_2O_7$

This chapter has been adapted, modified from Ref. [4], titled: Anisotropic Spin Stripe Domains in Bilayer $La_3Ni_2O_7$.

8.1 Overview

High temperature superconductivity ($T_C = 80$ K) has recently been identified in $La_3Ni_2O_7$ under hydrostatic pressure, setting of a search for magnetic order that may play a role in driving the superconductivity similar to other high temperature superconductors. To this end, spin density wave (SDW) order with a (1/4 1/4) wavevector was detected below 150 K at ambient pressure. However, key details about the nature of the SDW order are not yet known. In this study we probe the (1/4 1/4) SDW order in thin films of bilayer $La_3Ni_2O_7$ using polarization-dependent resonant soft x-ray scattering. We show that, unlike other nickelates, $La_3Ni_2O_7$ does not exhibit signatures of strong charge-disproportionation or CDW order. We also characterize the magnetic structure, showing that the magnetic moments of the SDW order orient within the NiO planes and perpendicular to Q_{SDW}, forming unidirectional spin stripes similar to FeTe. These spin stripes form in two sets of anisotropic, orthogonal spin domains that have shorter correlation lengths perpendicular to Q_{SDW} ($\xi_\perp = 134$ Å) versus parallel to Q_{SDW} ($\xi_{//} = 293$ Å), indicating that hidden nanoscale rotational symmetry breaking is a key feature of the SDW order. Finally, we develop a novel approach to probe defects of this magnetic order which we interpret as Bloch-like anti-ferromagnetic domain walls.

8.2 Introduction

The discovery of superconductivity with a transition temperature (T_c) above 80 K under hydrostatic pressure has ignited intense interest [196] in $La_3Ni_2O_7$ as a new platform to compare against the Cu- and Fe-based superconductors to understand which common ingredients are essential for realizing high T_c's. In both the cuprates and Fe-based families, parent antiferromagnetic states as well as nematicity are both known to play critical roles in their phase diagrams, the detailed understandings of which are essential for developing microscopic models. Presently, our understanding of the parent state from which the superconductivity condenses in $La_3Ni_2O_7$ remains incomplete. Recent resonant inelastic x-ray scattering (RIXS) [197], heat capacity and magnetic susceptibility [198, 199], nuclear magnetic resonance (NMR)[200, 201] and μSR [202, 203] measurements of bulk $La_3Ni_2O_7$ suggest the presence of a spin density wave (SDW) transition occurring around $T_{SDW} \approx 150$ K, with a wavevector of $(H = \frac{1}{4}, K = \frac{1}{4})$ deduced from RIXS.[197] However, essential information regarding the microscopic spin structure and orientation remains unresolved.

Here, we present detailed resonant soft x-ray scattering (RSXS) and polarimetry measurements on epitaxial thin films of bilayer $La_3Ni_2O_7$ which reveal that the detailed spin structure consists of equal domains of bicollinear spin stripes, with the spins lying in the NiO_2 plane and aligned perpendicular to the SDW wavevector. Temperature-dependent spectroscopic measurements support a scenario with only a single electronic Ni site, with no evidence for charge or bond disproportionation across T_{SDW}, and where the oxygen ligand holes are strongly hybridized with the Ni d orbitals. The SDW domains exhibit a surprising anisotropy in their correlation lengths parallel versus perpendicular to their wavevector, suggesting that nanoscale rotational symmetry breaking might also play an important role in $La_3Ni_2O_7$, reminiscent of the nematic order found in the cuprates and Fe-based superconductors. Finally, a detailed polarization and temperature-dependent analysis of the SDW Bragg peaks suggests the presence of extended, Bloch-like domain walls between orthogonal domains.

One of the challenges of investigating $La_3Ni_2O_7$ is the recent discovery of multiple structural polymorphs, including the expected $n = 2$ Ruddlesden-Popper structure comprised of bilayers of NiO_6 octahedra (dubbed "2222"), and a surprising naturally-formed superlattice of alternating single-layer and trilayer blocks of NiO_6 octahedra (dubbed "1313") [204, 205]. It is plausible that both polymorphs could exist within a single macroscopic bulk crystal sample, and both structures have been reported to be the superconducting phase [205]. Layer-by-layer reactive oxide molecular beam epitaxy (MBE) synthesis of thin films offers a solution to addressing this polymorphism. Here, we focus our investigation on phase-pure epitaxial thin films of the bilayer "2222" polymorph of $La_3Ni_2O_7$. Epitaxial

thin films of 16 nm thickness were grown on $NdGaO_3$ (110) substrates using reactive oxide molecular beam epitaxy with shuttered deposition at a pressure of 8 $\times 10^{-7}$ torr of 80 % distilled ozone and a temperature of 800° C. Samples were characterized by lab-based x-ray diffraction, electrical transport, and synchrotron-based hard x-ray diffraction. Multiple samples were synthesized and investigated and all exhibited qualitatively similar behaviors; data from two samples are shown in this manuscript.

In Figure 8.1b, we show RSXS measurements on the Ni L_3 edge in π-polarization along the $(1, 1, 1.85)$ direction for a series of temperatures. Here, we employ the pseudo-tetragonal lattice constants of $a = b = 3.84$ Å and $c = 20.44$ Å. Below 160 K, a sharp peak emerges at $(\frac{1}{4}, \frac{1}{4})$ whose intensity is approximately 45 times stronger in π versus σ polarization at 20 K, suggesting that the scattering originates from magnetic rather than charge ordering, consistent with previous measurements.[197] The resonance energy dependence of the peak at $(\frac{1}{4}, \frac{1}{4}, 1.86)$ is shown in Fig. 8.1c, together with the x-ray absorption spectrum (XAS), which demonstrates that the $(\frac{1}{4}, \frac{1}{4})$ Bragg peak is peaked only at the Ni L resonances, and not on the La M_4 edge or off-resonance. In Figure 8.1f, we show a scan as a function of L at the in-plane $(\frac{1}{4}, \frac{1}{4})$ wavevector on the Ni L_2 edge, corrected for absorption and geometric factors. The data indicate that the SDW Bragg peak is peaked at $L = 2$, but with only a 14 ± 4 Å correlation length along the c-direction, revealing the highly two-dimensional nature of the magnetic order in $La_3Ni_2O_7$. We note that both the resonance energy and L dependence of $(\frac{1}{4}, \frac{1}{4})$ SDW Bragg peak clearly establish that the SDW intrinsically originates from $La_3Ni_2O_7$ and not an impurity phase, as has plagued the identification of ostensible charge or spin density order in other related nickelates.[206, 207]

In most related nickelates in the Ruddlesden-Popper sequence, including $n = 1$ $La_{2-x}Sr_xNiO_4$ and $n = \infty$ perovskite $RENiO_3$ (RE = Nd, Pr, Sm), SDW order coincides with strong charge or bond disproportionation, where the local electronic and orbital environment of the Ni sites is strongly modulated at an atomic scale. Whether such behavior also occurs in $La_3Ni_2O_7$ remains an important open question that can be addressed by resonant x-ray diffraction and spectroscopy. First, there are no distinct changes in the Ni L edge XAS spectra across T_{SDW} (Figure 8.1e), unlike the situation of $RENiO_3$ where bond disproportionation results in spectroscopically distinct Ni sites in the Ni L edge XAS across the metal-insulator transition. [208, 209, 210] Second, a strongly varying charge density will also modulate the x-ray scattering form factors on the different Ni sites, resulting in the linear dichroism of the SDW peak intensity (σ versus π polarization) becoming energy dependent, as reported in $RENiO_3$ heterostructures [211]. In contrast, we find that the linear dichroism of the $(\frac{1}{4}, \frac{1}{4})$ peak in $La_3Ni_2O_7$ does not exhibit any observable energy dependence (Figure 8.1d), suggesting that only a single magnetic Ni site exists in the SDW state. These spectroscopic observations are consistent with transport and thermodynamic

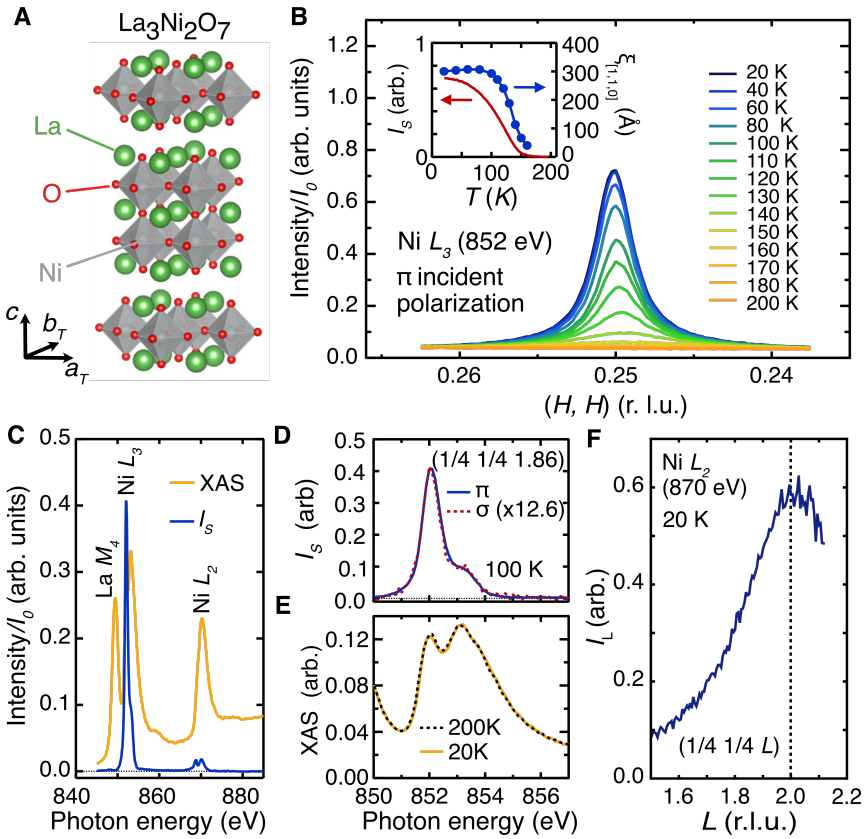


Figure 8.1: (**A**) The crystal structure of $La_3Ni_2O_7$, with the pseudo tetragonal axes a_T and b_T denoting the in plane NiO bond directions. (**B**) The $(\frac{1}{4}, \frac{1}{4}, 1.86)$ SDW as various temperatures measured at the Ni L_3 absorption edge with π incident polarization for sample A. Inset: The SDW peak amplitude (red) and correlation length along the [1 1] direction (blue) as a function of temperature. (**C**) The energy dependence of the $(\frac{1}{4}, \frac{1}{4}, 1.86)$ SDW peak amplitude through the Ni L and La M edges (blue), along with the x-ray absorption measured via partial fluorescence yield (orange). The scattering is peaked at the Ni L resonances, but is absent off resonance or at the La M_4 resonance. (**D**) The energy dependence of the $(\frac{1}{4}, \frac{1}{4}, 1.86)$ peak amplitude at the Ni L_3 edge with σ and π incident light. (**E**) The Ni L_3 x-ray absorption measured using partial fluorescence yield (PFY) at base temperature (20 K) and above the SDW phase transition (200 K). (**F**) The L dependence of the scattering cross-section, I_L of the $(\frac{1}{4}, \frac{1}{4}, L)$ peak at the Ni L_2 edge (870 eV) for sample B.

measurements which exhibit only weak anomalies across T_{SDW}, indicating that the dominant order parameter is magnetic and that unlike many other nickelates, any associated charge modulation is either weak or absent.

8.3 Measurement of Spin Configuration

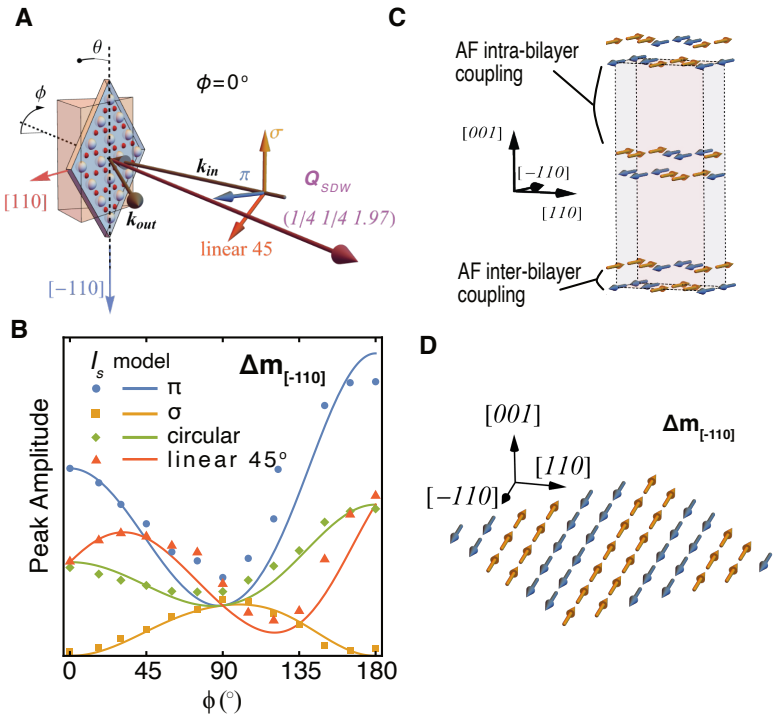


Figure 8.2: (**A**) The measurement geometry for azimuthal angle (ϕ) dependent measurements. The sample is mounted on a 43.7 deg wedge to align the $[\frac{1}{4}, \frac{1}{4}, 1.93]$ set of planes with the azimuthal rotation axis. The incident photon polarization is set to be σ, π, linear 45° ($\pi - \sigma$) or circular. The sample was rocked about the vertical axis by angle θ to measure the intensity and width of the $(\frac{1}{4}, \frac{1}{4}, 1.93)$ SDW peak. (**B**) The SDW peak amplitude, I_S versus ϕ for π, σ, circular and linear 45° incident polarization. Solid lines are the ϕ dependence calculated for a magnetic structure with $\Delta\vec{m}$ parallel to [−110], depicted in (**D**). (**C**) The 3D magnetic unit cell deduced from the azimuthal angle dependence and assuming anti-ferromagnetic bilayer coupling.

Here, we use the sensitivity of resonant scattering to incoming photon polarization

relative to the magnetic moments to determine the orientation of the staggered moments in the SDW state [212, 211, 213]. In our experiment, this is achieved by rotating the sample azimuthally by an angle ϕ about an axis normal to the $[\frac{1}{4}, \frac{1}{4}, L]$ set of lattice planes (here L is 1.93), as depicted in Figure 8.2a, which is accomplished by mounting the c-axis normal film on a 43.7° wedge. We omit details of the measurements in this thesis, readers may find a detailed discussion in ref. [4]

The measurements show agreement with the moments forming diagonal, bicollinear spin stripes (Figure 8.2d) with the magnetic moments lying entirely within the $a-b$ plane but oriented perpendicular to $\vec{Q}_{SDW}$. The SDW order is peaked at $L = 2$ and is minimal at $L = 1.5$, (Fig. 8.1f)) indicating that the coupling within the bilayer (intra-bilayer coupling) and between bilayers (inter-bilayer coupling) are either both ferromagnetic or both antiferromagnetic as depicted in Fig. 8.2c.

8.4 Anisotropic, Unidirectional Magnetic Domains

The unidirectional, stripe-like character of the antiferromagnetic order is also manifest in the shape of the SDW domains which break the rotational symmetry of the lattice. We measured the shapes and intensities of the SDW Bragg peaks in the $H-K$ plane for both sets of SDW domains with orthogonal $\vec{Q}$ vectors, around $(\frac{1}{4}, \frac{1}{4}, L)$ (in red) and $(\frac{1}{4}, -\frac{1}{4}, L)$ (in blue) using a two-dimensional microchannel plate detector, shown in Fig. 8.3a. The Bragg peaks around $(\frac{1}{4}, \frac{1}{4}, L)$ and $(\frac{1}{4}, -\frac{1}{4}, L)$ have equal intensities to within experimental uncertainty (± 3 %), indicating an equal population of domains. In both sets of domains, the SDW peaks have highly anisotropic shapes, with a 2D Lorentzian fit giving correlation lengths that are much longer parallel to $\vec{Q}_{SDW}$ ($\xi_{\parallel} = 292$ Å) versus perpendicular to $\vec{Q}_{SDW}$ ($\xi_{\perp} = 134$ Å).

This peak shape is consistent with anisotropic domains of unidirectional SDW order, with each domain characterized by either (1/4, 1/4) or (-1/4, 1/4) order, as depicted in Figure 8.3d. This is in contrast to anisotropic domains of bidirectional order or isotropic domains of unidirectional order, which would exhibit x-shaped or isotropic peak shapes respectively. This anisotropy could be associated with orthorhombic structural twin domains or may be orthogonal domains of unidirectional order occurring within a single structural domain. Intriguingly, this latter scenario is reminiscent of the anisotropic charge ordering reported in underdoped $YBa_2Cu_3O_{7-\delta}$ and $Bi_2Sr_{2-x}La_xCuO_{6+\delta}$, where the CDW Bragg peaks likewise exhibit an anisotropy, with longer correlations lengths parallel to the CDW wavevector, indicative of orthogonal anisotropic unidirectional CDW domains within a single orthorhombic structural domain.[146, 214]

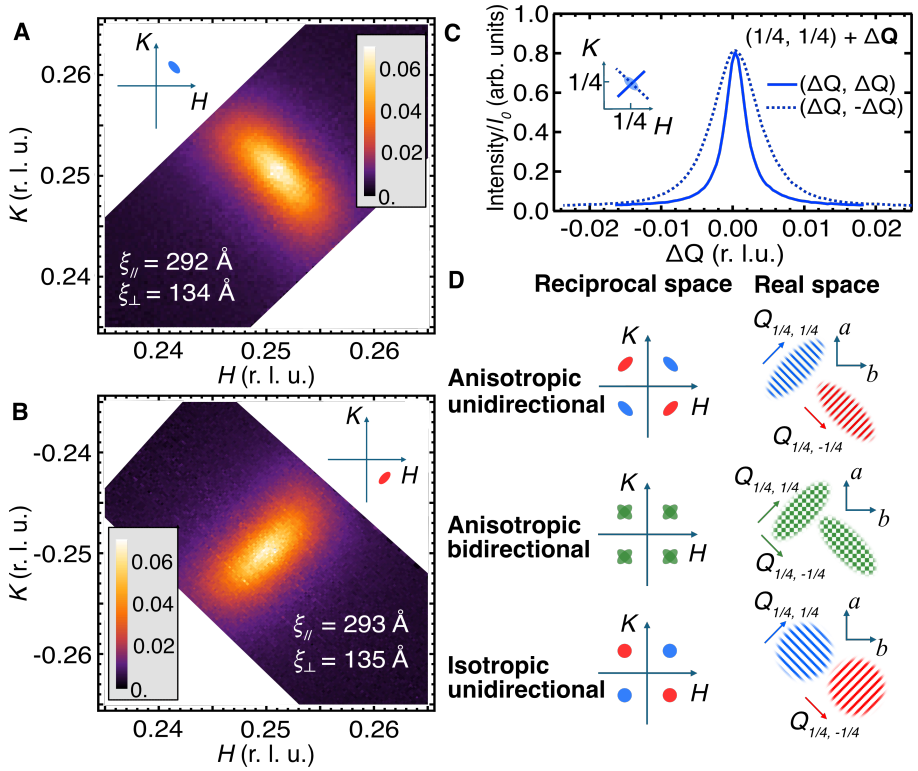


Figure 8.3: **Anisotropic Bragg peaks indicative of stripe-like SDW domains.** The shape of the a) (1/4 1/4 L) and b) (1/4 -1/4 L) Bragg peaks at 852 eV with π incident polarization. Measurement of H and K for sample A using a 2D channelplate detector (integrated between $L = 1.81$ and 1.90). The orthogonal peaks have the same intensities and widths. c) Cuts through the (1/4 1/4 1.85) Bragg peak parallel and perpendicular to the in-plane Q vector. d) The shape of Bragg peaks in reciprocal space and the corresponding domain structure in real space for anisotropic domains of unidirectional stripe order, anisotropic domains of bidirectional magnetic order and isotropic domains of unidirectional stripe order. The measurements in a) and b) are consistent with anisotropic domains of unidirectional stripe order.

8.5 Probing Magnetic Domain walls

In Figure 8.2, the orientation of the staggered moment at 20 K was determined to be almost entirely within the $a-b$ plane and perpendicular to $\vec{Q}_{SDW}$. Insights may be gleaned from the small discrepancies between the model and measurements. In particular, measurements

using σ polarization at $\phi = 0$ are at a minimum in intensity for this magnetic orientation, with deviations of the staggered moment parallel to $\vec{Q}_{SDW}$ or along [001] required to provide a finite scattering intensity. We now leverage this sensitivity of the polarization to the staggered moment orientation to investigate how the spin configuration evolves with temperature. In Figure 8.4b, we show a comparison between the temperature dependence of the SDW peak when measured with π versus σ polarization. At low temperatures ($T < 50K$), the intensity of the SDW peak measured in π polarization, I_π, is more than an order of magnitude stronger than in σ polarization, I_σ. Upon raising the temperature to T_{SDW}, I_π, smoothly decreases whereas I_σ exhibits a non-monotonic temperature dependence, growing in intensity before peaking around 130 K, and then falling rapidly to zero at T_{SDW}. On the other hand, the ratio of I_σ / I_π, shown in figure 8.4c grows smoothly and monotonically with increasing temperature all the way up to T_{SDW} when the peak vanishes, indicating that the component of the spins oriented away from the low T configuration (Figure 8.2b) grows with increasing temperature, with $I_\sigma/I_\pi > 0.6$ near T_{SDW}.

In addition to this anomalous temperature dependence, the width of the SDW Bragg peak is surprisingly broader when measured with σ versus π incident polarization (Fig. 8.4a and d). This indicates that the out-of-plane moments have a shorter correlation length than the in-plane moments, which would be inconsistent with a uniform, temperature-dependent canting of all the spins. Instead, this could be consistent with the existence of real-space defects of the magnetic order, such as Bloch-like domain walls or antiferromagnetic skyrmion-like topological defects. Indeed, Bloch-like domain walls should naturally exist between two orthogonal unidirectional domains, where the transition between domains would necessitate a reorientation of the spins by 90° from one domain to its orthogonal counterpart, which could occur over an extended region, depending on the relative magnitude of the magnetic anisotropy and exchange terms.

In the Bloch domain wall scenario, the staggered moments would rotate away from [110] or [-110] and out of the $a - b$ plane, as illustrated in Figure 8.4e. Here, I_π would probe the bicollinear spin stripe regions within the core of each domain, while I_σ would be sensitive to the rotated spin component in the domain walls. The relative volume fraction of domain walls would grow with increasing temperature until SDW order is lost at T_{SDW}. This interpretation could explain the broader peak for I_σ when compared to I_π, as shown in Fig. 8.4d. Finally, the influence of the domain walls may also be the source of the small deviations from a perfectly in-plane moment depicted in Fig. 8.2b.

This analysis represents a new approach to detecting defects in antiferromagnetic order. Unlike ferromagnetic domain walls, antiferromagnetic domain walls are often difficult to detect.[215] Further analysis of the polarization and temperature dependence of the (1/4 1/4) SDW peaks in $La_3Ni_2O_7$ may provide key insights into the width, density and

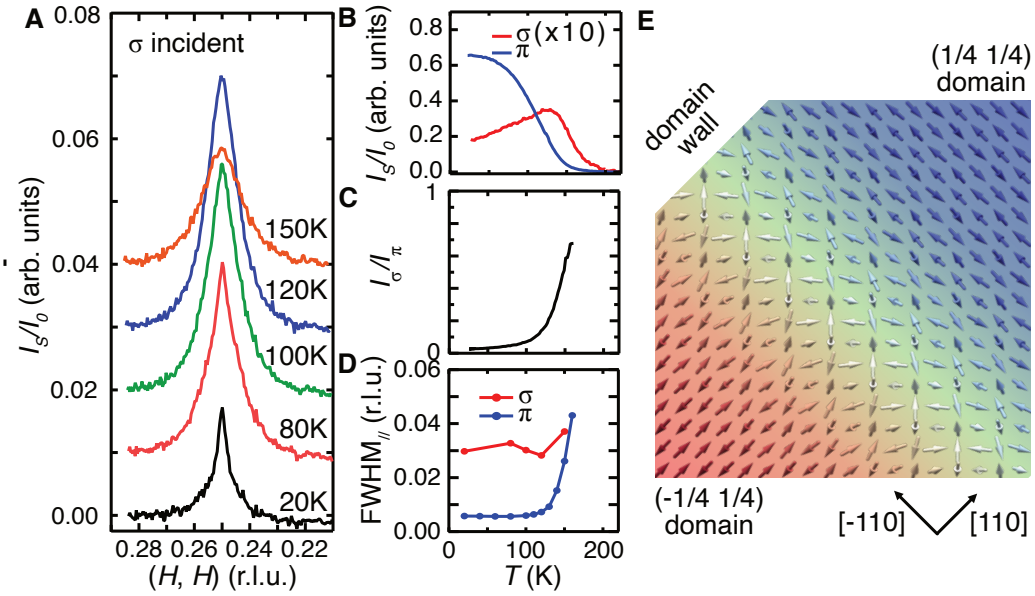


Figure 8.4: a) Cuts of the (1/4 1/4 1.93) peak at 852 eV with incident σ photon polarization at various temperatures. The peak is broader with σ polarization than with π polarization and exhibits a non-monotonic temperature dependence. b) The temperature dependence of the (1/4 1/4 1.93) peak amplitude with σ and π incident polarization. The peak emerges at 200 K, but peaks at 130 K with σ polarization. c) The ratio of the scattering intensity from σ and π incident light, I_σ/I_pi, which increases monotonically with increasing temperature. d) The FWHM of the (1/4 1/4) with σ and π incident light. With σ incident light, the peak is broader and exhibits a weak T dependence. e) A schematic of a domain wall between $\vec{Q}_{(110)}$ and $\vec{Q}_{(-110)}$ SDW domains. In the vicinity of a domain wall, the spin orientation may rotate to have a sizeable staggered moment out of the plane and/or parallel to $\vec{Q}$.

detailed magnetic configuration of the domain walls. Such investigations may be of key importance as the magnetic configuration within the domain walls may represent the melting of long-range SDW order as the material enters its superconducting phase, since a similar phenomenology also exists in the cuprates.

8.6 Discussion

A comparison between these experiments with those on bulk crystals [197] reveal a number of commonalities, including similar T_{SDW}'s, temperature dependences, photon polarization dependence, and peak widths along the (HHL) direction, suggesting that the results reported here are universal to both bulk and thin film samples.

The structure of the bicollinear spin stripe order in $La_3Ni_2O_7$ bears a strong resemblance to the magnetically ordered state in FeTe, but with a major distinction: in FeTe, the spin stripe ordering is accompanied by a monoclinic structural transition that stabilizes the magnetic order.[216, 217, 218] In contrast, temperature-dependent, synchrotron-based hard x-ray diffraction measurements of our $La_3Ni_2O_7$ thin films do not reveal any lowering of structural symmetry or the appearance of superlattice peaks upon entering the SDW state. Furthermore, the existence of domain walls or topological defects indicate that both orthogonal magnetic domains occur within a single NiO_2 plane. This may imply an inherent instability in $La_3Ni_2O_7$ to rotational symmetry breaking, possibly accompanied by disordered or frustrated nematic order,[219] analogous to the Fe-based and cuprate superconductors where unidirectional density wave and nematic orders are pervasive and closely intertwined with superconductivity. [11, 220] These close analogies with the cuprates and Fe-based superconductors suggest that the melting of this SDW state, via the likely formation of Bloch-like domain walls, is directly related to the formation of the superconducting state under high pressure.

8.7 Materials and Methods

Resonant soft x-ray scattering measurements were performed at the Canadian Light Source REIXS beamline.[101] The majority of the measurements were made using an energy resolved silicon drift detector, with measurements of the peak shape utilizing a 2D microchannel plate detector. The samples were oriented using the (001) Bragg peak of the NGO substrate at 2500 eV. The in-plane orientation was performed using $(\frac{1}{4}\frac{1}{4}L)$ SDW Bragg peaks at 852 eV. The samples were found to have a c axis lattice constant of 20.44 Å from lab-based x-ray diffraction. From the location of the $(\frac{1}{4}\frac{1}{4}L)$ peaks, $\sqrt{a_T^2 + b_T^2} = 5.426(3)$ Å

Chapter 9

Conclusions

In this thesis, we present resonant X-ray measurements (RXS) of electronic nematicity (rotational symmetry breaking) and charge density wave (CDW) order (translational symmetry breaking) on a series of stripe-ordered cuprate superconductors. Tackling the challenge of disentangling intertwined electronic phases in the pseudogap and superconducting phases of cuprates, we develop strategies to isolate and manipulate nematicity and CDW ordering when underlying structural anisotropies and disorder render most probes insensitive. Our principal conclusions are as follows.

We establish a time-resolved resonant X-ray scattering (tr-RXS) probe with the ability to isolate $Q = 0$ nematic order that co-exists with structural and charge anisotropies. We detect ultrafast signatures of nematicity dynamics in optimally doped $x = 0.15$ Eu-LSCO recovering at sub-picosecond timescales. While optimal doping hosts charge and spin density wave orders, we extend the search to the phase diagram extremities where CDW order is absent. We test the time-resolved tool to validate the vanishing signature of nematicity in overdoped $x = 0.24$ Eu-LSCO system slightly outside the pseudogap phase. Investigations of $x = 0.08$ Eu-LSCO, however, unveils a saturated nematic phase that equilibrium resonant X-ray scattering cannot detect. Along with disentangling nematicity from CDW order at optimal doping, the demarcation between a muted and a vanished nematic state establishes tr-RXS as an indispensable tool capable of recording nuances of electronic rotational-symmetry breaking with promising avenues for a wider class of quantum materials.

Extending the search of nematicity and CDW order as a function of hole doping to understand the phenomenology of symmetry-breaking phases in the physics of cuprate superconductors, we find that nematicity exists beyond the CDW order region and up

to the boundary of the pseudogap phase. Nematicty vanishes upon exiting the pseudogap either through its onset temperature T^* or critical doping p^*, hinting at a deeper connection between them. It has been recently identified that the pseudogap phase terminates at a putative quantum critical point in Eu-LSCO and Nd-LSCO which opens the discussion: if nematicity is stabilized in the pseudogap phase or manifests through nematic quantum criticality as observed in Fe-based superconductors. We find that nematicity starts to weaken, saturating as the superconductivity onsets. Our measurements across the phase diagram highlight a deeper role of nematicity in the physics of cuprate superconductors that has eluded investigations in the past.

Through measurements of in-plane compressive uniaxial stress along Cu-O-Cu and Cu-Cu bond directions, we distort the crystalline structure to manipulate the ground state conditions favouring formation of these phases. We are able to tune CDW order anisotropically without influencing its onset temperature. On applying compressive strain along Cu-O-Cu direction, only CDW order propagating parallel to applied strain is suppressed while the charge order propagating perpendicular to strain direction stays unaffected. We detect no change in either the CDW order amplitude or onset when the strain is along Cu-Cu direction. We are unable to confidently distinguish whether the loss of nematic response observed under uniaxial strain is of electronic origin or simply a structural artifact, given the strain-induced change in the low-temperature structural phases that allow conditions to detect nematicity.

With protocols derived from cuprates, we present RXS measurements on a recently discovered Ni-based bilayer superconductor $La_3Ni_2O_7$. We uncover the detailed magnetic structure of the spin-stripe order, showing that the magnetic moments orient within the planes and perpendicular to Q_{SDW}, forming unidirectional spin stripes similar to FeTe. The spin stripe domains bear a nematic character manifesting as anisotropic, orthogonal spin domains that have shorter correlation lengths perpendicular to versus parallel to; indicating nanoscale rotational symmetry breaking. By recording the temperature evolution of the polarization profile of these domains, we develop a novel approach to probe Bloch-like anti-ferromagnetic domain walls – harnessing the full power of resonant X-ray scattering.

This work provides insight into fundamental, pressing questions of cuprate superconductors and contributes to the technical development of resonant X-ray scattering as a powerful new tool to disentangle and tune intertwined quantum states of matter. The ability to manipulate quantum matter paves the way to orchestrate next generation of technological advances such as more practical superconducting devices, improved architecture for quantum computing, and developing higher transition temperature superconductors.

References

[1] M. Bluschke, N. K. Gupta, H. Jang, A. A. Husain, B. Lee, M. Kim, M. Na, B. D. Remedios, S. Smit, P. Moen, S.-Y. Park, M. Kim, D. Jang, H. Choi, R. Sutarto, A. H. Reid, G. L. Dakovski, G. Coslovich, Q. L. Nguyen, N. G. Burdet, M.-F. Lin, A. Revcolevschi, J.-H. Park, J. Geck, J. J. Turner, A. Damascelli, and D. G. Hawthorn, "Orbital-selective time-domain signature of nematicity dynamics in the charge-density-wave phase of $La_{1.65}Eu_{0.2}Sr_{0.15}CuO_4$," *Proceedings of the National Academy of Sciences*, vol. 121, no. 23, p. e2400727121, 2024.

[2] N. K. Gupta, C. McMahon, R. Sutarto, T. Shi, R. Gong, H. I. Wei, K. M. Shen, F. He, Q. Ma, M. Dragomir, B. D. Gaulin, and D. G. Hawthorn, "Vanishing nematic order beyond the pseudogap phase in overdoped cuprate superconductors," *Proceedings of the National Academy of Sciences*, vol. 118, no. 34, p. e2106881118, 2021.

[3] N. K. Gupta, R. Sutarto, R. Gong, S. H. J. Idziak, H. Hale, Y.-J. Kim, and D. G. Hawthorn, "Tuning charge density wave order and structure via uniaxial stress in a stripe-ordered cuprate superconductor," *Phys. Rev. B*, vol. 108, p. L121113, 2023.

[4] N. K. Gupta, R. Gong, Y. Wu, M. Kang, C. T. Parzyck, B. Z. Gregory, N. Costa, R. Sutarto, S. Sarker, A. Singer, D. G. Schlom, K. M. Shen, and D. G. Hawthorn, "Anisotropic spin stripe domains in bilayer $La_3Ni_2O_7$," *arXiv preprint arXiv:2409.03210*, 2024.

[5] J. G. Bednorz and K. A. Müller, "Possible high-T_c superconductivity in the Ba-La-Cu-O system," *Zeitschrift für Physik B Condensed Matter*, vol. 64, no. 2, pp. 189–193, 1986.

[6] J. Bardeen, L. N. Cooper, and J. R. Schrieffer, "Theory of superconductivity," *Phys. Rev.*, vol. 108, pp. 1175–1204, 1957.

[7] M.-K. Wu, J. R. Ashburn, C. J. Torng, P. H. Hor, R. L. Meng, L. Gao, Z. J. Huang, Y. Q. Wang, and C. W. Chu, "Superconductivity at 93 K in a new mixed-phase $Y - Ba - Cu - O$ compound system at ambient pressure," *Physical review letters*, vol. 58, no. 9, p. 908, 1987.

[8] P. Anderson, "The resonating valence bond state in La_2CuO_4 and superconductivity," *Science*, vol. 235, no. 4793, pp. 1196–1198, 1987.

[9] D. Scalapino, "The case for $d_{x^2-y^2}$ pairing in the cuprate superconductors," *Physics Reports*, vol. 250, no. 6, pp. 329–365, 1995.

[10] N. Singh, "Leading theories of the cuprate superconductivity: A critique," *Physica C: Superconductivity and its Applications*, vol. 580, p. 1353782, 2021.

[11] E. Fradkin, S. A. Kivelson, and J. M. Tranquada, "Colloquium: Theory of intertwined orders in high temperature superconductors," *Rev. Mod. Phys.*, vol. 87, pp. 457–482, 2015.

[12] L. Taillefer, "Scattering and pairing in cuprate superconductors," *Annu. Rev. Condens. Matter Phys.*, vol. 1, no. 1, pp. 51–70, 2010.

[13] B. Keimer, S. A. Kivelson, M. R. Norman, S. Uchida, and J. Zaanen, "From quantum matter to high-temperature superconductivity in copper oxides," *Nature*, vol. 518, pp. 179–186, 2015.

[14] R. Comin and A. Damascelli, "Resonant x-ray scattering studies of charge order in cuprates," *Annual Review of Condensed Matter Physics*, vol. 7, pp. 369–405, 2016.

[15] I. Vishik, M. Hashimoto, R. He, W. Lee, F. Schmitt, D. Lu, R. Moore, C. Zhang, W. Meevasana, T. Sasagawa, *et al.*, "Phase competition in trisected superconducting dome," *Proceedings of the National Academy of Sciences*, vol. 109, no. 45, pp. 18332–18337, 2012.

[16] E. Fradkin, S. A. Kivelson, M. J. Lawler, J. P. Eisenstein, and A. P. Mackenzie, "Nematic Fermi fluids in condensed matter physics," *Annu. Rev. Condens. Matter Phys.*, vol. 1, no. 1, pp. 153–178, 2010.

[17] V. J. Emery and S. A. Kivelson, "A phenomenological theory of the pseudogap state," *Nature*, vol. 374, no. 6521, pp. 434–437, 1995.

[18] A. Damascelli, Z. Hussain, and Z.-X. Shen, "Angle-resolved photoemission studies of the superconducting gap and pseudogap in $Bi_2Sr_2CaCu_2O_{8+\delta}$," *Reviews of Modern Physics*, vol. 75, no. 2, pp. 473–541, 2003.

[19] N. Doiron-Leyraud, O. Cyr-Choinière, S. Badoux, A. Ataei, C. Collignon, A. Gourgout, S. Dufour-Beauséjour, F. Tafti, F. Laliberté, M.-E. Boulanger, *et al.*, "Pseudogap phase of cuprate superconductors confined by Fermi surface topology," *Nature communications*, vol. 8, no. 1, p. 2044, 2017.

[20] C. E. Matt, C. G. Fatuzzo, Y. Sassa, M. Månsson, S. Fatale, V. Bitetta, X. Shi, S. Pailhes, M. Berntsen, T. Kurosawa, *et al.*, "Electron scattering, charge order, and pseudogap physics in $La_{1.6-x}Nd_{0.4}Sr_xCuO_4$: an angle-resolved photoemission spectroscopy study," *Physical Review B*, vol. 92, no. 13, p. 134524, 2015.

[21] J. E. Hoffman, K. McElroy, D.-H. Lee, K. M. Lang, H. Eisaki, S. Uchida, and J. C. Davis, "Experimental evidence for a Fermi surface in an insulating cuprate," *Science*, vol. 297, no. 5584, pp. 1148–1151, 2002.

[22] I. Vishik, "Photoemission perspective on pseudogap, superconducting fluctuations, and charge order in cuprates: a review of recent progress," *Reports on Progress in Physics*, vol. 81, no. 6, p. 062501, 2018.

[23] K. M. Shen, F. Ronning, D. H. Lu, F. Baumberger, N. J. C. Ingle, W. S. Lee, W. Meevasana, Y. Kohsaka, M. Azuma, M. Takano, H. Takagi, and Z.-X. Shen, "Direct observation of a Fermi surface in the pseudogap state of a high-T_c superconductor," *Science*, vol. 307, no. 5711, pp. 901–904, 2005.

[24] N. Doiron-Leyraud, C. Proust, D. LeBoeuf, J. Levallois, J.-B. Bonnemaison, R. Liang, D. A. Bonn, W. N. Hardy, and L. Taillefer, "Quantum oscillations and the fermi surface in an underdoped high-T_c superconductor," *Nature*, vol. 447, p. 563, 2007.

[25] Y. Cao, V. Fatemi, S. Fang, K. Watanabe, T. Taniguchi, E. Kaxiras, and P. Jarillo-Herrero, "Unconventional superconductivity in magic-angle graphene superlattices," *Nature*, vol. 556, no. 7699, pp. 43–50, 2018.

[26] A. V. Chubukov, "Pairing mechanism in Fe-based superconductors," *Annual Review of Condensed Matter Physics*, vol. 3, pp. 57–92, 2012.

[27] A. Achkar, "Charge density wave order in cuprate superconductors studied by resonant soft x-ray scattering," PhD Thesis, University of Waterloo, 2015.

[28] A. Achkar, F. He, R. Sutarto, J. Geck, H. Zhang, Y.-J. Kim, and D. Hawthorn, "Resonant x-ray scattering measurements of a spatial modulation of the Cu 3 d and O 2 p energies in stripe-ordered cuprate superconductors," *Physical Review Letters*, vol. 110, no. 1, p. 017001, 2013.

[29] J. Tranquada, B. Sternlieb, J. Axe, Y. Nakamura, and S. Uchida, "Evidence for stripe correlations of spins and holes in copper oxide superconductors," *Nature*, vol. 375, no. 6532, pp. 561–563, 1995.

[30] C. Proust and L. Taillefer, "The remarkable underlying ground states of cuprate superconductors," *Annu. Rev. Condens. Matter Phys.*, vol. 10, pp. 409–429, 2019.

[31] G. Ghiringhelli, M. Le Tacon, M. Minola, S. Blanco-Canosa, C. Mazzoli, N. B. Brookes, G. M. De Luca, A. Frano, D. G. Hawthorn, F. He, T. Loew, M. M. Sala, D. C. Peets, M. Salluzzo, E. Schierle, R. Sutarto, G. A. Sawatzky, E. Weschke, B. Keimer, and L. Braicovich, "Long-range incommensurate charge fluctuations in (Y,Nd)$Ba_2Cu_3O_{6+x}$," *Science*, vol. 337, no. 6096, pp. 821–825, 2012.

[32] A. J. Achkar, R. Sutarto, X. Mao, F. He, A. Frano, S. Blanco-Canosa, M. Le Tacon, G. Ghiringhelli, L. Braicovich, M. Minola, M. Moretti Sala, C. Mazzoli, R. Liang, D. A. Bonn, W. N. Hardy, B. Keimer, G. A. Sawatzky, and D. G. Hawthorn, "Distinct charge orders in the planes and chains of ortho-III-ordered $YBa_2Cu_3O_{6+\delta}$ superconductors identified by resonant elastic x-ray scattering," *Phys. Rev. Lett.*, vol. 109, p. 167001, 2012.

[33] S. Blanco-Canosa, A. Frano, E. Schierle, J. Porras, T. Loew, M. Minola, M. Bluschke, E. Weschke, B. Keimer, and M. Le Tacon, "Resonant X-ray scattering study of charge-density wave correlations in $YBa_2Cu_3O_{6+x}$," *Phys. Rev. B*, vol. 90, p. 054513, 2014.

[34] R. Comin, A. Frano, M. M. Yee, Y. Yoshida, H. Eisaki, E. Schierle, E. Weschke, R. Sutarto, F. He, A. Soumyanarayanan, Y. He, M. L. Tacon, I. S. Elfimov, J. E. Hoffman, G. A. Sawatzky, B. Keimer, and A. Damascelli, "Charge order driven by Fermi-arc instability in $Bi_2Sr_{2-x}La_xCuO_{6+\delta}$," *Science*, vol. 343, no. 6169, pp. 390–392, 2014.

[35] E. H. da Silva Neto, P. Aynajian, A. Frano, R. Comin, E. Schierle, E. Weschke, A. Gyenis, J. Wen, J. Schneeloch, Z. Xu, S. Ono, G. Gu, M. Le Tacon, and A. Yazdani, "Ubiquitous interplay between charge ordering and high-temperature superconductivity in cuprates," *Science*, vol. 343, no. 6169, pp. 393–396, 2014.

[36] J. Fink, V. Soltwisch, J. Geck, E. Schierle, E. Weschke, and B. Büchner, "Phase diagram of charge order in $La_{1.8-x}Eu_{0.2}Sr_xCuO_4$ from resonant soft x-ray diffraction," *Phys. Rev. B*, vol. 83, no. 9, p. 092503, 2011.

[37] P. Abbamonte, A. Rusydi, S. Smadici, G. Gu, G. Sawatzky, and D. Feng, "Spatially modulated 'Mottness' in $La_{2-x}Ba_xCuO_4$," *Nature Physics*, vol. 1, no. 3, pp. 155–158, 2005.

[38] S. B. Wilkins, M. P. M. Dean, J. Fink, M. Hücker, J. Geck, V. Soltwisch, E. Schierle, E. Weschke, G. Gu, S. Uchida, N. Ichikawa, J. M. Tranquada, and J. P. Hill, "Comparison of stripe modulations in $La_{1.875}Ba_{0.125}CuO_4$ and $La_{1.48}Nd_{0.4}Sr_{0.12}CuO_4$," *Phys. Rev. B*, vol. 84, p. 195101, 2011.

[39] A. J. Achkar, M. Zwiebler, C. McMahon, F. He, R. Sutarto, I. Djianto, Z. Hao, M. J. P. Gingras, M. Hücker, G. D. Gu, A. Revcolevschi, H. Zhang, Y.-J. Kim, J. Geck, and D. G. Hawthorn, "Nematicity in stripe-ordered cuprates probed via resonant x-ray scattering," *Science*, vol. 351, no. 6273, pp. 576–578, 2016.

[40] J. Chang, E. Blackburn, A. T. Holmes, N. B. Christensen, J. Larsen, J. Mesot, R. Liang, D. A. Bonn, W. N. Hardy, A. Watenphul, M. von Zimmermann, E. M. Forgan, and S. M. Hayden, "Direct observation of competition between superconductivity and charge density wave order in $YBa_2Cu_3O_{6.67}$," *Nat. Phys.*, vol. 8, no. 12, p. 871, 2012.

[41] L. E. Hayward, D. G. Hawthorn, R. G. Melko, and S. Sachdev, "Angular fluctuations of a multicomponent order describe the pseudogap of $YBa_2Cu_3O_{6+x}$," *Science*, vol. 343, no. 6177, pp. 1336–1339, 2014.

[42] J. Axe, A. Moudden, D. Hohlwein, D. Cox, K. Mohanty, A. Moodenbaugh, and Y. Xu, "Structural phase transformations and superconductivity in $La_{2-x}Ba_xCuO_4$," *Physical review letters*, vol. 62, no. 23, p. 2751, 1989.

[43] J. Axe and M. Crawford, "Structural instabilities in lanthanum cuprate superconductors," *Journal of Low Temperature Physics*, vol. 95, no. 1-2, pp. 271–284, 1994.

[44] M. Hücker, "Structural aspects of materials with static stripe order," *Physica C: Superconductivity*, vol. 481, pp. 3–14, 2012.

[45] M. Dragomir, Q. Ma, J. P. Clancy, A. Ataei, P. A. Dube, S. Sharma, A. Huq, H. A. Dabkowska, L. Taillefer, and B. D. Gaulin, "Materials preparation, single-crystal

growth, and the phase diagram of the cuprate high-temperature superconductor $La_{1.6-x}Nd_{0.4}Sr_xCuO_4$," *Phys. Rev. Mater.*, vol. 4, p. 114801, 2020.

[46] J. M. Tranquada, J. D. Axe, N. Ichikawa, Y. Nakamura, S. Uchida, and B. Nachumi, "Neutron-scattering study of stripe-phase order of holes and spins in $La_{1.48}Nd_{0.4}Sr_{0.12}CuO_4$," *Phys. Rev. B*, vol. 54, p. 7489, 1996.

[47] B. Michon, C. Girod, S. Badoux, J. Kačmarčík, Q. Ma, M. Dragomir, H. Dabkowska, B. Gaulin, J.-S. Zhou, S. Pyon, *et al.*, "Thermodynamic signatures of quantum criticality in cuprate superconductors," *Nature*, vol. 567, no. 7747, pp. 218–222, 2019.

[48] M. Hamidian, S. D. Edkins, S. H. Joo, A. Kostin, H. Eisaki, S. Uchida, M. Lawler, E.-A. Kim, A. P. Mackenzie, K. Fujita, *et al.*, "Detection of a cooper-pair density wave in $Bi_2Sr_2CaCu_2O_{8+\delta}$," *Nature*, vol. 532, no. 7599, pp. 343–347, 2016.

[49] M. Mitrano, S. Lee, A. A. Husain, L. Delacretaz, M. Zhu, G. de la Peña Munoz, S. X.-L. Sun, Y. I. Joe, A. H. Reid, S. F. Wandel, *et al.*, "Ultrafast time-resolved x-ray scattering reveals diffusive charge order dynamics in $La_{2-x}Ba_xCuO_4$," *Science advances*, vol. 5, no. 8, p. eaax3346, 2019.

[50] T. Shibauchi, A. Carrington, and Y. Matsuda, "A quantum critical point lying beneath the superconducting dome in iron pnictides," *Annu. Rev. Condens. Matter Phys.*, vol. 5, no. 1, pp. 113–135, 2014.

[51] T. Worasaran, M. S. Ikeda, J. C. Palmstrom, J. A. W. Straquadine, S. A. Kivelson, and I. R. Fisher, "Nematic quantum criticality in an Fe-based superconductor revealed by strain-tuning," *Science*, vol. 372, no. 6545, pp. 973–977, 2021.

[52] S. Badoux, W. Tabis, F. Laliberté, G. Grissonnanche, B. Vignolle, D. Vignolles, J. Béard, D. Bonn, W. Hardy, R. Liang, *et al.*, "Change of carrier density at the pseudogap critical point of a cuprate superconductor," *Nature*, vol. 531, no. 7593, pp. 210–214, 2016.

[53] C. Collignon, S. Badoux, S. A. A. Afshar, B. Michon, F. Laliberté, O. Cyr-Choinière, J.-S. Zhou, S. Licciardello, S. Wiedmann, N. Doiron-Leyraud, and L. Taillefer, "Fermi-surface transformation across the pseudogap critical point of the cuprate superconductor $La_{1.6-x}Nd_{0.4}Sr_xCuO_4$," *Phys. Rev. B*, vol. 95, p. 224517, 2017.

[54] Y. Fang, G. Grissonnanche, A. Legros, S. Verret, F. Laliberté, C. Collignon, A. Ataei, M. Dion, J. Zhou, D. Graf, *et al.*, "Fermi surface transformation at the pseudogap

critical point of a cuprate superconductor," *Nature Physics*, vol. 18, no. 5, pp. 558–564, 2022.

[55] Y. Sato, S. Kasahara, H. Murayama, Y. Kasahara, E.-G. Moon, T. Nishizaki, T. Loew, J. Porras, B. Keimer, T. Shibauchi, *et al.*, "Thermodynamic evidence for a nematic phase transition at the onset of the pseudogap in $YBa_2Cu_3O_y$," *Nature Physics*, vol. 13, no. 11, pp. 1074–1078, 2017.

[56] B. Ramshaw, S. Sebastian, R. McDonald, J. Day, B. Tan, Z. Zhu, J. Betts, R. Liang, D. Bonn, W. Hardy, *et al.*, "Quasiparticle mass enhancement approaching optimal doping in a high-T_c superconductor," *Science*, vol. 348, no. 6232, pp. 317–320, 2015.

[57] C. M. Varma, "Quantum-critical fluctuations in 2d metals: strange metals and superconductivity in antiferromagnets and in cuprates," *Reports on Progress in Physics*, vol. 79, no. 8, p. 082501, 2016.

[58] I. Paul and M. Garst, "Lattice effects on nematic quantum criticality in metals," *Physical Review Letters*, vol. 118, no. 22, p. 227601, 2017.

[59] K. Ishida, S. Hosoi, Y. Teramoto, T. Usui, Y. Mizukami, K. Itaka, Y. Matsuda, T. Watanabe, and T. Shibauchi, "Divergent nematic susceptibility near the pseudogap critical point in a cuprate superconductor," *Journal of the Physical Society of Japan*, vol. 89, no. 6, p. 064707, 2020.

[60] N. Auvray, B. Loret, S. Benhabib, M. Cazayous, R. Zhong, J. Schneeloch, G. Gu, A. Forget, D. Colson, I. Paul, *et al.*, "Nematic fluctuations in the cuprate superconductor $Bi_2Sr_2CaCu_2O_{8+\delta}$," *Nature communications*, vol. 10, no. 1, pp. 1–7, 2019.

[61] P.-G. De Gennes and J. Prost, *The physics of liquid crystals*, vol. 83. Oxford university press, 1993.

[62] Y. Ando, K. Segawa, S. Komiya, and A. N. Lavrov, "Electrical resistivity anisotropy from self-organized one dimensionality in high-temperature superconductors," *Phys. Rev. Lett.*, vol. 88, p. 137005, 2002.

[63] O. Cyr-Choinière, G. Grissonnanche, S. Badoux, J. Day, D. Bonn, W. Hardy, R. Liang, N. Doiron-Leyraud, and L. Taillefer, "Two types of nematicity in the phase diagram of the cuprate superconductor $YBa_2Cu_3O_{6+y}$," *Physical Review B*, vol. 92, no. 22, p. 224502, 2015.

[64] R. Daou, J. Chang, D. LeBoeuf, O. Cyr-Choinière, F. Laliberté, N. Doiron-Leyraud, B. J. Ramshaw, R. Liang, D. A. Bonn, W. N. Hardy, and L. Taillefer, "Broken rotational symmetry in the pseudogap phase of a high-T_c superconductor," *Nature*, vol. 463, p. 519, 2010.

[65] K. Fujita, A. R. Schmidt, E.-A. Kim, M. J. Lawler, D. Hai Lee, J. Davis, H. Eisaki, and S.-i. Uchida, "Spectroscopic imaging scanning tunneling microscopy studies of electronic structure in the superconducting and pseudogap phases of cuprate high-T_c superconductors," *Journal of the Physical Society of Japan*, vol. 81, no. 1, p. 011005, 2011.

[66] M. Lawler, K. Fujita, J. Lee, A. Schmidt, Y. Kohsaka, C. K. Kim, H. Eisaki, S. Uchida, J. Davis, J. Sethna, *et al.*, "Intra-unit-cell electronic nematicity of the high-T_c copper-oxide pseudogap states," *Nature*, vol. 466, no. 7304, pp. 347–351, 2010.

[67] V. Hinkov, D. Haug, B. Fauqué, P. Bourges, Y. Sidis, A. Ivanov, C. Bernhard, C. Lin, and B. Keimer, "Electronic liquid crystal state in the high-temperature superconductor $YBa_2Cu_3O_{6.45}$," *Science*, vol. 319, no. 5863, pp. 597–600, 2008.

[68] S. A. Kivelson, E. Fradkin, and V. J. Emery, "Electronic liquid-crystal phases of a doped mott insulator," *Nature*, vol. 393, no. 6685, pp. 550–553, 1998.

[69] S. A. Kivelson, I. P. Bindloss, E. Fradkin, V. Oganesyan, J. M. Tranquada, A. Kapitulnik, and C. Howald, "How to detect fluctuating stripes in the high-temperature superconductors," *Rev. Mod. Phys.*, vol. 75, no. 4, pp. 1201–1241, 2003.

[70] L. Nie, G. Tarjus, and S. A. Kivelson, "Quenched disorder and vestigial nematicity in the pseudogap regime of the cuprates," *Proceedings of the National Academy of Sciences*, vol. 111, no. 22, pp. 7980–7985, 2014.

[71] I. I. Pomeranchuk, "On the stability of a Fermi liquid," *Sov. Phys. JETP*, vol. 8, p. 361, 1958.

[72] H. Yamase and H. Kohno, "Instability toward formation of quasi-one-dimensional Fermi surface in two-dimensional *t-J* model," *Journal of the Physical Society of Japan*, vol. 69, pp. 2151–2157, 2000.

[73] H. Yamase, "Theoretical insights into electronic nematic order, bond-charge orders, and plasmons in cuprate superconductors," *Journal of the Physical Society of Japan*, vol. 90, no. 11, p. 111011, 2021.

[74] H. Yamase and R. Zeyher, "Superconductivity from orbital nematic fluctuations," *Phys. Rev. B*, vol. 88, p. 180502, 2013.

[75] C. McMahon, "Symmetry of the charge ordering phases in hole-doped cuprates studied by resonant x-ray absorption and scattering," 2019.

[76] R. Mankowsky, A. Subedi, M. Först, S. O. Mariager, M. Chollet, H. Lemke, J. S. Robinson, J. M. Glownia, M. P. Minitti, A. Frano, *et al.*, "Nonlinear lattice dynamics as a basis for enhanced superconductivity in $YBa_2Cu_3O_{6.5}$," *Nature*, vol. 516, no. 7529, pp. 71–73, 2014.

[77] M. Mitrano, A. Cantaluppi, D. Nicoletti, S. Kaiser, A. Perucchi, S. Lupi, P. Di Pietro, D. Pontiroli, M. Riccò, S. R. Clark, *et al.*, "Possible light-induced superconductivity in K_3C_{60} at high temperature," *Nature*, vol. 530, no. 7591, pp. 461–464, 2016.

[78] D. H. Torchinsky, F. Mahmood, A. T. Bollinger, I. Božović, and N. Gedik, "Fluctuating charge-density waves in a cuprate superconductor," *Nature materials*, vol. 12, no. 5, pp. 387–391, 2013.

[79] R. Fernandes, A. Chubukov, and J. Schmalian, "What drives nematic order in iron-based superconductors?," *Nature physics*, vol. 10, no. 2, pp. 97–104, 2014.

[80] J. Fink, E. Schierle, E. Weschke, and J. Geck, "Resonant elastic soft x-ray scattering," *Reports on Progress in Physics*, vol. 76, no. 5, p. 056502, 2013.

[81] N. K. Gupta, "A study of electronic nematicity in cuprate superconductors using resonant soft x-ray scattering," Master's thesis, University of Waterloo, 2020.

[82] J. Als-Nielsen and D. McMorrow, *Elements of modern X-ray physics*. John Wiley & Sons, 2011.

[83] Y. Joly, S. Matteo, and O. Bunău, "Resonant x-ray diffraction: Basic theoretical principles," *The European Physical Journal Special Topics*, vol. 208, no. 1, pp. 21–38, 2012.

[84] L. L. Foldy and S. A. Wouthuysen, "On the dirac theory of spin-1/2 particles and its non-relativistic limit," *Physical Review*, vol. 78, no. 1, p. 29, 1950.

[85] E. Beaurepaire, H. Bulou, F. Scheurer, and J. P. Kappler, *Magnetism: A synchrotron radiation approach*, vol. 697. Springer, 2006.

[86] J. J. Sakurai, *Advanced quantum mechanics*. Pearson Education India, 1967.

[87] M. Blume, "Magnetic scattering of x rays," *Journal of Applied Physics*, vol. 57, no. 8, pp. 3615–3618, 1985.

[88] M. Haverkort, N. Hollmann, I. Krug, and A. Tanaka, "Symmetry analysis of magneto-optical effects: The case of x-ray diffraction and x-ray absorption at the transition metal $L_{2,3}$ edge," *Physical Review B*, vol. 82, no. 9, p. 094403, 2010.

[89] D. Fausti, R. I. Tobey, N. Dean, S. Kaiser, A. Dienst, M. C. Hoffmann, S. Pyon, T. Takayama, H. Takagi, and A. Cavalleri, "Light-induced superconductivity in a stripe-ordered cuprate," *Science*, vol. 331, no. 6014, pp. 189–191, 2011.

[90] H. Jang, W.-S. Lee, H. Nojiri, S. Matsuzawa, H. Yasumura, L. Nie, A. V. Maharaj, S. Gerber, Y.-J. Liu, A. Mehta, D. A. Bonn, R. Liang, W. N. Hardy, C. A. Burns, Z. Islam, S. Song, J. Hastings, T. P. Devereaux, Z.-X. Shen, S. A. Kivelson, C.-C. Kao, D. Zhu, and J.-S. Lee, "Ideal charge-density-wave order in the high-field state of superconducting YBCO," *Proc. Natl. Acad. Sci. USA*, vol. 113, no. 51, pp. 14645–14650, 2016.

[91] H. Jang, H.-D. Kim, M. Kim, S. H. Park, S. Kwon, J. Y. Lee, S.-Y. Park, G. Park, S. Kim, H. Hyun, S. Hwang, C.-S. Lee, C.-Y. Lim, W. Gang, M. Kim, S. Heo, J. Kim, G. Jung, S. Kim, J. Park, J. Kim, H. Shin, J. Park, T.-Y. Koo, H.-J. Shin, H. Heo, C. Kim, C.-K. Min, J.-H. Han, H.-S. Kang, H.-S. Lee, K. S. Kim, I. Eom, and S. Rah, "Time-resolved resonant elastic soft x-ray scattering at Pohang accelerator laboratory x-ray free electron laser," *Review of Scientific Instruments*, vol. 91, no. 8, p. 083904, 2020.

[92] S. Wandel, F. Boschini, E. H. da Silva Neto, L. Shen, M. X. Na, S. Zohar, Y. Wang, S. B. Welch, M. H. Seaberg, J. D. Koralek, G. L. Dakovski, W. Hettel, M.-F. Lin, S. P. Moeller, W. F. Schlotter, A. H. Reid, M. P. Minitti, T. Boyle, F. He, R. Sutarto, R. Liang, D. Bonn, W. Hardy, R. A. Kaindl, D. G. Hawthorn, J.-S. Lee, A. F. Kemper, A. Damascelli, C. Giannetti, J. J. Turner, and G. Coslovich, "Enhanced charge density wave coherence in a light-quenched, high-temperature superconductor," *Science*, vol. 376, no. 6595, pp. 860–864, 2022.

[93] C. Giannetti, M. Capone, D. Fausti, M. Fabrizio, F. Parmigiani, and D. Mihailovic, "Ultrafast optical spectroscopy of strongly correlated materials and high-temperature superconductors: a non-equilibrium approach," *Advances in Physics*, vol. 65, no. 2, pp. 58–238, 2016.

[94] D. N. Basov, R. D. Averitt, D. van der Marel, M. Dressel, and K. Haule, "Electrodynamics of correlated electron materials," *Rev. Mod. Phys.*, vol. 83, pp. 471–541, 2011.

[95] C. L. Smallwood, J. P. Hinton, C. Jozwiak, W. Zhang, J. D. Koralek, H. Eisaki, D.-H. Lee, J. Orenstein, and A. Lanzara, "Tracking cooper pairs in a cuprate superconductor by ultrafast angle-resolved photoemission," *Science*, vol. 336, no. 6085, pp. 1137–1139, 2012.

[96] R. D. Averitt and A. J. Taylor, "Ultrafast optical and far-infrared quasiparticle dynamics in correlated electron materials," *Journal of Physics: Condensed Matter*, vol. 14, no. 50, pp. R1357–R1390, 2002.

[97] D. H. Torchinsky, F. Mahmood, A. T. Bollinger, I. Božović, and N. Gedik, "Fluctuating charge-density waves in a cuprate superconductor," *Nature Materials*, vol. 12, no. 5, pp. 387–391, 2013.

[98] S. J. Zhang, X. Y. Zhou, S. X. Xu, Q. Wu, L. Yue, Q. M. Liu, T. C. Hu, R. S. Li, J. Y. Yuan, C. C. Homes, G. D. Gu, T. Dong, and N. L. Wang, "Light-induced melting of competing stripe orders without introducing superconductivity in $La_{2-x}Ba_xCuO_4$," *Phys. Rev. X*, vol. 14, p. 011036, 2024.

[99] L. Perfetti, P. A. Loukakos, M. Lisowski, U. Bovensiepen, H. Eisaki, and M. Wolf, "Ultrafast electron relaxation in superconducting $Bi_2Sr_2CaCu_2O_{8+\delta}$ by time-resolved photoelectron spectroscopy," *Phys. Rev. Lett.*, vol. 99, no. 19, p. 197001, 2007.

[100] Y. Lu, "From itinerant to localized: an x-ray spectroscopic study of transition metal oxides," 2017.

[101] D. G. Hawthorn, F. He, L. Venema, H. Davis, A. J. Achkar, J. Zhang, R. Sutarto, H. Wadati, A. Radi, T. Wilson, G. Wright, K. M. Shen, J. Geck, H. Zhang, V. Novák, and G. A. Sawatzky, "An in-vacuum diffractometer for resonant elastic soft x-ray scattering," *Review of Scientific Instruments*, vol. 82, no. 7, p. 073104, 2011.

[102] E. Weschke and E. Schierle, "The UE46 PGM-1 beamline at BESSY II," *Journal of large-scale research facilities JLSRF*, vol. 4, pp. A127–A127, 2018.

[103] R. Vasquez, B. Hunt, and M. Foote, "Nonaqueous chemical etch for $YBa_2Cu_3O_{7-x}$," *Applied physics letters*, vol. 53, no. 26, pp. 2692–2694, 1988.

[104] B. Keimer and J. E. Moore, "The physics of quantum materials," *Nature Physics*, vol. 13, no. 11, pp. 1045–1055, 2017.

[105] R. Comin and A. Damascelli, "Resonant X-ray scattering studies of charge order in cuprates," *Annu. Rev. Conden. Ma. P.*, vol. 7, no. 1, pp. 369–405, 2016.

[106] J. Chang, E. Blackburn, O. Ivashko, A. T. Holmes, N. B. Christensen, M. Hücker, R. Liang, D. A. Bonn, W. N. Hardy, U. Rütt, M. v. Zimmermann, E. M. Forgan, and S. M. Hayden, "Magnetic field controlled charge density wave coupling in underdoped $YBa_2Cu_3O_{6+x}$," *Nat. Commun.*, vol. 7, p. 11494, 2016.

[107] H.-H. Kim, E. Lefrançois, K. Kummer, R. Fumagalli, N. B. Brookes, D. Betto, S. Nakata, M. Tortora, J. Porras, T. Loew, M. E. Barber, L. Braicovich, A. P. Mackenzie, C. W. Hicks, B. Keimer, M. Minola, and M. Le Tacon, "Charge density waves in $YBa_2Cu_3O_{6.67}$ probed by resonant x-ray scattering under uniaxial compression," *Phys. Rev. Lett.*, vol. 126, p. 037002, 2021.

[108] W. Tabis, B. Yu, I. Bialo, M. Bluschke, T. Kolodziej, A. Kozlowski, E. Blackburn, K. Sen, E. M. Forgan, M. v. Zimmermann, Y. Tang, E. Weschke, B. Vignolle, M. Hepting, H. Gretarsson, R. Sutarto, F. He, M. Le Tacon, N. Barišić, G. Yu, and M. Greven, "Synchrotron x-ray scattering study of charge-density-wave order in $HgBa_2CuO_{4+\delta}$," *Phys. Rev. B*, vol. 96, p. 134510, 2017.

[109] M. Bluschke, M. Yaari, E. Schierle, G. Bazalitsky, J. Werner, E. Weschke, and A. Keren, "Adiabatic variation of the charge density wave phase diagram in the 123 cuprate $(Ca_xLa_{1-x})(Ba_{1.75-x}La_{0.25+x})Cu_3O_y$," *Phys. Rev. B*, vol. 100, p. 035129, 2019.

[110] H. Jang, S. Song, T. Kihara, Y. Liu, S.-J. Lee, S.-Y. Park, M. Kim, H.-D. Kim, G. Coslovich, S. Nakata, Y. Kubota, I. Inoue, K. Tamasaku, M. Yabashi, H. Lee, C. Song, H. Nojiri, B. Keimer, C.-C. Kao, and J.-S. Lee, "Characterization of photoinduced normal state through charge density wave in superconducting $YBa_2Cu_3O_{6.67}$," *Science Advances*, vol. 8, no. 6, p. eabk0832, 2022.

[111] Y. Ando, A. N. Lavrov, and K. Segawa, "Magnetoresistance anomalies in antiferromagnetic $YBa_2Cu_3O_{6+x}$: Fingerprints of charged stripes," *Phys. Rev. Lett.*, vol. 83, pp. 2813–2816, 1999.

[112] T. Noda, H. Eisaki, and S. Uchida, "Evidence for one-dimensional charge transport in $La_{2-x-y}Nd_ySr_xCuO_4$.," *Science*, vol. 286, p. 265, 1998.

[113] H. A. Mook, P. Dai, F. Dogan, and R. D. Hunt, "One-dimensional nature of the magnetic fluctuations in $YBa_2Cu_3O_{6.6}$," *Nature*, vol. 404, no. 6779, pp. 729–731, 2000.

[114] C. Stock, W. J. L. Buyers, R. Liang, D. Peets, Z. Tun, D. Bonn, W. N. Hardy, and R. J. Birgeneau, "Dynamic stripes and resonance in the superconducting and normal phases of $YBa_2Cu_3O_{6.5}$ ortho-II superconductor," *Phys. Rev. B*, vol. 69, p. 014502, 2004.

[115] V. Hinkov, P. Bourges, S. Pailhès, Y. Sidis, A. Ivanov, C. D. Frost, T. G. Perring, C. T. Lin, D. P. Chen, and B. Keimer, "Spin dynamics in the pseudogap state of a high-temperature superconductor," *Nature Physics*, vol. 3, p. 780, 2007.

[116] A. Mesaros, K. Fujita, H. Eisaki, S. Uchida, J. C. Davis, S. Sachdev, J. Zaanen, M. J. Lawler, and E.-A. Kim, "Topological defects coupling smectic modulations to intra unit-cell nematicity in cuprates," *Science*, vol. 333, no. 6041, pp. 426–430, 2011.

[117] J. Wu, A. T. Bollinger, X. He, G. D. Gu, H. Miao, M. P. M. Dean, I. K. Robinson, and I. Božović, "Angle-resolved transport measurements reveal electronic nematicity in cuprate superconductors," *Journal of Superconductivity and Novel Magnetism*, vol. 33, no. 1, pp. 87–92, 2019.

[118] S. Wang, N. Kennedy, K. Fujita, S.-i. Uchida, H. Eisaki, P. D. Johnson, J. S. Davis, and S. M. O'Mahony, "Discovery of orbital ordering in $Bi_2Sr_2CaCu_2O_{8+x}$," *Nature Materials*, vol. 23, no. 4, pp. 492–498, 2024.

[119] S. A. Kivelson, E. Fradkin, and V. J. Emery, "Electronic liquid-crystal phases of a doped Mott insulator," *Nature*, vol. 393, pp. 550–553, 1998.

[120] J. Zaanen and O. Gunnarsson, "Charged magnetic domain lines and the magnetism of high-T_c oxides," *Phys. Rev. B*, vol. 40, no. 10, pp. 7391–7394, 1989.

[121] K. Machida, "Magnetism in La_2CuO_4 based compounds," *Physica C*, vol. 158, no. 1-2, pp. 192–196, 1989.

[122] M. Kato, K. Machida, H. Nakanishi, and M. Fujita, "Soliton lattice modulation of incommensurate spin density wave in two dimensional Hubbard model - A mean field study," *Journal of the Physical Society of Japan*, vol. 59, no. 3, pp. 1047–1058, 1990.

[123] V. Emery and S. Kivelson, "Frustrated electronic phase separation and high-temperature superconductors," *Physica C: Superconductivity*, vol. 209, no. 4, pp. 597–621, 1993.

[124] S. R. White and D. J. Scalapino, "Density matrix renormalization group study of the striped phase in the 2D $t - J$ model," *Phys. Rev. Lett.*, vol. 80, pp. 1272–1275, 1998.

[125] C. J. Halboth and W. Metzner, "d-wave superconductivity and pomeranchuk instability in the two-dimensional hubbard model," *Phys. Rev. Lett.*, vol. 85, pp. 5162–5165, 2000.

[126] J. Lorenzana and G. Seibold, "Metallic mean-field stripes, incommensurability, and chemical potential in cuprates," *Physical Review Letters*, vol. 89, no. 13, p. 136401, 2002.

[127] S. A. K. et al., "How to detect fluctuating stripes in the high-temperature superconductors," *Rev. Mod. Phys.*, vol. 75, no. 4, pp. 1201–1241, 2003.

[128] S. Gerber, H. Jang, H. Nojiri, S. Matsuzawa, H. Yasumura, D. A. Bonn, R. Liang, W. N. Hardy, Z. Islam, A. Mehta, S. Song, M. Sikorski, D. Stefanescu, Y. Feng, S. A. Kivelson, T. P. Devereaux, Z.-X. Shen, C.-C. Kao, W.-S. Lee, D. Zhu, and J.-S. Lee, "Three-dimensional charge density wave order in $YBa_2Cu_3O_{6.67}$ at high magnetic fields," *Science*, vol. 350, no. 6263, pp. 949–952, 2015.

[129] S. A. Kivelson, E. Fradkin, and T. H. Geballe, "Quasi-one-dimensional dynamics and nematic phases in the two-dimensional Emery model," *Physical Review B*, vol. 69, no. 14, p. 144505, 2004.

[130] M. H. Fischer, S. Wu, M. Lawler, A. Paramekanti, and E.-A. Kim, "Nematic and spin-charge orders driven by hole-doping a charge-transfer insulator," *New Journal of Physics*, vol. 16, no. 9, p. 093057, 2014.

[131] H. Yamase, "Theoretical insights into electronic nematic order, bond-charge orders, and plasmons in cuprate superconductors," *Journal of the Physical Society of Japan*, vol. 90, p. 111011, 2021.

[132] N. Gedik, M. Langner, J. Orenstein, S. Ono, Y. Abe, and Y. Ando, "Abrupt transition in quasiparticle dynamics at optimal doping in a cuprate superconductor system," *Phys. Rev. Lett.*, vol. 95, p. 117005, 2005.

[133] G. L. Dakovski, W.-S. Lee, D. G. Hawthorn, N. Garner, D. Bonn, W. Hardy, R. Liang, M. C. Hoffmann, and J. J. Turner, "Enhanced coherent oscillations in the superconducting state of underdoped $YBa_2Cu_3O_{6+x}$ induced via ultrafast terahertz excitation," *Physical Review B*, vol. 91, no. 22, p. 220506, 2015.

[134] F. Boschini, E. H. da Silva Neto, E. Razzoli, M. Zonno, S. Peli, R. P. Day, M. Michiardi, M. Schneider, B. Zwartsenberg, P. Nigge, R. D. Zhong, J. Schneeloch, G. D. Gu, S. Zhdanovich, A. K. Mills, G. Levy, D. J. Jones, C. Giannetti, and A. Damascelli, "Collapse of superconductivity in cuprates via ultrafast quenching of phase coherence," *Nature Materials*, vol. 17, no. 5, pp. 416–420, 2018.

[135] M. Mitrano, S. Lee, A. A. Husain, L. Delacretaz, M. Zhu, G. de la Peña Munoz, S. X.-L. Sun, Y. I. Joe, A. H. Reid, S. F. Wandel, G. Coslovich, W. Schlotter, T. van Driel, J. Schneeloch, G. D. Gu, S. Hartnoll, N. Goldenfeld, and P. Abbamonte, "Ultrafast time-resolved x-ray scattering reveals diffusive charge order dynamics in $La_{2-x}Ba_xCuO_4$," *Science Advances*, vol. 5, no. 8, p. eaax3346, 2019.

[136] M. Mitrano, S. Lee, A. A. Husain, M. Zhu, G. de la Peña Munoz, S. X.-L. Sun, Y. I. Joe, A. H. Reid, S. F. Wandel, G. Coslovich, W. Schlotter, T. van Driel, J. Schneeloch, G. D. Gu, N. Goldenfeld, and P. Abbamonte, "Evidence for photoinduced sliding of the charge-order condensate in $La_{1.875}Ba_{0.125}CuO_4$," *Physical Review B*, vol. 100, no. 20, p. 205125, 2019.

[137] W. Hu, S. Kaiser, D. Nicoletti, C. R. Hunt, I. Gierz, M. C. Hoffmann, M. L. Tacon, T. Loew, B. Keimer, and A. Cavalleri, "Optically enhanced coherent transport in $YBa_2Cu_3O_{6.5}$ by ultrafast redistribution of interlayer coupling," *Nature Materials*, vol. 13, no. 7, pp. 705–711, 2014.

[138] S. Kaiser, C. R. Hunt, D. Nicoletti, W. Hu, I. Gierz, H. Y. Liu, M. L. Tacon, T. Loew, D. Haug, B. Keimer, and A. Cavalleri, "Optically induced coherent transport far above T_c in underdoped $YBa_2Cu_3O_{6.}$," *Physical Review B*, vol. 89, no. 18, 2014.

[139] M. Först, R. Tobey, H. Bromberger, S. Wilkins, V. Khanna, A. Caviglia, Y.-D. Chuang, W. Lee, W. Schlotter, J. Turner, M. Minitti, O. Krupin, Z. Xu, J. Wen, G. Gu, S. Dhesi, A. Cavalleri, and J. Hill, "Melting of charge stripes in vibrationally driven $La_{1.875}Ba_{0.125}CuO_4$: Assessing the respective roles of electronic and lattice order in frustrated superconductors," *Physical Review Letters*, vol. 112, no. 15, p. 157002, 2014.

[140] M. Först, A. Frano, S. Kaiser, R. Mankowsky, C. R. Hunt, J. J. Turner, G. L. Dakovski, M. P. Minitti, J. Robinson, T. Loew, M. L. Tacon, B. Keimer, J. P. Hill, A. Cavalleri, and S. S. Dhesi, "Femtosecond x rays link melting of charge-density wave correlations and light-enhanced coherent transport in $YBa_2Cu_3O_{6.6}$.," *Physical Review B*, vol. 90, no. 18, p. 184514, 2014.

[141] V. Khanna, R. Mankowsky, M. Petrich, H. Bromberger, S. A. Cavill, E. Möhr-Vorobeva, D. Nicoletti, Y. Laplace, G. D. Gu, J. P. Hill, M. Först, A. Cavalleri, and S. S. Dhesi, "Restoring interlayer Josephson coupling in $La_{1.885}Ba_{0.115}CuO_4$ by charge transfer melting of stripe order," *Phys. Rev. B*, vol. 93, p. 224522, 2016.

[142] D. R. Baykusheva, H. Jang, A. A. Husain, S. Lee, S. F. TenHuisen, P. Zhou, S. Park, H. Kim, J.-K. Kim, H.-D. Kim, M. Kim, S.-Y. Park, P. Abbamonte, B. Kim, G. Gu, Y. Wang, and M. Mitrano, "Ultrafast renormalization of the on-site Coulomb repulsion in a cuprate superconductor," *Physical Review X*, vol. 12, no. 1, p. 011013, 2022.

[143] J. Fink, E. Schierle, E. Weschke, J. Geck, D. Hawthorn, V. Soltwisch, H. Wadati, H.-H. Wu, H. A. Durr, N. Wizent, B. Buchner, and G. A. Sawatzky, "Charge ordering in $La_{1.8-x}Eu_{0.2}Sr_xCuO_4$ studied by resonant soft x-ray diffraction," *Phys. Rev. B*, vol. 79, no. 10, p. 100502, 2009.

[144] M. X. Na, F. Boschini, A. K. Mills, M. Michiardi, R. P. Day, B. Zwartsenberg, G. Levy, S. Zhdanovich, A. F. Kemper, D. J. Jones, and A. Damascelli, "Establishing nonthermal regimes in pump-probe electron relaxation dynamics," *Phys. Rev. B*, vol. 102, p. 184307, 2020.

[145] Y. Kohsaka, C. Taylor, K. Fujita, A. Schmidt, C. Lupien, T. Hanaguri, M. Azuma, M. Takano, H. Eisaki, H. Takagi, S. Uchida, and J. C. Davis, "An intrinsic bond-centered electronic glass with unidirectional domains in underdoped cuprates," *Science*, vol. 315, no. 5817, pp. 1380–1385, 2007.

[146] R. Comin, R. Sutarto, E. H. da Silva Neto, L. Chauviere, R. Liang, W. N. Hardy, D. A. Bonn, F. He, G. A. Sawatzky, and A. Damascelli, "Broken translational and rotational symmetry via charge stripe order in underdoped $YBa_2Cu_3O_{6+y}$," *Science*, vol. 347, no. 6228, pp. 1335–1339, 2015.

[147] C. McMahon, A. J. Achkar, E. H. da Silva Neto, I. Djianto, J. Menard, F. He, R. Sutarto, R. Comin, R. Liang, D. A. Bonn, W. N. Hardy, A. Damascelli, and D. G. Hawthorn, "Orbital symmetries of charge density wave order in $YBa_2Cu_3O_{6+x}$," *Science Advances*, vol. 6, no. 45, p. eaay0345, 2020.

[148] M. Kang, J. Pelliciari, A. Frano, N. Breznay, E. Schierle, E. Weschke, R. Sutarto, F. He, P. Shafer, E. Arenholz, M. Chen, K. Zhang, A. Ruiz, Z. Hao, S. Lewin, J. Analytis, Y. Krockenberger, H. Yamamoto, T. Das, and R. Comin, "Evolution of charge

order topology across a magnetic phase transition in cuprate superconductors," *Nature Physics*, vol. 15, no. 4, 2019.

[149] F. Boschini, M. Minola, R. Sutarto, E. Schierle, M. Bluschke, S. Das, Y. Yang, M. Michiardi, Y. C. Shao, X. Feng, S. Ono, R. D. Zhong, J. A. Schneeloch, G. D. Gu, E. Weschke, F. He, Y. D. Chuang, B. Keimer, A. Damascelli, A. Frano, and E. H. da Silva Neto, "Dynamic electron correlations with charge order wavelength along all directions in the copper oxide plane," *Nature Communications*, vol. 12, no. 1, p. 597, 2021.

[150] S. D. Conte, C. Giannetti, G. Coslovich, F. Cilento, D. Bossini, T. Abebaw, F. Banfi, G. Ferrini, H. Eisaki, M. Greven, A. Damascelli, D. van der Marel, and F. Parmigiani, "Disentangling the electronic and phononic glue in a high-T_c superconductor," *Science*, vol. 335, no. 6076, pp. 1600–1603, 2012.

[151] M. L. Tacon, A. Bosak, S. M. Souliou, G. Dellea, T. Loew, R. Heid, K.-P. Bohnen, G. Ghiringhelli, M. Krisch, and B. Keimer, "Inelastic x-ray scattering in $YBa_2Cu_3O_{6.6}$ reveals giant phonon anomalies and elastic central peak due to charge-density-wave formation," *Nature Physics*, vol. 10, no. 1, pp. 52–58, 2013.

[152] B. I. Halperin, T. C. Lubensky, and S.-K. Ma, "First-order phase transitions in superconductors and smectic-A liquid crystals," *Phys. Rev. Lett.*, vol. 32, pp. 292–295, 1974.

[153] S. Lee, E. W. Huang, T. A. Johnson, X. Guo, A. A. Husain, M. Mitrano, K. Lu, A. V. Zakrzewski, G. A. de la Peña, Y. Peng, H. Huang, S.-J. Lee, H. Jang, J.-S. Lee, Y. I. Joe, W. B. Doriese, P. Szypryt, D. S. Swetz, S. Chi, A. A. Aczel, G. J. MacDougall, S. A. Kivelson, E. Fradkin, and P. Abbamonte, "Generic character of charge and spin density waves in superconducting cuprates," *Proceedings of the National Academy of Sciences*, vol. 119, no. 15, 2022.

[154] Q. Wang, M. Horio, K. von Arx, Y. Shen, D. J. Mukkattukavil, Y. Sassa, O. Ivashko, C. Matt, S. Pyon, T. Takayama, H. Takagi, T. Kurosawa, N. Momono, M. Oda, T. Adachi, S. Haidar, Y. Koike, Y. Tseng, W. Zhang, J. Zhao, K. Kummer, M. Garcia-Fernandez, K.-J. Zhou, N. Christensen, H. Rønnow, T. Schmitt, and J. Chang, "High-temperature charge-stripe correlations in $La_{1.675-x}Eu_{0.2}Sr_{0.125}CuO_4$," *Physical Review Letters*, vol. 124, no. 18, p. 187002, 2020.

[155] A. Zong, A. Kogar, Y.-Q. Bie, T. Rohwer, C. Lee, E. Baldini, E. Ergeçen, M. B. Yilmaz, B. Freelon, E. J. Sie, H. Zhou, J. Straquadine, P. Walmsley, P. E. Dolgirev,

A. V. Rozhkov, I. R. Fisher, P. Jarillo-Herrero, B. V. Fine, and N. Gedik, "Evidence for topological defects in a photoinduced phase transition," *Nature Physics*, vol. 15, no. 1, pp. 27–31, 2018.

[156] M. Hücker, M. v. Zimmermann, G. D. Gu, Z. J. Xu, J. S. Wen, G. Xu, H. J. Kang, A. Zheludev, and J. M. Tranquada, "Stripe order in superconducting $La_{2-x}Ba_xCuO_4$ ($0.095 \leq x \leq 0.155$)," *Phys. Rev. B*, vol. 83, no. 10, p. 104506, 2011.

[157] X. M. Chen, C. Mazzoli, Y. Cao, V. Thampy, A. M. Barbour, W. Hu, M. Lu, T. A. Assefa, H. Miao, G. Fabbris, G. D. Gu, J. M. Tranquada, M. P. M. Dean, S. B. Wilkins, and I. K. Robinson, "Charge density wave memory in a cuprate superconductor," *Nature Communications*, vol. 10, no. 1, 2019.

[158] W. Lee, Y. Chuang, R. Moore, Y. Zhu, L. Patthey, M. Trigo, D. Lu, P. Kirchmann, O. Krupin, M. Yi, M. Langner, N. Huse, J. Robinson, Y. Chen, S. Zhou, G. Coslovich, B. Huber, D. Reis, R. Kaindl, R. Schoenlein, D. Doering, P. Denes, W. Schlotter, J. Turner, S. Johnson, M. Först, T. Sasagawa, Y. Kung, A. Sorini, A. Kemper, B. Moritz, T. Devereaux, D.-H. Lee, Z. Shen, and Z. Hussain, "Phase fluctuations and the absence of topological defects in a photo-excited charge-ordered nickelate," *Nature Communications*, vol. 3, no. 1, 2012.

[159] Y. Lubashevsky, L. Pan, T. Kirzhner, G. Koren, and N. P. Armitage, "Optical birefringence and dichroism of cuprate superconductors in the THz regime," *Phys. Rev. Lett.*, vol. 112, p. 147001, 2014.

[160] J. Ishioka, Y. H. Liu, K. Shimatake, T. Kurosawa, K. Ichimura, Y. Toda, M. Oda, and S. Tanda, "Chiral charge-density waves," *Physical Review Letters*, vol. 105, no. 17, p. 176401, 2010.

[161] M. S. Ikeda, T. Worasaran, E. W. Rosenberg, J. C. Palmstrom, S. A. Kivelson, and I. R. Fisher, "Elastocaloric signature of nematic fluctuations," *Proceedings of the National Academy of Sciences*, vol. 118, no. 37, p. e2105911118, 2021.

[162] W. K. Huang, S. Hosoi, M. Čulo, S. Kasahara, Y. Sato, K. Matsuura, Y. Mizukami, M. Berben, N. E. Hussey, H. Kontani, T. Shibauchi, and Y. Matsuda, "Non-fermi liquid transport in the vicinity of the nematic quantum critical point of superconducting $FeSe_{1-x}S_x$," *Phys. Rev. Res.*, vol. 2, p. 033367, 2020.

[163] A. I. Coldea, S. F. Blake, S. Kasahara, A. A. Haghighirad, M. D. Watson, W. Knafo, E. S. Choi, A. McCollam, P. Reiss, T. Yamashita, *et al.*, "Evolution of the low-

temperature Fermi surface of superconducting $FeSe_{1-x}S_x$ across a nematic phase transition," *npj Quantum Materials*, vol. 4, no. 1, p. 2, 2019.

[164] C. Howald, H. Eisaki, N. Kaneko, M. Greven, and A. Kapitulnik, "Periodic density-of-states modulations in superconducting $Bi_2Sr_2CaCu_2O_{8+\delta}$," *Phys. Rev. B*, vol. 67, p. 014533, 2003.

[165] K. Fujita, M. H. Hamidian, S. D. Edkins, C. K. Kim, Y. Kohsaka, M. Azuma, M. Takano, H. Takagi, H. Eisaki, S. Uchida, A. Allais, M. J. Lawler, E.-A. Kim, S. Sachdev, and J. C. S. Davis, "Direct phase-sensitive identification of a *d*-form factor density wave in underdoped cuprates," *Proceedings of the National Academy of Sciences*, vol. 111, no. 30, pp. E3026–E3032, 2014.

[166] P. G. Radaelli, D. G. Hinks, A. W. Mitchell, B. A. Hunter, J. L. Wagner, B. Dabrowski, K. G. Vandervoort, H. K. Viswanathan, and J. D. Jorgensen, "Structural and superconducting properties of $La_{2-x}Sr_xCuO_4$ as a function of Sr content," *Phys. Rev. B*, vol. 49, pp. 4163–4175, 1994.

[167] B. Büchner, M. Breuer, A. Freimuth, and A. P. Kampf, "Critical buckling for the disappearance of superconductivity in rare-earth-doped $La_{2-x}Sr_xCuO_4$," *Phys. Rev. Lett.*, vol. 73, pp. 1841–1844, 1994.

[168] S.-H. Baek, P. C. Hammel, M. Hücker, B. Büchner, U. Ammerahl, A. Revcolevschi, and B. J. Suh, "Structural transitions in a doped lanthanum cuprate," *Phys. Rev. B*, vol. 87, p. 174505, 2013.

[169] O. Cyr-Choinière, R. Daou, F. Laliberté, C. Collignon, S. Badoux, D. LeBoeuf, J. Chang, B. J. Ramshaw, D. A. Bonn, W. N. Hardy, R. Liang, J.-Q. Yan, J.-G. Cheng, J.-S. Zhou, J. B. Goodenough, S. Pyon, T. Takayama, H. Takagi, N. Doiron-Leyraud, and L. Taillefer, "Pseudogap temperature T^* of cuprate superconductors from the nernst effect," *Phys. Rev. B*, vol. 97, p. 064502, 2018.

[170] C. Collignon, A. Ataei, A. Gourgout, S. Badoux, M. Lizaire, A. Legros, S. Licciardello, S. Wiedmann, J.-Q. Yan, J.-S. Zhou, Q. Ma, B. D. Gaulin, N. Doiron-Leyraud, and L. Taillefer, "Thermopower across the phase diagram of the cuprate $La_{1.6-x}Nd_{0.4}Sr_xCuO_4$: Signatures of the pseudogap and charge density wave phases," *Phys. Rev. B*, vol. 103, p. 155102, 2021.

[171] Q. Ma, K. C. Rule, Z. W. Cronkwright, M. Dragomir, G. Mitchell, E. M. Smith, S. Chi, A. I. Kolesnikov, M. B. Stone, and B. D. Gaulin, "Parallel spin stripes and

their coexistence with superconducting ground states at optimal and high doping in $La_{1.6-x}Nd_{0.4}Sr_xCuO_4$," *Phys. Rev. Res.*, vol. 3, p. 023151, 2021.

[172] H. Miao, G. Fabbris, R. Koch, D. Mazzone, C. Nelson, R. Acevedo-Esteves, G. Gu, Y. Li, T. Yilimaz, K. Kaznatcheev, *et al.*, "Charge density waves in cuprate superconductors beyond the critical doping," *npj Quantum Materials*, vol. 6, no. 1, p. 31, 2021.

[173] S. Mukhopadhyay, R. Sharma, C. K. Kim, S. D. Edkins, M. H. Hamidian, H. Eisaki, S. ichi Uchida, E.-A. Kim, M. J. Lawler, A. P. Mackenzie, J. C. S. Davis, and K. Fujita, "Evidence for a vestigial nematic state in the cuprate pseudogap phase," *Proceedings of the National Academy of Sciences*, vol. 116, no. 27, pp. 13249–13254, 2019.

[174] M. Platé, J. Mottershead, I. Elfimov, D. Peets, R. Liang, D. Bonn, W. Hardy, S. Chiuzbaian, M. Falub, M. Shi, *et al.*, "Fermi surface and quasiparticle excitations of overdoped $Tl_2Ba_2CuO_{6+\delta}$," *Physical Review Letters*, vol. 95, no. 7, p. 077001, 2005.

[175] A. V. Maharaj, I. Esterlis, Y. Zhang, B. J. Ramshaw, and S. A. Kivelson, "Hall number across a van hove singularity," *Phys. Rev. B*, vol. 96, p. 045132, 2017.

[176] S. Arumugam, N. Mori, N. Takeshita, H. Takashima, T. Noda, H. Eisaki, and S. Uchida, "Transport measurements of La-Nd-Sr-Cu-O superconductors under hydrostatic and uniaxial pressure," *Physica C: Superconductivity*, vol. 341-348, pp. 1759–1762, 2000.

[177] N. Takeshita, T. Sasagawa, T. Sugioka, Y. Tokura, and H. Takagi, "Gigantic anisotropic uniaxial pressure effect on superconductivity within the CuO_2 plane of $La_{1.64}Eu_{0.2}Sr_{0.16}CuO_4$: Strain control of stripe criticality," *Journal of the Physical Society of Japan*, vol. 73, no. 5, pp. 1123–1126, 2004.

[178] T. Sasagawa, Suryadijaya, K. Shimatani, and H. Takagi, "Control of stripes/superconductivity competition in $(La, Eu, Sr)_2CuO_4$ crystals using uniaxial pressure," *Physica B: Condensed Matter*, vol. 359-361, pp. 436–438, 2005.

[179] Z. Guguchia, D. Das, C. N. Wang, T. Adachi, N. Kitajima, M. Elender, F. Brückner, S. Ghosh, V. Grinenko, T. Shiroka, M. Müller, C. Mudry, C. Baines, M. Bartkowiak, Y. Koike, A. Amato, J. M. Tranquada, H.-H. Klauss, C. W. Hicks, and H. Luetkens, "Using uniaxial stress to probe the relationship between competing superconducting states in a cuprate with spin-stripe order," *Phys. Rev. Lett.*, vol. 125, p. 097005, 2020.

[180] H.-H. Kim, S. M. Souliou, M. E. Barber, E. Lefrançois, M. Minola, M. Tortora, R. Heid, N. Nandi, R. A. Borzi, G. Garbarino, A. Bosak, J. Porras, T. Loew, M. König, P. J. W. Moll, A. P. Mackenzie, B. Keimer, C. W. Hicks, and M. L. Tacon, "Uniaxial pressure control of competing orders in a high-temperature superconductor," *Science*, vol. 362, no. 6418, pp. 1040–1044, 2018.

[181] J. Choi, Q. Wang, S. Jöhr, N. B. Christensen, J. Küspert, D. Bucher, D. Biscette, M. H. Fischer, M. Hücker, T. Kurosawa, N. Momono, M. Oda, O. Ivashko, M. v. Zimmermann, M. Janoschek, and J. Chang, "Unveiling unequivocal charge stripe order in a prototypical cuprate superconductor," *Phys. Rev. Lett.*, vol. 128, p. 207002, 2022.

[182] T. J. Boyle, M. Walker, A. Ruiz, E. Schierle, Z. Zhao, F. Boschini, R. Sutarto, T. D. Boyko, W. Moore, N. Tamura, F. He, E. Weschke, A. Gozar, W. Peng, A. C. Komarek, A. Damascelli, C. Schüßler-Langeheine, A. Frano, E. H. da Silva Neto, and S. Blanco-Canosa, "Large response of charge stripes to uniaxial stress in $La_{1.475}Nd_{0.4}Sr_{0.125}CuO_4$," *Phys. Rev. Research*, vol. 3, p. L022004, 2021.

[183] E. Wahlberg, R. Arpaia, G. Seibold, M. Rossi, R. Fumagalli, E. Trabaldo, N. B. Brookes, L. Braicovich, S. Caprara, U. Gran, G. Ghiringhelli, T. Bauch, and F. Lombardi, "Restored strange metal phase through suppression of charge density waves in underdoped $YBa_2Cu_3O_{7-\delta}$," *Science*, vol. 373, no. 6562, pp. 1506–1510, 2021.

[184] Z. Guguchia, D. Das, G. Simutis, T. Adachi, J. Küspert, N. Kitajima, M. Elender, V. Grinenko, O. Ivashko, M. v. Zimmermann, *et al.*, "Designing the stripe-ordered cuprate phase diagram through uniaxial-stress," *Proceedings of the National Academy of Sciences*, vol. 121, no. 1, p. e2303423120, 2024.

[185] Q. Wang, K. von Arx, D. G. Mazzone, S. Mustafi, M. Horio, J. Küspert, J. Choi, D. Bucher, H. Wo, J. Zhao, W. Zhang, T. C. Asmara, Y. Sassa, M. Månsson, N. B. Christensen, M. Janoschek, T. Kurosawa, N. Momono, M. Oda, M. H. Fischer, T. Schmitt, and J. Chang, "Uniaxial pressure induced stripe order rotation in $La_{1.88}Sr_{0.12}CuO_4$," *Nature Communications*, vol. 13, no. 1, p. 1795, 2022.

[186] R. Frison, J. Küspert, Q. Wang, O. Ivashko, M. v. Zimmermann, M. Meven, D. Bucher, J. Larsen, C. Niedermayer, M. Janoschek, T. Kurosawa, N. Momono, M. Oda, N. B. Christensen, and J. Chang, "Crystal symmetry of stripe-ordered $La_{1.88}Sr_{0.12}CuO_4$," *Phys. Rev. B*, vol. 105, p. 224113, 2022.

[187] D. Vaknin, S. K. Sinha, D. E. Moncton, D. C. Johnston, J. M. Newsam, C. R. Safinya, and H. E. King, "Antiferromagnetism in La_2CuO_{4-y}," *Phys. Rev. Lett.*, vol. 58, pp. 2802–2805, 1987.

[188] J. D. Axe, A. H. Moudden, D. Hohlwein, D. E. Cox, K. M. Mohanty, A. R. Moodenbaugh, and Y. Xu, "Structural phase transformations and superconductivity in $La_{2-x}Ba_xCuO_4$," *Phys. Rev. Lett.*, vol. 62, pp. 2751–2754, 1989.

[189] T. Suzuki and T. Fujita, "Anomalous Change in Crystalline Structure of $(La_{1-x}Ba_x)_2CuO_{4-\delta}$," *Journal of the Physical Society of Japan*, vol. 58, no. 6, pp. 1883–1886, 1989.

[190] A. P. Kampf, D. J. Scalapino, and S. R. White, "Stripe orientation in an anisotropic $t-J$ model," *Phys. Rev. B*, vol. 64, p. 052509, 2001.

[191] J. Sears, Y. Shen, M. J. Krogstad, H. Miao, E. S. Bozin, I. K. Robinson, G. D. Gu, R. Osborn, S. Rosenkranz, J. M. Tranquada, and M. P. M. Dean, "Structure of charge density waves in $La_{1.875}Ba_{0.125}CuO_4$," *Phys. Rev. B*, vol. 107, p. 115125, 2023.

[192] D. G. Hawthorn, F. He, L. Venema, H. Davis, A. J. Achkar, J. Zhang, R. Sutarto, H. Wadati, A. Radi, T. Wilson, G. Wright, K. M. Shen, J. Geck, H. Zhang, V. Novák, and G. A. Sawatzky, "An in-vacuum diffractometer for resonant elastic soft x-ray scattering," *Rev. Sci. Instrum.*, vol. 82, no. 7, p. 073104, 2011.

[193] A. J. Achkar, T. Z. Regier, H. Wadati, Y.-J. Kim, H. Zhang, and D. G. Hawthorn, "Bulk sensitive x-ray absorption spectroscopy free of self-absorption effects," *Phys. Rev. B*, vol. 83, p. 081106(R), 2011.

[194] J. L. Sarrao, D. Mandrus, A. Migliori, Z. Fisk, I. Tanaka, H. Kojima, P. C. Canfield, and P. D. Kodali, "Complete elastic moduli of $La_{2-x}Sr_xCuO_4$ (x=0.00 and 0.14) near the tetragonal-orthorhombic structural phase transition," *Phys. Rev. B*, vol. 50, pp. 13125–13131, 1994.

[195] R. Arpaia and G. Ghiringhelli, "Charge order at high temperature in cuprate superconductors," *Journal of the Physical Society of Japan*, vol. 90, no. 11, p. 111005, 2021.

[196] H. Sun, M. Huo, X. Hu, J. Li, Z. Liu, Y. Han, L. Tang, Z. Mao, P. Yang, B. Wang, J. Cheng, D.-X. Yao, G.-M. Zhang, and M. Wang, "Signatures of superconductivity near 80 K in a nickelate under high pressure," *Nature*, vol. 621, no. 7979, pp. 493–498, 2023.

[197] X. Chen, J. Choi, Z. Jiang, J. Mei, K. Jiang, J. Li, S. Agrestini, M. Garcia-Fernandez, H. Sun, X. Huang, *et al.*, "Electronic and magnetic excitations in $La_3Ni_2O_7$," *Nature communications*, vol. 15, no. 1, p. 9597, 2024.

[198] Z. Liu, H. Sun, M. Huo, X. Ma, Y. Ji, E. Yi, L. Li, H. Liu, J. Yu, Z. Zhang, Z. Chen, F. Liang, H. Dong, H. Guo, D. Zhong, B. Shen, S. Li, and M. Wang, "Evidence for charge and spin density waves in single crystals of $La_3Ni_2O_7$ and $La_3Ni_2O_6$," *Science China Physics, Mechanics and Astronomy*, vol. 66, no. 1, p. 217411, 2022.

[199] G. Wu, J. J. Neumeier, and M. F. Hundley, "Magnetic susceptibility, heat capacity, and pressure dependence of the electrical resistivity of $La_3Ni_2O_7$ and $La_4Ni_3O_{10}$," *Phys. Rev. B*, vol. 63, p. 245120, 2001.

[200] M. Kakoi, T. Oi, Y. Ohshita, M. Yashima, K. Kuroki, T. Kato, H. Takahashi, S. Ishiwata, Y. Adachi, N. Hatada, T. Uda, and H. Mukuda, "Multiband metallic ground state in multilayered nickelates $La_3Ni_2O_7$ and $La_4Ni_3O_{10}$ probed by ^{139}La-NMR at ambient pressure," *Journal of the Physical Society of Japan*, vol. 93, no. 5, p. 053702, 2024.

[201] Z. Dan, Y. Zhou, M. Huo, Y. Wang, L. Nie, M. Wang, T. Wu, and X. Chen, "Spin-density-wave transition in double-layer nickelate $La_3Ni_2O_7$," 2024. arXiv:2402.03952 [cond-mat].

[202] K. Chen, X. Liu, J. Jiao, M. Zou, C. Jiang, X. Li, Y. Luo, Q. Wu, N. Zhang, Y. Guo, and L. Shu, "Evidence of spin density waves in $La_3Ni_2O_{7-\delta}$," *Phys. Rev. Lett.*, vol. 132, p. 256503, 2024.

[203] R. Khasanov, T. J. Hicken, D. J. Gawryluk, L. P. Sorel, S. Bötzel, F. Lechermann, I. M. Eremin, H. Luetkens, and Z. Guguchia, "Pressure-induced split of the density wave transitions in $La_3Ni_2O_{7-\delta}$," 2024. arXiv:2402.10485 [cond-mat].

[204] X. Chen, J. Zhang, A. S. Thind, S. Sharma, H. LaBollita, G. Peterson, H. Zheng, D. Phelan, A. S. Botana, R. F. Klie, and J. F. Mitchell, "Polymorphism in Ruddlesden-Popper $La_3Ni_2O_7$: Discovery of a hidden phase with distinctive layer stacking," *Journal of the American Chemical Society*, vol. 146, no. 6, pp. 3640–3645, 2024.

[205] P. Puphal, P. Reiss, N. Enderlein, Y.-M. Wu, G. Khaliullin, V. Sundaramurthy, T. Priessnitz, M. Knauft, A. Suthar, L. Richter, M. Isobe, P. A. van Aken, H. Takagi,

B. Keimer, Y. E. Suyolcu, B. Wehinger, P. Hansmann, and M. Hepting, "Unconventional crystal structure of the high-pressure superconductor $La_3Ni_2O_7$," *Phys. Rev. Lett.*, vol. 133, p. 146002, Oct 2024.

[206] C. T. Parzyck, N. K. Gupta, Y. Wu, V. Anil, L. Bhatt, M. Bouliane, R. Gong, B. Z. Gregory, A. Luo, R. Sutarto, F. He, Y.-D. Chuang, T. Zhou, G. Herranz, L. F. Kourkoutis, A. Singer, D. G. Schlom, D. G. Hawthorn, and K. M. Shen, "Absence of $3a_0$ charge density wave order in the infinite-layer nickelate $NdNiO_2$," *Nature Materials*, vol. 23, no. 4, pp. 486–491, 2024.

[207] B.-X. Wang, S. Rosenkranz, X. Rui, J. Zhang, F. Ye, H. Zheng, R. F. Klie, J. F. Mitchell, and D. Phelan, "Antiferromagnetic defect structure in $LaNiO_{3-\delta}$ single crystals," *Phys. Rev. Mater.*, vol. 2, p. 064404, 2018.

[208] C. Piamonteze, F. M. F. de Groot, H. C. N. Tolentino, A. Y. Ramos, N. E. Massa, J. A. Alonso, and M. J. Martínez-Lope, "Spin-orbit-induced mixed-spin ground state in $RNiO_3$ perovskites probed by x-ray absorption spectroscopy: Insight into the metal-to-insulator transition," *Phys. Rev. B*, vol. 71, p. 020406, 2005.

[209] J. Liu, M. Kareev, B. Gray, J. W. Kim, P. Ryan, B. Dabrowski, J. W. Freeland, and J. Chakhalian, "Strain-mediated metal-insulator transition in epitaxial ultrathin films of $NdNiO_3$," *Applied Physics Letters*, vol. 96, no. 23, p. 233110, 2010.

[210] F. Y. Bruno, S. Valencia, R. Abrudan, Y. Dumont, C. Carrétéro, M. Bibes, and A. Barthélémy, "Probing the metal-insulator transition in nickelates using soft x-ray absorption spectroscopy," *Applied Physics Letters*, vol. 104, no. 2, p. 021920, 2014.

[211] M. Hepting, R. J. Green, Z. Zhong, M. Bluschke, Y. E. Suyolcu, S. Macke, A. Frano, S. Catalano, M. Gibert, R. Sutarto, F. He, G. Cristiani, G. Logvenov, Y. Wang, P. A. van Aken, P. Hansmann, M. Le Tacon, J.-M. Triscone, G. A. Sawatzky, B. Keimer, and E. Benckiser, "Complex magnetic order in nickelate slabs," *Nature Physics*, vol. 14, no. 11, pp. 1097–1102, 2018.

[212] J. P. Hannon, G. T. Trammell, M. Blume, and D. Gibbs, "X-ray resonance exchange scattering," *Physical Review Letters*, vol. 61, no. 10, pp. 1245–1248, 1988.

[213] M. W. Haverkort, N. Hollmann, I. P. Krug, and A. Tanaka, "Symmetry analysis of magneto-optical effects: The case of x-ray diffraction and x-ray absorption at the transition metal $L_{2,3}$ edge," *Phys. Rev. B*, vol. 82, p. 094403, 2010.

[214] J. Choi, J. Li, A. Nag, J. Pelliciari, H. Robarts, C. C. Tam, A. Walters, S. Agrestini, M. García-Fernández, D. Song, H. Eisaki, S. Johnston, R. Comin, H. Ding, and K.-J. Zhou, "Universal stripe symmetry of short-range charge density waves in cuprate superconductors," *Advanced Materials*, vol. 36, no. 3, p. 2307515, 2024.

[215] S.-W. Cheong, M. Fiebig, W. Wu, L. Chapon, and V. Kiryukhin, "Seeing is believing: visualization of antiferromagnetic domains," *npj Quantum Materials*, vol. 5, no. 1, pp. 1–10, 2020.

[216] W. Bao, Y. Qiu, Q. Huang, M. A. Green, P. Zajdel, M. R. Fitzsimmons, M. Zhernenkov, S. Chang, M. Fang, B. Qian, E. K. Vehstedt, J. Yang, H. M. Pham, L. Spinu, and Z. Q. Mao, "Tunable ($\delta\pi$, $\delta\pi$)-type antiferromagnetic order in α-Fe(Te,Se) superconductors," *Phys. Rev. Lett.*, vol. 102, p. 247001, 2009.

[217] S. Li, C. de la Cruz, Q. Huang, Y. Chen, J. W. Lynn, J. Hu, Y.-L. Huang, F.-C. Hsu, K.-W. Yeh, M.-K. Wu, and P. Dai, "First-order magnetic and structural phase transitions in $Fe_{1+y}Se_xTe_{1-x}$," *Phys. Rev. B*, vol. 79, p. 054503, 2009.

[218] E. E. Rodriguez, D. A. Sokolov, C. Stock, M. A. Green, O. Sobolev, J. A. Rodriguez-Rivera, H. Cao, and A. Daoud-Aladine, "Magnetic and structural properties near the Lifshitz point in $Fe_{1+x}Te$," *Phys. Rev. B*, vol. 88, p. 165110, 2013.

[219] A. E. Böhmer, J.-H. Chu, S. Lederer, and M. Yi, "Nematicity and nematic fluctuations in iron-based superconductors," *Nature Physics*, vol. 18, no. 12, pp. 1412–1419, 2022.

[220] R. M. Fernandes, P. P. Orth, and J. Schmalian, "Intertwined vestigial order in quantum materials: Nematicity and beyond," *Annual Review of Condensed Matter Physics*, vol. 10, no. Volume 10, 2019, pp. 133–154, 2019.